TAMPEREEN TEKNILLINEN YLIOPISTO
TAMPERE UNIVERSITY OF TECHNOLOGY

Sami Holopainen

Modeling of Mechanical Behavior of Amorphous Glassy Polymers

Julkaisu 1109 • Publication 1109

Tampere 2013

Tampereen teknillinen yliopisto. Julkaisu 1109
Tampere University of Technology. Publication 1109

Sami Holopainen

Modeling of Mechanical Behavior of Amorphous Glassy Polymers

Thesis for the degree of Doctor of Science in Technology to be presented with due permission for public examination and criticism in Konetalo Building, Auditorium K1702, at Tampere University of Technology, on the 1st of February 2013, at 12 noon.

Tampereen teknillinen yliopisto - Tampere University of Technology
Tampere 2013

ISBN 978-952-15-3005-0 (printed)
ISBN 978-952-15-3458-4 (PDF)
ISSN 1459-2045

Abstract

This thesis is concerned with the mechanical behavior and constitutive modeling of amorphous polymers. Amorphous polymers are employed in numerous applications that cover electronics, optical instruments, the automotive industry as well as consumer products. This broad range of applications is due to their good optical properties, high chemical resistance, high flexibility, good reforming properties, low weight relative to strength and their high energy absorption under impact loadings. Due to the numerous engineering applications, the accurate modeling of mechanical behavior is of major importance.

Amorphous polymers are characterized by a disordered microstructure which is formed of long polymer chains. In constitutive models for amorphous polymers, the microstructure is usually represented by an overall chain network which consists of an assembly of individual chains arranged in unit cells. The transition from microstructure to macroscopic level is performed via a homogenization which allows the micro-stretches to fluctuate around the macro-stretches. The present state of modeling amorphous glassy polymers is revealed through reviewing several models that can be considered as pioneering works in this field of research. To evaluate the models, several numerical examples are presented.

A comparison of the state-of-the-art model responses and the experimental data reveals that the models are not able to capture the transient effects after loading rate changes and long-term behavior involving recovery, which is highly overestimated by the models. To compensate for the shortcomings of the models, this thesis proposes an extension for the eight-chain version of the Boyce *et al.* (1988) model (BPA model) and it will be termed the EBPA model. The isotropic part of intrinsic hardening in the material is rheologically described by a dashpot which is arranged in parallel with a nonlinear Langeving spring for modeling kinematic hardening. The two components for the isotropic and the kinematic hardening are modeled by the internal state variables. The purpose of the extra dashpot is to increase the isotropic hardening in relation to the kinematic hardening and thereby suppress a premature Bauchinger effect observed in the simulations. This is of major importance during relaxation simulations at low stress levels where the plastic evolution is particularly governed by the internal state variables under consideration. Moreover, the elastic spring in the original BPA model is replaced by a simple Kelvin-chain involving a Kelvin-like element in series with an elastic spring. The Kelvin element is employed for predicting creep and recovery, while its combination with the elastic spring is aimed at describing the stress relaxation.

In addition to homogenous deformation, the EBPA model is calibrated to experimental data for inhomogeneous deformation. The tests were performed in the Laboratory of the Department of Materials Science (DMS) in Tampere university of Technology (TUT). The data acquired from the cold drawing of the dumbbell-shaped polycarbonate specimen contains the load-displacement diagrams for monotonic as well as non-monotonic loadings involving several loading cycles and long-term recovery.

Based on the calibration of the EBPA model both for the homogeneous and inhomogeneous deformation, the cold drawing process is simulated using the finite element method. The model responses obtained from the simulations show that the parameters which were derived from calibration for homogeneous deformation cannot be used to predict experimental response of inhomogeneous deformation. In order to find the mechanisms that are able to explain this discrepancy, the role of strain localization in the chain density, the initiation and propagation of shear bands and crazes as well as in the nucleation and growth of voids is investigated. The finite element simulations for inhomogeneous deformation indicated only a small influence of the number of entanglements and chain density on the macroscopic stress response when they were modeled without taking volume changes into consideration. However, a reduction in chain density together with void growth and crazing led to more diffuse and stable neck. The present numerical results also indicated that the plastic stability is essentially controlled by crazing, whereas void growth in conjunction with an increased interaction between the voids reduces amount of intrinsic softening during localized deformation. As a result, the difference between the model calibrations governing intrinsic softening under homogeneous and inhomogeneous deformation decreased considerably. The EBPA model augmented by the models for void growth and crazing allows the simulation of inhomogeneous deformation by utilizing the material parameters obtained from simple uniaxial tests for homogeneous deformation.

Using the calibrated parameters, the predictive capability of the EBPA model both for homogeneous and inhomogeneous deformation is evaluated. Despite the relative simplicity of this model, a comparison with the experimental results shows that the model is well able to capture the nonlinear response of amorphous glassy polymers during monotonic loading, unloading, creep and recovery. The proposed model is also found to be predictive for isothermal responses at various strain rates as well as for large strain anisotropic responses of preoriented polymers.

Preface

The research presented in this thesis was conducted during the years 2008-2011 at the Division of Solid Mechanics in Lund University and from 2011 to 2012 at the Department of Mechanics and Design in Tampere University of Technology. I would like to take this opportunity to express my sincere gratitude to my supervisor, Professor Reijo Kouhia for his guidance and support during my graduation period in Tampere. I am also grateful to Dr. Jari Mäkinen for fruitful discussions, his guidance and for arranging all the facilities I have needed in my studies. My preceding supervisor Mathias Wallin in Lund deserves special thanks for his guidance as well as for his TEXnical assistance. I am also grateful to the head of the department, Professor Timo Kalema, for giving me the opportunity to continue my studies and for the excellent working environment. I would also like to thank Professor Matti Ristinmaa in Lund for providing me with this interesting research topic.

I further acknowledge Dr. Seppo Syrjälä, M.Sc. Ilari Jönkkäri and Mr. Voitto Känkänen for sharing their expertise in the field of measurements. I would also like to thank all the people at the department for the pleasant working atmosphere.

Professors Erik Van der Giessen in Delft University and Martin Kroon in Royal Institute of Technology, Stockholm, are gratefully acknowledged for pre-examination and their valuable comments for improving the manuscript.

During the graduation period, I had the good fortune to be involved with inspiring, professional and internationally working research groups. I learned to push the limits of what it really means to take the final steps towards producing concise and understandable scientific reporting.

Lastly, I want to thank my family for their patience, encouragement and support.

This thesis is dedicated to my dear son *Eino.*

Tampere, December 2012

Sami Holopainen

Contents

1 Introduction

1.1 Scope of the study

The first objective of this thesis is to present the current state of modeling amorphous polymers and evaluate the importance of different rheological properties employed in the models for regarding mechanical behavior of amorphous polymers under different stress states, strain rates, temperatures and anisotropic state of preoriented polymers. The research related to this topic was carried out during 2008-11 at the Department of Solid Mechanics in Lund University, Sweden. The chapters 2-5 are concerned with the first objective being a part of the licentiate dissertation which was accomplished in Lund at the end of 2011, cf. Holopainen (2011). The research was continued and finished at the Department of Mechanics and Design in Tampere University of Technology during 2011-2012.

Motivated by the shortcomings observed in the current models, the second objective is the development of a state-of-the-art model (termed the EBPA model) which is able to predict transient effects, i.e nonlinear loading-unloading response, creep and recovery for different strain levels, stress levels and for various dwell periods. The EBPA model including both viscoelastic and viscoplastic ingredients is based on the 8-chain version of the Boyce *et al.* (1988) constitutive model for amorphous polymers. The aim of the proposed model is to significantly improve the prediction of the mechanical response during complex loading situations compared to existing models in this field. The proposed model is implemented in a finite-element program for simulation of inhomogeneous deformation.

The third objective of this thesis is evaluation of the proposed EBPA model on the basis of the calibration to the experimental data both for homogeneous and inhomogeneous deformation modes. Various loading situations are experimented involving cold drawing test program which was conducted by using the Instron© tension/compression electromechanical testing machine in the Laboratory of DMS. Comparison of the model and the experimental responses showed that the parameters which were obtained from calibration to homogeneous deformation cannot be used to predict satisfactorily the experimental response of inhomogeneous deformation. As the fourth objective, role of strain localization into this discrepancy is investigated and its importance into initiation and propagation of shear bands and crazes as well as into the number of entanglements is addressed. In order to investigate nucleation and growth of voids as well as shear band propagation within the ligaments between the voids, the Gurson model is augmented for these purposes and it in conjunction with the EBPA model is implemented in a finite-element program. Influence of the model parameters on the macroscopic responses as well as on the deformation behavior is discussed in detail. Using the calibrated parameters, the predictive capability of the EBPA model under various loading conditions is evaluated.

1.2 Characterization of polymers

The word *polymer* refers to a long-chain molecule which consists of a large number of repeated units of identical structure called monomers. Moreover, the term polymer is frequently used to describe the whole material continuum. Polymers can be found in nature, called natural polymers, while others are produced synthetically in a process which is called polymerization, cf. Fig. 1.1. In this work, the interest is placed on synthetic, ductile amorphous polymers which excludes e.g. brittle amorphous polymers and composite polymers. Even though amorphous polymers are able to resemble different states involving solid, liquid and even gas, only their glassy and melt states are considered in the present study. For further reading, the textbooks by Haward and Young (1997), Perez (1998), Courtney (1999), Ward and Sweeney (2004) and Fried (2009) give comprehensive overviews of polymer science, covering the material characteristics and mechanical behavior of amorphous polymers.

Synthetic polymers are typically formed by hundreds or thousands of identical repeated units having a high molecular weight. Polymer molecules constituting of fewer than ten repeated units and thus a low molecular weight are termed oligomers. Polymers having only a single type of repeated unit are termed homopolymers, while polymers comprised of different repeated units are termed copolymers. Each repeated unit consists of a backbone and a molecule which is often built up of carbon, chloride, hydrogen or nitrogen, cf. Fig. 1.2. The backbone of a repeated unit enables substituent to be attached to the polymer. The connections within the backbone are relatively weak secondary bonds termed the van der Waals forces. The molecules are connected together via the end units with chemical bonds in a certain order and at a rotation angle that defines the geometric structure termed the conformation. Synthetic polymers can be classified in several ways. Here, the process-

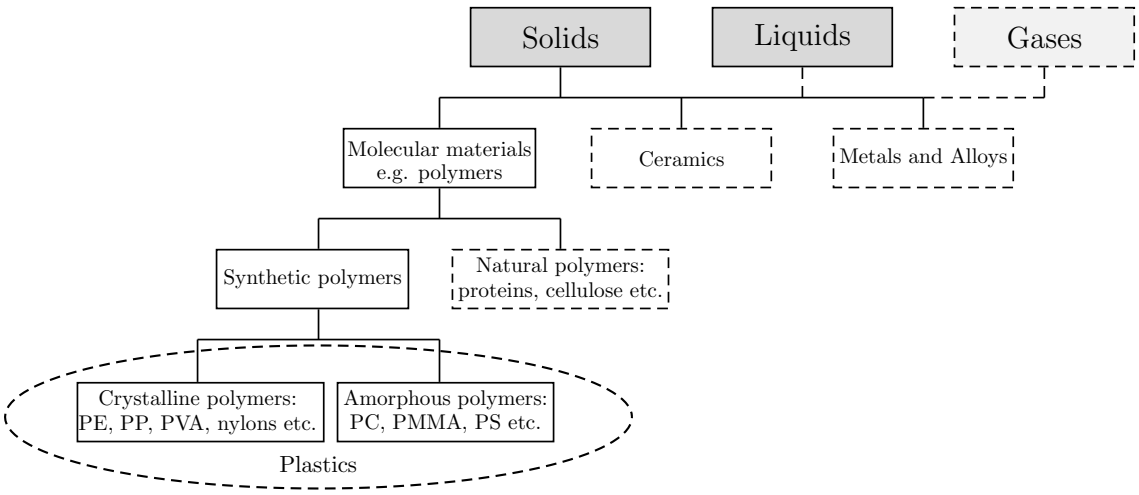

Figure 1.1: Classification of materials.

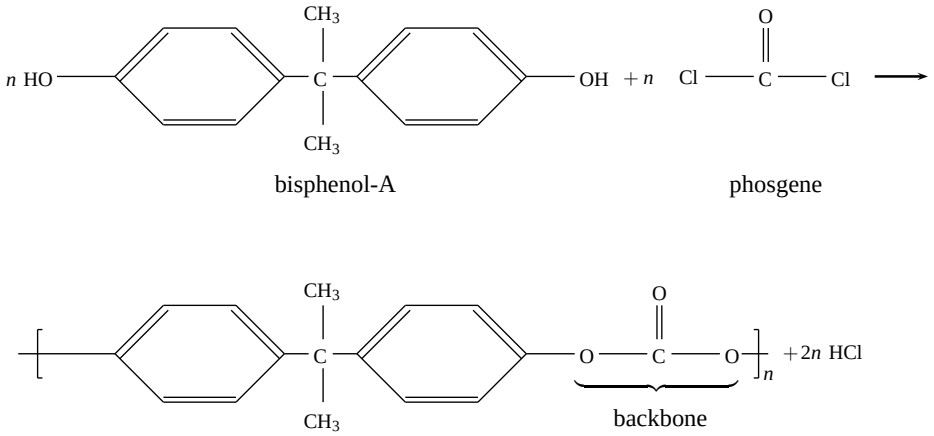

Figure 1.2: Polymerization of bisphenol A polycarbonate (BPA-PC). The repeated units of BPA-PC consist of a molecule and a backbone. The full molecule consists of a large number n of repeated units connected together by end units, cf. Fried (2009).

ing characteristics and the polymerization mechanism will be considered. Based on their processing characteristics, polymers can be divided into thermoplastics and thermosets, cf. Fried (2009). Thermoplastics can be reformed by a heat-softening process, whereas thermosets, once formed, cannot be thermally processed. Since amorphous polymers belong to the set of thermoplastics, thermosets are not considered in this work.

Based on the polymerization mechanism, polymers can be classified as *addition* or *condensation* polymers. This classification, however, is a bit old-fashioned and more recently polymerization mechanisms are classified as either *step-growth* or *chain-growth*. Most of the addition polymers are formed through chain-growth, i.e. a high-molecular-weight polymer is formed early during the polymerization, which results in the sequential addition of monomers. An example of chain-growth polymers is polymethyl methacrylate (PMMA). In contrast to addition polymers, a majority of condensation polymers are produced via step-growth, i.e. a high-molecular-weight polymer is only formed near the end of the polymerization process. An important example of step-growth polymerization is polycarbonate (PC) which is processed from bisphenol A and phosgene in the presence of an acid catalyst such as hydrogen chloride, cf. Fig. 1.2. As a result of the polymerization, two molecules of hydrogen chloride HCl are formed for each repeated unit of PC, generating long polymer chains. In this case, the backbone consists of hydrogen and carbon atoms. However, the backbone can be flexible, i.e. it can obtain different conformations depending on the polymerization process. Note, that in literature bisphenol A is often simply called PC.

1.3 Description of the chain network

The microstructure of polymers is defined by a network of molecular chains. The chains can be arranged in different ways and the structure of the chains have different forms: long linear, branched and cross-linked, cf. Fig. 1.3. If single chains are solely coiled

to each other without branching, the chains are called linear whereas in the branched structure, substituent side chains are connected to long linear or main chains. Due to the side branches, the distance between the main chains increases which results in a lower chain density, i.e. the branched structure may be weaker than the linear chain structure. In a cross-linked structure, the chains are connected by strong chemical bonds which do not allow significant slipping between the chains. Based on the microstructure, polymers

Figure 1.3: Chain structure of polymers: linear chain, branched chain and cross-linked network. The molecules are connected through chemical bonds.

can be classified into amorphous or non-crystalline, and crystalline polymers. This split is based on the degree of crystallinity which is due to the chain length and chain branching. Crystallinity can be expressed in terms of a weight fraction or as a volume fraction of the crystalline regions, typically ranging from 10% to 80%, cf. Fried (2009). Methods used to evaluate the degree of crystallinity are e.g. differential scanning calorimetry (DSC) and X-ray diffraction (XRD). Polymers having a low degree of crystallinity are called amorphous, whereas other polymers are termed crystalline or semi-crystalline. In contrast to crystalline polymers where the chains are branched or cross-linked, the chains of amorphous polymers have a linear structure, cf. Fig. 1.4. PC is an important example of amorphous polymers, having numerous applications ranging from soda bottles to applications in the automotive and aerospace industries. Another important amorphous polymer is PMMA. Due to its transparency, it is also termed acrylic glass. Compared to PC, PMMA is brittle and does not contain the environmentally harmful bisphenol A. An example of semi-crystalline polymers is polyethylene (PE) which is the most widely produced thermoplastic polymer. Since PE is a cheap and tough polymer, it is frequently used in packaging products.

The degree of crystallinity in a polymer is not fixed but varies between solid and melt. The temperature at which a polymer transforms from a solid to a melt is called the glass transition temperature, T_g. The glass transition occurs gradually which results in the glass transition temperature not being unique, but is instead defined as an average temperature. The glass transition temperature can be defined based on the energy release during heating in differential scanning calorimetry (DSC), cf. Fig. 1.5.

In general, the glass transition temperature of polymers with a flexible backbone and high molecular weight is relatively low compared to polymers with a rigid backbone and low weight, i.e. there exists a wide range of glass transition temperatures. For example, the glass transition temperature of PC is 150°C, whereas for high density atactic polypropylene (PP) room temperature represents a relative high temperature compared to its glass transition temperature, −20°C.

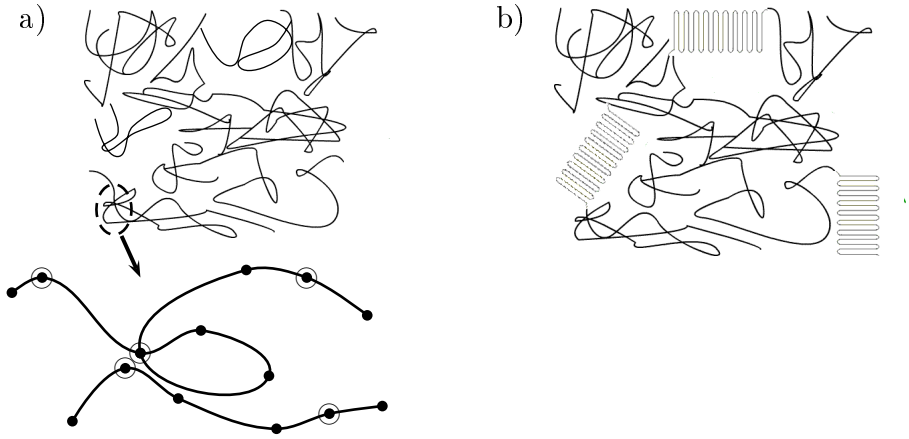

Figure 1.4: Microstructure of a) amorphous and b) semi-crystalline polymers. In the amorphous region, polymer chains are intertwined in a network of entangled chains (entanglements). The markers • indicate the statistical links in the chain between entangled points, ⊙.

Frequently, the terms amorphous and glassy are used synonymously. However, the term glassy should be considered as a special case of amorphous being firmly connected to the transformation from a solid into a melt upon heating through the glass transition temperature. Following this definition, certain gels, thin films and nanostructured polymers can be classified as amorphous polymers but not necessarily as glassy polymers. Furthermore, no polymer is completely crystalline and therefore crystalline polymers may also exhibit a glass transition temperature. In this work, the term *amorphous glassy polymer* denotes polymers which are both amorphous and glassy.

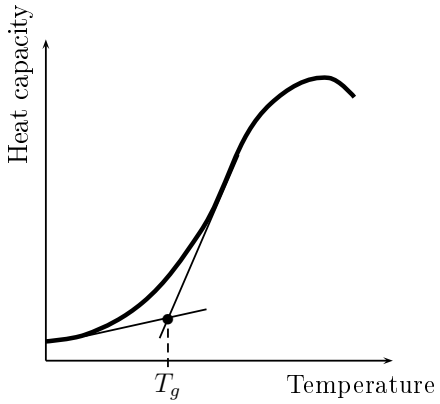

Figure 1.5: Determination of the glass transition temperature T_g based on the energy release during heating in differential scanning calorimetry.

The chains in crystalline polymers are connected compactly together in ordered regions, cf. Fig. 1.4(b). The connections between the chains are formed by secondary, crystalline bonds. In contrast to crystalline polymers, the chains in amorphous polymers are coiled and randomly oriented and connected to each other by relatively weak secondary bonds called van der Waals forces. In addition to the van der Waals forces, the long polymer chains in an amorphous chain network are connected via physical entanglements in entangled points. The part of a chain between entanglements is called a chain segment, cf. Fig. 1.6. The secondary bonds are closely related to the physical entanglements; an increasing grade of entanglements activates more bonds and increases the van der Waals forces which results in the resistance to slipping between chains increases. Due to the different level of crystallinity, chain density etc., the ability to form entanglements varies between polymers. Entanglements are also of major importance in

relation to mechanical properties such as stress relaxation and creep; an issue of that will be discussed in subsequent sections.

During initial deformation the chains slip against each other and under large strains they align with the loading direction which results in an anisotropic response. After initial yielding, the threshold for significant slipping between the chains is reached and the material response suddenly softens. Once a majority of the chains have aligned with the loading direction, a significant increase in stiffness can be observed. A representative macroscopic stress-strain response is shown in Fig. 2.1. In contrast to the glassy state, the mobility of individual chains above the glass transition temperature strongly increases which results in the material softening towards a melt.

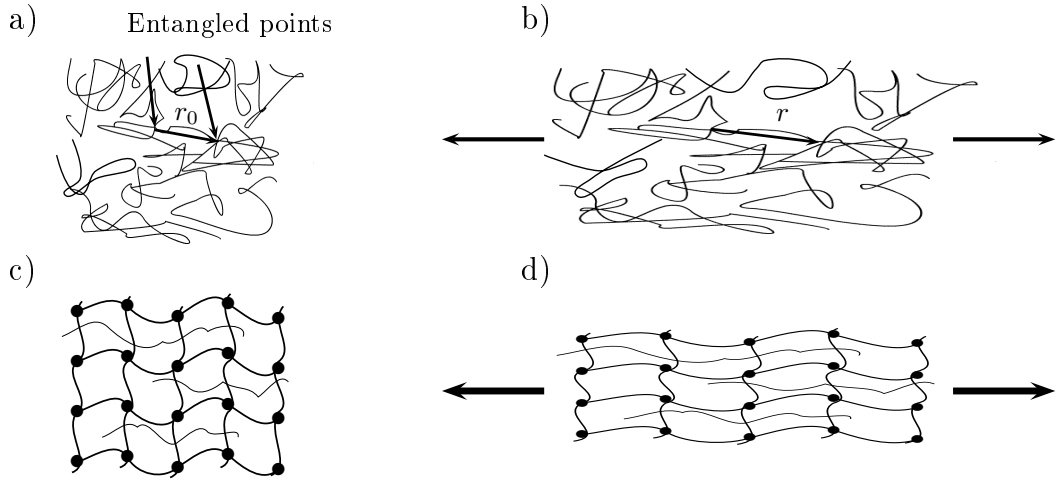

Figure 1.6: Microstructure of amorphous polymers represented in a) undeformed and b) deformed configuration. Microstructure of rubbery polymers in c) undeformed and d) deformed configuration. Chains in rubbery polymers are cross-linked whereas the network of amorphous polymers is formed by chain segments of initial length r_0 and current end-to-end distance r between entanglements. The thin chains in c) and d) indicate non-equilibrium networks extending between entanglements with an equilibrium network, cf. Bergström and Boyce (1998).

Comparison of rubbery polymers and amorphous glassy polymers

Elastomers, also termed rubbery or rubber-like polymers, share many characteristics with amorphous glassy polymers, including e.g. the high energy absorption under impact loadings and good formability properties that allow reuse and manufacturing of geometrically challenging consumer products. Moreover, since both rubbery and amorphous glassy polymers are often comprised of similar constituents and they share many similar processing techniques, the manufacturing of rubbery and amorphous polymers is more or less clustered. However, their network structure differs considerably which results in different mechanical behavior.

An important difference in the rubbery polymers, compared to the amorphous glassy polymers, is the dominating non-linear elastic behavior which can already be observed

in small strains. The Poisson's ratio for the majority of amorphous glassy polymers varies between 0.35-0.40 whereas 0.45-0.49 is a typical range for rubbery polymers indicating almost incompressible deformation. In contrast to the rubbery polymers, the amorphous glassy polymers are characterized by the plastic behavior which initiates immediately under deformation. Since the plastic deformation is close to incompressible, amorphous glassy polymers can also be considered nearly incompressible at large deformations.

In Fig. 1.6, the networks of rubbery and amorphous glassy polymers are compared. In contrast to the rubbery polymers, in which the network is cross-linked by chemical bonds, the network of amorphous glassy polymers is formed by the physical junctions. Moreover, the rubbery chain network forms the ground-state network for the superimposed chains. Similar to the entangled points in the amorphous network, the superimposed chains are connected to the ground-state network at the points which resemble entangled points in their function. The stretching of superimposed chains is assumed to be the source of the viscous response while the deformation of the ground-state network results in the macroscopic equilibrium stress-strain curve, cf. Fig. 1.7. As a result of the microstructure, the rubbery chain network can stretch without significant chain slipping.

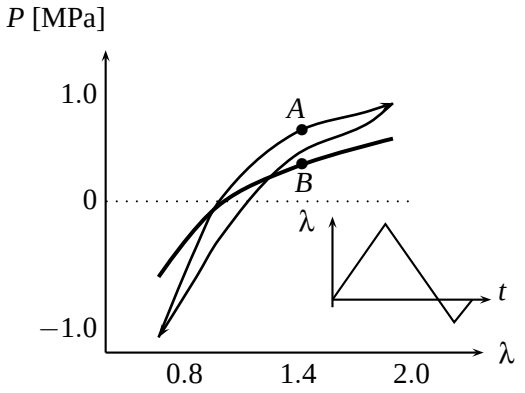

Figure 1.7: Nominal stress vs strain response of HNBR50 rubber-like polymer in uniaxial cyclic deformation (thin line), cf. Göktepe (2007). A relaxation of viscous over-stress is depicted by non-equilibrium point A and equilibrium point B. The elastic equilibrium curve without hysteresis is depicted by the thick line.

To this end, amorphous glassy polymers can be characterized as follows:

- Light weight relative to strength, high flexibility, and good reforming properties.
- Polymer chains are formed by a large number of repeated units that consist of a molecule and a backbone.
- Polymer network is formed by long linear chains that are coiled and randomly distributed.
- The chains are connected together by weak van der Waal forces and via entangled points.
- Network is relatively weak compared to crystalline and rubbery polymers.
- An increase of temperature increases mobility of chains and leads to the transformation from a solid towards a melt.

2 Mechanical behavior of amorphous glassy polymers

A variety of experiments on amorphous glassy polymers have been performed during the last decades, most of which have been uni- and biaxial compression/tensile tests, simple shear tests, micro-indentation experiments and birefringence measurements. The ompression/tensile/shear tests are conventionally applied in macro-scale (millimeters), whereas the other methods are suitable in micro/nano-scales (micro/nanometers). The latter method is an optical procedure, which is used to estimate the anisotropy of the material from thin polymer slices. Due to the high energy absorption, amorphous glassy polymers are sensitive to the plasticity induced and adiabatic heating. To avoid the heating during the compression/tension tests, relatively low strain rates, typically ranging from $0.0001 - 0.01\, s^{-1}$, are employed. Moreover, the response of glassy polymers is highly rate-dependent giving rise to the need for experiments at different loading rates. To circumvent the inhomogeneous deformation present in tensile experiments, compression tests have frequently been employed to investigate the macroscopic stress-strain response. Among more recent methods, G'Sell *et al.* (2002) developed a video-controlled tensile testing method for determination of volume changes during inhomogeneous deformation.

In order to learn about the underlying microstructural deformation mechanisms of amorphous polymers, a specialized experimentation is needed. Apart from the above experimental methods, the density fluctuation and amount of free volume around the chain molecules have been estimated by X-ray scattering and by positron annihilation spectroscopy employed on the thin polymer slices, cf. Hasan *et al.* (1993). The rapid development of depth-sensing experiments for nano/micro-indentation during the past two decades allows accurate experiments on very small volumes. For instance, Hochstetter *et al.* (2002) determined the true stress-strain curves of PC, PMMA and diethylene glycol bisallyl carbonate (CR39) employing nano-indentation. Anand and Ames (2006) conducted micro-indentation experiments on PMMA to investigate creep and recovery at different load levels. The inventions of optical instruments, such as the atomic force microscope (AFM), the magnetic levitation force microscope (MLFM) as well as the single molecule force spectroscopy (SMFS), have made possible to measure the physical properties of materials at the molecular level and led to the new field of nanomechanics, cf. Ortiz and Hadziioannou (1999).

2.1 Influence of microstructure on macroscopic mechanical behavior

The microstructure of amorphous polymers is to a large extent a result of the manufacturing process, such as forging, stamping or extruding which are collectively known as solid phase deformation processes. During these processes, temperature, pressure as well as deformation state of the material vary. At the end of the forming process, the material shows microscopic, direction-dependent characteristics which are due to the evolution of micro-cracks and shear banding. Brown and Ward (1968) conducted tension tests to inves-

tigate the effects of initial anisotropy on polyethylene terephthalate (PET). Also Arruda *et al.* (1993) investigated the effects of initial anisotropy on PC and PMMA at different temperatures and strain rates. Their uni- and biaxial compression experiments, as well as the birefringence measurements, indicated that the resulting anisotropic response is virtually unaffected by the strain history. The yield stress, strain hardening and limit of extensibility were remarkably similar when subjected to different level of straining prior to the experiments at different temperatures. However, Capaldi *et al.* (2004) showed that the mechanical behavior may considerably alter due to certain mechanical pre-conditioning, e.g. by quenching and slow-cooling. In Caddell and Woodliff (1977), Melick (2003) and Weltevreden (2009), the direction-dependent yield behavior through both initially isotropic and pre-strained glassy polymers was investigated. It was observed that the compressive yield stress of initially isotropic material is higher than the yield stress in extension, whereas the yield stress of the pre-strained material in tension typically reaches considerable larger values than in compression.

Several experiments have been conducted in order to gain knowledge of the underlying deformation mechanisms of amorphous polymers. Based on experiments on PMMA, Hasan *et al.* (1993) and later also Stachurski (2003) proposed a way to represent the evolution of plastic deformation in terms of microstructural characteristics. Capaldi *et al.* (2004) and Lyulin *et al.* (2006) conducted molecular dynamics (MD) simulations to investigate the influence of microstructure on plastic deformation. It can be concluded that the macroscopic mechanical behavior stems from three major microstructural characteristics: the number of entanglements and statistical links between the entanglements, the growth of shear bands, and the extent of free volume around the chain molecules.

Raha and Bowden (1972) and Arruda *et al.* (1995) conducted experiments that indicated that the number of entanglements is not constant, but depends on temperature. According to Tomita and Uchida (2003), the number of chains n in a unit volume and the number of statistical links N on a chain between entanglements can also vary under isothermal loading conditions while the molecular weight of the polymer remains unchangeable. As a result of reduced chain density, the stiffness of the network reduces. The concept of free volume is frequently employed to describe the loosely packed regions having reduced chain density. Due to the existence of free volume around the chain molecules, the yield behavior of amorphous glassy polymers depends on hydrostatic pressure. Experiments on amorphous polymers processed by quenching show a much lower yield stress and greater amount of free-volume compared to the experiments on slowly cooled amorphous polymers, cf. Anand and Ames (2006).

In tensile tests, the initial chain distribution have been found to be macroscopically uniform while large-scale MD simulations have shown that the chain distribution locally is heterogeneous. The heterogeneity is assumed to generate nucleation sites for shear bands. As a result of heterogeneity, polymer material shows localized deformation where microscopic shear bands in closely packed regions develop and annihilate into macroscopic shear bands, cf. Tomita and Uchida (2003). Bowden and Raha (1970) conducted plane strain

compression tests on PMMA and polystyrene (PS) to investigate the formation of shear bands. According to their observations, the growth of shear bands is the primary source for the evolution of plastic deformation in amorphous glassy polymers. The plane strain tension tests by Tomita and Uchida (2003) showed a remarkable drop in the macroscopic stress immediately after development of the macroscopic shear bands. During continued deformation, the propagation of shear bands and development of inhomogeneous deformation were observed which is macroscopically manifested by necking. The neck propagation is discussed below.

2.2 Macroscopic mechanical behavior

The mechanical properties of amorphous glassy polymers are to a large extent dictated by their chemical composition and microstructure. As temperature increases, most amorphous glassy polymers show increased deformability in shear. Moreover, experiments show strong strain rate sensitivity, although this decreases during transition from a solid to a melt, cf. Arruda *et al.* (1995). The mechanical behavior of amorphous glassy polymers is characterized by initial yielding and subsequent strain softening, followed by strain hardening due to the reorientation of polymer chains, cf. Haward and Thackray (1968) and Argon (1973). A representative "S-shaped" true stress-strain curve is presented in Fig. 2.1. Once the chains reach their limit for extensibility, a dramatic increase of stress can be observed.

When the deformation is small and the deformation rate is slow, the molecules have enough time to relax and the amorphous structure remains unaltered. At this state, the plastic deformation is yet small and the response is nearly linear elastic. During continued deformation, the plastic strains develop and the total plastic strain near the limiting strain is at least ten times greater than the initial elastic strain up to the elastic limit, cf. Haward and Thackray (1968). The evolution of plastic deformation in amorphous glassy polymers is a thermally activated statistical process whose rate is proportional to $\exp(-\Delta G_f/kT)$ where ΔG_f, k and T are the amount of activation free enthalpy, the Boltzmann constant, and the absolute temperature, respectively. The yield stress is reached once the level of thermal activation energy for chain segment rotation is reached. This barrier is closely related to the intermolecular resistance. The isotropic hardening results from intermolecular resistance to chain segment rotation while the softening in the material is believed to be the result of localized shear band formation which usually occurs at strains between 5%-50%, cf. Argon (1973), Boyce *et al.* (1988) and Hasan and Boyce (1995).

During deformation, the chains align with the principal plastic stretches of continuum which results in an anisotropic response. Moreover, amorphous glassy polymers exhibit localized deformation which is due to shear band propagation under shearing and neck propagation under tension. Neck propagation can be utilized in forming processes, e.g. it is exploited in cold drawing which results in a strongly oriented structure in amorphous polymer materials. During cold drawing, the load is nearly constant as the neck propagates through the structure. Several studies have been conducted to investigate neck propagation, cf. G'Sell and Jonas (1979), Stokes and Nied (1986) and Miehe *et al.* (2009). Stokes

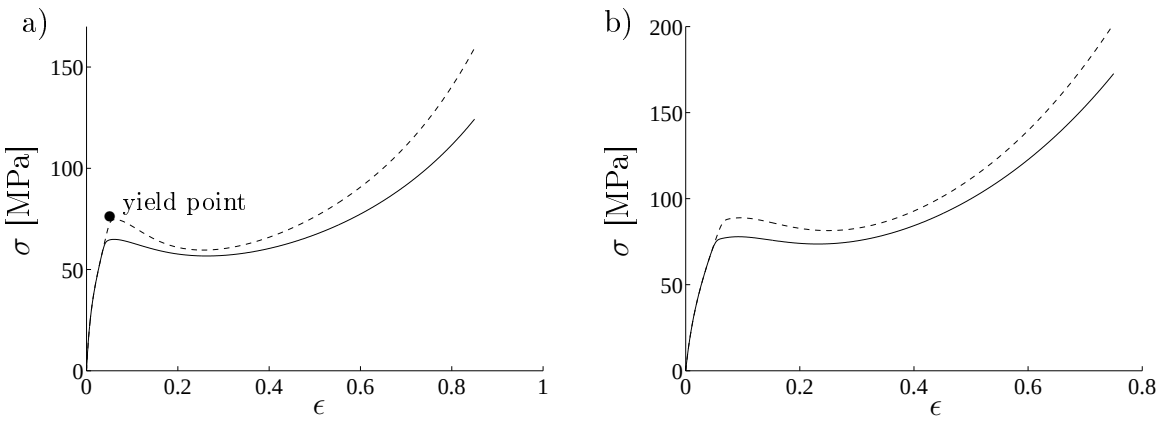

Figure 2.1: Stress vs strain response of PC in a) uniaxial and b) plane strain compression. The tests have been performed by Arruda and Boyce (1993a) at two constant true strain rates $\dot{\epsilon} = 0.001\,s^{-1}$ (solid line) and $\dot{\epsilon} = 0.01\,s^{-1}$ (dashed line) at room temperature. An increase of $\dot{\epsilon}$ results in the yield stress increasing.

and Nied (1986) performed tension tests on PC, polybutylene terephthalate (PBT) and polyetherimide (PEI) which indicated that the limit of elastic deformation is followed by the onset of localized deformation through a neck formation. The propagation of the neck results in the alignment of the chains which appears macroscopically as a highly anisotropic response. Near the limiting strain, there appears a stiffening of the material and a considerable increase in stress.

Strain rate and temperature dependence

Experiments indicate that the mechanical behavior of amorphous glassy polymers is strongly strain rate and temperature-dependent. Haward and Thackray (1968) and Arruda *et al.* (1995) performed uniaxial tests that indicated a strong strain rate dependence in yield stress and in strain hardening.

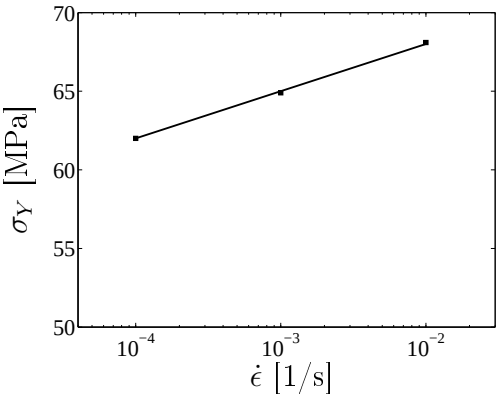

Figure 2.2: Yield stress versus strain rate for PC. The marker ■ represents experimental data point and the solid line a fit using the Eyring relation.

The representative stress-strain responses of PC under uniaxial and plane strain compression at different strain rates are depicted in Fig. 2.1. An increased loading rate results in an increased stress level which indicates the material behavior is rate-dependent. The yield stress σ_Y is proportional to the logarithmic strain rate $\dot{\epsilon}$ and it can be described using the Eyring relation

$$\sigma_Y = \frac{kT}{V^*} \sinh^{-1}\left(\frac{\dot{\epsilon}}{\dot{\epsilon}_0}\right) \qquad (2.1)$$

where V^* is the activation volume and $\dot{\epsilon}_0$ is a pre-exponential factor, cf. Fig. 2.2. In addition to the strain rate dependence, the yield stress is substantially influenced by pres-

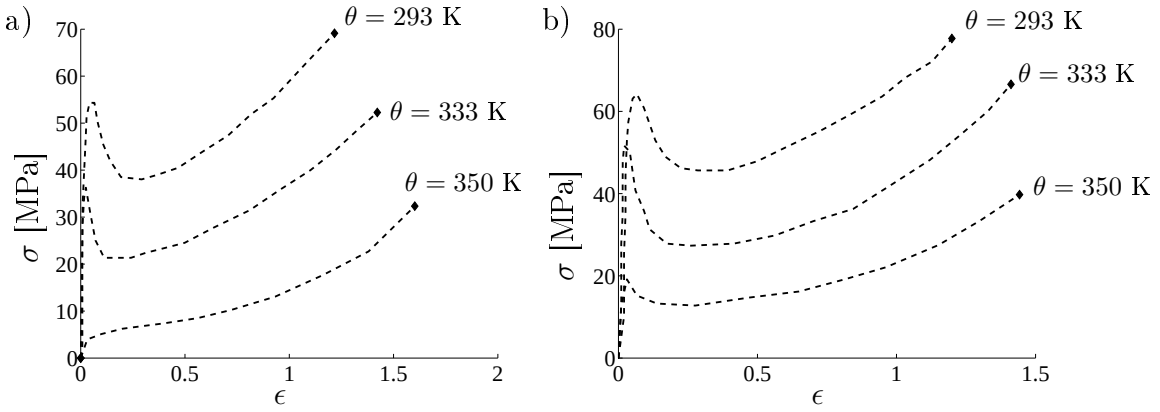

Figure 2.3: Stress vs strain response of PETG in uniaxial compression at $293\,K$, $333\,K$ and at glass transition temperature $350\,K$. The tests have been performed by Dupaix and Boyce (2005) employing constant true strain rates, a) $\dot{\epsilon} = 0.01\,s^{-1}$ and b) $\dot{\epsilon} = 0.5\,s^{-1}$. An increase of temperature results in the yield stress as well as large strain hardening decrease.

sure, cf. Christiansen *et al.* (1971). According to the experiments by Ginzburg (2005), the stress-strain curve of semi-crystalline polymers is also shown to depend on the temperatures during the manufacturing processes prior to the cold drawing. At high strain rates, temperature and strain rate are coupled which is due to the plasticity induced heating.

Dupaix and Boyce (2005) and Dupaix and Boyce (2007) conducted experiments on polyethylene terephthalate (PET) and polyethylene terephthalate-glycol (PETG) over a wide range of temperatures. The experimental uniaxial stress-strain curves at three different temperatures are depicted in Fig. 2.3. A rise in temperature increases the molecular chain flexibility, and that leads to a reduction in the yield stress and the elastic stiffness. Around the glass transition temperature, the experimental response shows less hardening and the yield peak and the ensuing softening are considerably reduced. A comparison of Figs. 2.3(a-b) shows the effects of the changes in strain rate and temperature. An interesting remark is that the yield peak and the following softening below the glass transition temperature cannot be observed at $\dot{\epsilon} = 0.01\,s^{-1}$, whereas they both are present at $\dot{\epsilon} = 0.5\,s^{-1}$.

G'Sell and Jonas (1981) performed tension experiments that indicated strong transient effects after strain rate changes in PE, polytetrafluoroethylene (PTFE), PP, PVC, and polyamide (PA), cf. Fig. 2.4(a). Lu and Ravi-Chandar (1999) conducted tension experiments on PC that showed relatively small hysteresis and only minor transient effects at small strains before softening. Arruda *et al.* (1995) conducted uniaxial compression experiments on PMMA which indicated that the yield stress increases and the strain hardening decreases with the increased strain rate. More recently, Khan and Zhang (2001) and Khan (2006) investigated the influence of strain rate on strain hardening, creep and relaxation for PTFE, and Zaïri *et al.* (2005) for PC. Krempl and Khan (2003) conducted a set of uniaxial monotonic tests at several loading rates that showed similarities in deformation behavior between polymers and metals: almost linear elastic phase, nonlinear strain rate

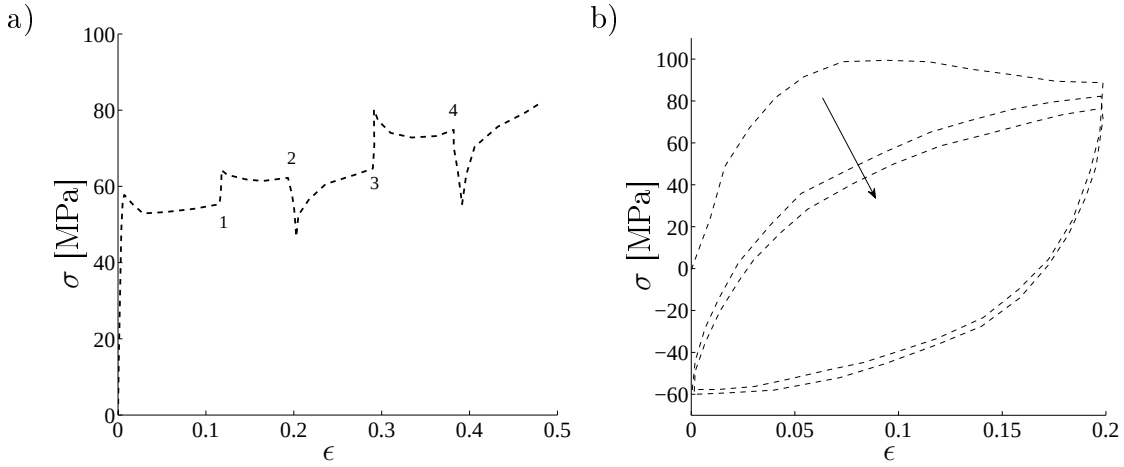

Figure 2.4: a) Transient effects in experimental stress vs strain response of PVC after strain rate changes, cf. G'Sell and Jonas (1981). The numbers 1 and 3 indicate the change from $\dot{\epsilon} = 0.001\,s^{-1}$ to $\dot{\epsilon} = 0.01\,s^{-1}$ and 2, 4 from $\dot{\epsilon} = 0.01\,s^{-1}$ to $\dot{\epsilon} = 0.001 s^{-1}$. b) Experimental stress vs strain response of PMMA in cyclic uniaxial compression, cf. Anand and Ames (2006). The arrow indicates the direction of the shift between cycles in the hysteresis loops.

sensitivity, nonlinear creep and hysteresis during a loading cycle. Colac and Dusunceli (2008) performed uniaxial tensile tests that showed a strong strain rate sensitivity and creep/relaxation behavior on semi-crystalline high density polyethylene (HDPE). Anand and Ames (2006) showed that PMMA exhibits a strong Bauschinger-like effect when unloaded. Their experiments also indicated a progressive shift between cycles in the hysteresis loops, cf. Fig. 2.4(b).

Dreistadt *et al.* (2009) conducted uniaxial experiments to investigate the influence of relaxation time and repeated unloadings on bisphenol A polycarbonate (BPA-PC). The

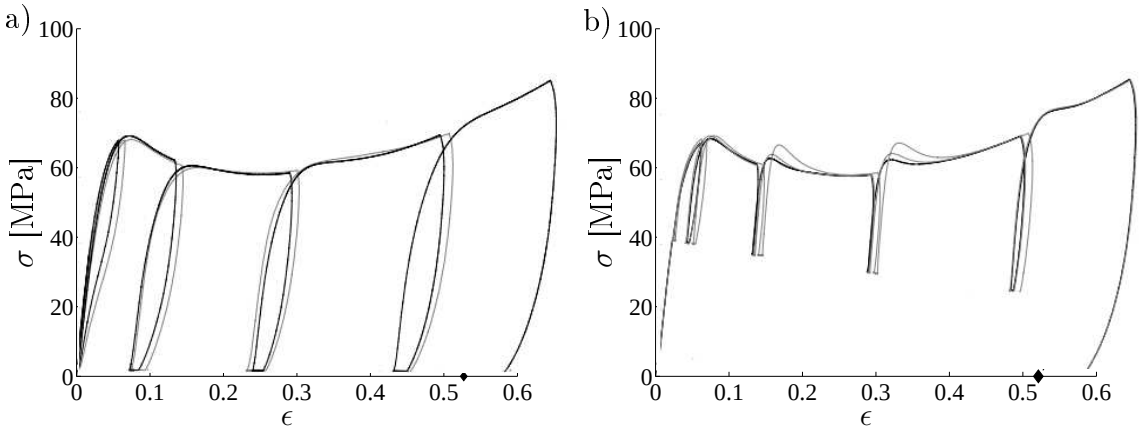

Figure 2.5: Compression responses for bisphenol A polycarbonate (BPA-PC) involving a) repeated unloadings to the given nominal stress $\pi = 1.2$ MPa followed by dwell of 120 s and 12,000 s. b) Repeated unloadings to $\pi = 42$ MPa followed by dwell of 120, 1200 and 12,000 s. The marker ♦ indicates recovery developing during the dwell period of 400 days at zero stress. The tests were performed at constant true strain rate $\dot{\epsilon} = 0.001\,s^{-1}$, cf. Dreistadt *et al.* (2009).

experimental stress-strain responses are depicted in Fig. 2.5. At the beginning of the unloading phase, the response shows continued deformation opposite to the loading rate direction. In contrast to many other materials, this feature is frequently observed in amorphous polymers. During reloadings, the response shows significant stress peaks which are followed by softening back to the monotonic loading path. As shown, the response is not sensitive to the duration of dwell at the given stress levels. It will be pointed out, however, that recovery is progressively replaced by creep and it strongly depends on the prescribed dwell period when the dwell stress increases, cf. also Dreistadt *et al.* (2009).

To this end, the material behavior of amorphous glassy polymers can be summarized as follows:

- Initial yielding and subsequent strain softening followed by strain hardening can be described by the typical "S-shaped" stress-strain response.
- The initial response prior to the stress drop is nearly linear.
- Due to the existence of loosely packed regions (free volume) around the chain molecules, the yield behavior of amorphous glassy polymers depends on hydrostatic pressure.
- Temperature- and strain rate-dependence: decreasing strain rate and increasing temperature result in a lower yield stress.
- Changes in loading rate cause strong transient effects: creep/recovery (dwell) and stress relaxation.

3 Characterization of constitutive models

Most constitutive models for amorphous glassy polymers are based on network models originally designed for rubber elasticity. These models date back to the beginning of the last century, cf. e.g. James and Guth (1943) and Wang and Guth (1952). In amorphous polymers, long molecular chains are randomly distributed in space. The description of the chain distribution is based on statistical models which can be divided into two categories: Gaussian and non-Gaussian statistics. In probability theory, Gaussian distribution is called the normal distribution, being one of the simplest continuous probability distributions. It is frequently used to describe real-valued random variables having a widely known "bell"-shaped probability density function. However, at large strains the distribution of polymer chains does not follow Gaussian statistics, i.e. non-Gaussian statistics is frequently employed. In statistical models, one end of the chain is fixed while the other end has some probability to reach an infinitesimal volume dv. This simple model is termed an ideal or a freely jointed chain. Applying non-Gaussian statistics, the probability for finding the end-position in dv is expressed by the two limits: initial random walk-type mean-square value r_0 and the fully extended chain length, r_L. Non-Gaussian models have been applied to amorphous glassy polymers since 1960s. In the pioneering work by Haward and Thackray (1968), a one-dimensional model was presented. In this model, the rate-dependent softening/hardening behavior was captured by using an Eyring dashpot in parallel with a

Langevin spring which takes the kinematic hardening into account.

In contrast to Newtonian fluids, viscosity of amorphous glassy polymers is not constant but depends on the rate of deformation. Based on spring-dashpot analogies there exist two main strategies to systematically build relatively simple models. The first approach is based on a modification of the Kelvin-Voigt model involving a nonlinear viscous dashpot in parallel with a nonlinear spring which takes hardening into account at large strains. Moreover, the initial elastic behavior is captured via an elastic spring. A schematic representation of this approach is given in Fig. 4.6. Furthermore, a model can consist of several such Kelvin-Voigt elements arranged in series, cf. Fig. 4.11. In the second approach, two or more Maxwell elements involving a spring and a viscous dashpot in series are arranged in parallel. One spring is linear, whereas a nonlinear spring captures hardening in the material. This approach is schematically represented in Fig. 4.13. Models consisting of Kelvin-Voigt elements are typically employed for modeling of amorphous polymers in the glassy state, cf. Arruda and Boyce (1993a), whereas the Maxwell-based approach is applied to amorphous polymers in the rubbery or melt state, cf. e.g. Boyce and Arruda (2000) and Dupaix and Boyce (2007).

Models for amorphous glassy polymers involve both phenomenological and micromechanically based aspects. The strain energy is frequently described phenomenologically in terms of the principal invariants. In contrast to the strain energy, the plastic potential as well as the chain motion are usually described by a physically motivated network model. In both the phenomenological and the network models, the strain invariant $I_1 := \sum_i \lambda_i^2$ is of major significance. However, the strain energy expressions must be highly nonlinear in I_1 to capture the non-Gaussian nature of a large deformation. In addition to the mixed phenomenological and micromechanically based models, there are also purely phenomenological models. Zaïri *et al.* (2005) developed a phenomenological model which adequately captures the behavior of PC during monotonic loading, creep and stress relaxation. This model, however, involves a large number of constitutive parameters. Despite the small number of material parameters employed in micromechanically based models, they are found to accurately support experimental results. Due to the success of micromechanically based models for amorphous glassy polymers, all subsequent considerations will be discussed on this basis.

Modeling of the chain network

In the network models, the overall chain network is modeled by single chains which are arranged in small cells. The network models can be categorized to full-network models and to models, where a reduced set of chains in a cell are assumed to be representative for the entire network. In the early models, the cells were described as tetrahedrons or cubes involving three or four chains, cf. James and Guth (1943) and Treloar (1946). Since the 3- and 4-chain model cannot accurately reproduce the strain hardening in different deformation modes, the 8-chain model has become the most popular model during the

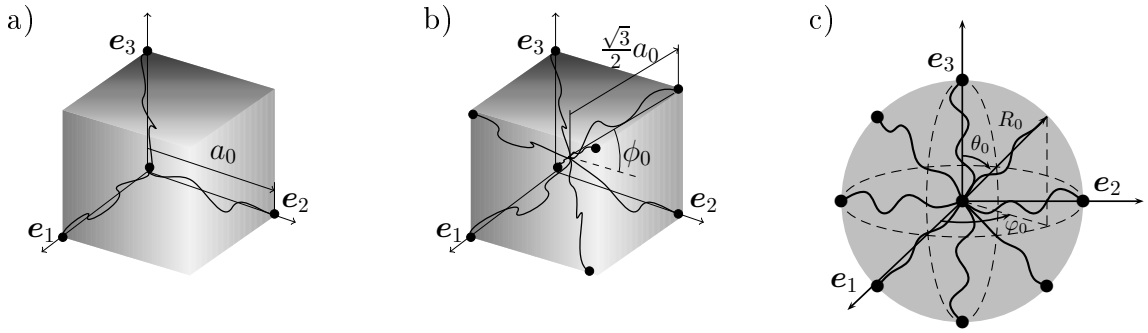

Figure 3.1: The idealized chain structure according to a) the 3-chain model, b) the 8-chain model and c) the full network model. The dimension of the 3- and the 8-chain cube is a_0, and R_0 denotes the radius of the micro-sphere.

last two decades, cf. Arruda and Boyce (1991) and Arruda and Boyce (1993a). In the 8-chain model, the cells consist of eight polymer chains that extend from the center along the diagonals, cf. Fig. 3.1. In full network models, the chains extend from the center of a micro-sphere and cross the surface forming a continuous chain distribution on the sphere, cf. Fig. 3.1. The overall plastic potential in the full network models, found by integrating the plastic part of the free energies of all the individual chains over the unit sphere, is computationally very expensive. For this reason, full network models are usually employed in reduced dimensions. Treloar (1954) proposed a full network model for simple uniaxial tension which was later extended to biaxial tensile deformations by Treloar and Riding (1979). In the Wu and Van der Giessen (1993) full network model, the distribution of chains is governed by a chain orientation distribution function (CODF). The stretch of individual chains is assumed to follow the continuum deformation which makes the Wu and Van der Giessen (1993) model affine in that sense. As it was pointed out by Boyce and Arruda (2000), the affine stretch assumption, however, is not able to capture deformation behavior at large strains. Later, Beatty (2003) showed that the 3-chain model by James and Guth (1943) and the 8-chain model by Arruda and Boyce (1993b) follow on from the Wu and Van der Giessen (1993) full network model. Wu and Van der Giessen (1993) also showed that the 3-chain model overestimates the stiffness of the network while the 8-chain model gives a lower bound. Motivated by these observations and also to avoid the expensive integration in the full network model, Wu and Van der Giessen (1993) proposed an approximation where the response is obtained from a linear combination of the 3- and the 8-chain model. In the same spirit, Miehe *et al.* (2002) proposed a model in which the integration over the unit sphere is approximated by a 21-point integration scheme.

The key in mechanical models for amorphous glassy polymers is to find the link between the micro-stretches of chains and the macro-stretches of continuum. There exist two major principles for this transition: affine models where the micro-stretches follow continuum deformation, and non-affine models where the micro-stretches are allowed to fluctuate

around the macro-stretches. Some authors refer to affine models as models in which the number of entangled points of molecular chains are assumed to remain unaltered during deformation. In that sense, the models mentioned above are affine. In this work, however, the affinity is determined on the basis of micro-stretches of chains. The motivation for non-affine network models is that the affine network models are not able to reach the limit of extensibility. Near the limiting strain, some of the chains in the real network are stretched more than predicted by affine models, while some chains are stretched less, especially in the direction of the principal stretches. As a result, the affine assumption of chain deformation is devalued which necessitates the development of more capable non-affine models.

One of the pioneering models for amorphous glassy polymers, including orientational hardening, is a non-affine 3-chain model proposed by Boyce *et al.* (1988). Later, Arruda and Boyce (1991) proposed a non-affine 8-chain network model which improves the strain hardening behavior at large strains and in different deformation states (and will herein be termed the BPA model). These pioneering works were confirmed by Arruda and Boyce (1993a), Arruda *et al.* (1993), Hasan and Boyce (1995), Arruda *et al.* (1995) and Anand and Gurtin (2003) to mention a few. In the 8-chain model, the micro-macro transition is determined by an average network stretch which is given in terms of principal plastic stretches. Based on the 8-chain model, Anand and Ames (2006) proposed a viscoelastic-viscoplastic constitutive model which was originally used to predict micro-indentation. However, due to the large number of material parameters included, this model is difficult to calibrate and apply in practice. Miehe *et al.* (2004) proposed a full network model for finite rubber elasticity which was later extended to amorphous glassy polymers by Göktepe (2007). In this model, a continuous distribution of chains is represented by a micro-sphere, and the micro-macro transition is given by a p-root averaging operator.

Modeling of macroscopic deformation

Basically, the kinematical approaches for modeling macroscopic deformation of amorphous glassy polymers can be split into the two main categories based on:

(i) the multiplicative decomposition of the total deformation gradient $\boldsymbol{F}$ into an elastic and a plastic component,

(ii) an additive kinematical concept based on the notion of a plastic metric.

In the first approach (i), the plastic component $\boldsymbol{F}^p$ represents the irreversible deformation from the reference configuration to the intermediate configuration and is considered to be an internal variable which describes the macroscopic plastic deformation. The elastic component $\boldsymbol{F}^e$ represents the elastic deformation from the intermediate configuration to the current configuration. Based on the second approach (ii) Miehe *et al.* (2002) proposed a model for anisotropic plasticity in which the elastic strain is conceptually defined in additive form $\boldsymbol{\epsilon}^e := \boldsymbol{\epsilon} - \boldsymbol{\epsilon}^p$. In Miehe *et al.* (2009), the multiplicative approach and the kinematical

approach by Miehe *et al.* (2002) are compared for both isotropic and anisotropic materials and the results indicate similarities for a wide range of boundary value problems.

The micromechanically based models can be regarded as a three dimensional extension of the constitutive model for rubber elasticity by Wang and Guth (1952), in parallel with the rate- and temperature-dependent Argon (1973) model. The Argon (1973) model is based on the double-kink theory which results in a rate- and temperature-dependent evolution equation for the plastic flow. Later Boyce *et al.* (1988) improved the Argon (1973) model by making yield pressure sensitive and by introducing softening. In addition to the Argon (1973) model, the temperature-dependent plastic evolution law proposed by Robertson (1966) should be mentioned. In contrast to the Argon (1973) model where the resistance to plastic deformation is attributed to intermolecular interactions, the evolution of the plastic flow in the Robertson (1966) model requires a threshold for the intramolecular resistance to be reached. Compared to the Argon (1973) model, the Robertson (1966) model yields more accurate results both close to the glass transition temperature and in melt state, whereas the Argon (1973) model is superior in glassy state. It can be concluded that the intermolecular resistance is of major importance in the evolution of the plastic deformation below the glass transition temperature.

Despite the intensive research during the past decades, the physical link between the microstructure and the macroscopic mechanical behavior is not yet fully understood. Stachurski (2003) made a review of the studies which concern the influence of micromechanisms on the macroscopic stress-strain behavior. These studies pointed to the conclusion that the plastic deformation evolves due to the tension in the chain segments which results in slipping through neighboring entanglement sites. Furthermore, in Kameda *et al.* (2007), a large number of experiments have been studied to find the mechanisms for the onset of plastic deformation in non-crystalline polymers. The development of computational power and molecular dynamics (MD) simulation methods have facilitated investigation of microscopic deformation behavior especially at high strain rates. Recently, Capaldi *et al.* (2004) and Lyulin *et al.* (2006) conducted MD simulations to investigate the effects of temperature on deformation of the molecular structure when subjected to high strain rates.

In conclusion, the main features of current models of amorphous glassy polymers can be summarized as follows:

- Material behavior is described as elastic-viscoplastic or viscoelastic-viscoplastic.
- Models can be classified as phenomenological and micromechanically based models.
- The 8-chain model and full network models with a reduced integration scheme are considered most capable micromechanically based models.
- Micromechanically motivated models are based on non-Gaussian statistical mechanics and on non-affine chain motion.
- The micro-macro transformation is determined by an average network stretch which allows fluctuation of the micro-stretches around the macro-stretches.

4 State-of-the-art models of amorphous glassy polymers

Despite the vast amount of research carried out during the past four decades, modeling of amorphous glassy polymers is still an active research field. The objective of the ongoing research is to develop constitutive models which are able to reproduce the experimental response at a minimum number of material parameters while temperature, loading rate and deformation state vary. Moreover, to be of practical importance, the models should be suitable for numerical solution methods. A comparison of models and experimental results in the literature reveals that models based on the 8-chain model and the full network models with reduced integration schemes are most capable for modeling of amorphous glassy polymers. The models by Boyce *et al.* (1988), Arruda and Boyce (1991), Arruda and Boyce (1993a), Wu and Van der Giessen (1993) and Anand and Gurtin (2003) are some examples of models within this group. These models can be considered as three-dimensional extensions of the James and Guth (1943) 3-chain model for rubber elasticity and the Haward and Thackray (1968) model for glassy polymers. However in detail, these models differ and many recent studies are based on them.

In this chapter, the 8-chain model by Arruda and Boyce (1993a) and the full network model by Wu and Van der Giessen (1993) will be discussed in detail. In Sweeney (1999), these two models are compared and it was concluded that the Arruda and Boyce (1993a) model better captures the rubber-like material behavior. A comparison of rubber-like materials also reveals that the stress response by the Wu and Van der Giessen (1993) model is in between those of the 3-chain model by Boyce *et al.* (1988) and the 8-chain model by Arruda and Boyce (1993a).

In addition to the celebrated Arruda and Boyce (1993a) and Wu and Van der Giessen (1993) models, the recent models by Anand and Ames (2006), Dupaix and Boyce (2007) and Miehe *et al.* (2009) will be reviewed in this chapter. The major difference between the reviewed models is the description of the polymer network. The models by Wu and Van der Giessen (1993) and Miehe *et al.* (2009) are full network models, whereas the other models are based on the 8-chain network model. Due to the inability of affine networks models to predict the behavior at large deformations, the only affine model considered here is the one by Wu and Van der Giessen (1993). In all models, the plastic evolution equation relies on the well-accepted double-kink theory of Argon (1973).

In Miehe *et al.* (2009), the macroscopic deformation is described by the concept of a plastic metric, whereas the multiplicative split of the deformation gradient is employed in the remaining models. An advantage of the Miehe *et al.* (2009) concept is that the plastic spin never enters into the formulation, whereas the multiplicative split results in the rotation of the intermediate configuration not being unique. To specify the orientation of the intermediate configuration, a constitutive law for the plastic spin must be postulated. A detailed discussion of that matter can be found e.g. in Boyce *et al.* (1989). In the Anand and Ames (2006) and Dupaix and Boyce (2007) models, the plastic spin is assumed to vanish whereas in the Arruda and Boyce (1993a) and Wu and Van der Giessen (1993)

models, the elastic part of the deformation gradient is assumed to be symmetric which results in the plastic spin being nonzero.

In state-of-the-art models considered in this thesis, the plastic deformation stems from isotropic resistance due to chain segment rotations parallel with anisotropic resistance, which results from the stretching of the entire network and reorientation of the polymer chains. This notion for the hardening mechanism is usable under isothermal loading conditions far below the glass transition temperature T_g as well as it is motivated by the complete reversibility of plastic deformation at temperatures higher than T_g, cf. Melick (2003). However, several claims that show evidence against this approach are presented in the literature. Boyce and Haward (1997) showed that the strain hardening tends to decrease with increasing temperature and the dynamic mechanical thermal analysis (DMTA) performed by Melick (2003) indicated that hardening close to the glass transition temperature is essentially governed by the chain density of the polymer network. According to Tomita and Tanaka (1995), the extension along the chain direction and compression perpendicular to the chain direction increases the number of entanglements and affects hardening in the material. Basu *et al.* (2005) proposed a constitutive model where yield, network hardening and disentanglement are accounted for fibril growth and failure. Klompen *et al.* (2005) and Hoy and Robbins (2007) pointed out that the strain hardening scales with both the yield stress and viscosity of the material. In Bardenhagen *et al.* (1997) and Khan and Zhang (2001), viscosity, which was attributed to the disentanglement of chain network, was shown to increase with elastic strain and reduce with the increasing strain rate. It should be mentioned that many of these approaches, as will be shown, can be readily implemented as a part of state-of-the-art models. One consequence of their application is that the number of material parameters needed in the models increases. Simulations, however, indicate that such complexity is required to satisfactorily predict the experimentally observed thermomechanical behavior of polymer glasses.

In all the models under consideration, the single chain deformation is described in a similar manner. However, the description of the transformation from a single chain deformation to the continuum deformation differs considerably between the 8-chain model and full network models. Hence, the single chain deformation, continuum deformation as well as the Argon (1973) model will be discussed together, whereas the micro-macro transformation and its contribution to macroscopic stresses will be discussed separately.

4.1 Basic kinematics - multiplicative approach

Since most of the constitutive models of amorphous glassy polymers rely on the multiplicative split, the fundamental elements of that approach will be reviewed below. The local deformation is governed by the deformation gradient $\boldsymbol{F}$ which can be considered as a linear map of the referential vectors $d\boldsymbol{X}$ onto the spatial counterparts $d\boldsymbol{x}$, i.e. $d\boldsymbol{x} = \boldsymbol{F} d\boldsymbol{X}$, cf. Fig. 4.1. The reference and the spatial positions in a material body within the Euclidean space are given by the reference and the spatial coordinates $\boldsymbol{X}$ and $\boldsymbol{x}$, respectively. Based

on the total deformation, the constitutive laws in the models under consideration are defined in terms of the Cauchy-Green deformation tensor $\boldsymbol{C}$ or the Finger tensor $\boldsymbol{b}$, defined as

$$\boldsymbol{C} := \boldsymbol{F}^T \boldsymbol{F} \tag{4.1}$$

and

$$\boldsymbol{b} := \boldsymbol{F} \boldsymbol{F}^T \tag{4.2}$$

respectively. The superscript T denotes the transpose. According to the multiplicative decomposition, the deformation gradient is split into its elastic and plastic component as

$$\boldsymbol{F} = \boldsymbol{F}^e \boldsymbol{F}^p. \tag{4.3}$$

The intermediate configuration $\bar{\mathcal{N}}$ is only locally defined, i.e. the elastic and the plastic deformation gradient, $\boldsymbol{F}^e$ and $\boldsymbol{F}^p$ respectively, are not true deformation gradients. However, both are mappings for which $det(\boldsymbol{F}^e) > 0$ and $det(\boldsymbol{F}^p) > 0$, i.e. the inverses $\boldsymbol{F}^{e-1}$ and $\boldsymbol{F}^{p-1}$ exist. Using (4.3), $d\boldsymbol{x}$ is given by $d\boldsymbol{x} = \boldsymbol{F}^e \boldsymbol{F}^p d\boldsymbol{X}$ and since the inverse $\boldsymbol{F}^{e-1}$ exists, the vectors in the intermediate configuration are given by $d\bar{\boldsymbol{X}} = \boldsymbol{F}^p d\boldsymbol{X} = \boldsymbol{F}^{e-1} d\boldsymbol{x}$, cf. Fig. 4.1. Moreover, the elastic constitutive law can be given in terms of the elastic finger tensor

$$\boldsymbol{b}^e := \boldsymbol{F}^e \boldsymbol{F}^{e,T}. \tag{4.4}$$

In the intermediate setting, the elastic constitutive law is defined by the elastic Cauchy-Green deformation tensor

$$\bar{\boldsymbol{C}}^e := \boldsymbol{F}^{e,T} \boldsymbol{F}^e. \tag{4.5}$$

The plastic deformation can be defined via the plastic deformation tensor

$$\boldsymbol{b}^p := \boldsymbol{F}^p \boldsymbol{F}^{p,T} \tag{4.6}$$

or alternatively in the reference configuration by

$$\boldsymbol{C}^p := \boldsymbol{F}^{p,T} \boldsymbol{F}^p. \tag{4.7}$$

In accordance with the polar decomposition, the deformation gradient can be given in terms of the rotation tensor $\boldsymbol{R}$ and the symmetric, positive definite stretches $\boldsymbol{v}$ and $\boldsymbol{U}$ as

$$\boldsymbol{F} = \boldsymbol{v} \boldsymbol{R} = \boldsymbol{R} \boldsymbol{U}. \tag{4.8}$$

In analogy with (4.8), the polar decomposition of the elastic deformation gradient $\boldsymbol{F}^e$ results in

$$\boldsymbol{F}^e = \boldsymbol{v}^e \boldsymbol{R}^e = \boldsymbol{R}^e \bar{\boldsymbol{U}}^e \tag{4.9}$$

where $\boldsymbol{v}^e$ and $\bar{\boldsymbol{U}}^e$ are symmetric, positive definite left and the right elastic stretch tensor, respectively, and $\boldsymbol{R}^e$ is the elastic rotation. In accordance with (4.9), use will be made of

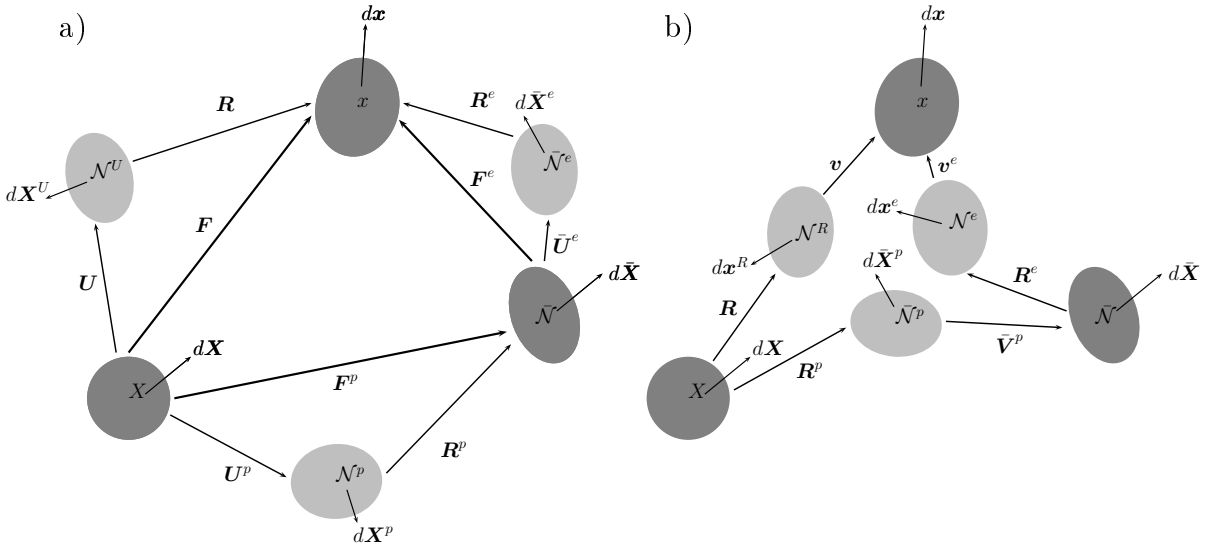

Figure 4.1: Deformation of a solid body and the mappings between different configurations. a) The multiplicative decomposition of the deformation gradient $\boldsymbol{F}$ into an elastic and a plastic part $\boldsymbol{F}^e$ and $\boldsymbol{F}^p$, and the polar decompositions based on the right stretches $\boldsymbol{U}$, $\bar{\boldsymbol{U}}^e$ and $\boldsymbol{U}^p$. b) The polar decompositions based on the left stretches $\boldsymbol{v}$, $\bar{\boldsymbol{V}}^p$ and $\boldsymbol{v}^e$.

the polar decomposition of $\boldsymbol{F}^p$, i.e.

$$\boldsymbol{F}^p = \bar{\boldsymbol{V}}^p \boldsymbol{R}^p = \boldsymbol{R}^p \boldsymbol{U}^p \tag{4.10}$$

where $\bar{\boldsymbol{V}}^p$ and $\boldsymbol{U}^p$ are the plastic stretches and $\boldsymbol{R}^p$ is the plastic rotation. The deformation rate corresponding to decomposition (4.3) is given by the spatial velocity gradient $\boldsymbol{l}$ defined as

$$\boldsymbol{l} := \dot{\boldsymbol{F}}\boldsymbol{F}^{-1} = \boldsymbol{l}^e + \boldsymbol{F}^e \bar{\boldsymbol{L}}^p \boldsymbol{F}^{e-1} =: \boldsymbol{l}^e + \boldsymbol{l}^p \tag{4.11}$$

where $\boldsymbol{l}^p := \boldsymbol{F}^e \bar{\boldsymbol{L}}^p \boldsymbol{F}^{e-1}$ is the spatial form of the plastic velocity gradient $\bar{\boldsymbol{L}}^p$. In (4.11) $\dot{(\cdot)}$, denotes the material time derivative. The elastic and the plastic velocity gradients $\boldsymbol{l}^e$ and $\bar{\boldsymbol{L}}^p$ introduced in (4.11), are defined as

$$\dot{\boldsymbol{F}}^e = \boldsymbol{l}^e \boldsymbol{F}^e, \quad \dot{\boldsymbol{F}}^p = \bar{\boldsymbol{L}}^p \boldsymbol{F}^p. \tag{4.12}$$

Based on (4.12) the rate of the plastic deformation tensor $\dot{\boldsymbol{b}}^p$ can be derived as

$$\begin{aligned} \dot{\boldsymbol{b}}^p &= \dot{\overline{\boldsymbol{F}^p \boldsymbol{F}^{p,T}}} = \dot{\boldsymbol{F}}^p \boldsymbol{F}^{p,T} + \boldsymbol{F}^p \dot{\boldsymbol{F}}^{p,T} = \dot{\boldsymbol{F}}^p \boldsymbol{F}^{p-1} \boldsymbol{F}^p \boldsymbol{F}^{p,T} + \boldsymbol{F}^p \boldsymbol{F}^{p,T} \boldsymbol{F}^{p-T} \dot{\boldsymbol{F}}^{p,T} \\ &= \bar{\boldsymbol{L}}^p \boldsymbol{b}^p + \boldsymbol{b}^p \bar{\boldsymbol{L}}^{p,T}. \end{aligned} \tag{4.13}$$

For later purposes, the spatial velocity gradient is decomposed into its symmetric and skew-symmetric parts as

$$\boldsymbol{l} = \boldsymbol{d} + \boldsymbol{\omega} \tag{4.14}$$

where $\boldsymbol{d} := sym(\boldsymbol{l})$ is the rate of deformation and $\boldsymbol{\omega} := skew(\boldsymbol{l})$ is the spin both given in the spatial configuration. The symmetric and the skew-symmetric part were defined by $sym := 1/2([\cdot] + [\cdot]^T)$ and $skew := 1/2([\cdot] - [\cdot]^T)$, respectively. Similar to (4.14), the elastic and plastic velocity gradients can be decomposed into their symmetric and skew-symmetric part, i.e.

$$\boldsymbol{l}^e = \boldsymbol{d}^e + \boldsymbol{\omega}^e, \quad \bar{\boldsymbol{L}}^p = \bar{\boldsymbol{D}}^p + \bar{\boldsymbol{W}}^p \tag{4.15}$$

where

$$\begin{aligned} \boldsymbol{d}^e &:= sym(\boldsymbol{l}^e), \qquad \boldsymbol{\omega}^e := skew(\boldsymbol{l}^e), \\ \bar{\boldsymbol{D}}^p &:= sym(\bar{\boldsymbol{L}}^p), \qquad \bar{\boldsymbol{W}}^p := skew(\bar{\boldsymbol{L}}^p). \end{aligned} \tag{4.16}$$

Based on (4.16), the rate of the elastic deformation tensor $\dot{\boldsymbol{C}}^e$ can be determined as

$$\dot{\boldsymbol{C}}^e = \overline{\boldsymbol{F}^{e,T}\boldsymbol{F}^e}^{\cdot} = \boldsymbol{F}^{e,T}\boldsymbol{F}^{e-T}\dot{\boldsymbol{F}}^{e,T}\boldsymbol{F}^e + \boldsymbol{F}^{e,T}\dot{\boldsymbol{F}}^e\boldsymbol{F}^{e-1}\boldsymbol{F}^e = 2\boldsymbol{F}^{e,T}\boldsymbol{d}^e\boldsymbol{F}^e, \tag{4.17}$$

i.e. $\dot{\boldsymbol{C}}^e$ is related to the spatial rate of elastic deformation $\boldsymbol{d}^e$ through $\boldsymbol{F}^e$. As a consequence of the multiplicative decomposition of the deformation gradient,

$$\boldsymbol{F} = \boldsymbol{F}^e\tilde{\boldsymbol{R}}\tilde{\boldsymbol{R}}^T\boldsymbol{F}^p = \tilde{\boldsymbol{F}}^e\tilde{\boldsymbol{F}}^p,$$

i.e. the rotation $\tilde{\boldsymbol{R}}$ of the relaxed, stress-free intermediate configuration is not unique and certain additional kinematical assumptions are needed. In the Anand and Ames (2006) and Dupaix and Boyce (2007) models, the plastic spin is assumed to vanish, whereas in the Arruda and Boyce (1993a) and Wu and Van der Giessen (1993) models the plastic spin $\bar{\boldsymbol{W}}^p$ is considered as nonzero. Agah-Tehrani *et al.* (1987) derived an expression for $\bar{\boldsymbol{W}}^p$ based on the assumption that the elastic rotation $\boldsymbol{R}^e$ is unity. Post multiplying (4.11) by $\boldsymbol{F}^e$ and making use of (4.14) and (4.15) yield

$$(\boldsymbol{d} + \boldsymbol{\omega})\boldsymbol{F}^e = \dot{\boldsymbol{F}}^e + \boldsymbol{F}^e(\bar{\boldsymbol{D}}^p + \bar{\boldsymbol{W}}^p). \tag{4.18}$$

Taking the skew-symmetric part of (4.18) results in the following component relation

$$F^e_{ij}(\omega_{jk} - \bar{W}^p_{jk}) + (\omega_{ij} - \bar{W}^p_{ij})F^e_{jk} = F^e_{ij}(d_{jk} + \bar{D}^p_{jk}) - (d_{ij} + \bar{D}^p_{ij})F^e_{jk}, \ i,j,k = 1,2,3, \tag{4.19}$$

where $F^e_{ij} = F^e_{ji}$ due to the irrotational elastic deformation. The equation (4.19) reveals that the spin terms $(\omega_{\alpha\beta} - \bar{W}^p_{\alpha\beta})$ can be given in terms of $(d_{\alpha\beta} + \bar{D}^p_{\alpha\beta})$.

4.2 Single chain deformation

To avoid a complex and computationally expensive treatment of the chain network at the microscopic level, a representative network model is required as well as the transition between micro- and macro-stretches must be determined. The description of a network structure is given in terms of the four idealized quantities: (1) average initial length of chain segments r_0 between physical entanglements, cf. Fig. 4.2; (2) average fully extended length r_L of a chain segment; (3) function of entangled points; and (4) the average orientation distribution of the chain segments.

Once the deformation is applied, the chains extend while the configurational entropy decreases. To describe the deformation of a single chain, a model of freely jointed and volumeless chains is frequently used as the starting point. One end of this hypothetical chain is fixed (e.g. the center point in a cell) while the other end has a finite probability to reach any other position in some infinitesimal volume dv, cf. Flory (1969) and Fried (2009). The non-Gaussian finite extensibility of a single chain is given by the contour length as $r_L = lN$ where N is the number of statistical links (also called "kinks", cf. Argon (1973), Tomita and Tanaka (1995)) of length l between the physical entanglements, cf. Fig. 4.2. Because the chain is freely jointed, the three axes are independent of each other and the probability that a chain has an end-position in dv is the product of the probabilities $W(x)$, $W(y)$ and $W(z)$ for each of the axes considered separately. One of many possibilities to describe the original undeformed length r_0 is defined by a simple stochastic process which results in the random walk a Gaussian distribution

$$\int_V W(x)W(y)W(z)dxdydz = (\frac{\beta}{\sqrt{\pi}})^3 4\pi r^2 e^{-\beta^2 r^2} dr =: W(r)dr.$$

The maximum value of this distribution occurs at $r_{max} = 1/\beta \approx 0.82l\sqrt{N}$. The mean-squared value of r is found by the integrating

$$\langle r^2 \rangle = \int_0^\infty r^2 W(r)dr = l^2 N,$$

which is used to define the random walk-type mean-squared value r_0 as $r_0 = \sqrt{\langle r^2 \rangle} = l\sqrt{N}$. Hence, the chain locking stretch is given by

$$\lambda_L = r_L/r_0 \in (1, \sqrt{N}]. \tag{4.20}$$

The current stretch of a single chain is given by the end-to-end distance $r \in (0, r_L)$ as

$$\lambda = \frac{r}{r_0} \in (0, \sqrt{N}). \tag{4.21}$$

Chains are oriented along the directions for which $\lambda > 1$ and coiled along the directions having $\lambda < 1$.

So far, the chain density n has not explicitly been taken into account. In the models under consideration, the number of entanglements is assumed to be constant. However,

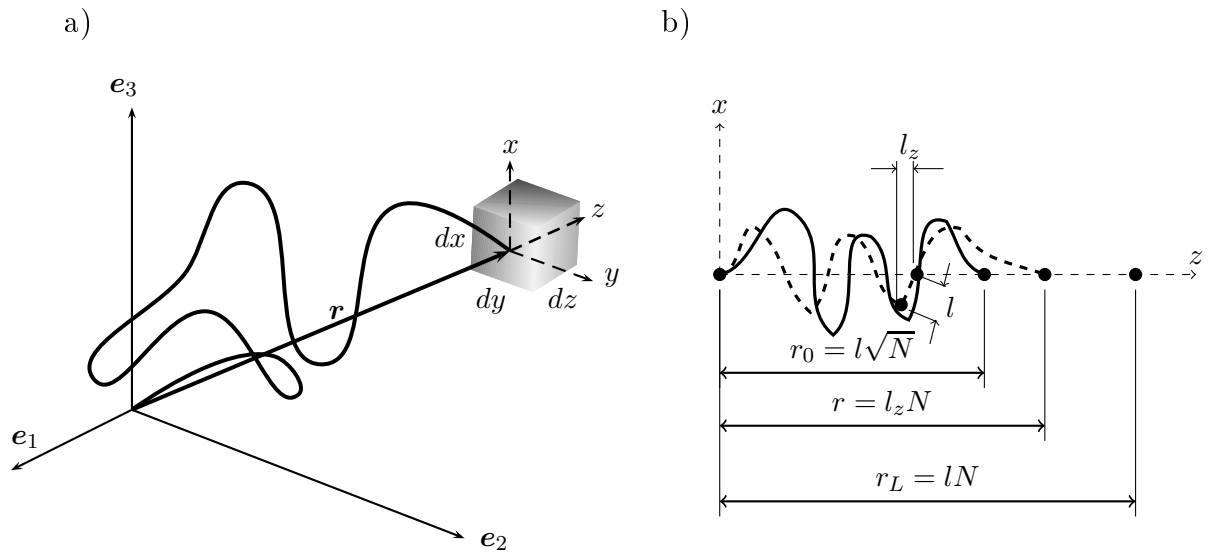

Figure 4.2: Illustration of a freely jointed polymer chain in different configurations: a) the current end-to-end vector $\boldsymbol{r}$ and b) the geometry of a single polymer chain consisting of N segments of equal length l between physical entanglements. The probability for finding the end-position in infinitesimal volume $dv = dxdydz$ during deformation is expressed by the limits: initial random walk-type mean-square value r_0 and the fully extended chain length r_L.

according to the experiments by Raha and Bowden (1972) and Tomita and Uchida (2003), the number of entanglements may change due to deformation and temperature changes. In terms of network theory, increasing number of chains n decreases the number of statistical links N on a chain between the entanglements. Also, the chain density is closely related to the number of entangled points and increasing chain density causes stiffening in the material and results in the extensibility being decreased. Motivated by these observations, the chain density n is assumed to be related to the number of statistical links N between the entanglements via

$$n(\theta)N(\theta) = N_{tot} = const. \tag{4.22}$$

where θ is temperature, cf. Arruda *et al.* (1995).

4.3 Micro-macro transition

The key in network models is to find a link between the deformation of a single chain and the macroscopic, continuum deformation. According to the affine stretch assumption, the macro-stretch $\bar{\lambda}$ of the continuum and the micro-stretch of a single chain λ defined by (4.21) are equal, i.e.

$$\lambda = \bar{\lambda}. \tag{4.23}$$

This relation, however, was originally used to describe the deformation of a single polymer chain between the junctions of a cross-linked network, cf. Treloar and Riding (1979). Later Arruda and Boyce (1993b) showed that the affine stretch assumption is not suitable for large strains and the extensibility of chains should be determined on the basis of non-Gaussian statistics. To allow the micro-stretch of the chains to fluctuate around the macro-stretch,

(4.23) is generalized to

$$\lambda = \bar{\lambda} f \tag{4.24}$$

where the multiplier f is the stretch-fluctuation field on the unit sphere which in a multiplicative format transforms the affine stretch. As it was pointed out in the preceding section, the location of the free end of a freely jointed chain is given by non-Gaussian statistics. In contrast to the end points of chains, the intersections of chains and the surface of a unit sphere define the transformation between the micro- and macro-stretches.

Let us now consider the averaging of a microscopic variable h. Let p denote the probability for finding the crossing point of a single chain within the infinitesimal area element $da := \sin(\theta) d\theta d\varphi$, $\theta \in [0, \pi]$, $\varphi \in [0, 2\pi]$ on the unit sphere. The average of a microscopic variable h under a continuous chain distribution p is defined as

$$\langle h \rangle := \int_{\mathcal{A}} p(a) h(a) da \tag{4.25}$$

where $\mathcal{A}$ denotes the surface of the unit sphere. The homogenization (4.25) allows us to define the homogenized micro-stretch $\langle \lambda \rangle$ as

$$\langle \lambda \rangle := \int_{\mathcal{A}} \lambda p da. \tag{4.26}$$

The non-affine micro-stretch λ is assumed to be constrained by

$$\langle \lambda \rangle = \langle \bar{\lambda} \rangle, \tag{4.27}$$

i.e. the influence of chain fluctuation around the network stretch $\bar{\lambda}$ vanishes in homogenization. In many amorphous polymers, the initial chain distribution p_0 is uniform which results in $p_0 = 1/A$, $A = 4\pi$ being constant. The representation of (4.26) in the referential configuration is derived by the transformation $\lambda(\theta, \varphi) = \lambda(\theta_0, \varphi_0)$, i.e.

$$\langle \lambda \rangle = \int_{A} \lambda(\theta_0, \varphi_0) p_0 dA \tag{4.28}$$

where $dA = \sin(\theta_0) d\theta_0 d\varphi_0$, $\theta_0 \in [0, \pi]$, $\varphi_0 \in [0, 2\pi]$. Taking advantage of (4.27), $p_0 = 1/A$ in (4.28) yields

$$\langle \bar{\lambda} \rangle = \frac{1}{A} \int_{\mathcal{A}} \bar{\lambda} da. \tag{4.29}$$

In addition to the averaging (4.29), Göktepe (2007) proposed an alternative averaging of $\bar{\lambda}$

$$\langle \bar{\lambda} \rangle_m = \big(\frac{1}{A} \int_A (\bar{\lambda})^m dA \big)^{\frac{1}{m}}, \quad m > 0 \tag{4.30}$$

which can be considered as the p-root average of $\bar{\lambda}$. Based on the minimization of the averaged free energy Göktepe (2007) concluded that the non-affine micro-stretch is obtained

only if $\lambda = \bar{\lambda} f$ being constant. Together with (4.27) this gives

$$\lambda = \langle \bar{\lambda} \rangle_m. \tag{4.31}$$

Moreover, let us also remark that the specific choice $m = 2$ in (4.30) corresponds to the non-affine micro-stretch used in the 8-chain model and it will be presented in the next section. In the following, the homogenized macro-stretches $\langle \bar{\lambda} \rangle$ and $\langle \bar{\lambda} \rangle_m$ will be termed the network stretch.

4.3.1 The 8-chain model

In the 8-chain model, the initial orientation of a single chain segment is governed by the initial end-to-end vector $\boldsymbol{r}_0$. The angles between the reference axes and the end-to-end vector have the same initial value $\phi_0 = 54.7°$, cf. Fig. 3.1. During deformation, the chains in the prism remain linked through the fixed center point which results in the elongation of the chains being equal. The current end-to-end vector is denoted by $\boldsymbol{r}$.

In the models for amorphous glassy polymers, the description of the micro-macro transition is based on chain stretching which is due to the plastic deformation. The edges of the 8-chain prism are assumed to align with the unit eigenvectors $\bar{\boldsymbol{N}}_\alpha$, $\alpha = 1, 2, 3$, which are the principal directions of the plastic stretch $\bar{\boldsymbol{V}}^p$, cf. Fig. 4.3. The plastic micro-stretch λ^p is defined by analogy to (4.21), i.e.

$$\lambda^p = \bar{r}/r_0 \tag{4.32}$$

where $\bar{r}$ denotes the end-to-end vector solely due to the plastic stretching. In contrast to the affine deformation, the plastic micro-stretch λ^p is allowed to fluctuate around the continuum deformation. In terms of the unit vector $\bar{\boldsymbol{N}} := 1/\sqrt{3} \sum_\alpha \bar{\boldsymbol{N}}_\alpha$, let us define the

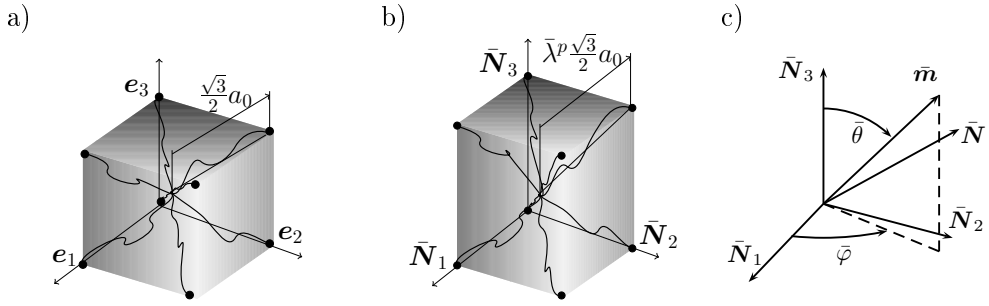

Figure 4.3: The chain geometry according to the 8-chain model in a) undeformed and b) deformed configuration. The base vectors $\bar{\boldsymbol{N}}_\alpha$, $\alpha = 1, 2, 3$, align with the unit eigenvectors of $\bar{\boldsymbol{V}}^p$. The dimension of the undeformed element is a_0 and $\bar{\lambda}^p$ denotes the plastic chain stretch which appears in the direction $\bar{\boldsymbol{m}}$. The unit vector $\bar{\boldsymbol{m}}$ is defined by the angles $\bar{\theta}$ and $\bar{\varphi}$, whereas the plastic network stretch λ^p_{ec} is related to the direction $\bar{\boldsymbol{N}}$.

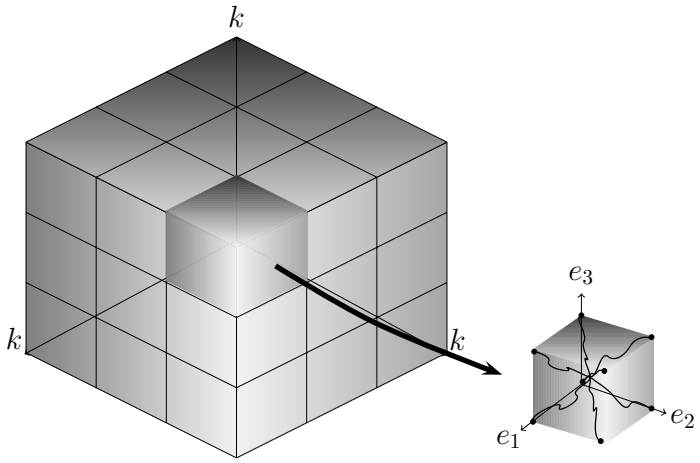

Figure 4.4: Illustration of an 8-chain polymer model. A material body comprises k^3 pieces of 8-chain elements with equal dimension, $a_0 = 2/\sqrt{3}r_0$. The total number of entangled points (black nodes) in a body can be evaluated via the number of entangled points in one element.

plastic network stretch λ_{ec}^p as

$$\lambda_{ec}^p = \sqrt{\bar{\boldsymbol{N}} \cdot \boldsymbol{b}^p \bar{\boldsymbol{N}}} = \frac{1}{\sqrt{3}} \sqrt{\sum_\alpha (\bar{\lambda}_\alpha^p)^2} =: \frac{1}{\sqrt{3}} \sqrt{I_1^p}. \tag{4.33}$$

In (4.33), $(\bar{\lambda}_\alpha^p)^2$, $\alpha = 1, 2, 3$, denote the principal stretches of $\boldsymbol{b}^p$. It emerges from (4.33) that the plastic network stretch is obtained as a projection of the plastic deformation in the direction $\bar{\boldsymbol{N}}$, whereas the single chain direction is given by $\bar{\boldsymbol{m}} = \sum_\alpha \bar{m}_\alpha \bar{\boldsymbol{N}}_\alpha$ with the components $\bar{m}_1 = \sin\bar{\theta}\cos\bar{\varphi}$, $\bar{m}_2 = \sin\bar{\theta}\sin\bar{\varphi}$ and $\bar{m}_3 = \cos\bar{\theta}$, cf. Fig. 4.3. Since the plastic network stretch λ_{ec}^p is independent of $\bar{\theta}$ and $\bar{\varphi}$, (4.27) in (4.30) yields

$$\langle \lambda_{ec}^p \rangle_m = \lambda_{ec}^p, \tag{4.34}$$

i.e. the general non-affine chain model presented in the previous section includes the eight chain model as a special case.

The following small example illuminates the construction of the chain network in the 8-chain model. Assuming that the material body is a rectangular prism comprising k^3 pieces of 8-chain cubes with the dimension $a_0 = 2/\sqrt{3}r_0$, cf. Fig. 4.4. The number of chains in the prism is $q = 8k^3$ and the number of entangled points is $j = (k+1)^3 + k^3$. For a large k, the ratio becomes $q/j = 4$. The relation (4.22) then gives the number of kinks in a single chain is to be found by $N = N_{tot}/(4j)$. For instance, the set of parameters for PC on the first line in Table 5.1 yields $N_{tot} = 6.73 \cdot 10^{27}$, cf. Tomita and Tanaka (1995).

4.3.2 Full network models

Similar to the 8-chain model, the orientation of the chains is described by the vector $\boldsymbol{r}$ having the length $r \in [r_0, r_L]$. The chain orientation distribution over the unit sphere is

given by the distribution function p which must satisfy the normalization condition

$$\int_{\theta=0}^{\pi}\int_{\varphi=0}^{2\pi} p(\theta,\varphi;t)da = 1. \tag{4.35}$$

In the Wu and Van der Giessen (1993) full network model, the distribution function p is termed the Chain Orientation Distribution Function (CODF), cf. also the contribution Harrysson *et al.* (2010) in this regard. The Lagrangian form of the chain distribution as well as the representation in the intermediate configuration can be found by the transformations

$$\int_{\mathcal{A}} pda = \int_{\bar{A}} \bar{p}d\bar{A} = \int_{A} p_0 dA = 1 \tag{4.36}$$

where the infinitesimal area elements are

$$da = \sin(\theta)d\theta d\varphi,\ d\bar{A} = \sin(\bar{\theta})d\bar{\theta}d\bar{\varphi},\ dA = \sin(\theta_0)d\theta_0 d\varphi_0.$$

The infinitesimal area elements da, $d\bar{A}$ and dA on the unit sphere in the reference, intermediate and the spatial configuration, respectively, can be represented via the unit normal vectors and the corresponding infinitesimal area element vectors $d\boldsymbol{a}$, $d\bar{\boldsymbol{A}}$ and $d\boldsymbol{A}$ as

$$da = \boldsymbol{m}^\flat \cdot d\boldsymbol{a}, \quad d\bar{A} = \bar{\boldsymbol{m}}^\flat \cdot d\bar{\boldsymbol{A}}\,, \quad dA = \boldsymbol{m}^0 \cdot d\boldsymbol{A} \tag{4.37}$$

where the unit normals $\boldsymbol{m}^\flat$, $\bar{\boldsymbol{m}}^\flat$ and $\boldsymbol{m}^0$ are covariant vectors. Since the unit normal vector $\boldsymbol{m}^0$ is equal to the initial direction of a single chain, one can define $\boldsymbol{m}^0 := \boldsymbol{r}_0/r_0$. Moreover, the unit normals $\bar{\boldsymbol{m}}^\flat$ and $\boldsymbol{m}^\flat$ are nothing but the representations of the initial normal vector $\boldsymbol{m}^0$ in the intermediate and the spatial configuration, respectively, and they can be derived via the linear maps

$$\boldsymbol{m}^\flat = \frac{r_0}{r}\boldsymbol{F}^{-T}\boldsymbol{m}^0 = \frac{1}{\bar{\lambda}}\boldsymbol{F}^{-T}\boldsymbol{m}^0, \quad \bar{\boldsymbol{m}}^\flat = \frac{r_0}{\bar{r}}\boldsymbol{F}^{p-T}\boldsymbol{m}^0 = \frac{1}{\bar{\lambda}^p}\boldsymbol{F}^{p-T}\boldsymbol{m}^0. \tag{4.38}$$

In (4.38), the affine assumption $\lambda = \bar{\lambda}$ was employed. Since the network stretches follow the continuum deformation, they can be found by

$$\bar{\lambda} = \sqrt{\boldsymbol{m}^0 \cdot \boldsymbol{C}\boldsymbol{m}^0}, \quad \bar{\lambda}^p = \sqrt{\boldsymbol{m}^0 \cdot \boldsymbol{C}^p\boldsymbol{m}^0}. \tag{4.39}$$

Since the plastic deformation is assumed to be isochoric, $det(\boldsymbol{F}^p) = 1$. Employing the Nanson's formula $d\boldsymbol{a} = J\boldsymbol{F}^{-T}d\boldsymbol{A}$ and $d\bar{\boldsymbol{A}} = \boldsymbol{F}^{p-T}d\boldsymbol{A}$ in (4.36) together with (4.38) and (4.37) results in

$$\begin{aligned}
\int_{\mathcal{A}} pda - \int_{A} p_0 dA &= \int_{A} (Jp\frac{1}{\bar{\lambda}}\boldsymbol{m}^0\boldsymbol{C}^{-1} - p_0\boldsymbol{m}^0)d\boldsymbol{A} \\
\int_{\bar{A}} \bar{p}d\bar{A} - \int_{A} p_0 dA &= \int_{A} (\bar{p}\frac{1}{\bar{\lambda}^p}\boldsymbol{m}^0\boldsymbol{C}^{p-1} - p_0\boldsymbol{m}^0)d\boldsymbol{A}
\end{aligned}$$

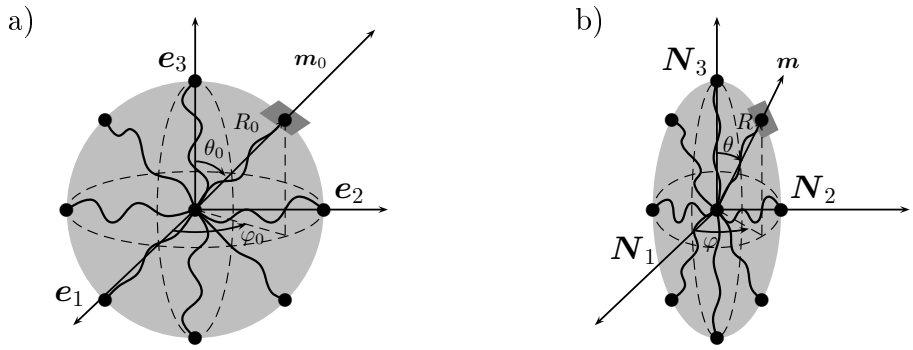

Figure 4.5: The chain geometry according to the full network model in a) undeformed and b) deformed configurations. The initial radius $R_0 = 1$ and R denotes the current distance from the center point to the deformed surface. The orientation of a chain is determined by the angles θ and φ with the initial values θ_0 and φ_0. The base vectors $\boldsymbol{N}_\alpha$, $\alpha = 1, 2, 3$ align with the unit eigenvectors of $\boldsymbol{C}$.

which allow the distributions to be written as

$$p(\theta, \varphi; t) = \frac{p_0}{J}\bar{\lambda}(\theta_0, \varphi_0; t)^3, \quad \bar{p}(\bar{\theta}, \bar{\varphi}; t) = p_0\bar{\lambda}^p(\bar{\theta}, \bar{\varphi}; t)^3. \tag{4.40}$$

Let us now consider an averaging of a microscopic variable h in (4.25). For later purposes, use is made of the intermediate setting. The number of chains $d\bar{Q}$ in an infinitesimal area $d\bar{A}$ is given by

$$d\bar{Q} = n\bar{p}(\bar{\theta}, \bar{\varphi}; t)d\bar{A} \tag{4.41}$$

where n is the number of chains per unit volume. With (4.41), the averaging (4.25) becomes

$$\langle h \rangle = \int_{\bar{A}} \bar{p}(\bar{\theta}, \bar{\varphi}; t)h(\bar{\theta}, \bar{\varphi}; t)nd\bar{A}. \tag{4.42}$$

Substitution of $(4.40)_2$ into (4.42) yields

$$\langle h \rangle = \int_{\bar{A}} (\bar{\lambda}^p)^3 hp_0 nd\bar{A}. \tag{4.43}$$

For a uniform distribution, the average of h can be extracted from (4.43) taking $p = p_0 = 1/A$ into account, i.e

$$\langle h \rangle = \frac{n}{A}\int_{\bar{A}} (\bar{\lambda}^p)^3 hd\bar{A}. \tag{4.44}$$

The averaging (4.44) is employed in the Wu and Van der Giessen (1993) full network model for the plastic part of the free energy φ^p.

4.4 Elasto-viscoplasticity

In this section, the fundamental ingredients of elasto-viscoplasticity suitable for amorphous glassy polymers will be reviewed. In the models considered, the plastic deformation stems from two sources: a) isotropic resistance due to chain segment rotations parallel with b) anisotropic resistance which results from the stretching of the entire network and reorientation of the polymer chains.

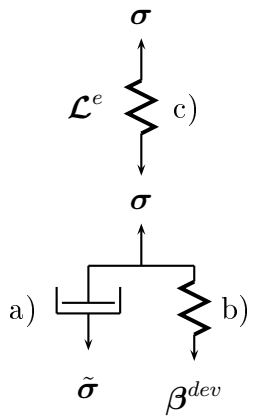

Figure 4.6: Schematic representation of the applied models. The models are governed by the elements: a) viscoplastic dashpot, b) nonlinear Langevin spring and c) elastic spring.

A schematic representation of the model is given in Fig. 4.6. Resistance a) is described by a viscous dashpot representing rate- and temperature-dependent yield while a nonlinear Langevin spring in resistance b) allows the stiffening at large strains to be modeled. In addition, the initial elastic response is modeled by a linear spring having the stiffness $\boldsymbol{\mathcal{L}}^e$. During deformation the distribution of chains becomes non-uniform which results in an anisotropic response.

Without loss of generality, let us consider the setting in the intermediate configuration, cf. e.g. Arruda and Boyce (1993a). The thermomechanical potential, also called Helmholz' free energy per unit volume, is assumed to be given by

$$\varphi = \varphi(\bar{\boldsymbol{C}}^e, \boldsymbol{b}^p) = \varphi^e(\bar{\boldsymbol{C}}^e) + \varphi^p(\boldsymbol{b}^p) \tag{4.45}$$

where φ^e and φ^p are the elastic and the plastic part of the free energy, respectively. The elastic and the plastic deformation tensor $\bar{\boldsymbol{C}}^e$ and $\boldsymbol{b}^p$ were defined by (4.5) and (4.6), respectively. As it was pointed out in Sec. 2, the elastic deformation of amorphous glassy polymers is relatively small, cf. e.g. Haward and Thackray (1968). As a consequence, Arruda and Boyce (1991) and Arruda and Boyce (1993a), for example, assumed the initial response is linear without viscoelastic effects. Moreover, the initial response is considered isotropic due to the uniform chain distribution. The elastic response of many amorphous glassy polymers can be modeled in terms of an isotropic strain energy, i.e.

$$\varphi^e = \frac{1}{2}\kappa(I_1^e)^2 + 2\mu J_2^e \tag{4.46}$$

where κ and μ are the bulk and the shear modulus, respectively. The logarithmic invariants present in (4.46), are defined as

$$I_1^e := trace(\ln \bar{\boldsymbol{U}}^e) = \ln J^e \text{ and } J_2^e := 1/2(\ln \bar{\boldsymbol{U}}^e)^{dev} : (\ln \bar{\boldsymbol{U}}^e)^{dev}$$

where $J^e := det(\bar{\boldsymbol{U}}^e)$. The deviatoric part is defined as $(\cdot)^{dev} := (\cdot) - 1/3 trace(\cdot)\bar{\boldsymbol{I}}$ in which $\bar{\boldsymbol{I}}$ is the identity tensor. Concerning tensorial notations, see e.g. Bonet and Wood (1997) and Belytschko *et al.* (2000) for a more detailed account. In contrast to the plastic part of the free energy, the strain energy expression (4.46) is purely phenomenological. To derive the constitutive relations for the stresses, let us consider the rate of the free energy $\dot{\varphi}$. Assuming isothermal conditions to prevail, the local dissipation per unit volume in the reference configuration is governed by

$$\mathcal{D} := \boldsymbol{S} : \dot{\boldsymbol{E}} - \dot{\varphi} \geq 0 \tag{4.47}$$

where the second Piola-Kirchhoff stress $\boldsymbol{S}$ and the rate of the Green-Lagrange strain $\dot{\boldsymbol{E}}$ are defined as

$$\boldsymbol{S} := \boldsymbol{F}^{-1}\boldsymbol{\tau}\boldsymbol{F}^{-T}, \quad \dot{\boldsymbol{E}} := \boldsymbol{F}^T d\boldsymbol{F} \tag{4.48}$$

and $\boldsymbol{\tau}$ is the Kirchhoff stress. The rate of the free energy becomes

$$-\dot{\varphi}(\bar{\boldsymbol{C}}^e, \boldsymbol{b}^p) = -\frac{\partial \varphi^e(\bar{\boldsymbol{C}}^e)}{\partial \bar{\boldsymbol{C}}^e} : \dot{\bar{\boldsymbol{C}}}^e - \frac{\partial \varphi^p(\boldsymbol{b}^p)}{\partial \boldsymbol{b}^p} : \dot{\boldsymbol{b}}^p, \tag{4.49}$$

Using (4.17) it follows directly that

$$\frac{\partial \varphi^e}{\partial \bar{\boldsymbol{C}}^e} : \dot{\bar{\boldsymbol{C}}}^e = 2(\boldsymbol{F}^e \frac{\partial \varphi^e}{\partial \bar{\boldsymbol{C}}^e} \boldsymbol{F}^{e,T}) : \boldsymbol{d}^e. \tag{4.50}$$

Taking the symmetric part of (4.11) yields

$$\boldsymbol{d} = \boldsymbol{d}^e + \boldsymbol{d}^p. \tag{4.51}$$

Taking advantage of (4.13) and assuming that the plastic part of the free energy is an isotropic function of $\boldsymbol{b}^p$ yields

$$\frac{\partial \varphi^p}{\partial \boldsymbol{b}^p} : \dot{\boldsymbol{b}}^p = 2sym(\frac{\partial \varphi^p}{\partial \boldsymbol{b}^p} \boldsymbol{b}^p) : \bar{\boldsymbol{D}}^p. \tag{4.52}$$

Substituting (4.50) and (4.52) into the dissipation inequality (4.47) and taking (4.51) into account give

$$\mathcal{D} := \left(\boldsymbol{\tau} - 2\boldsymbol{F}^e \frac{\partial \varphi^e}{\partial \bar{\boldsymbol{C}}^e} \boldsymbol{F}^{e,T} \right) : \boldsymbol{d} + 2(\boldsymbol{F}^e \frac{\partial \varphi^e}{\partial \bar{\boldsymbol{C}}^e} \boldsymbol{F}^{e,T}) : \boldsymbol{d}^p - \bar{\boldsymbol{B}} : \bar{\boldsymbol{D}}^p \geq 0 \tag{4.53}$$

where the backstress $\bar{\boldsymbol{B}}$ in the intermediate configuration was defined as

$$\bar{\boldsymbol{B}} := 2sym(\frac{\partial \varphi^p(\boldsymbol{b}^p)}{\partial \boldsymbol{b}^p} \boldsymbol{b}^p). \tag{4.54}$$

Using the arguments by Coleman and Gurtin (1967) turns out the following expression for

the Kirchhoff stress $\boldsymbol{\tau}$

$$\boldsymbol{\tau} = 2\boldsymbol{F}^e \frac{\partial \varphi^e}{\partial \bar{\boldsymbol{C}}^e} \boldsymbol{F}^{e,T}. \tag{4.55}$$

Taking advantage of (4.55), the local dissipation (4.53) reduces to

$$\mathcal{D} := \bar{\boldsymbol{\Sigma}} : \bar{\boldsymbol{D}}^p - \bar{\boldsymbol{B}} : \bar{\boldsymbol{D}}^p \geq 0 \tag{4.56}$$

where the Mandel stress

$$\bar{\boldsymbol{\Sigma}} = 2\bar{\boldsymbol{C}}^e \frac{\partial \varphi^e}{\partial \bar{\boldsymbol{C}}^e} \tag{4.57}$$

was introduced. For later purposes, the dissipation inequality (4.56) can be represented as

$$\mathcal{D} := \tilde{\boldsymbol{\Sigma}} : \bar{\boldsymbol{D}}^p \geq 0, \quad \tilde{\boldsymbol{\Sigma}} := \bar{\boldsymbol{\Sigma}} - \bar{\boldsymbol{B}} \tag{4.58}$$

where $\tilde{\boldsymbol{\Sigma}}$ is the thermodynamic driving stress in the intermediate configuration. Since not all of the plastic work is dissipated, a part of the plastic work is stored in the material during deformations. In the models, the backstress represents the non-dissipative stored stress. Later on, it will be shown that the models under consideration satisfy (4.56) and (4.58).

It should be noted that the Mandel stress in general is not symmetric. However, if the strain energy φ^e is assumed to be an isotropic tensor function, it turns out that the Mandel stress is symmetric. Expressing the elastic deformation tensor $\bar{\boldsymbol{C}}^e$ in terms of the eigenvectors $\bar{\boldsymbol{N}}^e_\alpha$ and the elastic principal stretches $\bar{\lambda}^e_\alpha = \sqrt{\bar{\boldsymbol{N}}^e_\alpha \cdot \bar{\boldsymbol{C}}^e \bar{\boldsymbol{N}}^e_\alpha}$, $\alpha = 1, 2, 3$, and using the chain rule in the isotropic strain energy φ^e results in

$$\frac{\partial \bar{\varphi}^e(\bar{\boldsymbol{C}}^e)}{\partial \bar{\boldsymbol{C}}^e} = \sum_{\alpha=1}^{3} \frac{1}{2(\bar{\lambda}^e_\alpha)^2} \frac{\partial \bar{\varphi}^e}{\partial \ln \bar{\lambda}^e_\alpha} \bar{\boldsymbol{N}}^e_\alpha \otimes \bar{\boldsymbol{N}}^e_\alpha. \tag{4.59}$$

Substitution of (4.59) into (4.55) yields

$$\boldsymbol{\tau} = 2\boldsymbol{F}^e \frac{\partial \bar{\varphi}^e}{\partial \bar{\boldsymbol{C}}^e} \boldsymbol{F}^{e,T} = \boldsymbol{F}^e \Big(\sum_{\alpha=1}^{3} \frac{1}{(\bar{\lambda}^e_\alpha)^2} \frac{\partial \bar{\varphi}^e}{\partial \ln \bar{\lambda}^e_\alpha} \bar{\boldsymbol{N}}^e_\alpha \otimes \bar{\boldsymbol{N}}^e_\alpha \Big) \boldsymbol{F}^{e,T}. \tag{4.60}$$

Taking $\boldsymbol{F}^e \bar{\boldsymbol{N}}^e_\alpha = \bar{\lambda}^e_\alpha \boldsymbol{R}^e \bar{\boldsymbol{N}}^e_\alpha$ into account in (4.60) and noting $\bar{\lambda}^e_\alpha = \lambda^e_\alpha$, the Kirchhoff stress $\boldsymbol{\tau}$ takes the following form

$$\boldsymbol{\tau} = \sum_{\alpha=1}^{3} \frac{\partial \varphi^e}{\partial \ln \lambda^e_\alpha} \boldsymbol{R}^e \bar{\boldsymbol{N}}^e_\alpha \otimes \bar{\boldsymbol{N}}^e_\alpha \boldsymbol{R}^{e,T}. \tag{4.61}$$

Since $\boldsymbol{C}^e \bar{\boldsymbol{N}}^e_\alpha = (\bar{\lambda}^e_\alpha)^2 \bar{\boldsymbol{N}}^e_\alpha$, the Mandel stress becomes

$$\bar{\boldsymbol{\Sigma}} := 2\Big(\frac{\partial \bar{\varphi}^e(\bar{\boldsymbol{C}}^e)}{\partial \bar{\boldsymbol{C}}^e} \bar{\boldsymbol{C}}^e \Big) = \sum_{\alpha=1}^{3} \frac{\partial \bar{\varphi}^e}{\partial \ln \bar{\lambda}^e_\alpha} \bar{\boldsymbol{N}}^e_\alpha \otimes \bar{\boldsymbol{N}}^e_\alpha. \tag{4.62}$$

Comparison of (4.61) and (4.62) reveals that

$$\bar{\boldsymbol{\Sigma}} = \boldsymbol{R}^{e,T}\boldsymbol{\tau}\boldsymbol{R}^{e} \tag{4.63}$$

and thus for the assumption $\boldsymbol{R}^e$ being unity, the components of the Mandel stress and the Kirchhoff stress are equal. Using the strain energy (4.46), the Mandel stress $\bar{\boldsymbol{\Sigma}}$ takes the following form

$$\bar{\boldsymbol{\Sigma}} = 2\mu(\ln \bar{\boldsymbol{U}}^e)^{dev} + \kappa \ln J^e \bar{\boldsymbol{I}}. \tag{4.64}$$

4.5 Argon (1973) plastic evolution model

In this section, the evolution equation for plastic deformation by Argon (1973) is outlined. The details involving the double-kink theory can be found in Love (1944), Li and Gilman (1970) and Argon (1973). The plastic deformation of amorphous glassy polymers is a thermally activated stochastic process which is described by the Arrhenius-type equation, i.e.

$$\dot{\gamma}^p = \dot{\gamma}_0 \exp(-\Delta G_f / kT) \tag{4.65}$$

where $\dot{\gamma}_0$ is a constitutive parameter and ΔG_f is the amount of activation free enthalpy. According to the double-kink theory, the rotation of the polymer molecule segments generates the plastic deformation. The activation free enthalpy ΔG_f is due to the formation of a pair of kinks in a polymer molecule segment embedded in the surrounding material. Let

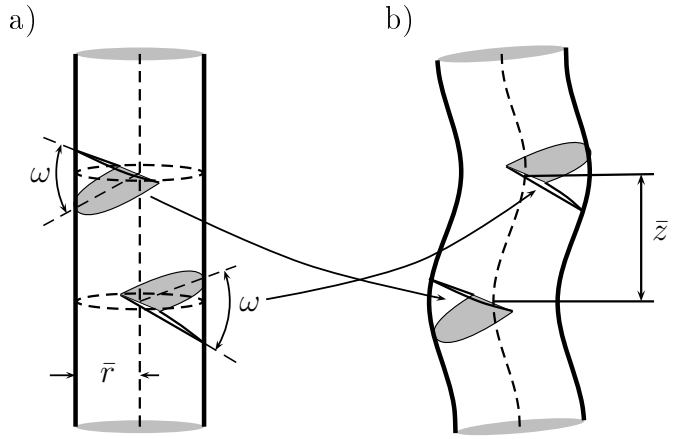

Figure 4.7: Modeling of a kink pair by the Argon (1973) model. a) A pair of kinks are formed by taking two circular cuts of radius $\bar{r}$, removing wedges of angle ω and b) finally arranging the wedges in the opposite side. The distance of the wedges is denoted by $\bar{z}$.

us consider a reference cylinder of a radius $\bar{r}$ which represents a straight chain molecule being embedded in an elastic media, cf. Fig. 4.7. The pair of molecular kinks can be formed by removing two wedges separated by a distance $\bar{z}$, then inserting the wedges into the opposite side and finally joining the parts together. The amount of activation free

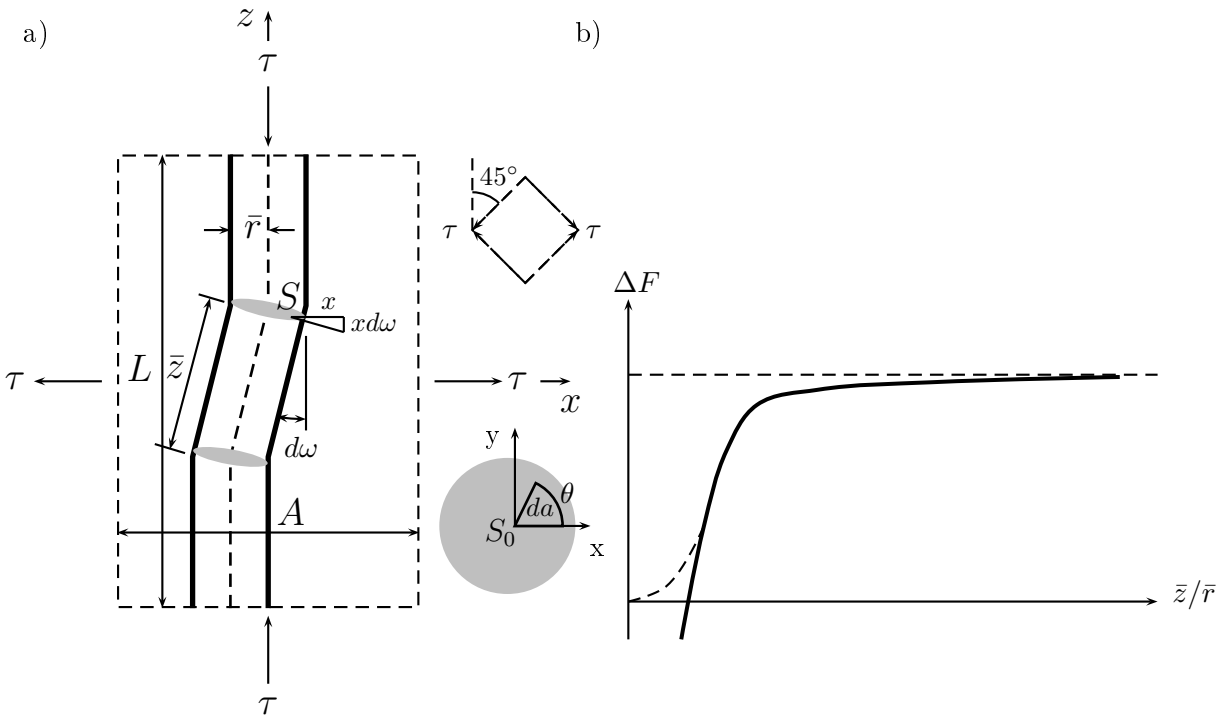

Figure 4.8: Illustration of Argon (1973) double-kink theory. a) Formation of double-kink by a pair of wedge disclination loops of a molecule segment in the surrounding material. The plane AL aligns with the xz-directions which are the principal directions of the applied shear stress state. The initial cut-surface S_0 of a loop is in the xy-plane perpendicular to z-direction. b) The micro-free energy ΔF as a function of distance ratio $\bar{z}/\bar{r}$.

enthalpy required for the kink formation is defined as the difference

$$\Delta G_f = \Delta W - \Delta F \tag{4.66}$$

where ΔW is the work done by an externally applied stress τ during the formation of the disclination loops, cf. Fig. 4.8. In the material surrounding the chain, the effective shear stress τ is considered constant. ΔF in (4.66) is the change in the free energy due to the formation of a pair of disclination loops in the surrounding material. In amorphous polymers, disclinations are primarily caused by chain kinking called wedge disclinations, whereas twist disclinations can be ignored, cf. Li and Gilman (1970). Also dislocations, which are recognized as common defects in crystalline polymers, are not sufficient to execute arbitrary conformational changes in amorphous polymers. For a wedge disclination loop, the rotation angle is denoted by ω and the axis of the rotation is in the plane of the loop, cf. Fig. 4.8. Once the wedge disclination loops are formed, the rotation results in an average compressive strain increment $\Delta\epsilon_{zz}$. Based on simple linear kinematics,

$$\Delta\epsilon_{zz} = -\frac{\pi\bar{r}^2}{AL}\bar{z}(1-\cos(\omega)) \approx -\frac{\pi\bar{r}^3}{2AL}\frac{\bar{z}}{\bar{r}}\omega^2$$

where A is the cross-sectional area and L is the length of the domain under consideration, cf. Fig. 4.8. The latter result relies on an expansion for $\omega << 1$. Since the kinking takes place around the y-axis and the continuum in the y-direction is considered infinite, the

plane strain state prevails, i.e. $\Delta\epsilon_{yy} = 0$. Moreover, first order changes in volume are considered negligible and hence $\Delta\epsilon_{xx} = -\Delta\epsilon_{zz}$. Hence, the work done by the applied stress τ becomes

$$\Delta W = \int_L \int_A (-\tau \cdot \Delta\epsilon_{zz} + \tau \cdot -\Delta\epsilon_{zz}) dA dL = -2AL\tau \cdot \Delta\epsilon_{zz} = \pi \bar{r}^3 \omega^2 \tau \frac{\bar{z}}{\bar{r}}. \tag{4.67}$$

Next, let us consider the approximation of the free energy ΔF based on the distant stress field. For further reading, Huang and Mura (1972) conducted more accurate computations for the elastic free energy outside the disclination loops. In the formation of wedge disclinations, ΔF is primarily due to the work done by the stress component $\sigma_{zz}(x, y, z)$. Following Li and Gilman (1970), the free energy ΔF consists of two parts. The first part ΔF_{self} is due to the elastic interaction of the two wedge disclination loops with their neighbours, and the second part ΔF_{int} is due to the interaction between the two disclination loops. The displacement field at large distances from the loop is obtained by applying the Volterra method, cf. Volterra (1907) and Love (1944). For instance the displacement $u_{xx}(x, y, z)$ is caused by a point force f_{xx} applied at a location $P(x, y, z)$ of an elastic surrounding. Since the Volterra method is beyond the scope of this work, the displacements are extracted from Li and Gilman (1970):

$$\begin{aligned}
u_{xx} &= \frac{3\omega\bar{r}^4}{32(1-\nu)}\left(\frac{z^2}{R^5}\left(\frac{5x^2}{R^2} - 1\right) + \frac{1-2\nu}{R^3}\left(\frac{1}{3} - \frac{x^2}{R^2}\right)\right), \\
u_{yy} &= \frac{3\omega\bar{r}^4 xy}{32(1-\nu)R^5}\left(\frac{5z^2}{R^2} - 1 + 2\nu\right), \\
u_{zz} &= \frac{3\omega\bar{r}^4 xz}{32(1-\nu)R^5}\left(\frac{5z^2}{R^2} + 1 - 2\nu\right)
\end{aligned} \tag{4.68}$$

where ν is the Poisson's ratio and $R := \sqrt{x^2 + y^2 + z^2}$. The displacements (4.68) give rise to the strain field

$$\begin{aligned}
\epsilon_{xx} &= \frac{15x\omega\bar{r}^4}{32R^5(1-\nu)}\left(\frac{z^2}{R^2}\left(3 - \frac{7x^2}{R^2}\right) - (1-2\nu)\left(\frac{3}{5} - \frac{x^2}{R^2}\right)\right), \\
\epsilon_{yy} &= \frac{15x\omega\bar{r}^4}{32R^5(1-\nu)}\left(\frac{z^2}{R^2}\left(1 - \frac{7y^2}{R^2}\right) - (1-2\nu)\left(\frac{1}{5} - \frac{y^2}{R^2}\right)\right), \\
\epsilon_{zz} &= \frac{15x\omega\bar{r}^4}{32R^5(1-\nu)}\left(\frac{z^2}{R^2}\left(3 - \frac{7z^2}{R^2}\right) + (1-2\nu)\left(\frac{1}{5} - \frac{z^2}{R^2}\right)\right).
\end{aligned} \tag{4.69}$$

Based on the strains (4.69) at large distances from the loops, and assuming linear elasticity, the stress component σ_{zz} becomes

$$\sigma_{zz} = \frac{3\bar{r}^4\mu\omega}{16(1-\nu)}\frac{x}{R^5}\left(1 + \frac{10z^2}{R^2} - \frac{35z^4}{R^4}\right) \tag{4.70}$$

where μ is the shear modulus. In the derivation of (4.70), first order changes in volume were neglected. The stress field σ_{zz} is shown in Fig. 4.9. The micro-free energy ΔF

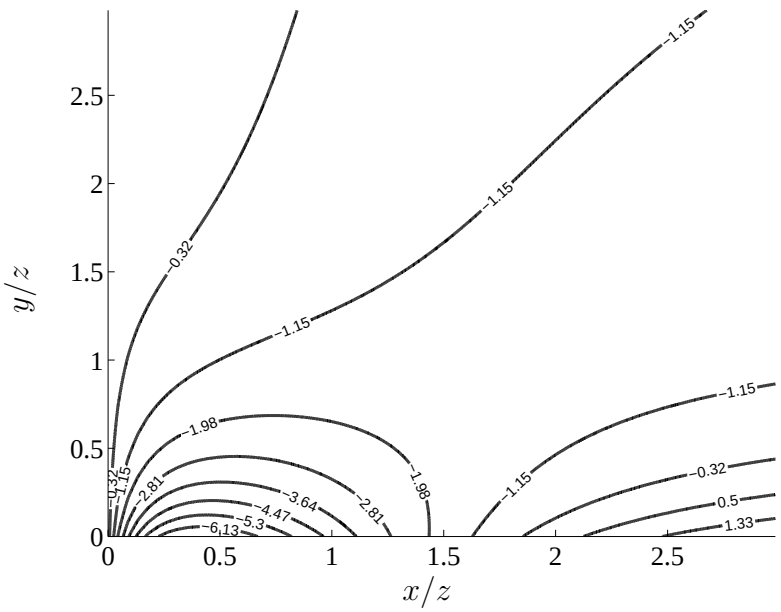

Figure 4.9: Stress field σ_{zz} of a wedge disclination loop. The stress is scaled by $3\bar{r}^4\omega\mu/16(1-\nu)z^4$.

is due to the work done by the infinitesimal force $d\Delta f_{zz} = \sigma_{zz}da$, which results in the infinitesimal displacement $du_{zz} = xd\omega$, cf. Fig. 4.8. Since the self energy ΔF_{self} arises from the resistance of the elastic surroundings, it is obtained by integrating the stress field σ_{zz} at the cut plane $z = 0$ outside the two disclination loops. The infinitesimal area element outside the disclination loop is given by $da = rdrd\theta$ and the integration yields

$$\Delta F_{self} = 2\int_0^{2\pi}\int_{\bar{r}}^{\infty}\int_0^{\omega}\sigma_{zz}(xd\omega)rdrd\theta = \frac{3\pi\bar{r}^3\mu\omega^2}{16(1-\nu)}. \tag{4.71}$$

This result can be considered as an estimate since the stress field is only accurate at large distances from the loops in atomic dimensions, cf. Li and Gilman (1970). The interaction energy ΔF_{int} is due to the formation of the second loop within the stress field of the first loop. The infinitesimal area element inside the disclination loop is given by $da = 1/2rdrd\theta$, cf. Fig. 4.8. The integration over the stress field σ_{zz} inside the two disclination loops results in the amount of the interaction energy being

$$\Delta F_{int} = -2\int_0^{2\pi}\int_0^{\bar{r}}\int_0^{\omega}\sigma_{zz}(xd\omega)\frac{1}{2}rdrd\theta = -\frac{9\pi\bar{r}^3\mu\omega^2}{8(1-\nu)}\left(\frac{\bar{r}}{\bar{z}}\right)^5 \tag{4.72}$$

where $z = \bar{z}$, i.e. the distance between the two disclination loops. Since $\bar{r} << \bar{z}$, a comparison of (4.71) and (4.72) reveals that the micro-free energy ΔF results primarily from the self energies of the loops. The micro-free energy ΔF as a function of distance ratio $\bar{z}/\bar{r}$ is represented in Fig. 4.8(b). In the derivation of (4.72), the two loops are assumed to be relatively far apart and the stress field is assumed to be linear elastic. As a result, the free energy ΔF does not vanish as the ratio $\bar{z}/\bar{r}$ goes zero. Substitution of (4.67), (4.71)

and (4.72) into (4.66) yields

$$\Delta G_f = \Delta F - \Delta W = \frac{3\pi\bar{r}^3\mu\omega^2}{16(1-\nu)} - \frac{9\pi\bar{r}^3\mu\omega^2}{8(1-\nu)}\big(\frac{\bar{r}}{\bar{z}}\big)^5 - \pi\bar{r}^3\mu\omega^2\big(\frac{\tau}{\mu}\big)\big(\frac{\bar{z}}{\bar{r}}\big). \tag{4.73}$$

The extremum of the total activation energy ΔG_f is determined by setting the derivative of ΔG_f with respect to the ratio $(\bar{z}/\bar{r})$ to zero. This yields the extremum

$$(\bar{z}/\bar{r})^* = (\frac{45}{8(1-\nu)}\frac{\mu}{\tau})^{1/6}$$

and the substitution of $(\bar{z}/\bar{a})^*$ into (4.73) yields,

$$\Delta G_f^* = \frac{3\pi\bar{r}^3\mu\omega^2}{16(1-\nu)}\big(1 - (\frac{\tau}{s_0})^{\frac{5}{6}}\big) \tag{4.74}$$

where s_0 is the athermal shear strength having a constant value $s_0 = 0.077\mu/(1-\nu)$. Use of (4.74) in (4.65) yields the evolution law for the plastic deformation, i.e.

$$\dot{\gamma}^p = \dot{\gamma}_0 \exp\big(-\frac{As}{T}(1 - (\frac{\tau}{s_s})^{\frac{5}{6}})\big) \tag{4.75}$$

where $A := 39\pi\omega^2\bar{r}^3/(16k)$. The constant athermal stress s_0 in (4.74) is replaced by s_s which takes pressure into account, i.e.

$$s_s = s + \alpha p, \quad p = -1/3 trace(\boldsymbol{\sigma}) \tag{4.76}$$

where s is the athermal stress. The parameter α is the pressure dependence factor, ranging from 0.1-0.2 for amorphous glassy polymers, cf. Bowden and Jukes (1972). According to Boyce *et al.* (1988), the athermal shear strength s is assumed to obey the evolution rule

$$\dot{s} = h(1 - s/s_{ss})\dot{\gamma}^p, \quad s(0) = s_0 \tag{4.77}$$

where h and s_{ss} are constitutive parameters.

4.6 Plastic part of the free energy φ_c^p of a single chain

The free energy of the entire network is assumed to be equal to the sum of the free energies of the single chains. Since the description of the macroscopic deformation through all singe chains becomes very complicated, statistical methods are employed. Based on statistical mechanics, the polymer chains are described by an idealized chain which consists of freely rotating links. The idealized chain is composed of N statistical links having an equal length l. Based on the fundamental postulate of statistical mechanics for an isolated system in macroscopic equilibrium, the rotation of each link has an equal probability, i.e. no mutual correlation exists between adjacent links, cf. Diu *et al.* (1990). However, the rotations of

links in real polymers are constrained by neighboring chains to vary on a limited interval. It then follows from this assumption that the undeformed length of a chain is given by the random walk-type mean-square value as $r_0 = l\sqrt{N}$. The goal of using a statistical approach is to describe the mean behavior of a chain in equilibrium. The constrained neighborhood of a chain is considered as a heat reservoir which keeps one or some of the quantities, such as energy, volume, pressure or temperature in a chain constant, but allows the energy exchange between the chain and the heat reservoir, cf. Göktepe (2007).

Let us first consider a freely jointed chain in a state where energy exchange between the chain and the reservoir is solely due to heating while the temperature of the chain is constant. The chain within the reservoir constitutes a system which consists of $i = 1, ..., N$ links. The task is then to find the statistical distribution of the microscopic states which maximizes the statistical entropy

$$\eta = -k \sum_i p_i \ln p_i \tag{4.78}$$

with the constraints

$$\sum_i p_i = 1, \quad e = \sum_i p_i e_i = \text{ constant} \tag{4.79}$$

where k is the (positive) Bolzmann's constant and p_i is the probability of finding the freely jointed chain in the state with internal energy e_i, cf. Diu *et al.* (1990). The second constraint, e being constant, states that the externally imposed total energy of the system is fixed. Moreover, if one configuration has the probability $p_k = 1$, $k \in [1, ..., N]$, the entropy vanishes. The solution of the maximization problem (4.78) can be found using the method of Lagrange multipliers which leads us to the following form

$$\mathbb{L} = \sum_i p_i \ln p_i + \beta(\sum_i p_i e_i - e + \sum_i p_i - 1) \tag{4.80}$$

where $\beta := 1/kT$ is the Lagrange multiplier. The necessary condition for the minimization problem is that the gradient of the Lagrangian function vanishes, i.e. $\partial \mathbb{L}/\partial p_i = 0$, $i = 1, ..., N$, and the result is

$$p_i = \frac{\exp(-\beta e_i)}{Z}. \tag{4.81}$$

In the solution (4.81), the partition function $Z = \hat{Z}(T) = \sum_i(\exp(-\beta e_i))$ is found by substituting the probabilities (4.81) into $(4.79)_1$. With the probabilities (4.81), the total energy e is obtained as the sum over the chains, i.e.

$$e = \sum_i e_i p_i = \frac{\sum_i e_i(\exp(-\beta e_i))}{Z}. \tag{4.82}$$

From (4.82), it can be concluded that

$$e = -\frac{\partial \ln Z}{\partial \beta}. \tag{4.83}$$

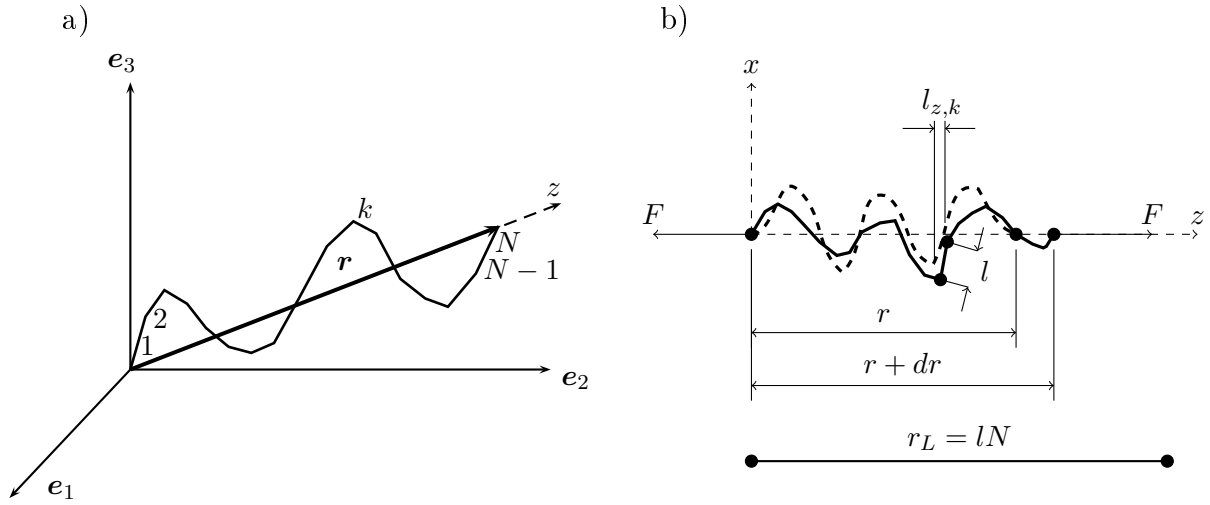

Figure 4.10: A chain configuration. a) Idealized geometry of a single polymer chain consisting of N segments of equal length l. b) The elongation of a chain is due to a constant force F and the projections of the segments on z-axis is denoted by $l_{z,i}$, $i = 1, ..., k, ..., N$.

Moreover, $ed\beta = -(\partial \ln Z/\partial\beta)d\beta =: -d(\ln Z)$. Using the product derivative rule results in

$$ed\beta = d(e\beta) - \beta de = -d(\ln Z). \tag{4.84}$$

Since the energy change de is solely due to heat exchange, $de = Td\eta$ which together with (4.84) yields

$$ed\beta = d(e\beta) - \beta T d\eta = -d(\ln Z). \tag{4.85}$$

Taking note of the total energy change being e, integration of (4.85) yields the following mean value for entropy

$$\eta = k(\ln Z + \beta e) \tag{4.86}$$

For brevity, the integration constants were suppressed in the derivation of (4.86). However, in addition to the constant temperature, the chain is also subjected to constant pressure. In this situation, the chain is neither isolated nor rigid, i.e. an energy change between the chain and the reservoir takes place in the form of both heat and work. The work on the surroundings is done by a constant axial "tip force" $F := \partial\varphi/\partial\lambda$ where φ denotes the free energy of a single chain, cf. Fig 4.10(b). A configuration of the chain is described by $l_{z,i}$, $i = 1, ..., N$, which are the projections of each segment of equal length l on the z-axis. All admissible configurations belong to the set

$$\mathcal{A} := \left\{ \{l_{z,i},\, i = 1, 2, ..., N\} \,|\, r = \hat{r}(l_{z,i}) = \sum_{i}^{N} l_{z,i} =: N l_z \right\} \tag{4.87}$$

where l_z is the average projection length. The chain configuration in equilibrium possesses the enthalpy of each segment $h_i = \hat{h}_i(r) = \hat{e}_i(r) - Fr$, $i = 1, ..., N$ where the end-to-end distance r is considered as an internal variable that continuously changes within the domain $\mathcal{A}$. The problem at hand is now to find a configuration in $\mathcal{A}$ that maximizes the statistical

entropy

$$\eta = \int_{\mathcal{A}} -k \sum_i (p_i \ln p_i) dr \tag{4.88}$$

subjected to the constraints

$$\int_{\mathcal{A}} \sum_i p_i dr = 1, \quad h = \int_{\mathcal{A}} \sum_i p_i h_i dr = \text{ constant}, \quad e = \int_{\mathcal{A}} \sum_i p_i e_i dr = \text{ constant}. \tag{4.89}$$

Using the method of Lagrange multipliers in the same way as above, the solution of the maximization problem becomes

$$p_i = \hat{p}_i(r) = \frac{\exp(-\beta \hat{h}_i(r))}{Z} \tag{4.90}$$

where

$$Z = \hat{Z}(T, F) = \int_{\mathcal{A}} \sum_i \exp(-\beta \hat{h}_i(r)) dr. \tag{4.91}$$

Using the probabilities p_i in (4.90) the mean enthalpy h is derived in analogy to (4.82), i.e.

$$h = \int_{\mathcal{A}} \sum_i p_i h_i dr = \int_{\mathcal{A}} \frac{\sum_i h_i(\exp(-\beta h_i))}{Z} dr. \tag{4.92}$$

Similar to (4.83), the mean enthalpy h can be identified as

$$h = -\frac{\partial \ln Z}{\partial \beta} \tag{4.93}$$

and the average end-to-end distance as

$$r = \frac{1}{\beta} \frac{\partial \ln Z}{\partial F}. \tag{4.94}$$

Multiplication of h by $d\beta$ yields

$$h d\beta = -d(\ln Z). \tag{4.95}$$

In addition to the energy change $de = T d\eta$, the change of enthalpy dh includes the infinitesimal work $r dF$, i.e. $dh = -r dF + T d\eta$. Taking this result into account and using the product derivative rule, (4.95) can be rewritten as

$$h d\beta = d(h\beta) - \beta dh = d(h\beta) - \beta(-r dF + T d\eta) = -d(\ln Z). \tag{4.96}$$

Taking note of F being constant and the total enthalpy of the system being h, the integration of (4.96) yields the entropy

$$\eta = k(\ln Z + \beta h) = k \ln Z + \frac{e - Fr}{T}. \tag{4.97}$$

Using the entropy (4.97) in the definition of the free energy $\varphi := e - T\eta$ results in

$$\varphi = -kT \ln Z + Fr. \tag{4.98}$$

Since the length of each segment is l, the projections are restricted to the interval $l_{z,i} \in [-l, l]$, cf. Fig 4.10. Moreover, since orientation of each chain segment is a priori uniform, the normalization condition results in

$$\int_{-l}^{l} p(l_{z,i}) dl_{z,i} = 1 \;\Rightarrow\; p_i(l_{z,i}) = 1/(2l),$$

i.e. the probability density in all directions is equal $p_i(r(l_{z,i})) = p_j(r(l_{z,j}))$ for all $i, j = 1, ..., N$. It then follows from (4.90) that h_i as well as e_i, $i = 1, ..., N$ are equal. Taking this result into account and using the properties of the exponential function allow the partition function (4.91) to be written as

$$Z = \hat{Z}(T, F) = \int_{\mathcal{A}} \exp(\beta F r) dr. \tag{4.99}$$

Note, that the constant terms were neglected in (4.99) due to the identity $d(\ln Z) = 1/Z dZ$, which was needed to obtain the free energy (4.98). Let us then consider an infinitesimal change in the chain configuration. The change in the chain length is denoted by dr and it is due to the change in a chain configuration with the equal distributions $p_i = \hat{p}_i(l_{z,i}) = 1/2l$ for each segment $i = 1, ..., k, ..., N$. The probability that the segment k obtains the projection length $l_{z,k}$ is given by $P_k = l_{z,k}/2l$. Since the chain motion is Brownian, the alignment of each segment takes place simultaneously. As mentioned above, the alignment of the segments is assumed to be independent from the others which defines the probability dP for an infinitesimal change of the projection length l_z to be calculated by the multiplicative rule, i.e.

$$dP = \prod_i dP_i = \prod_i p_i dl_{z,i} = (\frac{1}{2l})^N \prod_i dl_{z,i} \approx (\frac{dl_z}{2l})^N \tag{4.100}$$

where the error in approximation vanishes as the number of chain segments N approaches to infinity. It then follows from (4.87) that $dr = r dP = N l_z dP$ which together with (4.100) in (4.99) yields

$$Z(T, F) = \big(\frac{1}{2l} \int_{-l}^{l} \exp(\beta F l_z) dl_z\big)^N = \big(\frac{\sinh(\chi)}{\chi}\big)^N \tag{4.101}$$

where $\chi := \beta F l$. Substitution of (4.101) into (4.94) gives the end-to-end distance $r = lN\mathfrak{L}(\chi)$, where $\mathfrak{L}$ is the Langevin function defined by $\mathfrak{L}(\chi) = \coth(\chi) - 1/\chi$. The inversion of the Langevin function results in $\chi := \mathfrak{L}^{-1}(r/lN) = \mathfrak{L}^{-1}(\lambda/\sqrt{N})$ and thus

$$F = \frac{kT}{l} \mathfrak{L}^{-1}(\lambda/\sqrt{N}). \tag{4.102}$$

When evaluating the inverse of the Langevin function, the Pade approximation $\mathfrak{L}^{-1}(\lambda/\sqrt{N}) =$

$\lambda(3-(\lambda)^2)/(1-(\lambda)^2)$ proposed by Cohen (1991) is employed. The error associated with this approximation vanishes as N approaches to infinity. In the extension of the non-Gaussian free energy for rubber elasticity to the plastic potential for glassy polymers, the principal stretches of $\boldsymbol{v}$ are replaced by the principal plastic stretches of $\bar{\boldsymbol{V}}^p$. Let us then assume that $\bar{r}$ is the end-to-end distance of the chain which results solely from plastic deformation. The plastic micro-stretch was already given by (4.32), i.e. $\lambda^p = \bar{r}/r_0$. Using λ^p, insertion of (4.102) into (4.98) results in the following expression for the plastic part of the free energy of a single chain

$$\varphi_c^p = kNT\big(\frac{\lambda^p}{\sqrt{N}}\chi + \ln\big(\frac{\chi}{\sinh(\chi)}\big)\big). \tag{4.103}$$

Based on the expression (4.103) the total stored energy will be determined for the state-of-the-art models.

4.7 The BPA model

In this section, the BPA model will be reviewed, cf. Arruda and Boyce (1991) and Arruda and Boyce (1993a). In the BPA model, the chain network is modeled by the 8-chain model, i.e. the chain segments extend from the center point of the cubic cell along its diagonals. Since the stretch of all chain segments is identical, the total stored energy consists of the stored energies φ_c^p of n single chains according to

$$\varphi^p = n\varphi_c^p. \tag{4.104}$$

The stored energy of each chain φ_c^p was given by (4.103) where the plastic chain stretch λ^p is now replaced by a non-affine plastic network stretch λ_{ec}^p. In analogy to (4.33), the plastic network stretch can be defined in terms of the plastic deformation tensor $\boldsymbol{b}^p$ as

$$\lambda_{ec}^p = \sqrt{\bar{\boldsymbol{N}} \cdot \boldsymbol{b}^p \bar{\boldsymbol{N}}} = \sqrt{1/3 trace(\boldsymbol{b}^p)} \tag{4.105}$$

where $\bar{\boldsymbol{N}} := 1/\sqrt{3}\sum_\alpha \bar{\boldsymbol{N}}_\alpha$ and $\bar{\boldsymbol{N}}_\alpha$, $\alpha = 1,2,3$, are the principal directions of $\boldsymbol{b}^p$. Applying the chain rule in (4.54) yields

$$\bar{\boldsymbol{B}} := 2sym\big(\frac{\partial\varphi^p(\lambda_{ec}^p)}{\partial\lambda_{ec}^p}\frac{\partial\lambda_{ec}^p}{\partial\boldsymbol{b}^p}\boldsymbol{b}^p\big), \quad \frac{\partial\varphi^p(\lambda_{ec}^p)}{\partial\lambda_{ec}^p} = nkT\sqrt{N}\mathfrak{L}^{-1}\big(\frac{\lambda_{ec}^p}{\sqrt{N}}\big). \tag{4.106}$$

The inverse Langevin function present in (4.106) results in an asymptotically increasing backstress as the stretch in the chains reaches the limit λ_L, cf. (4.20). Differentiation of (4.105) and multiplication by $\boldsymbol{b}^p$ yield

$$2\frac{\partial\lambda_{ec}^p}{\partial\boldsymbol{b}^p}\boldsymbol{b}^p = \frac{1}{3\lambda_{ec}^p}\boldsymbol{b}^p. \tag{4.107}$$

Substitution of $(4.106)_2$ and (4.107) into $(4.106)_1$ yields

$$\bar{\boldsymbol{B}} = \frac{C^R}{3\lambda_{ec}^p}\sqrt{N}\mathfrak{L}^{-1}(\frac{\lambda_{ec}^p}{\sqrt{N}})\boldsymbol{b}^p \tag{4.108}$$

where $C_R := nkT$ is a material parameter, also termed the hardening modulus. In the BPA model, the flow rule is postulated in terms of the Cauchy stress $\boldsymbol{\sigma}$ according to

$$\bar{\boldsymbol{D}}^p := \frac{\dot{\gamma}^p}{\sqrt{2}}\boldsymbol{n}, \quad \boldsymbol{n} = \frac{\tilde{\boldsymbol{\sigma}}^{dev}}{\tau}, \quad \tilde{\boldsymbol{\sigma}}^{dev} := \boldsymbol{\sigma}^{dev} - \boldsymbol{\beta}^{dev}, \quad \tau := \sqrt{\frac{1}{2}\tilde{\boldsymbol{\sigma}}^{dev} : \tilde{\boldsymbol{\sigma}}^{dev}} \tag{4.109}$$

where $\dot{\gamma}^p$ is given by (4.75) involving the pressure-dependent athermal shear strength which evolves according to (4.77). The principal components of the deviatoric part of the back-stress in the intermediate configuration are given by

$$\bar{B}_\alpha^{dev} = \frac{C_R}{3\lambda_{ec}^p}\sqrt{N}\mathfrak{L}^{-1}(\frac{\lambda_{ec}^p}{\sqrt{N}})\big((\bar{\lambda}_\alpha^p)^2 - (\lambda_{ec}^p)^2\big). \tag{4.110}$$

In the BPA model, the elastic response is considered as isotropic and the elastic rotation is assumed to be unity, which result in the components of the Mandel stress (4.64) being equal with the components of the Kirchhoff stress $\boldsymbol{\tau}$ via the relation (4.63). The elastic constitutive law in the BPA model is given by

$$\boldsymbol{\tau} = 2sym(\frac{\partial\varphi^e}{\partial\boldsymbol{b}^e}\boldsymbol{b}^e). \tag{4.111}$$

Since $I_1^e(\bar{\boldsymbol{U}}^e) = I_1^e(\boldsymbol{v}^e)$ and $I_2^e(\bar{\boldsymbol{U}}^e) = I_2^e(\boldsymbol{v}^e)$, the Kirchhoff stress becomes

$$\boldsymbol{\tau} = 2\mu(\ln\boldsymbol{v}^e)^{dev} + \kappa\ln J^e\boldsymbol{i} \tag{4.112}$$

where $\boldsymbol{i}$ is the spatial identity tensor. In the original BPA model, however, the Cauchy stress $\boldsymbol{\sigma} = 1/J\boldsymbol{\tau}$ is used. Based on (4.112), the elastic constitutive law can be formulated as

$$\boldsymbol{\sigma} = \frac{1}{J}\boldsymbol{\mathcal{L}}^e : \ln\boldsymbol{v}^e \tag{4.113}$$

where $\boldsymbol{\mathcal{L}}^e := 2\mu(\boldsymbol{\mathcal{I}} + (3\kappa - 2\mu)/(6\mu)\boldsymbol{i}\otimes\boldsymbol{i})$ is the fourth order stiffness tensor and $\boldsymbol{\mathcal{I}}$ is the fourth order identity tensor. The components of $\boldsymbol{\mathcal{L}}^e$ in an orthonormal cartesian coordinate system are given by

$$\mathcal{L}^e{}_{ijkl} := 2\mu\left[\frac{1}{2}\left(\delta_{ik}\delta_{jl} + \delta_{il}\delta_{jk}\right) + \frac{3\kappa - 2\mu}{6\mu}\delta_{ij}\delta_{kl}\right]. \tag{4.114}$$

In the flow rule (4.109), the rate of plastic deformation $\bar{\boldsymbol{D}}^p$ is assumed to align with the spatial normalized direction of $\tilde{\boldsymbol{\sigma}}^{dev}$. This assumption is based on the fact that the elastic stretches in many applications are small compared to the plastic stretches. Moreover, comparison of (4.64) and (4.112) reveals that the stress components in the intermediate

and spatial configurations are equal. It can be concluded that the plastic deformation which follows from the evolution law (4.109) is isochoric. Since, the volumetric deformation is suppressed in (4.109), the flow rule is generally inappropriate for modeling crazing. The BPA model is summarized in Table 4.1.

4.8 The Wu and Van der Giessen (1993) model

In the Wu and Van der Giessen (1993) model, the chain network is modeled by the full network model. According to the full network model, the chain segments extending from the center point of the unit sphere are continuously distributed on its surface. The end-to-end vector $\bar{\boldsymbol{r}}$ in the intermediate configuration is obtained from stretching and rotating of the initial end-to-end vector $\boldsymbol{r}_0$ in an affine manner, i.e. $\bar{\boldsymbol{r}} = \boldsymbol{F}^p \boldsymbol{r}_0$. Thus, the plastic network stretch $\bar{\lambda}^p$ in the direction of unit vector $\boldsymbol{m}^0 = \boldsymbol{r}_0/r_0$ is given by

$$\bar{\lambda}^p = \sqrt{\boldsymbol{m}^0 \cdot \boldsymbol{C}^p \boldsymbol{m}^0}. \tag{4.115}$$

The stored energy is represented in terms of the plastic network stretch $\bar{\lambda}^p$ in the reference configuration, and it is derived by an integration over the unit sphere

$$\varphi^p = \int_Q \varphi_c^p dQ, \quad \varphi_c^p = \bar{\varphi}_c^p(\bar{\lambda}^p) \tag{4.116}$$

where φ_c^p was given by (4.103). Analogously with (4.41), the number of chains on an infinitesimal area of a unit sphere dQ is defined as

$$dQ = n p_0(\theta_0, \varphi_0; \lambda_\alpha^p) dA = n \frac{dA}{4\pi}, \quad dA := \sin(\theta_0) d\theta_0 d\varphi_0. \tag{4.117}$$

Substitution of (4.117) into (4.116) results in the plastic part of the free energy being

$$\varphi^p = \frac{n}{4\pi} \int_A \varphi_c^p dA. \tag{4.118}$$

The backstress in the reference configuration is given by

$$\boldsymbol{B} := 2sym(\frac{\partial \varphi^p}{\partial \boldsymbol{C}^p} \boldsymbol{C}^p) = 2sym(\frac{\partial \varphi^p(\bar{\lambda}^p)}{\partial \bar{\lambda}^p} \frac{\partial \bar{\lambda}^p}{\partial \boldsymbol{C}^p} \boldsymbol{C}^p) \tag{4.119}$$

where

$$\frac{\partial \varphi^p(\bar{\lambda}^p)}{\partial \bar{\lambda}^p} = \frac{n}{4\pi} \int_A \frac{\partial \varphi_c^p}{\partial \bar{\lambda}^p} dA = \frac{nkT}{4\pi} \sqrt{N} \int_A \mathfrak{L}^{-1}(\frac{\bar{\lambda}^p}{\sqrt{N}}) dA. \tag{4.120}$$

Making use of (4.115), the second term in (4.119) takes the following form

$$\frac{\partial \bar{\lambda}^p}{\partial \boldsymbol{C}^p} = (2\bar{\lambda}^p)^{-1} \boldsymbol{m}^0 \otimes \boldsymbol{m}^0. \tag{4.121}$$

Substitution of (4.120) and (4.121) into (4.119) leads us to the form

$$\boldsymbol{B} = \frac{C_R\sqrt{N}}{4\pi}\int_A \mathfrak{L}^{-1}(\frac{\bar{\lambda}^p}{\sqrt{N}})(\bar{\lambda}^p)^{-1} sym(\boldsymbol{m}^0 \otimes \boldsymbol{m}^0) dA \cdot \boldsymbol{C}^p. \tag{4.122}$$

Let $\boldsymbol{N}_\alpha$, $\alpha = 1,2,3$ be the principal directions of $\boldsymbol{C}^p$. The direction of the chains can then be expressed as $\boldsymbol{m}^0 = \sum_\alpha m^0_\alpha \boldsymbol{N}_\alpha$. The components of $\boldsymbol{m}^0$ are given by $m^0_1 = \sin\theta_0 \cos\varphi_0$, $m^0_2 = \sin\theta_0 \sin\varphi_0$ and $m^0_3 = \cos\theta_0$. Multiplication of (4.122) from both sides by $\boldsymbol{N}_\alpha$ results in the principal components of the backstress being

$$B_\alpha = \frac{C_R\sqrt{N}}{4\pi}\int_A \mathfrak{L}^{-1}(\frac{\bar{\lambda}^p}{\sqrt{N}})(\bar{\lambda}^p)^{-1}(\lambda^p_\alpha)^2 (m^0_\alpha)^2 dA. \tag{4.123}$$

Similar to the BPA model, the backstress can be identified in the intermediate configuration. The unit vector in the direction of $\bar{\boldsymbol{r}}$ is $\bar{\boldsymbol{m}} = \sum_\alpha \bar{m}_\alpha \bar{\boldsymbol{N}}_\alpha$. For further reference, it is noted that the principal plastic stretches $\bar{\lambda}^p_\alpha$ and λ^p_α of $\boldsymbol{b}^p$ and $\boldsymbol{C}^p$ are equal. Employing the relationship $\boldsymbol{F}^p \boldsymbol{N}_\alpha = \bar{\lambda}^p_\alpha \bar{\boldsymbol{N}}_\alpha$ one obtains

$$\bar{\boldsymbol{r}} = \bar{r}\bar{\boldsymbol{m}} = \bar{r}\bar{m}_\alpha \bar{\boldsymbol{N}}_\alpha = \boldsymbol{F}^p \boldsymbol{r}_0 = r_0 \boldsymbol{F}^p \boldsymbol{m}^0 = r_0 m^0_\alpha \lambda^p_\alpha \bar{\boldsymbol{N}}_\alpha,$$

from which together with $\bar{r} = \bar{\lambda}^p r_0$ it follows that

$$\boldsymbol{m}^0 = \bar{\lambda}^p \bar{\boldsymbol{m}} \boldsymbol{F}^{p-T} \text{ and } m^0_\alpha = \bar{m}_\alpha \frac{\bar{\lambda}^p}{\bar{\lambda}^p_\alpha}. \tag{4.124}$$

Using (4.40) in (4.41), the number of chains crossing an infinitesimal area element $d\bar{A}$ on the unit sphere is given by

$$d\bar{Q} = n p_0 (\bar{\lambda}^p)^3 d\bar{A} = \frac{n}{4\pi}(\bar{\lambda}^p)^3 d\bar{A}, \quad d\bar{A} = \sin\bar{\theta} d\bar{\theta} d\bar{\varphi}. \tag{4.125}$$

Hence, the plastic part of the free energy in the intermediate configuration takes the form

$$\bar{\varphi}^p = \frac{n}{4\pi}\int_{\bar{A}} (\bar{\lambda}^p)^3 \varphi^p_c d\bar{A} \tag{4.126}$$

and thus

$$\frac{\partial \bar{\varphi}^p}{\partial \bar{\lambda}^p} = \frac{nkT}{4\pi}\sqrt{N}\int_{\bar{A}} \mathfrak{L}^{-1}(\frac{\bar{\lambda}^p}{\sqrt{N}})(\bar{\lambda}^p)^3 d\bar{A}. \tag{4.127}$$

The backstress $\bar{\boldsymbol{B}}$ in the intermediate configuration is derived as the push-forward of (4.122) by $\boldsymbol{F}^p$ and using the transformation (4.124) which together with (4.127) yield

$$\bar{\boldsymbol{B}} = \frac{C_R\sqrt{N}}{4\pi}\int_{\bar{A}} \mathfrak{L}^{-1}(\frac{\bar{\lambda}^p}{\sqrt{N}})(\bar{\lambda}^p)^4 (\bar{\boldsymbol{m}} \otimes \bar{\boldsymbol{m}}) d\bar{A}. \tag{4.128}$$

Similar to the BPA model, the plastic stretching is constitutively described by (4.109). The deviatoric part of the backstress $\boldsymbol{\beta}^{dev}$ present in (4.109) is derived by the push-forward of (4.128) to the spatial configuration by $\boldsymbol{F}^e$. The principal deviatoric components of (4.128) are

$$\bar{B}_\alpha^{dev} = \frac{C_R\sqrt{N}}{4\pi}\int_A \mathfrak{L}^{-1}(\frac{\bar{\lambda}^p}{\sqrt{N}})(\bar{\lambda}^p)^4(\bar{m}_\alpha^2 - \frac{1}{3})d\bar{A}. \tag{4.129}$$

In the 8-chain model, the non-affine network stretch λ_{ec}^p does not depend on the angles θ_0, φ_0. Moreover, the unit direction vectors $\boldsymbol{m}^0$ in (4.122) are replaced by $\boldsymbol{N} = 1/\sqrt{3}\sum_\alpha \boldsymbol{N}_\alpha$, $\alpha = 1,2,3$. Hence, the representation (4.122) becomes

$$\boldsymbol{B} = \frac{C_R\sqrt{N}}{4\pi}\mathfrak{L}^{-1}(\frac{\lambda_{ec}^p}{\sqrt{N}})(\lambda_{ec}^p)^{-1}\int_A \boldsymbol{N}\otimes\boldsymbol{N}dA\cdot\boldsymbol{C}^p = \frac{C_R}{3\lambda_{ec}^p}\sqrt{N}\mathfrak{L}^{-1}(\frac{\lambda_{ec}^p}{\sqrt{N}})\boldsymbol{C}^p. \tag{4.130}$$

A comparison of (4.108) and (4.130) reveals that the components of the backstresses are equal, i.e. in the component level, the Wu and Van der Giessen (1993) model is reduced to the BPA model as a special case.

Based on the simulations of rubber-like materials, Wu and Van der Giessen (1993) concluded that the stress response by the Wu and Van der Giessen (1993) model lies between those of the 3-chain Boyce *et al.* (1988) model and the 8-chain Arruda and Boyce (1993a) model. As with the approximation of stresses for rubber-like materials, this observation motivated an approximation of the backstress by

$$\bar{B}_\alpha = (1-\rho)\bar{B}_\alpha^{tc} + \rho\bar{B}_\alpha^{ec}, \quad \alpha = 1,2,3,$$

where $\rho \in [0,1]$ is the fitting parameter, and $\bar{B}_\alpha^{tc}$ and $\bar{B}_\alpha^{ec}$ are the principal backstresses according to the 3- and the 8-chain model, respectively, cf. Wu and Van der Giessen (1993). The kinematics and the constitutive equations of the Wu and Van der Giessen (1993) model are summarized in Table 4.2.

4.9 The Miehe *et al.* (2009) model

The stored energy in the Miehe *et al.* (2009) model is given by the sum of the stored energies of the single chains φ_c^p, i.e. $\varphi^p = n\varphi_c^p$. The plastic micro-stretches λ^p of the chains are allowed to fluctuate around the plastic macro-stretches $\bar{\lambda}^p$ in the format (4.24). The fluctuation field f for the plastic stretch is derived from the minimization principle for the average free energy, which results in the micro-stretch being relaxed by (4.31). Using the p-root averaging operator (4.28), the non-affine plastic network stretch is

$$\langle\bar{\lambda}^p\rangle_m = \big(\frac{1}{A}\int_A(\bar{\lambda}^p)^m dA\big)^{\frac{1}{m}}, \quad m > 0, \tag{4.131}$$

and the total stored energy is given by $\varphi^p(\langle\bar{\lambda}^p\rangle_m)$. In the Miehe *et al.* (2009) model, the plastic network stretch is given in terms of the reference plastic metric $\boldsymbol{G}^p$ which allows

the logarithmic plastic strain to be defined as

$$\boldsymbol{\epsilon}^p := \frac{1}{2}\ln \boldsymbol{G}^p. \tag{4.132}$$

Using the total logarithmic strain $\boldsymbol{\epsilon} = \ln \boldsymbol{U}$, Miehe *et al.* (2009) defined the elastic strain $\boldsymbol{\epsilon}^e$ as

$$\boldsymbol{\epsilon}^e := \boldsymbol{\epsilon} - \boldsymbol{\epsilon}^p. \tag{4.133}$$

It should be noted that the elastic strain is conceptually defined and is not the result of kinematical considerations. The backstress is derived by the differentiation of the plastic potential $\varphi^p(\langle\bar{\lambda}^p(\boldsymbol{G}^p)\rangle_m)$ with respect to the plastic metric $\boldsymbol{G}^p$ applying the chain rule, i.e.

$$\boldsymbol{\beta} := \frac{\partial\varphi^p(\langle\bar{\lambda}^p\rangle_m)}{\partial\langle\bar{\lambda}^p\rangle_m}\frac{\partial\langle\bar{\lambda}^p\rangle_m}{\partial\boldsymbol{\epsilon}^p} = \frac{\partial\varphi^p(\langle\bar{\lambda}^p\rangle_m)}{\partial\langle\bar{\lambda}^p\rangle_m}\frac{\partial\langle\bar{\lambda}^p\rangle_m}{\partial\boldsymbol{G}^p} : \frac{\partial\boldsymbol{G}^p}{\partial\boldsymbol{\epsilon}^p} \tag{4.134}$$

where

$$\frac{\partial\varphi^p(\langle\bar{\lambda}^p\rangle_m)}{\partial\langle\bar{\lambda}^p\rangle_m} = kT\sqrt{N}\mathfrak{L}^{-1}(\frac{\langle\bar{\lambda}^p\rangle_m}{\sqrt{N}}). \tag{4.135}$$

In the Miehe *et al.* (2009) model, the plastic macro-stretch $\bar{\lambda}^p$ is given in terms of the plastic metric as

$$\bar{\lambda}^p = \sqrt{\boldsymbol{m}^0\cdot\boldsymbol{G}^p\boldsymbol{m}^0} \tag{4.136}$$

where $\boldsymbol{m}^0 = \boldsymbol{r}_0/r_0$. Making use of (4.136) and (4.131), one obtains

$$\frac{\partial\langle\bar{\lambda}^p\rangle_m}{\partial\boldsymbol{G}^p} = \frac{\langle\bar{\lambda}^p\rangle_m^{1-m}}{2}\langle(\bar{\lambda}^p)^{m-2}\boldsymbol{m}^0\otimes\boldsymbol{m}^0\rangle, \quad \langle(\bullet)\rangle = (\frac{1}{4\pi}\int_A(\bullet)^m dA)^{\frac{1}{m}}. \tag{4.137}$$

Substituting (4.135) and (4.137) into (4.134) yields

$$\boldsymbol{\beta} = C_R\sqrt{N}\langle\bar{\lambda}^p\rangle_m^{1-m}\mathfrak{L}^{-1}(\frac{\langle\bar{\lambda}^p\rangle_m}{\sqrt{N}})sym\left(\langle(\bar{\lambda}^p)^{m-2}\boldsymbol{m}^0\otimes\boldsymbol{m}^0\rangle : \frac{\partial\boldsymbol{G}^p}{\partial\boldsymbol{\epsilon}^p}\right). \tag{4.138}$$

In the Miehe *et al.* (2009) model, the flow rule is postulated according to

$$\dot{\boldsymbol{\epsilon}}^p := \frac{\dot{\gamma}^p}{\sqrt{2}}\boldsymbol{n}, \quad \boldsymbol{n} = \frac{\tilde{\boldsymbol{\tau}}^{dev}}{\tau}, \quad \tilde{\boldsymbol{\tau}}^{dev} := \boldsymbol{\tau}^{dev} - \boldsymbol{\beta}^{dev}, \quad \tau := \sqrt{\frac{1}{2}\tilde{\boldsymbol{\tau}}^{dev} : \tilde{\boldsymbol{\tau}}^{dev}} \tag{4.139}$$

where the stress $\boldsymbol{\tau}$ is defined in terms of the elastic logarithmic strain $\boldsymbol{\epsilon}^e$ as

$$\boldsymbol{\tau} := 2\mu(\boldsymbol{\epsilon}^e)^{dev} + \kappa\, trace(\boldsymbol{\epsilon}^e)\boldsymbol{I}.$$

As in previously presented models, the isotropic hardening is defined via the evolution law (4.77) and $\dot{\gamma}^p$ is given by (4.75). Employing the Gauss theorem, one can show that isotropy and the stress-free state are satisfied through the constraints $\langle\boldsymbol{m}^0\rangle = \boldsymbol{0}$ and $\langle\boldsymbol{m}^0\otimes\boldsymbol{m}^0\rangle = 1/3\boldsymbol{I}$. In the eight chain model, the plastic network stretch λ^p_{ec} does not

depend on the spherical coordinates θ_0 and φ_0 when the special choice of $m = 2$ results in (4.105) and (4.131) being equal, i.e. $\langle \bar{\lambda}^p \rangle_m = \lambda^p_{ec}$. As a result, the representation (4.138) becomes

$$\boldsymbol{\beta} = \frac{C_R}{3\lambda^p_{ec}} \sqrt{N} \mathfrak{L}^{-1}\left(\frac{\lambda^p_{ec}}{\sqrt{N}}\right) sym\left(\boldsymbol{I} : \frac{\partial \boldsymbol{G}^p}{\partial \boldsymbol{\epsilon}^p}\right). \tag{4.140}$$

A comparison of the representations (4.140) and (4.108) reveals that the backstresses in the BPA model and in the Miehe *et al.* (2009) model differ. It appears from (4.106) and (4.134) that their component representations are equal only if $\partial \varphi^p / \partial \boldsymbol{\epsilon}^p = 2sym(\partial \varphi^p / \partial \boldsymbol{G}^p \cdot \boldsymbol{G}^p)$. The Miehe *et al.* (2009) model is summarized in Table 4.3.

4.10 The Anand and Ames (2006) model

Anand and Ames (2006) proposed a viscoelastic-viscoplastic constitutive model which was originally developed for predicting micro-indentation. In contrast to classical linear viscoelasticity, which is described by one Kevin-Voigt element, the Anand and Ames (2006) model consists rheologically of several Kelvin-Voigt elements arranged in series, cf. Fig. 4.11, element b).

One consequence of this relatively complex model is that the number of material parameters used in the model is large. Simulations, however, indicate that such complexity is required to satisfactorily predict the experimentally observed load-indentation (P-h) curves. The Kelvin-Voigt-like elements represent inelastic micromechanisms involving the evolution of isotropic and anisotropic hardening. Viscoelastic effects are taken into account through the micromechanisms $i = 1, ..., N$ and the nonlinear Langevin spring, cf. Fig. 4.11, element c). The strain softening in each micromechanism $i = 0, ..., N$ is modeled by taking the athermal shear stress s_i to evolve to a saturation value $s_{ss,i}$. Moreover, the plastic deformation in each micromechanism is given by $\bar{\boldsymbol{D}}^p_i$ and the scalar variable φ which represents the local free volume. The chain network is described by the 8-chain model which has already been touched upon in Sec. 4.3.1. In accordance with the BPA model, the kinematics is based on the multiplicative decomposition of the deformation gradient into an elastic and a plastic part, cf. Sec. 4.1, and the macroscopic stress is given in terms of a homogenized network stretch $\hat{\lambda}_{ec}$. As with the models above, Anand and Ames (2006) model has been formulated for isothermal conditions below the glass transition temperature. For thermodynamical considerations of the model, we refer to Anand and Gurtin (2003), Anand and Ames (2006) and Srivastava *et al.* (2010).

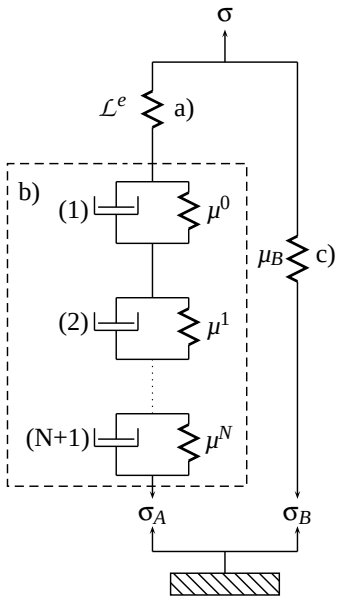

Figure 4.11: Schematic representation of the Anand and Ames (2006) model. The model is governed by the elements: a) elastic spring, b) Kelvin-Voigt elements, $i = 0, ..., N$, and c) nonlinear Langevin spring.

Let us first consider the stress $\boldsymbol{\sigma}_A$ in the leg A. According to (4.63), the Mandel stress in the case of isotropic elasticity can be considered as the elastically rotated Kirchhoff stress $\boldsymbol{\sigma}_A = 1/J^e \boldsymbol{\tau}_A = 1/J^e \boldsymbol{R}^e \bar{\boldsymbol{\Sigma}}_A \boldsymbol{R}^{e,T}$. The Mandel stress $\bar{\boldsymbol{\Sigma}}_A$ is defined analogously with (4.64) in the intermediate configuration, i.e.

$$\bar{\boldsymbol{\Sigma}}_A = 2\mu(\ln \bar{\boldsymbol{U}}^e)^{dev} + \kappa \ln J^e \bar{\boldsymbol{I}}. \tag{4.141}$$

The stress $\boldsymbol{\sigma}_B$ in the leg B is obtained analogously with (4.108), i.e.

$$\begin{aligned} \boldsymbol{\sigma}_B &= \frac{1}{J^e}\mu_B \hat{\boldsymbol{b}}^{dev} := \frac{1}{J^e}\frac{\mu^R}{3\hat{\lambda}_{ec}}\sqrt{N}\mathfrak{L}^{-1}(\frac{\hat{\lambda}_{ec}}{\sqrt{N}})\hat{\boldsymbol{b}}^{dev}, \\ \hat{\lambda}_{ec} &= \frac{1}{\sqrt{3}}\sqrt{trace(\hat{\boldsymbol{b}})} = \frac{1}{\sqrt{3}}\sqrt{\sum_\alpha (\hat{\lambda}_\alpha)^2}. \end{aligned} \tag{4.142}$$

In (4.142), μ_R is a constitutive parameter and $\hat{\boldsymbol{b}} := J^{e-2/3}\boldsymbol{b}$ is the isochoric part of the Finger tensor $\boldsymbol{b}$. To suppress the volume change during the viscous flow, the stress $\boldsymbol{\sigma}_B$ is considered to be deviatoric and the deviatoric principal components are given by

$$\sigma^{dev}_{B,\alpha} = \frac{1}{J^e}\frac{\mu_R}{3\hat{\lambda}_{ec}}\sqrt{N}\mathfrak{L}^{-1}(\frac{\hat{\lambda}_{ec}}{\sqrt{N}})\big((\hat{\lambda}_\alpha)^2 - (\hat{\lambda}_{ec})^2\big). \tag{4.143}$$

The total stress is the sum of the two components $\boldsymbol{\sigma} = \boldsymbol{\sigma}_A + \boldsymbol{\sigma}^{dev}_B$. In contrast to the BPA model where the plastic spin is nonzero as a result of the imposed symmetry of $\boldsymbol{F}^e$, Anand and Ames (2006) assumed that the plastic spin vanishes. As a result, the evolution equation for the plastic deformation takes the form $\bar{\boldsymbol{D}}^p = \dot{\boldsymbol{F}}^p \boldsymbol{F}^{p-1}$. The rate of plastic deformation $\bar{\boldsymbol{D}}^p$ is constitutively described by the sum of the plastic stretching in each $N+1$ micromechanism

$$\bar{\boldsymbol{D}}^p = \sum_{i=0}^{N} \bar{\boldsymbol{D}}^p_i = \sum_{i=0}^{N} \dot{\gamma}^p_i \bar{\boldsymbol{N}}_i \tag{4.144}$$

where $\dot{\gamma}^p_i \geq 0$, $i = 0, ..., N$, are defined below. The direction of the plastic flow is given by

$$\bar{\boldsymbol{N}}_i := \frac{\tilde{\boldsymbol{S}}^{dev}_i}{2\tau_i}, \quad \tilde{\boldsymbol{S}}^{dev}_i := \bar{\boldsymbol{\Sigma}}^{dev}_A - \bar{\boldsymbol{B}}^{dev}_i, \quad \tau_i := \sqrt{\frac{1}{2}\tilde{\boldsymbol{S}}^{dev}_i : \tilde{\boldsymbol{S}}^{dev}_i}. \tag{4.145}$$

It follows from (4.144) and (4.145) that the plastic deformation is volume conserving, i.e. $trace(\bar{\boldsymbol{D}}^p) = 0$ and $det(\boldsymbol{F}^p) = 1$. The backstresses $\bar{\boldsymbol{B}}_i$ in (4.145) are given by

$$\bar{\boldsymbol{B}}_i = \mu_i \bar{\boldsymbol{A}}_i \tag{4.146}$$

where the internal variables $\bar{\boldsymbol{A}}_i$ evolve according to

$$\dot{\bar{\boldsymbol{A}}}_i = \bar{\boldsymbol{D}}^p_i \bar{\boldsymbol{A}}_i + \bar{\boldsymbol{A}}_i \bar{\boldsymbol{D}}^p_i.$$

For a single mechanism, $\dot{\bar{\boldsymbol{A}}}_i = \dot{\bar{\boldsymbol{A}}} = \dot{\boldsymbol{b}}^p$, i.e. $\bar{\boldsymbol{A}} = \boldsymbol{b}^p := \boldsymbol{F}^p \boldsymbol{F}^{p,T}$. In (4.146), the backstress moduli μ_i, $i = 0, ..., N$, is chosen to evolve with the free volume $\varphi_i = \varphi$, i.e.

$$\dot{\mu}_i := c_i(1 - \frac{\mu_i}{\mu_{i,s}})\dot{\varphi}, \quad \mu_i(\varphi(0)) = \mu_{i,0} \tag{4.147}$$

where c_i, $\mu_{i,s}$ and $\mu_{i,0}$ are positive material constants defined for each micromechanism. The evolution equation for the free volume φ is defined below. Since in the model $\mu_{i,0} \geq \mu_{i,s}$, the backstress moduli μ_i decreases to its saturation value $\mu_{i,s}$ as the free volume increases.

In contrast to the other presented models, where the Argon (1973) model is used to describe the magnitude of the plastic flow, Anand and Ames (2006) made use of a simple power-law, i.e.

$$\dot{\gamma}_i^p := \dot{\gamma}_0^p (\frac{\tau_i}{s_i + \alpha p})^{\frac{1}{m_i}}, \ i = 0, ..., N \tag{4.148}$$

where $p = -1/3 trace(\boldsymbol{\sigma}_A)$ is the pressure and $\dot{\gamma}_0^p > 0$ is the reference shear strain rate being equal for each micromechanism. The strain rate sensitivity parameters $m_i > 0$ of the ith micromechanism result in the limit $m_i \to 0$ in the rate-independent plasticity. In (4.148), α is the pressure-dependence factor, assumed to coincide in all micromechanisms. The micromechanism represented by the Kelvin-voigt element with index $i = 0$ represents the dominant macro-yield response. For the athermal shear strength s_0 with initial value $s_{0,0}$ the evolution equation (4.77) is employed but its saturation value $s_{0,ss}$ is assumed to depend on the free volume φ as

$$s_{0,ss} := s_{cv}(1 + b(\varphi_{cv} - \varphi)) \tag{4.149}$$

where b, φ_{cv} and s_{cv} are constitutive parameters. The evolution equation for the free volume φ is coupled to athermal strength s_0 according to

$$\dot{\varphi} = g_0(\frac{s_0}{s_{cv}} - 1)\dot{\gamma}_0^p, \quad \varphi(0) = \varphi_0 \tag{4.150}$$

where g_0 is a material parameter and the initial free volume $\varphi_0 \leq \varphi_{cv}$. Since by (4.77) s_0 decreases, a glance at (4.150) reveals that the free volume φ increases until the saturation value s_{cv} of s_0 is reached, i.e. $\varphi = \varphi_{cv}$ in (4.149). The internal scalar variables s_i associated to the remaining micromechanisms are assumed to be constants, i.e. $s_i = s_i(0), i = 1, ..., N$. As a result, the material parameters $(12 + 5(N + 1)$ pcs.) that are needed in the proposed model for micro-indentation are

$$\mu, \kappa, \mu_R, N, \dot{\gamma}_0^p, \alpha, h, m_i, g_0, s_{cv}, b, s_{i,0}, \varphi_{cv}, \varphi_0, c_i, \mu_{i,0}, \mu_{i,s}, \quad i = 0, ..., N$$

where the first seven parameters also appear in the BPA model. The kinematics and the constitutive equations of the model are summarized in Table 4.4.

4.11 The Dupaix and Boyce (2007) model

During increasing temperature, the slip resistance begins to reduce which results in the solid polymer transforming from a solid towards a melt. During the transformation, the short-range motion of the chains decreases, and near the glass transition temperature the polymer chains start to move by local Brownian motion restricted by the neighboring chains. In accordance with Brownian motion, the velocity of a chain is infinite which represents an idealized approximation of the actual random physical motion having a finite time scale. This motion of chains in the melt state is called the long-range motion, or reptation, and is described by the reptation theory (snakelike motion), cf. Fried (2009). According to reptation theory, the motion of a single chain is confined within a tube which is defined by the neighboring entanglement sites, cf. Fig. 4.12. The decreasing temperature through glass transition may result in crystallization and the reptation ceases. Dupaix and Boyce (2007) proposed a model for amorphous glassy polymers which captures the finite strain behavior under a wide range of strain rates and temperatures. This model, however, does not take strain-induced crystallization during glass transition into account.

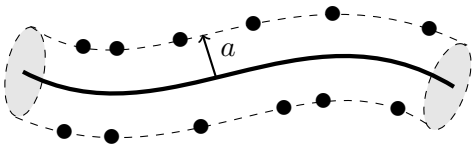

Figure 4.12: Illustration of a virtual tube of radius a and motion of a single chain (thick line) according to the reptation model. The black nodes represent the neighboring entanglement sites.

In the Dupaix and Boyce (2007) model, the mechanical behavior of glassy polymers is caused by two mechanisms: resistances due to (i) intermolecular interactions and (ii) stretching and reorientation of the molecular chain network. The rheological representation of the model is given in Fig. 4.13. Resistance (i) is intended to capture the interactions between neighboring chain segments between physical entanglements. It is the primary source of the initial stiffness, and also results in the plastic flow which is modeled by the viscoplastic dashpot, cf. Fig. 4.13, element b). Resistance (ii) affects stiffening in the large strain regime and it also captures molecular relaxation during glass transition, cf. Fig. 4.13, elements c) and d). The viscous dashpot in resistance (ii) also takes reptation at high temperatures into account, cf. Bergström and Boyce (1998). Since the two resistances work in parallel, the deformation gradients in both resistances must be equal to the total deformation gradient, i.e.

$$\boldsymbol{F} = \boldsymbol{F}_{(i)} = \boldsymbol{F}_{(ii)}. \tag{4.151}$$

Moreover, the total stress is the sum of the stresses in the two parallel resistances

$$\boldsymbol{\sigma} = \boldsymbol{\sigma}_{(i)} + \boldsymbol{\sigma}_{(ii)}. \tag{4.152}$$

Modeling of resistance (i)

Since the multiplicative decomposition for the two arms shown in Fig. 4.13 is employed, it then follows from (4.151) that

$$\boldsymbol{F}_{(i)} = \boldsymbol{F}^e_{(i)}\boldsymbol{F}^p_{(i)}. \tag{4.153}$$

The kinematics of resistance (i) is described by (4.9)-(4.12) and (4.14)-(4.15). The elastic constitutive law is given by

$$\boldsymbol{\sigma}_{(i)} = \frac{1}{J^e_{(i)}}\boldsymbol{\mathcal{L}}^e : \ln \boldsymbol{v}^e_{(i)} \tag{4.154}$$

where $\ln \boldsymbol{v}^e_{(i)}$ is the Hencky strain in resistance (i) and $J^e_{(i)} = det(\boldsymbol{F}^e_{(i)})$. The fourth order stiffness tensor is given by

$$\boldsymbol{\mathcal{L}}^e := 2\mu\boldsymbol{\mathcal{I}} + \frac{3\kappa - 2\mu}{3}\boldsymbol{i}\otimes\boldsymbol{i}$$

where the shear modulus μ is temperature-dependent. The evolution of the plastic deformation is governed by

$$\boldsymbol{d}^p_{(i)} = \dot{\gamma}^p \boldsymbol{n}_{(i)} \tag{4.155}$$

where $\dot{\gamma}^p$ is assumed to be thermally activated according to

$$\dot{\gamma}^p = \dot{\gamma}_0 \exp\big(-\frac{\Delta G}{kT}(1 - (\frac{\tau_{(i)}}{s}))\big). \tag{4.156}$$

The athermal shear strength s is considered as constant or it can be replaced by (4.76) which takes pressure into account. The direction of the plastic flow in resistance (i) $\boldsymbol{n}_{(i)}$ is assumed to be aligned with the deviatoric stress, i.e.

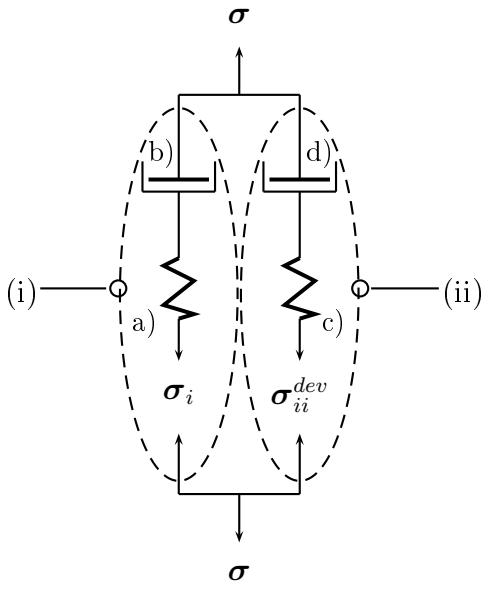

Figure 4.13: Rheological illustration of the Dupaix and Boyce (2007) model. The model consists of two resistances (i) and (ii). Resistance (i) is governed by a) an elastic spring and b) a viscoplastic dashpot, and resistance (ii) by c) a nonlinear spring and d) a viscous dashpot.

$$\boldsymbol{n}_{(i)} := \frac{\boldsymbol{\sigma}^{dev}_{(i)}}{\sqrt{2}\tau_{(i)}}, \quad \tau_{(i)} := \sqrt{\frac{1}{2}\boldsymbol{\sigma}^{dev}_{(i)} : \boldsymbol{\sigma}^{dev}_{(i)}}. \tag{4.157}$$

To make the plastic evolution law for resistance (i) complete, the plastic spin $\boldsymbol{\omega}^p_{(i)}$ is chosen to vanish.

Modeling of resistance (ii)

As with resistance (i), the deformation gradient in resistance (ii) is multiplicatively split, i.e.

$$\boldsymbol{F}_{(ii)} = \boldsymbol{F}^e_{(ii)}\boldsymbol{F}^p_{(ii)}. \tag{4.158}$$

The kinematics of resistance (ii) is given through (4.4), (4.9)-(4.12) and (4.14)-(4.15). According to the Dupaix and Boyce (2007) model, the backstress used in the BPA model is not able to reproduce the deformation behavior of PETG either at large strains or in a melt state. As a remedy, Dupaix and Boyce (2007) described the network stretch in terms of the principal elastic stretches $\hat{\lambda}^e_{(ii),\alpha}$, $\alpha = 1,2,3$ as

$$\hat{\lambda}^e_{(ii)} = \frac{1}{\sqrt{3}}\sqrt{trace(\hat{\boldsymbol{b}}^e_{(ii)})} = \frac{1}{\sqrt{3}}\sqrt{\sum_{\alpha}(\hat{\lambda}^e_{(ii),\alpha})^2}. \tag{4.159}$$

In (4.159), $\hat{\boldsymbol{b}}^e_{(ii)} = \hat{\boldsymbol{F}}^e_{(ii)}\hat{\boldsymbol{F}}^{e,T}_{(ii)}$, $\hat{\boldsymbol{F}}^e_{(ii)} = J^{e-1/3}_{(ii)}\boldsymbol{F}^e_{(ii)}$ and $J^e_{(ii)} := det(\boldsymbol{F}^e_{(ii)})$. The network stress in resistance (ii) is taken to be analogous with (4.110), i.e. in terms of elastic stretches $\hat{\lambda}^e_{(ii),\alpha}$, $\alpha = 1,2,3$, it is given by

$$\sigma^{dev}_{(ii),\alpha} = \frac{1}{J^e_{(ii)}}\frac{C_R}{3\hat{\lambda}^e_{(ii)}}\sqrt{N}\mathfrak{L}^{-1}(\frac{\hat{\lambda}^e_{(ii)}}{\sqrt{N}})\big((\hat{\lambda}^e_{(ii),\alpha})^2 - (\hat{\lambda}^e_{(ii)})^2\big). \tag{4.160}$$

The inverse Langevin function $\mathfrak{L}^{-1}$ results in the stress rising dramatically once $\hat{\lambda}^e_{(ii)}$ reaches the limiting stretch, $\sqrt{N}$.

The rate of the molecular relaxation in resistance (ii) is analogously described with the evolution of plastic deformation in resistance (i), i.e.

$$\boldsymbol{d}^p_{(ii)} = \dot{\gamma}^p_{(ii)}\boldsymbol{n}_{(ii)} \tag{4.161}$$

where

$$\boldsymbol{n}_{(ii)} := \frac{\boldsymbol{\sigma}^{dev}_{(ii)}}{\sqrt{2}\tau_{(ii)}}, \quad \tau_{(ii)} := \sqrt{\frac{1}{2}\boldsymbol{\sigma}^{dev}_{(ii)} : \boldsymbol{\sigma}^{dev}_{(ii)}}. \tag{4.162}$$

To comply with the plastic evolution laws, the plastic spin $\boldsymbol{\omega}^p_{(ii)}$ in resistance (ii) is assumed to vanish. The rate of molecular relaxation $\dot{\gamma}^p_{(ii)}$ is experimentally determined as a function of viscosity at different strain levels and temperatures, cf. Dupaix and Boyce (2007). Based on the experiments, Dupaix and Boyce (2007) determined the rate of the relaxation as a function of $\tau_{(ii)}$ as

$$\dot{\gamma}^p_{(ii)} = \tilde{C}\tau^{\frac{1}{n}}_{(ii)} \tag{4.163}$$

where n is a positive parameter and $\tilde{C}$ is a micromechanically based variable which includes the temperature dependence of the molecular relaxation and also takes the chain orientation during deformation into account. The chain motion is described by the chain reptation where the chains slide through tube-like paths created by the entangled chains around them, cf. Fig. 4.12. As has already been mentioned in preceding sections, the Argon (1973) double-kink theory cannot capture the deformation behavior through the glass transition temperature. Dupaix and Boyce (2007) conducted experiments on PETG which indicated that the alignment of the chains at the limiting stretch is independent of strain rate,

temperature as well as deformation state. Motivated by this observation, they introduced an orientation parameter ϕ_c which governs $\dot{\gamma}^p_{(ii)}$. The reorientation and the elongation of single chains in a representative volume element during deformation are expressed by the orientation angle, cf. Fig. 4.14. In the undeformed state, the angles between the principal

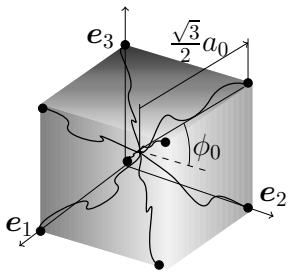

Figure 4.14: The idealized chain structure according to the 8-chain model. The dimension of the 8-chain cube is a_0 and ϕ_0 denotes the initial orientation angle between a chain and the principal axes. The unit vectors $\boldsymbol{e}_\alpha$, $\alpha = 1, 2, 3$, align with the principal directions of $\boldsymbol{b}^e$.

axis and a chain are equal, i.e. $\phi_i = \phi_0 = 54.7°$, $i = 1, 2, 3$ (0.955 rad). As deformation proceeds, the angles are no longer equal and the orientation parameter ϕ_c is defined as $\phi_c := \pi/2 - \phi_{max}$, where $\phi_{max} := max\{\phi_i, i = 1, 2, 3\}$. According to experiments, the limiting stretch of chains is reached at a common value, $\bar{\phi}_{max}$ being independent of strain rate and temperature. In accordance with Adams *et al.* (2000), Dupaix and Boyce (2007) proposed a model for molecular relaxation in terms of the orientation angle, i.e.

$$\dot{\gamma}^p_{(ii)} = \frac{(\frac{\phi}{\phi_c} - 1)}{(\frac{\phi_R}{\phi_c} - 1)}(C\phi\tau_{(ii)})^{1/n} \tag{4.164}$$

where $\phi_R := \pi/2 - \phi_0$ and ϕ is the current orientation angle. Based on single chain geometry, $\cos(\phi) = 1/\sqrt{3}\lambda_2/\bar{\lambda}$ where λ_2 is the second principal stretch of $\boldsymbol{C}$ and $\bar{\lambda}$ was given by (4.39). The parameter C includes the temperature dependence of the molecular relaxation according to $C = D\exp(-Q/(R\theta))$ where D and Q are material parameters and R is the gas constant, cf. Dupaix and Boyce (2007).

Temperature dependent material constants

Since the glass transition takes place gradually, the glass transition temperature is not well-defined. Dupaix and Boyce (2007) defined the glass transition as being initialized at the phase where a solid material starts rapidly soften to a rubbery-like state. The initial elastic response is primarily governed by the elastic spring in resistance (i) which is given in terms of the bulk modulus κ and the temperature-dependent shear modulus μ. Based on the dynamic mechanical analysis (DMA) experiments, Dupaix and Boyce (2007) proposed

the following approximation for the shear modulus:

$$\mu = \frac{1}{2}\big((\mu_g + \mu_r) - (\mu_g - \mu_r)\big) \cdot \tanh\big(\frac{\chi}{\Delta\theta}(\theta - \theta_g)\big) + X_g(\theta - \theta_g) \tag{4.165}$$

where μ_g and μ_r are the shear modulus in the glassy and rubbery regions, respectively, and $\Delta\theta$ represents the temperature interval in which polymer transforms from the glassy phase to the melt phase.

In (4.165), the coefficient $X_g < 0$ denotes the slope of the $\mu - \theta$ curve outside the glass transition, whereas χ is the average slope of the $\mu - \theta$ curve in glass transition. The parameter values are obtained using the fitting to the experimental $\mu - \theta$ response. In Fig. 4.15, the temperature dependence of the shear modulus is presented, this being typical for high-molecular-weight amorphous polymers, cf. Fried (2009). In the glass transition regime, the shear modulus depends strongly on the strain rate. The dependence of the strain rate $\dot{\epsilon}$ is taken into account by shifting the glass transition temperature as

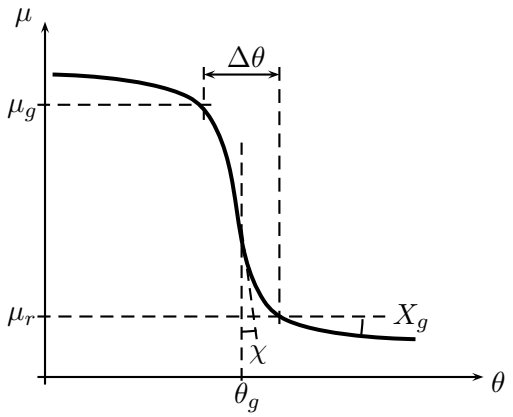

Figure 4.15: The temperature dependence of the shear modulus μ and an illustration of the slope-parameters, X_g and χ. The curve is based on the DMA-experiments on PETG for uniaxial compression, cf. Dupaix and Boyce (2007).

$$\theta_g = \xi \log_{10}\left(\frac{\sqrt{3}\dot{\epsilon}}{\dot{\gamma}_{ref}}\right) + \zeta + \theta_g^* \tag{4.166}$$

where $\dot{\gamma}_{ref}$, ξ and ζ are material constants and θ_g^* is the reference transition temperature. These parameters can be found by taking the shifting θ_g into account in the fitting to the experimental $\mu - \theta$ response. At slow strain rates, $\theta_g = \theta_g^*$, cf. Dupaix and Boyce (2007). For the sake of convenience, the constitutive model proposed by Dupaix and Boyce (2007) is summarized in Table 4.5.

4.12 Summary of state-of-the-art models

Table 4.1: Summary of the BPA model.

1.	Kinematics: $\boldsymbol{F} = \boldsymbol{F}^e\boldsymbol{F}^p$, $\boldsymbol{b}^p := \boldsymbol{F}^p\boldsymbol{F}^{p,T}$, $\boldsymbol{b}^e := \boldsymbol{F}^e\boldsymbol{F}^{e,T}$, $\boldsymbol{v}^e := \sqrt{\boldsymbol{b}^e}$, $\boldsymbol{R}^e$ is unity.
2.	Stress: $\boldsymbol{\sigma} := \frac{1}{J^e}(2\mu(\ln \boldsymbol{v}^e)^{dev} + \kappa \ln J^e \boldsymbol{i})$.
3.	Micro-macro transition: $\lambda^p_{ec} = \frac{1}{\sqrt{3}}\sqrt{trace(\boldsymbol{b}^p)}$.
4.	Flow rule: $\bar{\boldsymbol{D}}^p = \dot{\gamma}^p \boldsymbol{n}$, $\boldsymbol{n} := \frac{\tilde{\boldsymbol{\sigma}}^{dev}}{\sqrt{2}\tau}$, $\tilde{\boldsymbol{\sigma}}^{dev} := \boldsymbol{\sigma}^{dev} - \frac{1}{J^e}\boldsymbol{\beta}^{dev}$, $\tau := \sqrt{\frac{1}{2}\tilde{\boldsymbol{\sigma}}^{dev} : \tilde{\boldsymbol{\sigma}}^{dev}}$.
5.	Backstress: $\bar{\boldsymbol{B}}^{dev} = \frac{C^R}{3\lambda^p_{ec}}\sqrt{N}\mathfrak{L}^{-1}(\frac{\lambda^p_{ec}}{\sqrt{N}})(\boldsymbol{b}^p)^{dev}$ push-forward $\rightarrow$ $\boldsymbol{\beta}^{dev}$
6.	Isotropic hardening: $\dot{\gamma}^p := \dot{\gamma}_0 \exp\big(-\frac{As}{T}(1 - (\frac{\tau}{s_s})^{\frac{5}{6}})\big)$, $s_s = s + \alpha p$, $p = -\frac{1}{3}trace(\boldsymbol{\sigma})$, s is given by (4.77) and $s(0) = s_0$.

Table 4.2: Summary of the Wu and Van der Giessen (1993) model.

1.	Kinematics: $\boldsymbol{F} = \boldsymbol{F}^e\boldsymbol{F}^p$, $\boldsymbol{C}^p := \boldsymbol{F}^{p,T}\boldsymbol{F}^p$, $\boldsymbol{b}^e := \boldsymbol{F}^e\boldsymbol{F}^{e,T}$, $\boldsymbol{v}^e := \sqrt{\boldsymbol{b}^e}$, $\boldsymbol{R}^e$ is unity.
2.	Stress: $\boldsymbol{\sigma} := \frac{1}{J^e}(2\mu(\ln \boldsymbol{v}^e)^{dev} + \kappa \ln J^e \boldsymbol{i})$.
3.	Micro-macro transition: $\bar{\lambda}^p = \sqrt{\boldsymbol{m}^0 \cdot \boldsymbol{C}^p \boldsymbol{m}^0} \in (0, \sqrt{N})$ where $m^0_1 = \sin\theta_0 \cos\varphi_0$, $m^0_2 = \sin\theta_0 \sin\varphi_0$, $m^0_3 = \cos\theta_0$.
4.	Flow rule: $\bar{\boldsymbol{D}}^p = \dot{\gamma}^p \boldsymbol{n}$, $\boldsymbol{n} := \frac{\tilde{\boldsymbol{\sigma}}^{dev}}{\sqrt{2}\tau}$, $\tilde{\boldsymbol{\sigma}}^{dev} := \boldsymbol{\sigma}^{dev} - \frac{1}{J^e}\boldsymbol{\beta}^{dev}$, $\tau := \sqrt{\frac{1}{2}\tilde{\boldsymbol{\sigma}}^{dev} : \tilde{\boldsymbol{\sigma}}^{dev}}$.
5.	Backstress: $\bar{\boldsymbol{B}}^{dev} = \frac{C_R\sqrt{N}}{4\pi}(\int_{\bar{A}} \mathfrak{L}^{-1}(\frac{\bar{\lambda}^p}{\sqrt{N}})(\bar{\lambda}^p)^4(\bar{\boldsymbol{m}} \otimes \bar{\boldsymbol{m}})^{dev} d\bar{A})$ where $\bar{\boldsymbol{m}} = \bar{\lambda}^{p-1}\boldsymbol{F}^p\boldsymbol{m}^0$ push-forward $\rightarrow$ $\boldsymbol{\beta}^{dev}$.
6.	Isotropic hardening: $\dot{\gamma}^p := \dot{\gamma}_0 \exp\big(-\frac{As}{T}(1 - (\frac{\tau}{s_s})^{\frac{5}{6}})\big)$, $s_s = s + \alpha p$, $p = -\frac{1}{3}trace(\boldsymbol{\sigma})$, s is given by (4.77) and $s(0) = s_0$.

Table 4.3: Summary of the Miehe *et al.* (2009) model.

1. Kinematics: $\boldsymbol{\epsilon}^e := \boldsymbol{\epsilon} - \boldsymbol{\epsilon}^p, \quad \boldsymbol{G}^p := \exp(2\boldsymbol{\epsilon}^p).$
2. Stress: $\boldsymbol{\tau} := 2\mu(\boldsymbol{\epsilon}^e)^{dev} + \kappa\, trace(\boldsymbol{\epsilon}^e)\boldsymbol{I}.$
3. Micro-macro transition: $\langle\bar{\lambda}^p\rangle_m = \big(\frac{1}{A}\int_A (\bar{\lambda}^p)^m dA\big)^{\frac{1}{m}}, \quad m > 0,$ where
   $\bar{\lambda}^p = \sqrt{\boldsymbol{m}^0 \cdot \boldsymbol{G}^p \boldsymbol{m}^0} \in (0, \sqrt{N}), \;\; m_1^0 = \sin\theta_0 \cos\varphi_0, \;\; m_2^0 = \sin\theta_0 \sin\varphi_0, \;\; m_3^0 = \cos\theta_0.$
4. Flow rule: $\dot{\boldsymbol{\epsilon}}^p = \dot{\gamma}^p \boldsymbol{n}, \quad \boldsymbol{n} := \dfrac{\tilde{\boldsymbol{\tau}}^{dev}}{\sqrt{2}\tau}, \quad \tilde{\boldsymbol{\tau}}^{dev} := \boldsymbol{\tau}^{dev} - \boldsymbol{\beta}^{dev}, \quad \tau := \sqrt{\frac{1}{2}\tilde{\boldsymbol{\tau}}^{dev} : \tilde{\boldsymbol{\tau}}^{dev}}.$
5. Backstress: $\boldsymbol{\beta}^{dev} = C_R\sqrt{N}\langle\bar{\lambda}^p\rangle_m^{1-m}\mathfrak{L}^{-1}(\frac{\langle\bar{\lambda}^p\rangle_m}{\sqrt{N}})\, sym\left(\langle(\bar{\lambda}^p)^{m-2}\boldsymbol{m}^0 \otimes \boldsymbol{m}^0\rangle : \dfrac{\partial \boldsymbol{G}^p}{\partial \boldsymbol{\epsilon}^p}\right)^{dev}.$
6. Isotropic hardening: $\dot{\gamma}^p := \dot{\gamma}_0 \exp\big(-\frac{As}{T}(1 - (\frac{\tau}{s_s})^{\frac{5}{6}})\big), \quad s_s = s + \alpha p,$
   $p = -\frac{1}{3} trace(\frac{1}{J^e}\boldsymbol{\tau}),$ s by (4.77) and $s(0) = s_0.$

Table 4.4: Summary of the Anand and Ames (2006) model.

1. Kinematics: $\boldsymbol{F} = \boldsymbol{F}^e\boldsymbol{F}^p, \;\; \hat{\boldsymbol{b}} = J^{-2/3}\boldsymbol{b}, \;\; \bar{\boldsymbol{C}}^e := \boldsymbol{F}^{e,T}\boldsymbol{F}^e, \quad \bar{\boldsymbol{U}}^e = \sqrt{\bar{\boldsymbol{C}}^e}, \;\; \boldsymbol{R}^e = \boldsymbol{F}^e\bar{\boldsymbol{U}}^{e-1}.$
2. Stresses: $\bar{\boldsymbol{\Sigma}}_A = 2\mu(\ln\bar{\boldsymbol{U}}^e)^{dev} + \kappa \ln J^e \bar{\boldsymbol{I}}, \quad \boldsymbol{\sigma}_A = \dfrac{1}{J^e}\boldsymbol{R}^e\bar{\boldsymbol{\Sigma}}_A\boldsymbol{R}^{e,T},$
   $\boldsymbol{\sigma}_B^{dev} = \dfrac{1}{J^e}\dfrac{\mu_R}{3\hat{\lambda}_{ec}}\sqrt{N}\mathfrak{L}^{-1}(\dfrac{\hat{\lambda}_{ec}}{\sqrt{N}})\hat{\boldsymbol{b}}^{dev}$ and $\boldsymbol{\sigma} = \boldsymbol{\sigma}_A + \boldsymbol{\sigma}_B^{dev}.$
2. Micro-macro transition: $\hat{\lambda}_{ec} = \dfrac{1}{\sqrt{3}}\sqrt{trace(\hat{\boldsymbol{b}})}.$

Micromechanisms: $i = 0, ..., N$:

3. Flow rule: $\bar{\boldsymbol{D}}^p = \sum_{i=0}^{N} \dot{\gamma}_i^p \bar{\boldsymbol{N}}_i, \quad \bar{\boldsymbol{W}}^p = \boldsymbol{0}, \quad \bar{\boldsymbol{N}}_i := \dfrac{\tilde{\boldsymbol{S}}_i^{dev}}{2\tau_i}, \quad \tilde{\boldsymbol{S}}_i^{dev} := \bar{\boldsymbol{\Sigma}}_A^{dev} - \bar{\boldsymbol{B}}_i^{dev}$ and
   $\tau_i := \sqrt{\frac{1}{2}\tilde{\boldsymbol{S}}_i^{dev} : \tilde{\boldsymbol{S}}_i^{dev}}.$
4. Internal kinematical variables: $\dot{\bar{\boldsymbol{A}}}_i = \bar{\boldsymbol{D}}_i^p\bar{\boldsymbol{A}}_i + \bar{\boldsymbol{A}}_i\bar{\boldsymbol{D}}_i^p.$
5. Backstresses: $\bar{\boldsymbol{B}}_i = \mu_i\bar{\boldsymbol{A}}_i, \quad \dot{\mu}_i := c_i(1 - \dfrac{\mu_i}{\mu_{i,s}})\dot{\varphi}, \quad \mu_i(\varphi(0)) = \mu_{i,0} > \mu_{i,s}.$
6. Isotropic hardening: $\dot{\gamma}_i^p := \dot{\gamma}_0^p(\dfrac{\tau_i}{s_i + \alpha p})^{\frac{1}{m^i}}, \;\; p = -\dfrac{1}{3} trace(\boldsymbol{\sigma}_A), \;\; s_i(0) = s_{i,0}, \;\; s_0$ by (4.77)
   in which $s_{0,ss} := s_{cv}(1 + b(\varphi_{cv} - \varphi))$ and $\dot{\varphi} = g_0(\dfrac{s_0}{s_{cv}} - 1)\dot{\gamma}_0^p, \;\; \varphi(0) = \varphi_0 < \varphi_{cv}.$

Table 4.5: Summary of the Dupaix and Boyce (2007) model.

1. Kinematics: $\boldsymbol{F} = \boldsymbol{F}_{(i)} = \boldsymbol{F}_{(ii)},\ \boldsymbol{F}_{(i)} = \boldsymbol{F}^e_{(i)}\boldsymbol{F}^p_{(i)},\ \boldsymbol{F}_{(ii)} = \boldsymbol{F}^e_{(ii)}\boldsymbol{F}^p_{(ii)},\ \boldsymbol{b}^e_{(i)} := \boldsymbol{F}^e_{(i)}\boldsymbol{F}^{e,T}_{(i)},$
$$\boldsymbol{v}^e_{(i)} = \sqrt{\boldsymbol{b}^e_{(i)}}, \quad \boldsymbol{b}^e_{(ii)} := \boldsymbol{F}^e_{(ii)}\boldsymbol{F}^{e,T}_{(ii)}, \quad \hat{\boldsymbol{b}}^e_{(ii)} = J^{-2/3}\boldsymbol{b}^e_{(ii)}.$$
2. Stresses: $\boldsymbol{\sigma}_{(i)} = \dfrac{1}{J^e_{(i)}}(2\mu(\ln \boldsymbol{v}^e_{(i)})^{dev} + \kappa \ln J^e_{(i)}\boldsymbol{i})$ where $\mu = \mu(\theta)$ by (4.165),
$$\boldsymbol{\sigma}^{dev}_{(ii)} = \frac{1}{J^e_{(ii)}}\frac{C_R}{3\hat{\lambda}^e_{(ii)}}\sqrt{N}\mathfrak{L}^{-1}(\frac{\hat{\lambda}^e_{(ii)}}{\sqrt{N}})(\hat{\boldsymbol{b}}^e_{(ii)})^{dev}, \quad \boldsymbol{\sigma} = \boldsymbol{\sigma}_{(i)} + \boldsymbol{\sigma}^{dev}_{(ii)}$$
3. Micro-macro transition: $\bar{\lambda}^e_{(ii)} = \dfrac{1}{\sqrt{3}}\sqrt{trace(\hat{\boldsymbol{b}}^e_{ii})}.$
4. Flow rules: $\boldsymbol{d}^p_{(i)} = \dot{\gamma}^p_{(i)}\boldsymbol{n}_{(i)}, \quad \boldsymbol{\omega}^p_{(i)} = \boldsymbol{0}, \quad \boldsymbol{n}_{(i)} := \dfrac{\boldsymbol{\sigma}^{dev}_{(i)}}{\sqrt{2}\tau_{(i)}}, \quad \tau_{(i)} := \sqrt{\dfrac{1}{2}\boldsymbol{\sigma}^{dev}_{(i)} : \boldsymbol{\sigma}^{dev}_{(i)}},$
$$\boldsymbol{d}^p_{(ii)} = \dot{\gamma}^p_{(ii)}\boldsymbol{n}_{(ii)}, \quad \boldsymbol{\omega}^p_{(ii)} = \boldsymbol{0}, \ \boldsymbol{n}_{(ii)} := \frac{\boldsymbol{\sigma}^{dev}_{(ii)}}{\sqrt{2}\tau_{(ii)}}, \ \tau_{(ii)} := \sqrt{\frac{1}{2}\boldsymbol{\sigma}^{dev}_{(ii)} : \boldsymbol{\sigma}^{dev}_{(ii)}}.$$
5. Isotropic hardening: $\dot{\gamma}^p_{(i)} = \dot{\gamma}_0 \exp\big(-\dfrac{\Delta G}{kT}(1 - (\dfrac{\tau_{(i)}}{s}))\big)$
where $s = const.$ or it is replaced by s_s, cf. (4.76).
6. Molecular relaxation: $\dot{\gamma}^p_{(ii)} = \dfrac{(\frac{\phi}{\phi_c} - 1)}{(\frac{\phi_R}{\phi_c} - 1)}(C\phi\tau_{(ii)})^{1/n}$, cf. (4.164).

5 Predictive capability of state-of-the-art models

In this chapter, the capability of the presented models will be evaluated and compared to experimental results available for homogeneous deformation involving various deformation modes, deformation rates and a wide range of temperatures. The models are calibrated to the experimental data for homogeneous deformation using least-square fitting based on the Nelder-Mead simplex algorithm. The homogeneous deformation modes allow the numerical integration to be performed using an ODE-solver instead of solving entire boundary value problem. The integration of the constitutive equations is performed by a Runge-Kutta integration scheme, the details of the Runge-Kutta-based method employed can be found in Shampine *et al.* (1999).

5.1 The BPA model - monotonic loading

Let us first consider uniaxial and plane strain compression modes. Arruda and Boyce (1990a) conducted monotonic compression experiments on PC at room temperature. To investigate the rate dependence, the tests were performed at several strain rates. Here, the two constant strain rates $\dot{\epsilon} = 0.001\ s^{-1}$ and $\dot{\epsilon} = 0.01\ s^{-1}$ will be considered. The simulations are performed using the material parameters taken from Wu and Van der Giessen (1993) as well as using the parameters calibrated herein. In the calibration, both the uniaxial and the plane strain compression responses, as well as both strain rates, were taken into consideration. The parameters obtained from the calibrations are listed in Table 5.1.

The simulations and the experimental responses are shown in Figs. 5.1-5.2. The model predictions fit well to the experimental data for both compression modes and strain rates $\dot{\epsilon} = 0.001\ s^{-1}$ and $\dot{\epsilon} = 0.01\ s^{-1}$. However, the yield peak as well as the initial strain softening are not accurately captured by the model. According to Hasan and Boyce (1995), these shortcomings are due to the linear elastic constitutive assumption. A comparison of Figs. 5.1 and 5.2 reveals that an increase of $\dot{\epsilon}$ results in the yield stress increasing. Moreover, the yield stress is lower in uniaxial compression than in plane strain compression, which is assumed to be caused by the pressure dependence of the yield stress, cf. Arruda and Boyce (1993a).

Table 5.1: Constitutive parameters of the BPA model for PC are taken from Wu and Van der Giessen (1993) based on the experiments by Arruda and Boyce (1990a). The calibrations are based on the experimental data for PC and BPA-PC given in Arruda and Boyce (1990a) and Dreistadt *et al.* (2009), respectively.

	E	ν	s_0	s_{ss}	h	$\dot{\gamma}_0$	A	C^R	N	α
	MPa		MPa	MPa	MPa	s^{-1}	MPa^{-1}K	MPa		
PC Wu and van der Giessen	2300	0.30	97	76.6	500	$2.0 \cdot 10^{15}$	240	12.8	2.15	0.08
Calibrated parameters										
PC, $\dot{\epsilon} = (1\ and\ 10) \cdot 10^{-3}\ s^{-1}$	2348	0.30	85.9	75.9	458	$6.39 \cdot 10^{7}$	140	10.6	2.19	0.12
BPA-PC	2300	0.37	99	73	370	$2.0 \cdot 10^{15}$	241	14	1.85	0.08

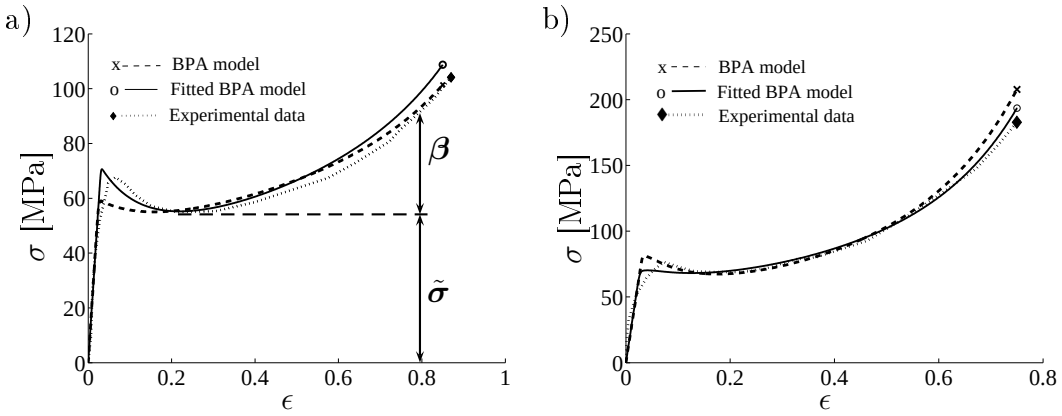

Figure 5.1: Comparison of a) uniaxial and b) plane strain compression responses for PC between the experiments and the BPA model. The tests were performed by Arruda and Boyce (1990a) at constant true strain rate $\dot{\epsilon} = 0.001\,s^{-1}$ at room temperature. Simulations are performed using both the calibrated parameters and the parameters taken from Wu and Van der Giessen (1993), cf. Table 5.1. Both uni- and biaxial deformation states and the two strain rates $\dot{\epsilon} = 0.001\,s^{-1}$ and $\dot{\epsilon} = 0.01\,s^{-1}$ were taken into account in the calibration. Mixed isotropic hardening and softening results in the stress, $\tilde{\boldsymbol{\sigma}}$, whereas anisotropic strain hardening results in the backstress, $\boldsymbol{\beta}$.

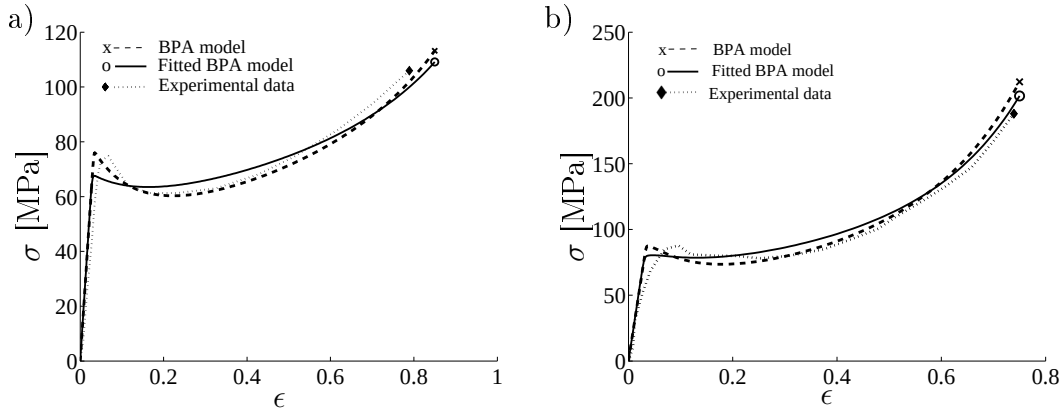

Figure 5.2: Comparison of a) uniaxial and b) plane strain compression responses for PC between the experiments and the BPA model. The tests were performed by Arruda and Boyce (1990a) at constant true strain rate $\dot{\epsilon} = 0.01\,s^{-1}$ at room temperature. Simulations are performed using both the the calibrated parameters and the parameters taken from Wu and Van der Giessen (1993), cf. Table 5.1. Both uni- and biaxial deformation states and the two strain rates $\dot{\epsilon} = 0.001\,s^{-1}$ and $\dot{\epsilon} = 0.01\,s^{-1}$ are taken into account in the calibration.

The following strain hardening is relatively well captured by the model in both compression modes. The hardening in plane strain compression increases more rapidly than in uniaxial compression. The deformation state dependence in hardening can be explained by the different chain orientation. It can be concluded that the BPA model is able to capture the deformation state dependence as well as the strain rate dependence during monotonic loading.

5.2 Non-monotonic loading

Next, the BPA model is evaluated under non-monotonic loading. Dreistadt *et al.* (2009) conducted uniaxial experiments on bisphenol A polycarbonate (BPA-PC) for complex load histories and a wide range of time spans. In contrast to the experiments by Arruda and Boyce (1990a), the aim of these experiments was to investigate the deformation behavior of PBA-PC during long-term non-monotonic loading. In the experiments, a constant true strain rate $\dot{\epsilon} = 0.001\,s^{-1}$ was employed and the specimen was stretched up to 0.75 which is well below the limiting stretch, λ_L. In the simulations, the BPA model is employed using elastic constitutive parameters $E = 2300$ MPa and $\nu = 0.37$ and the rest of the model parameters were calibrated to the experimental data for monotonic loading taken from Dreistadt *et al.* (2009). The material parameters are listed in Table 5.1. In the first experiment, the loading phase is followed by unloading, during which the resulting force is linearly removed. The specimen was then kept unstressed for 400 days. The simulated and the experimental response are presented in Fig. 5.3.

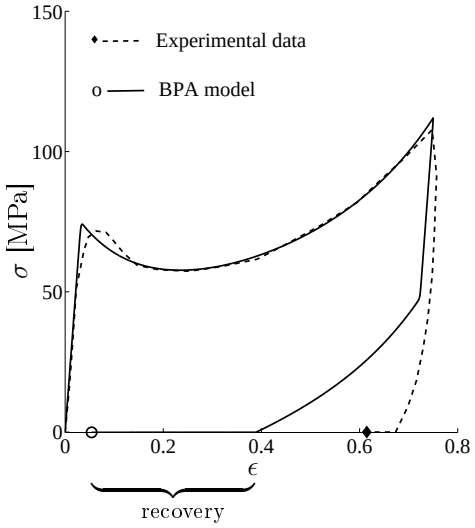

Figure 5.3: Comparison of simulated and experimental uniaxial compression responses for bisphenol A polycarbonate. After unloading the specimen is kept unstressed 400 days. The test has been performed by Dreistadt *et al.* (2009) at constant true strain rate $\dot{\epsilon} = 0.001\,s^{-1}$ at room temperature.

As with the previous examples, the BPA model captures the monotonic loading accurately. At the beginning of unloading, however, the experimental response shows increasing strain whereas the model results in almost linear response. Later in the unloading phase, the model shows a reversed plasticity which is initialized at $\sigma = 45$ MPa. In contrast to the model predictions, the experimental response shows a smooth transition. At the end of unloading, a premature Bauchinger effect is observed in the model response and the predicted true strain at zero stress is approximately 0.40. After the dwell period of 400 days the experiments indicates a permanent strain of 0.62, whereas the model predicts one magnitude lower value, 0.062. It can be concluded that the model is incapable of predicting unloading and recovery. Hasan and Boyce (1995) and Anand and Ames (2006) pointed out that accurate modeling of the viscoelastic behavior early in the loading phase is essential to predict the subsequent nonlinear unloading as well as a creep response. However, the Arruda and Boyce (1991) model is based on the linear elastic constitutive description.

Next, the uniaxial compression responses for repeated unloadings are simulated. Following Dreistadt *et al.* (2009), unloadings are performed at five progressively increasing

strain levels: $\epsilon = 0.05$, 0.13, 0.27, 0.45 and 0.59. After each unloading, the nominal stress is kept fixed during a prescribed dwell period. To examine creep and recovery, two different stress levels $\pi = 59$ MPa and $\pi = 1.2$ MPa and a relatively long dwell period of 12,000 s are considered. After each dwell period, the reloadings are performed until the next unloading level is reached. The final unloading is performed to zero stress.

Let us first consider the dwell stress $\pi = 59$ MPa. The model predicts exaggerated creep during the first two dwell periods and the predicted strain at the end of the second dwell period is close to the unloading strain value of the third cycle, cf. Fig. 5.4(a). In contrast to the model predictions, the experimental response shows considerably less creep during the first two dwell periods. Moreover, the stress peak during reloading is not captured by the model which tends directly back to the monotonic loading path. Similar to the single unloading, premature Bauchinger effect is observed during the last unloading and consequently the true strain becomes strongly underestimated at the end of this unloading phase.

A comparison of Figs. 5.4(a) and 5.4(b) reveals that creep is replaced by recovery when the dwell stress decreases from $\pi = 59$ MPa to $\pi = 1.2$ MPa. The first cycle is nearly elastic whereas increasing recovery is observed in the subsequent cycles. As shown in Fig. 5.4(b), the BPA model strongly underestimates recovery during the second and the third cycles, whereas recovery during the fourth cycle is highly overestimated.

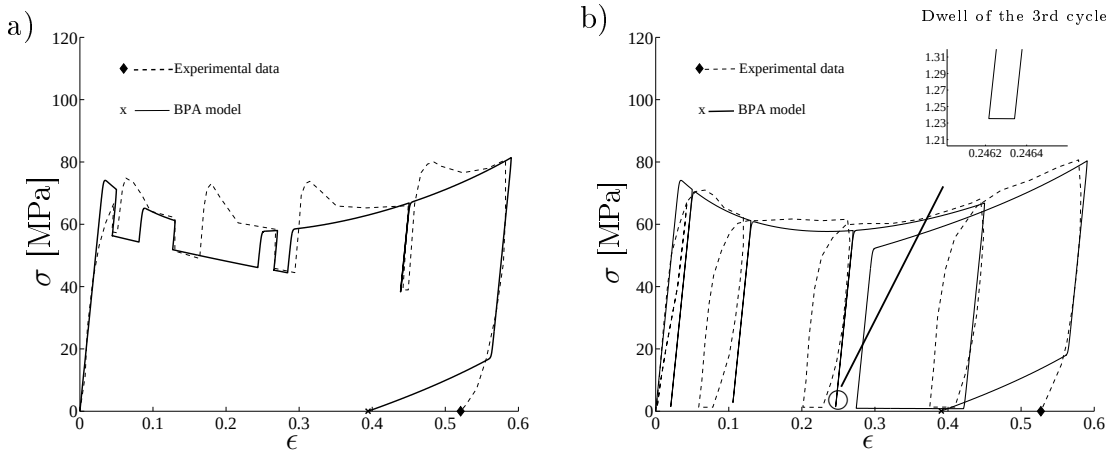

Figure 5.4: Uniaxial compression responses of BPA-PC. The repeated unloadings are performed to a) $\pi = 59$ MPa and b) $\pi = 1.2$ MPa and then the nominal stress π is kept fixed for 12000 s. The last unloading is performed to zero stress. The experiments are performed by Dreistadt *et al.* (2009) at room temperature and at a constant strain rate, $\dot{\epsilon} = 0.001\, s^{-1}$.

5.3 The Anand and Ames (2006) model

In addition to the micro-indentation experiments on PMMA, Anand and Ames (2006) conducted uniaxial compression experiments in the macro-scale involving monotonic loading followed by unloading to zero stress. In their experiments, the two constant strain rates $\dot{\epsilon} = 0.0003\,s^{-1}$ and $\dot{\epsilon} = 0.003\,s^{-1}$ were employed. The test specimens were annealed at the glass transition temperature 105 °C for 2 h and then furnace-cooled to room temperature over 15 h to avoid the formation of loosely packaged regions (free volume) in the material. Based on the Anand and Ames (2006) model using four micromechanisms, $i = 0, 1, 2, 3$, the material parameters were calibrated to this data taking both strain rates into account. In the calibration, the elastic modulus $E = 4200$ MPa, the Poisson's ratio $\nu = 0.34$ and the pressure-dependence parameter $\alpha = 0.204$ were kept fixed. The calibration resulted in $\mu_R = 22$ MPa, $N = 2.52$, $s_{cv} = 32.5$ MPa, $c_1 = 4.2$ TPa and $m_0 = 0.085$, whereas the other parameters are taken from Anand and Ames (2006). In their calibration, only a single strain rate $\dot{\epsilon} = 0.0003\,s^{-1}$ was employed. The calibrated parameters are listed in Table 5.2.

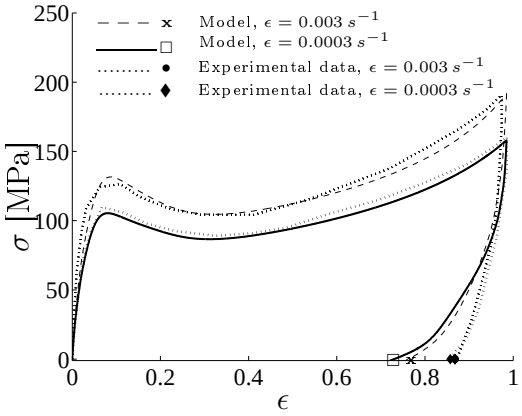

Figure 5.5: Comparison of the Anand and Ames (2006) model and the experimental responses for PMMA in uniaxial compression at constant true strain rates $\dot{\epsilon} = 0.0003\,s^{-1}$ and $= 0.003\,s^{-1}$. The calibration was performed to experimental data taken from Anand and Ames (2006). In calibration, both strain rates are taken into account.

A comparison of the simulations to the experiments shows that the proposed model captures not only the monotonic loading, but also the transient effects during initial yielding and initial unloading, cf. Fig. 5.5. The strain at the end of unloading, however, is underestimated. A comparison of the experimental and model responses at different strain rates indicates that the model is able to capture the strain rate dependency relatively well.

Table 5.2: Calibrated constitutive parameters of the Anand and Ames (2006) model for PMMA. The calibration was performed to the experimental data for the two strain rates $\dot{\epsilon} = 0.0003\,s^{-1}$ and $\dot{\epsilon} = 0.003\,s^{-1}$. The experimental data is taken from Anand and Ames (2006).

m_0	m_i	g_0	E	h	$\dot{\gamma}_0$	b	μ^R	N	φ_{cv}	φ_0	$\mu_{0,0}$	$\mu_{i,0}$
			MPa	MPa	s^{-1}		MPa				MPa	MPa
0.085	0.19	0.009	4200	4500	$5 \cdot 10^{-4}$	825	22	2.52	0.001	0	0	3500
$s_{0,0}$	$s_{1,0}$	$s_{2,0}$	$s_{3,0}$	s_{sv}	$\mu_{0,s}$	$\mu_{1,s}$	$\mu_{2,s}$	$\mu_{3,s}$	c_0	c_1	c_2	c_3
MPa	MPa	MPa	MPa	MPa	MPa	MPa	MPa	MPa	TPa	TPa	TPa	TPa
35	13	23	33	32.5	0	1100	400	200	5.0	4.2	1.8	1.3

5.4 Simulation of the glass transition - the Dupaix and Boyce (2007) model

The Dupaix and Boyce (2007) model is applied to polyethyle terephthalate-glycol (PETG) and the capability is evaluated over a broad range of temperatures. Since PETG does not undergo strain-induced crystallization near the glass transition temperature, the Dupaix and Boyce (2007) model can be used in the simulations. In contrast to (4.156), the evolution of the plastic deformation in resistance (i) is based on the Argon (1973) model via (4.75) and the isotropic hardening is modeled according to (4.77). The temperature dependence of the molecular relaxation $\dot{\gamma}^p_{(ii)}$ in (4.164) is governed by the parameters $D \approx 2.46$ MPa^{-1}s^{-n}, $Q/R \approx 10200$ K and $n \approx 0.15$. The values of the parameters have been obtained by least-square fitting to the experimentally observed viscosity-shear strain rate response at different values of the orientation parameter ϕ_c, cf. Dupaix and Boyce (2007). Moreover, the uniaxial compression tests on PETG indicated that the limiting stretch is reached by the constant maximum angle $\phi_{max} \approx 1.52$ between the principal axis and the individual chains and thus $\phi_c \approx 0.05$. The parameters $\dot{\gamma}_{ref} = 0.00173$ s^{-1}, $\xi = 3$ K, $\zeta = 8.23$ K and the reference transition temperature $\theta^*_g = 346$ K have been derived by fitting the $\mu - \theta$ response to the DMA experiments at various strain rates. The rest of the material parameters employed in the simulations were obtained using the least-square fitting to the experimental uniaxial stress-strain curves at 333 K and at the two constant strain rates $\dot{\epsilon} = 0.01$ s^{-1} and $\dot{\epsilon} = 0.5$ s^{-1}. The experimental data is taken from Dupaix and Boyce (2007). During calibration, both the strain rates were taken into account. The calibrated parameters are listed in Table 5.3.

In Fig. 5.6, the model and the experimental stress-strain curves are compared at three different temperatures: a) at room temperature, b) at calibration temperature 333 K and c) in the glass transition temperature, 350 K. As both the strain rates are taken into account in calibration, it follows that the model captures the experimental responses on average: at $\dot{\epsilon} = 0.01$ s^{-1} the model underestimates the stress response, whereas the experimental response at $\dot{\epsilon} = 0.5$ s^{-1} is more or less below the model results. It can be concluded that the Dupaix and Boyce (2007) model is able to capture the mechanical behavior of PETG relatively well over a wide range of temperatures. During the glass transition, the free volume in amorphous polymers as well as the stiffness and the yield stress decrease simultaneously with increasing pressure. As a result, the value of the pressure dependence factor α in (4.76) should be manipulated so that the initial isotropic hardening and post-yield softening decrease, cf. Kameda *et al.* (2007). This feature as well as reduced free

Table 5.3: Constitutive parameters employed in the simulations for PETG. The calibrations were performed for uniaxial test data taken from Dupaix and Boyce (2007). In the calibration, both strain rates $\dot{\epsilon} = 0.5\,s^{-1}$ and $\dot{\epsilon} = 0.01\,s^{-1}$ were taken into account. The average slope factor $X_g = 5.0$ MPa K^{-1} and $s_0 = 0.15\mu$.

κ	s_{ss}/s_0	μ_r	μ_g	h	$\dot{\gamma}_0$	A	C^R	N	α	$\Delta\theta/\chi$
MPa		MPa	MPa	MPa	s^{-1}	MPa^{-1}K	MPa			K
1248	0.80	15.68	453	700	$2.73 \cdot 10^7$	147	8.59	4.57	0.10	31.8

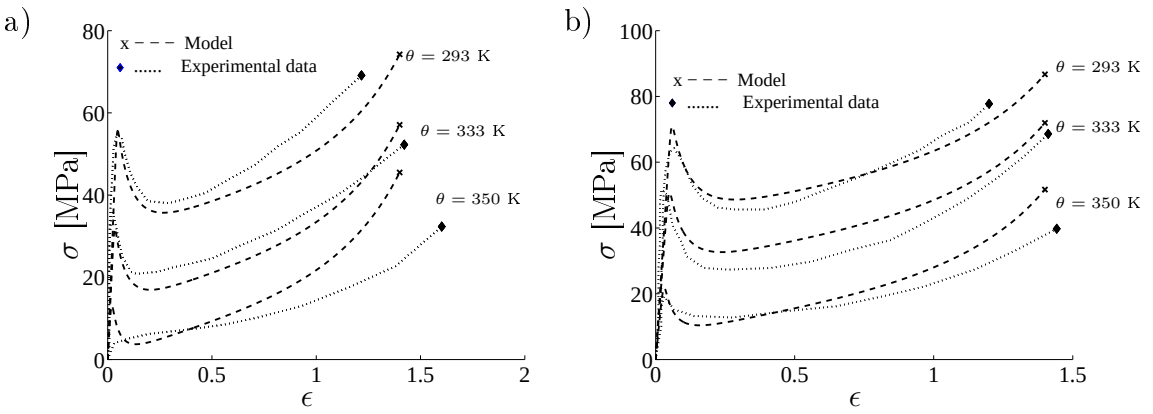

Figure 5.6: Comparison of the model and experimental responses for PETG in uniaxial compression at $293\,K$, $333\,K$, and $350\,K$. The tests have been performed by Dupaix and Boyce (2005) employing constant true strain rates, a) $\dot{\epsilon} = 0.01\,s^{-1}$ and b) $\dot{\epsilon} = 0.5\,s^{-1}$. The material parameters are calibrated for both strain rates, and they are given in Table 5.3.

volume, however, are neglected in the model under consideration which partially explains the overprediction of the yield stress around the glass transition temperature. Moreover, the Dupaix and Boyce (2007) model does not include the effects of aging which also reduces the temperature sensitivity of the yield stress near the glass transition temperature, cf. Hasan *et al.* (1993).

5.5 Comparison of the models

Next, the capability of the models are compared under non-monotonic loading. The models were calibrated to the experimental data for BPA-PC, cf. Sec. 5.2. The common parameters of the models are given in Table 5.4. In addition, the parameters $s_{1,0} = 4.0$ MPa, $s_{2,0} = 9.0$ MPa, $s_{3,0} = 28$ MPa and $s_{sv} = 17.5$ MPa in the Anand and Ames (2006) model are recalibrated. The rest of the parameters are equal to those listed in Tables 5.2 and 5.3 for the Anand and Ames (2006) and the Dupaix and Boyce (2007) models, respectively.

Table 5.4: Calibrated common parameters of the models for BPA-PC. In addition, the calibrated parameters $s_{1,0} = 4.0$ MPa, $s_{2,0} = 9.0$ MPa, $s_{3,0} = 28$ MPa and $s_{sv} = 17.5$ MPa are used in the Anand and Ames (2006) model. The rest of the parameters are equal to those listed in Tables 5.2 and 5.3 for the Anand and Ames (2006) and the Dupaix and Boyce (2007) models, respectively. The experimental data for BPA-PC employed in the calibrations is given in Dreistadt *et al.* (2009).

	E	ν	s_0	s_{ss}	h	$\dot{\gamma}_0$	A	C^R	N	α
	MPa		MPa	MPa	MPa	s^{-1}	MPa^{-1}K	MPa		
BPA model	2300	0.37	99	73	370	$2.0 \cdot 10^{15}$	241	14	1.85	0.08
A&A model	2300	0.37	35		4500	$5.0 \cdot 10^{-4}$		19	2.00	0.20
D&B model	2230	0.38	94	72	370	$2.0 \cdot 10^{15}$	241	14	1.78	0.08

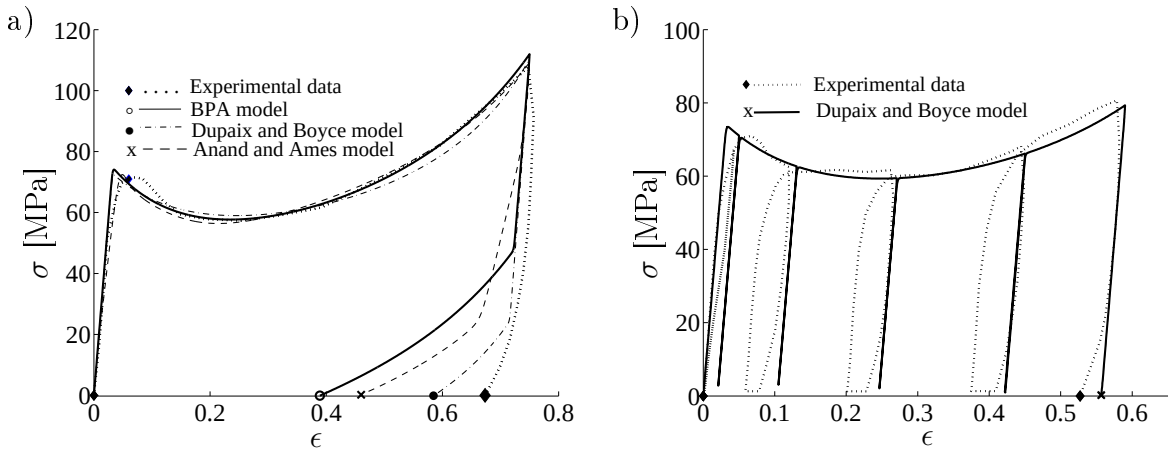

Figure 5.7: a) Comparison of the model responses for BPA-PC under uniaxial compression. The test has been performed by Dreistadt *et al.* (2009) at constant true strain rate $\dot{\epsilon} = 0.001\,s^{-1}$ at room temperature. b) The Dupaix and Boyce (2007) model response for BPA-PC. The repeated unloadings are performed to $\pi = 1.2$ MPa and then the nominal stress π is kept fixed for 1200 s. The last unloading is performed to zero stress.

The model and the experimental response are presented in Fig. 5.7(a). During monotonic loading up to the strain limit of 0.75, the models accurately capture the experimental response and no significant differences between the responses can be observed. In the initial unloading, the models cannot predict the increasing strain but result in almost linear response. The differences between the models become apparent later during the unloading phase. Similar to the BPA model response, the Anand and Ames (2006) model cannot accurately reproduce the transient effect of the PBA-PC response, but yields a premature Bauchinger effect and as a result the strain $\epsilon \approx 0.46$ at the end of unloading is underestimated. A comparison of the model responses reveals that the Dupaix and Boyce (2007) model is able to satisfactorily predict the experimental data, the strain at the end of unloading is $\epsilon \approx 0.59$.

In addition to the monotonic loading, the models are also evaluated for repeated unloadings. Since the Dupaix and Boyce (2007) model is aimed at modeling the mechanical behavior close to the glass transition temperature, the backstress is not included in the model. It then follows that the Bauchinger-like effects via the backstress cannot be reproduced by that model. As shown in Fig. 5.7(b), the Dupaix and Boyce (2007) model cannot reproduce recovery and simulations also result in vanishing creep.

Let us then consider the Anand and Ames (2006) model for the dwell stress level $\pi = 59$ MPa and the dwell period 1200 s. Similar to the BPA model, the Anand and Ames (2006) model is accurate for monotonic loading but it fails during creep, i.e. the strain at the end of the first cycle is significantly overpredicted and the model cannot reproduce the stress peaks followed by reloadings, cf. Fig. 5.8(a). However, creep during the following cycles is satisfactorily captured and the Bauchinger effect does not evolve during the dwell period of 1200 s. In contrast to the BPA model, the Anand and Ames (2006) model is also able to reproduce recovery during the first cycles, cf. Fig. 5.8(b). Moreover, comparison of Figs.

5.8(b) and 5.9(b) reveals that recovery during the cycles as well as the Bauchinger effect during the last unloading are more accurately estimated by the Anand and Ames (2006) model than by the BPA model.

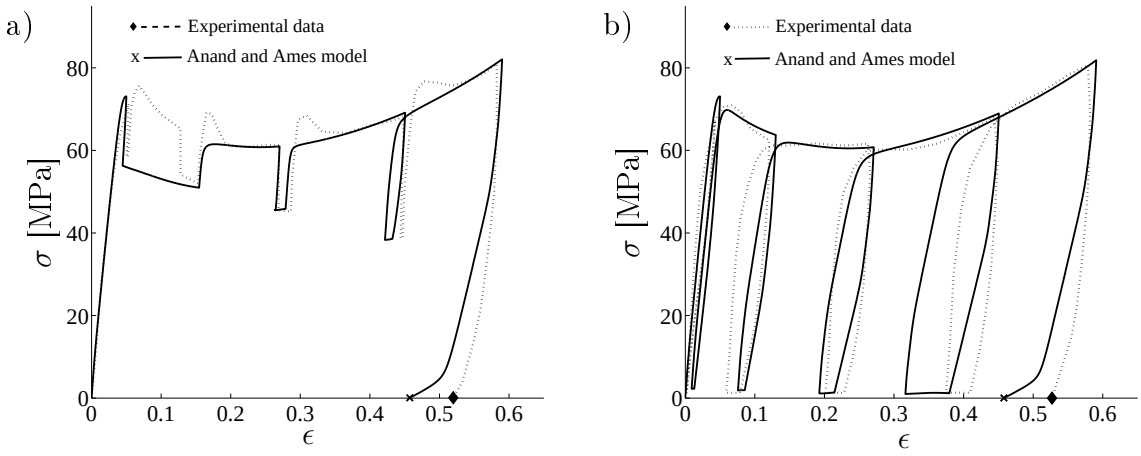

Figure 5.8: The Anand and Ames (2006) model responses for BPA-PC at room temperature and at a constant strain rate, $\dot{\epsilon} = 0.001\,s^{-1}$. The repeated unloadings are performed to a) $\pi = 59$ MPa and b) $\pi = 1.2$ MPa and then the nominal stress π is kept fixed for 1200 s. The last unloading is performed to zero stress. Uniaxial compression data is taken from Dreistadt *et al.* (2009).

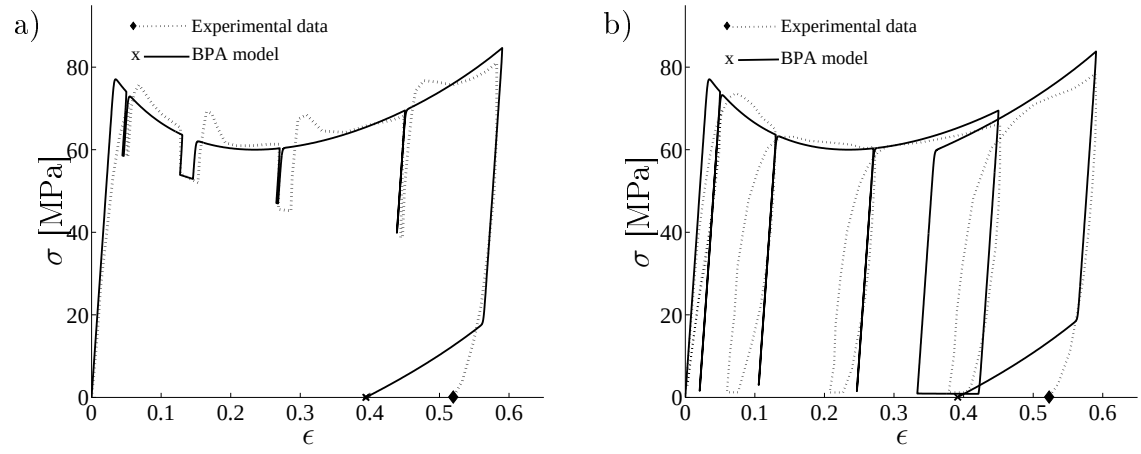

Figure 5.9: The BPA model responses for BPA-PC at room temperature and at a constant strain rate, $\dot{\epsilon} = 0.001\,s^{-1}$. The repeated unloadings are performed to a) $\pi = 59$ MPa and b) $\pi = 1.2$ MPa and then the stress π is kept fixed for 1200 s. The last unloading is performed to zero stress. Uniaxial compression data is taken from Dreistadt *et al.* (2009).

6 The BPA model extension

6.1 Model description

A comparison of the model and the experimental responses reveals the following shortcomings in the present models:

- The models predict a premature Bauchinger effect.
- The long-term recovery is highly overpredicted by the models.
- The models are not able to capture a nonlinear response during initial loading, unloading and reloading.

To compensate for the shortcomings of the models, an extension for the BPA model is proposed in this work. State-of-the-art (entropic network) models postulate that the backstress favors strain reduction but that relaxation is too slow to observe during unloading and may lead to excessive strain relaxation during long-term dwell, cf. Haward and Thackray (1968) and Arruda and Boyce (1993a). In thermodynamic terms, the chains, which are extended and then released, tend to the most probable, unstretched and high-entropy state. The present models, however, are not able to trace this state correctly. Motivated by these findings, two dashpots in parallel with the nonlinear Langevin spring are used in the Extended BPA (EBPA) model to capture isotropic hardening behavior in the material. The purpose of the extra dashpot is to increase the isotropic hardening effect and thereby suppress the influence of kinematic hardening. A rheological illustration of the EBPA model is shown in Fig. 6.1. The original and extra dashpot are modeled by the internal state variables s_1 and s_2, respectively, i.e.

$$s = s_1 + s_2. \tag{6.1}$$

The evolution laws for the isotropic hardening variables s_1 and s_2 are taken as

$$\begin{aligned} \dot{s}_1 &= h_1(1 - s_1/s_{ss})\dot{\gamma}^p, \quad s_1(0) = s_0, \\ \dot{s}_2 &= h_2(1 - \mathcal{H}(s_2 - \bar{s}_2))\dot{\gamma}^p, \quad s_2(0) = 0 \end{aligned} \tag{6.2}$$

where $\dot{\gamma}^p$ was introduced in (4.75), s_{ss} is a constitutive parameter and $\mathcal{H}$ is the Heaviside-function which prevents an excessive hardening e.g. during cyclic loading. The threshold $\bar{s}_2$ can be found experimentally. To take the pressure into account, the internal state variable s in (4.75) is replaced by s_s which was given by (4.76). Here, h_1 and h_2 are constitutive parameters governing the isotropic softening and hardening. A glance at (4.75) and $(6.2)_2$ reveals that $\dot{s}_2$ is positive and thus, s_2 is monotonically increasing. Since $s_2 > 0$ the amount of isotropic hardening increases compared to the original BPA model which, thanks to the model calibration, suppresses the evolution of the backstress in the EBPA model. Having a less pronounced evolution of the backstress is of major importance during relaxation simulations at a low-stress level, where the plastic evolution is particularly governed by the internal stress state, i.e. by the backstress. Hoy and Robbins (2007) showed that

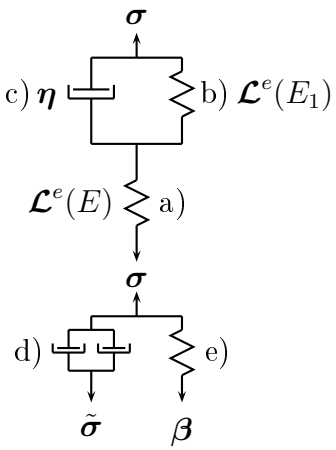

Figure 6.1: Rheological illustration of the EBPA model. The model is governed by the elements: two elastic springs a) and b), a viscoelastic dashpot c), two viscoplastic dashpots d) and a nonlinear Langevin spring e).

the network of entangled chains has ability to prevent chains from deorienting without recovery of the macroscopic strain. Since this effect is reduced in the EBPA model results, isotropic hardening mechanism may be related to this microstructural characteristic of polymer glasses.

Viscoelasticity

Since the initial response of amorphous glassy polymers can be considered nearly elastic, most of the models are based on a linear elastic constitutive assumption. However, such models are not able to satisfactorily reproduce transient effects during non-monotonic loading, which shortcomings are primarily a consequence of neglected viscoelastic effects, cf. Hasan and Boyce (1995). The influence of viscoelasticity becomes also apparent in creep and relaxation as well as in cyclic loading processes, cf. Miehe and Keck (2000). The time-dependent behavior is a one consequence of the macromolecular characters of the molecules: the molecules need a relaxation time to attain the equilibrium state after deformation. Based on the experiments on amorphous polymers the following typical viscoelastic characteristics can be observed:

- Under a constant stress, the strain increases (creep) or decreases (recovery) over time, cf. Figs. 2.5 and 5.4.
- Under a constant strain, the stress decreases over time (relaxation), cf. Fig. 6.2.
- The effective stiffness as well as the magnitude of the stress response depend on the applied loading rate, cf. Figs. 2.1 and 2.4.
- Hysteresis during a loading cycle is observed already in small strains, cf. Fig. 2.4.

There are two ways to describe viscoelastic material behavior: linear and nonlinear viscoelasticity. For an overview of viscoelastic theory, see e.g. Findley *et al.* (1989). The underlying assumption of linear viscoelasticity is the Boltzmann superposition principle

which states that load or deformation responses applied to a material at different times are linearly additive, i.e. the stress is separable in both load and creep response according to

$$\sigma(t) = E_r\epsilon(t) + \int_0^t F(t-t')\dot{\epsilon}(t')dt', \quad \text{or} \quad \epsilon(t) = \frac{\sigma(t)}{E_c} + \int_0^t K(t-t')\dot{\sigma}(t')dt'. \tag{6.3}$$

In (6.3), E_r and E_c are the elastic moduli for relaxation and creep, respectively, and F and K denote the relaxation and creep function, respectively. Nonlinear viscoelasticity is when the stress cannot be separated. According to (6.3), the stress depends on the entire deformation history or conversely, the strain depends on the entire stress history. In contrast to the integral formulation, a multiplicity of viscoelastic models rely on differential formulations, which allow use of spring dashpot analogies.

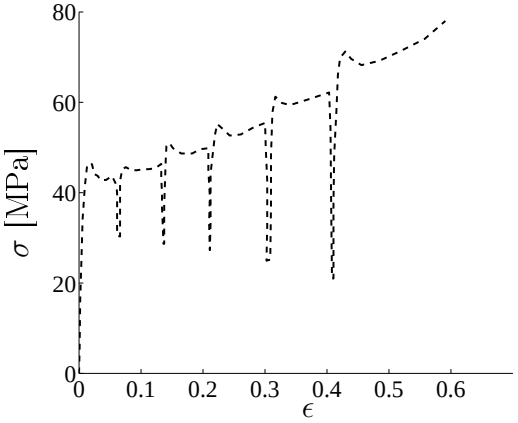

Figure 6.2: Influence of the relaxation time on the stress vs strain response of PVC. The test specimen was subjected to relaxation for periods of 10 s, 20 s, 30 s, 40 s and 60 s. Experimental data is taken from G'Sell and Jonas (1981).

Many of the nonlinear viscoelastic models for amorphous polymers are based on the Langevin statistic employed for rubber elasticity, cf. e.g. Wu and Van der Giessen (1993), Zhang and Huang (2004) and Anand and Ames (2006). Klompen *et al.* (2005) proposed a nonlinear viscoelastic-plastic model which also takes the physical aging into account. This model is shown to accurately capture the yield stress and the mechanical response during monotonic loading. However, the characterization of aging kinetics needs several material parameters to be determined.

Examples of linear viscoelastic models are the Zener (1948) model, which consists of an elastic spring in parallel with a Maxwell element and the Burger's model, which consists of an elastic spring and a damper arranged in series with the Kelvin element. These simple models are later employed instead of generalized Kelvin and Maxwell models (Prony-series) to avoid the identification of a large number of material parameters. In order to describe hysteresis of filled rubbers, Huber and Tsakmakis (2000) proposed a modified Zener model which was later used by Amin *et al.* (2002) to predict the rate-dependent behavior of high damping natural rubbers. Bergström and Boyce (1998) proposed a rate-dependent model in which two networks are used to describe the mechanical behavior of rubber; one network captures the elastic behavior, whereas a Maxwell element is used to predict the viscoelastic behavior. The Bergström and Boyce (1998) model was later extended to the modeling of mechanical behavior of filled polymers in high strain rates, cf. Quintavalla and Johnson (2004). In contrast to the nonlinear viscoelastic models, many of the linear viscoelastic models can satisfactorily be applied to model practical behavior of glassy polymers in only small strains and strain rates, cf. Ward (1983) and Amin *et al.*

(2002). Cao *et al.* (2012) proposed a linear viscoelastic model consisting of a spring and a Maxwell element for modeling the rate-dependent deformation behavior of glassy polymers prior to yielding. To account for nonlinear deformation behavior in large strains, the models which include both viscoelastic and viscoplastic ingredients need to be applied, cf. Chaboche (2008). Among such models, Khan and Zhang (2001) and Khan *et al.* (2006) proposed a nonlinear viscoelastic-plastic model which is able to capture the deformation behavior of PTFE and Adiprene-L100 polymer, respectively. Based on the modified viscoelasticity-plasticity theory with overstress (VBO), Colac and Dusunceli (2006) modeled mechanical behavior of high density polyethylene (HDPE) under uniaxial monotonic and cyclic loading. Hasanpour and Ziaei-Rad (2008) presented a model based on the assumption that stress can be decomposed into viscoelastic and elastic-plastic component. However, the capability of the models mentioned above is addressed only in a restricted set of loading situations and many of them deal with a numerical approach where an applicable hypoelastic stress equation must be applied in care.

To better capture a large strain mechanical response during unloading and reloading, the EBPA model needs to be further modified. In this extension, the elastic spring in the BPA model is replaced by a simple Kelvin chain involving a viscoelastic dashpot and an elastic intermediate spring (Kelvin-Voigt element) in series with an elastic spring, cf. Fig. 6.1. The Kelvin-Voigt element is employed for predicting creep and recovery, while its combination with the elastic spring is aimed at describing the stress relaxation. Moreover, the viscoelastic constitutive description allows the rate-dependent stress response to be captured by the EBPA model.

The idea to replace a single elastic spring by a Kelvin chain is motivated by the constitutive models for polymers, able to capture the initial viscoelastic response prior to the macroscopic yielding. Since the Kelvin model alone is not able to describe the magnitude of creep and recovery in glassy polymers correctly, a spring needs to be added in series in order to take non-recoverable portion of strain into consideration. Albeit the two distinct Kelvin-like elements present in the EBPA model are widely applied in modeling of the elastic and plastic deformation, respectively, their combination has not been employed by author's knowledge. For high stresses and strain rates, the viscoelastic dashpot resists elongation of the parallel spring, whereas the effect of the dashpot becomes negligible in low stress and strain rate levels. As a result, the dashpot dominates deformation behavior in high strain rates prior to yielding and results in an increased effective stiffness, i.e. the stress being increased and the strain decreased. For low strain rates and longer time periods, the effect of the viscoelastic dashpot is attenuated and the intermediate spring contributes to the total strain in the system.

In terms of microstructural characteristics, the entanglements connected to strongly extended chains slip past one another during yield, while coiled neighboring chains result in an increase in the number of chain segments between entanglements, cf. Fig. 7.7. This mechanism is attributed to the disentanglement process and it results in viscosity being increased, cf. Khan and Zhang (2001) and Hoy and Robbins (2007). If a high strain rate in relation to the relaxation time of the material is applied, the molecules have

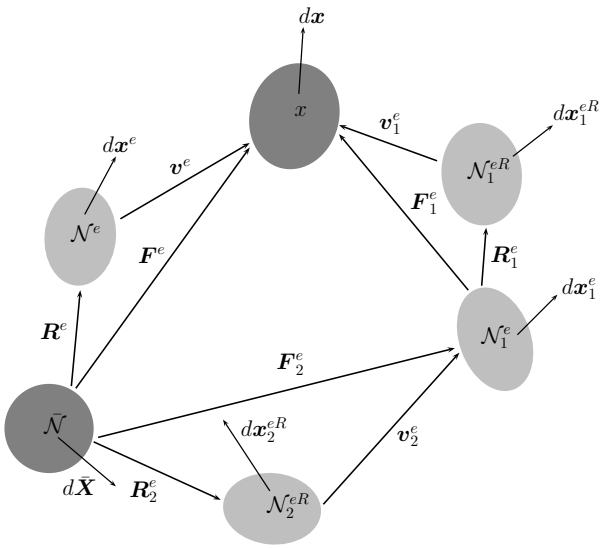

Figure 6.3: The multiplicative decomposition of the elastic deformation gradient $\boldsymbol{F}^e$ into the two parts $\boldsymbol{F}_1^e$ and $\boldsymbol{F}_2^e$, and the polar decompositions based on the left stretches $\boldsymbol{v}^e$, $\boldsymbol{v}_1^e$ and $\boldsymbol{v}_2^e$.

not enough time to relax and reach their equilibrium. According to Bardenhagen *et al.* (1997), elastic stretching causes an increase in viscosity, while increasing elastic strain rate reduces viscosity of the material. Based on these observations, viscosity is related to disentanglement, it depends on strain level and rate and it is modeled in the EBPA model by the two Kelvin-like elements which are related to the plastic and elastic stretching, respectively.

To improve the accuracy of the linear viscoelastic models in large multi-dimensional deformations, a multiplicative decomposition of the elastic deformation gradient $\boldsymbol{F}^e$ into a viscous and an elastic part needs to be applied, i.e.

$$\boldsymbol{F}^e = \boldsymbol{F}_1^e \boldsymbol{F}_2^e \tag{6.4}$$

where $\boldsymbol{F}_1^e$ and $\boldsymbol{F}_2^e$ take the elastic stretching in the spring a) and b) into account, cf. Fig. 6.1. Similar to (4.9), use will be made of the polar decomposition of $\boldsymbol{F}_1^e$ and $\boldsymbol{F}_2^e$, i.e.

$$\boldsymbol{F}_1^e = \boldsymbol{v}_1^e \boldsymbol{R}_1^e \quad \text{and} \quad \boldsymbol{F}_2^e = \boldsymbol{v}_2^e \boldsymbol{R}_2^e \tag{6.5}$$

which define the orientation of the intermediate elastic configuration in terms of the elastic stretch tensors $\boldsymbol{v}_1^e$ and $\boldsymbol{v}_2^e$ and the elastic rotations $\boldsymbol{R}_1^e$ and $\boldsymbol{R}_2^e$, cf. Fig. 6.3.

One consequence of the viscoelasticity is that the rate form of the elasticity equation must be derived. The governing equation for the system illustrated in Fig. 6.1 is given by

$$\boldsymbol{\tau} = \boldsymbol{\mathcal{L}}^e(E) : \ln \boldsymbol{v}_1^e = \boldsymbol{\eta} : \frac{d}{dt}(\ln \boldsymbol{v}_2^e) + \boldsymbol{\mathcal{L}}^e(E_1) : \ln \boldsymbol{v}_2^e \tag{6.6}$$

where the fourth order elasticity tensor $\boldsymbol{\mathcal{L}}^e$ was introduced by (4.114), E and E_1 are elastic constitutive parameters and $\boldsymbol{\eta}$ is the stiffness of the viscous damper. In general, $\boldsymbol{\eta}$ is

regarded as a fourth order tensor and it depends on temperature, pressure and deformation rate, cf. e.g. Khan *et al.* (2006). Typically, such conditions can be met in manufacturing processes, less under operating conditions. Considering relatively low strain rates under isothermal conditions and assuming viscosity η to be a scalar, only three new material parameters h_2, E_1 and η enter the extended model. The details for the numerical treatment of the proposed model under homogeneous and inhomogeneous deformation are given in the Appendix A and in Sec. 7.1, respectively.

6.2 Calibration of the EBPA model

Glassy polymers show a strong dependence on a deformation state and therefore, the EBPA model is calibrated for three deformation modes: simple shear, uniaxial compression and plane strain compression. These homogenous deformation modes allow the numerical integration to be performed using an ODE-solver instead of solving the boundary value problem. The details of the Runge-Kutta-based method employed can be found in Appendix A.

6.2.1 Compression and simple shear - monotonic loading

First, the EBPA model is calibrated to uni- and bi-axial compression as well as to simple shear tests for PC, conducted by Arruda and Boyce (1993a) and G'Sell and Gopez (1985), respectively. During the tests, the stress-strain response of each deformation mode has been recorded for evaluation of the mechanical behavior of polymers. The tests have been performed at room temperature using a constant strain rate, $\dot{\epsilon} = 0.001\,1/s$ for compression and $\dot{\gamma} = 0.003\,1/s$ for simple shear. The elastic constitutive parameters $E = 3300$ MPa, $E_1/E = 0.35$ and $\nu = 0.3$ are kept fixed in the calibration and the parameters, A and α, are taken to coincide with the values in Wu and Van der Giessen (1993). Identification of the viscosity $\eta = 6.0 \cdot 10^4$ MPas is done by fitting the initial response to the experimental data. The threshold value of the shear strength $\bar{s}_2 = 40$ MPa in (6.2) is determined through calibration to a uniaxial compression test program. According to this test, a specimen is first compressed to $\epsilon = 0.8$ followed by unloading to zero stress, then kept unstressed until the strain $\epsilon = 0.66$ is reached and finally reloaded at the same strain rate $\dot{\epsilon} = 0.001$ 1/s, cf.

Table 6.1: Constitutive parameters of the BPA and EBPA model for PC. The calibration of the EBPA model is based on the experiments given in Arruda and Boyce (1993a) and G'Sell and Gopez (1985) for the compression and simple shear, respectively. The BPA model parameters are taken from Wu and Van der Giessen (1993).

	E	ν	s_0	s_{ss}	h_1	h_2	$\dot{\gamma}_0$	A	C^R	N	α
	MPa		MPa	MPa	MPa	MPa	s^{-1}	MPa^{-1}K	MPa		
BPA	2300	0.30	97	76.6	500		$2.0 \cdot 10^{15}$	240	12.8	2.15	0.08
EBPA	3300	0.30	96	61.3	168	9.9	$5.4 \cdot 10^{15}$	240	17.8	2.42	0.08

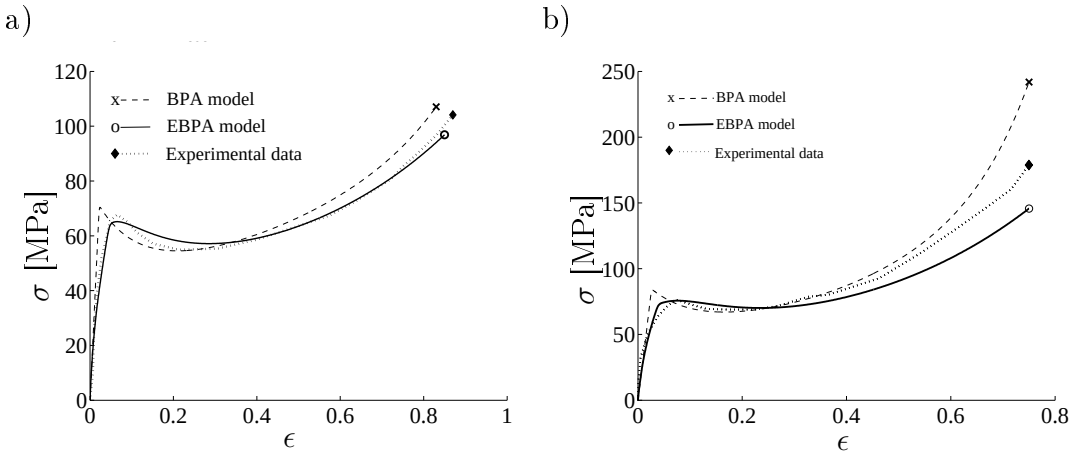

Figure 6.4: Stress-strain curves for a) uniaxial and b) plane strain compression of PC. Experimental data is taken from Arruda and Boyce (1993a). The test has been performed at room temperature using a constant strain rate $\dot{\epsilon} = 0.001$ 1/s.

Arruda *et al.* (1995). The remaining parameters C^R, N, s_0, s_{ss}, h_1, h_2, and $\dot{\gamma}_0$ are obtained using the least-square fitting. The optimization problem is solved using the Nelder-Mead simplex algorithm. The calibrated set of parameters for the EBPA model is given in Table 6.1. For comparison, the original BPA model parameters, taken from Wu and Van der Giessen (1993), are also presented.

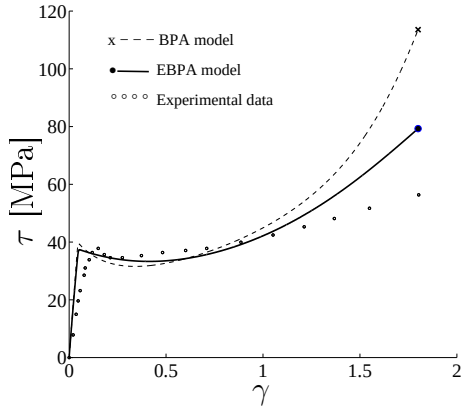

Figure 6.5: Stress-strain curves for simple shear of PC. G'Sell and Gopez (1985) performed the test at room temperature using a constant strain rate $\dot{\gamma} = 0.003$ 1/s.

Let us first consider the compression modes. Based on the parameters in Table 6.1 the response of the original and the extended BPA model are simulated and compared to the experimental results, cf. Figs. 6.4. Due to the linear elastic constitutive law being used in the BPA model, cf. Eq. (4.113), its initial elastic response deviates from the EBPA model and the experimental results that show nonlinear response. Later, in large plastic strains the model predictions fit well to the uniaxial experimental data. Under plain strain compression, the EBPA model first overestimates the stress response whereas in large strains the EBPA and the BPA models give the lower and the upper bounds, respectively.

In contrast to the uniaxial and plane strain compression modes, the principal directions alter during simple shear, and consequently the plastic spin is nonzero. Despite the viscoelastic constitutive description, the EBPA model prediction also deviates from the initial experimental response and as a result the strain at the stress peak is underestimated, cf. Fig. 6.5. After the initial yielding, the response is satisfactorily captured by both the

models. When the shear strain reaches approximately 1.0, both the model predictions deviate significantly from the experiment. This discrepancy between the models and the experiment can be explained by shear band propagation and boundary effects, cf. G'Sell and Gopez (1985).

6.2.2 Influence of the entanglements

The softening/hardening behavior of amorphous glassy polymers is ascribed to specific microstructural mechanisms. It is widely acknowledged that the softening of amorphous glassy polymers is mainly due to the activation and growth of microscopic shear bands. Argon (1973) and Bowden and Raha (1970) showed that softening followed by the yield point is associated with the thermally activated overcoming of van der Waals interaction between neighboring macromolecules. The van der Waals interaction is closely related to the physical entanglements; an increasing grade of entanglements sustains the van der Waals forces which results in an increase in the resistance to slipping between chains.

Melick (2003) investigated the direction-dependent behavior of both initially isotropic and pre-strained glassy polymers. They observed that the yield stress and the hardening behavior in tension considerably differ from those in compression. Tomita and Tanaka (1995) pointed out that the extension along the chain direction increases the number of entanglements and affects the stiffening of the material. Unlike in the tests for homogeneous deformation, the experimental response of inhomogeneous deformation shows that the specimen's elongation takes place almost at constant force, cf. e.g. Tomita and Tanaka (1995) and Wu and Van der Giessen (1995). Deformation localizes in fine shear bands which grow during elongation and prevent hardening in large strains. G'Sell and Gopez (1985) observed that the deformation behavior in shear is, for the one part, attributed to the intrinsic material behavior and for the other part to the propagation of macroscopic shear bands. Wu and Van der Giessen (1994) concluded that the most important factor that controls the initiation of shear bands is the intrinsic softening, whereas the orientational hardening is crucial for widening and localization of the shear bands.

In contrast to the affine network models, where the number of entangled points of molecular chains is considered to be constant, the experimental investigations implicitly suggest the possibility of changing the number of entanglements due to the plastic deformation, cf. Tomita and Tanaka (1995). Melick (2003) performed uniaxial tests on semi-crystalline polymers, which indicated strain hardening being dominated by the resulting number of entanglements. Chain slip and decrease in entanglement density, i.e. disentanglement, were found to decrease strain hardening and stress build-up. To evaluate the influence of the entanglements, a simple evolution equation for the number of entanglements will be presented based on the following material characteristics:

- The extension of a chain and the compression perpendicular to the direction of the chain increase the number of entanglements and vice versa, whereas
- the number of entanglements reduces due to the shear deformation parallel to the chain direction.

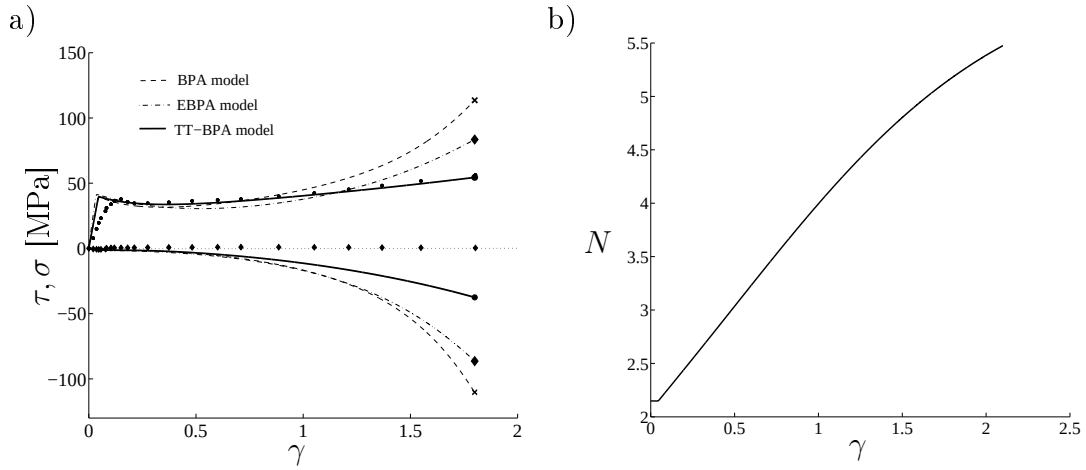

Figure 6.6: a) Comparison of the BPA, EBPA and TT-BPA model responses under simple shear. b) N vs γ curve based on the evolution equation (6.7). Experimental data points of the shear and normal stress are depicted by the markers "•" and "⧫", respectively. Experimental data is taken from Wu and Van der Giessen (1994). In accordance with the experiment, the strain rate $\dot{\gamma} = 0.003$ is employed in the simulations.

Based on the work of Tomita and Tanaka (1995), the number of entanglements m evolves according to

$$\dot{m} = \boldsymbol{\chi}(\theta) : \bar{\boldsymbol{D}}^p, \quad m(0) = m_0 \tag{6.7}$$

where $\boldsymbol{\chi}(\theta)$ is a temperature-dependent tensor-valued coefficient, and $\bar{\boldsymbol{D}}^p$ is the rate of plastic deformation. In the direction of principal plastic stretches, the material characteristics are satisfied by the following components

$$\chi_{ii} = c_1(\theta)(1 - \frac{m}{m_u}), \quad \chi_{ij} = c_2(\theta)(1 - \frac{m}{m_l}), \quad i \neq j = 1, 2, 3 \tag{6.8}$$

where c_1 and c_2 are temperature-dependent positive variables, m_u is the upper and m_l the lower bound of the number of entanglements. Based on (4.22) Tomita and Tanaka (1995) proposed the following relation for the kink number

$$N = \frac{N_A}{4m}. \tag{6.9}$$

Since the molecular weight of the polymer remains unchangeable, the total number of statistical links N_A in the material element is constant, cf. Fig. 4.4. Using $T = 296$ K, the BPA model parameters in Table 6.1 and the relation $C_R = nkT$ in which k is the Bolzmann constant, one obtains $N_A = 6.73 \cdot 10^{27}$ m^{-3} and $m_0 = 7.83 \cdot 10^{26}$ m^{-3}. The additional parameters needed in the model are $m_u = m_0$, $m_l = 0.34 m_0$, $c_1 = 0$ and $c_2 = 0.43 m_0$, cf. Tomita and Tanaka (1995).

Fig. 6.6(a) shows the model responses under homogeneous simple shear deformation. In contrast to the BPA and the EBPA models, the BPA model augmented by the evolution equation (6.7) (termed here the TT-BPA model) is able to accurately capture the experimental data also in large strains, $\gamma > 1.0$. The evolution of the number of chain segments

N during deformation is illustrated in Fig. 6.6(b). The growth of N is almost 170% which, in consistent with (4.22), results in that the number of chains n and entanglements m in a unit volume significantly decrease during the shear deformation, cf. also Arruda *et al.* (1995). As a result of disentanglement, the stiffness of the chain network reduces and the shear stress response shows reduced hardening in the material.

6.2.3 Strain rate dependence

Experimental tests on amorphous polymers indicate their significant sensitivity to strain rate, which appears as increasing yield stress, overall stiffness, compressive strength and increasing strain energy as the strain rate increases. Due to dissipative heating, the strain rate and temperature are coupled under high rates of plastic deformation. Even at the relatively low strain rate $\dot{\epsilon} = 0.1$ 1/s, Arruda and Boyce (1990b) observed a 20 °C temperature rise in compressed PMMA disks in large plastic strains. As a result, softening has two contributions - material strain softening and thermal softening, cf. Arruda *et al.* (1995). Mulliken and Boyce (2006) assumed that the thermal softening in large strains is due to the heat generation in the material, since the plastic part of the strain energy does not have time to transfer to the surroundings but is stored in the material as the deformation rate increases.

Based on the calibrated material parameters, the ability of the EBPA model to capture strain rate dependence of PC and PMMA is evaluated. Both the model results and the experimental data for PC and PMMA at two different strain rates are depicted in Fig. 6.7. Let us first consider the model predictions for PC. Even though the initial elastic stiffness

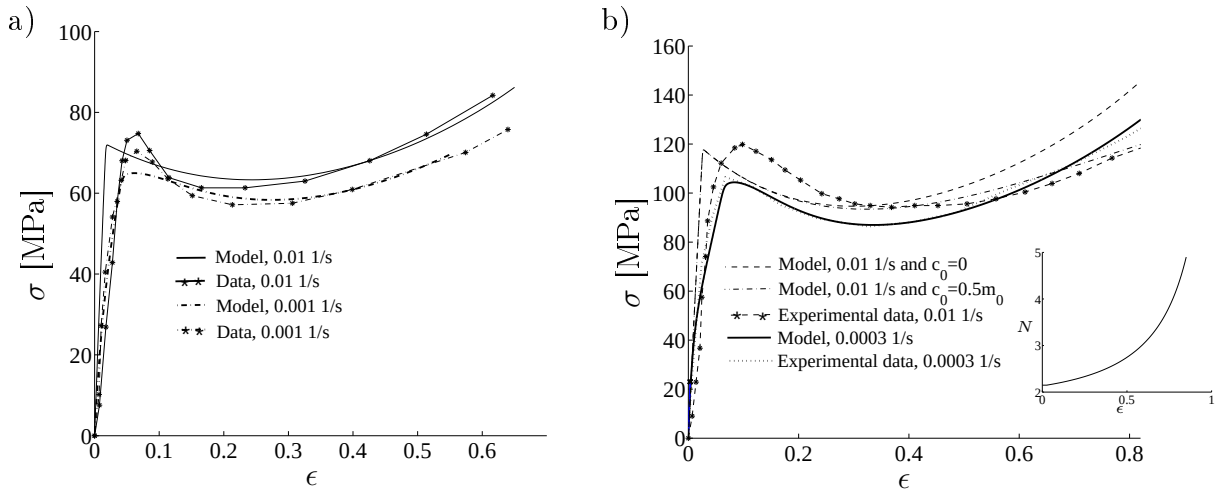

Figure 6.7: Comparison of the experimental and the model responses for a) PC and b) PMMA under uniaxial compression at different strain rates. Experimental data for PC at $\dot{\epsilon} = 0.001 - 0.01$ 1/s is taken from Arruda and Boyce (1993a). Experimental data for PMMA at $\dot{\epsilon} = 0.01$ 1/s is taken from Arruda *et al.* (1995) and at $\dot{\epsilon} = 0.0003$ 1/s data is taken from Anand and Ames (2006). The parameters needed in (6.10) are $m_0 = 1.09 \cdot 10^{27}$, $c_0 = 0.5m_0$, $\beta_c = 100$ s and $\dot{\epsilon}_{ref} = 0.001$ 1/s. The EBPA model parameters for PC and PMMA are listed in Table 6.1 and 6.2, respectively.

corresponding to the strain rate $\dot{\epsilon} = 0.01$ 1/s is overestimated, and as a result the strain at the yield point is underestimated, the experimental response is relatively well captured in the strains greater than 0.1. At the low strain rate $\dot{\epsilon} = 0.001$ 1/s, the experimental data is accurately captured in small strains as well. In contrast to the predictions for PC, the experimental and the EBPA model responses for PMMA are almost inseparable when the low strain rate $\dot{\epsilon} = 0.0003$ 1/s is employed. As the strain rate increases, the EBPA model cannot reproduce the characteristic features of the PMMA-response involving reduced hardening in large strains. In order to capture the hardening behavior in large strains, the following material characteristics are assumed to be of major importance:

- An increased rate of chain extension and chain compression perpendicular to the chain direction increase the number of entanglements.
- The number of entanglements reduces due to an increased rate of chain compression and chain tension perpendicular to the chain direction.

Basically, the above assumptions are satisfied by the evolution equation (6.7). To strengthen the strain rate effect, the parameter c_1 needed for the components in (6.8) is taken to be a linear function of the strain rate, i.e.

$$c_1(\dot{\epsilon}) = c_0(1 + \beta_c(|\pm\dot{\epsilon}| - \dot{\epsilon}_{ref})) > 0 \tag{6.10}$$

where c_0 and β_c are material parameters and $0 < \dot{\epsilon}_{ref} < |\dot{\epsilon}|$ is the reference strain rate. The minus sign for $\dot{\epsilon}$ refers to compression.

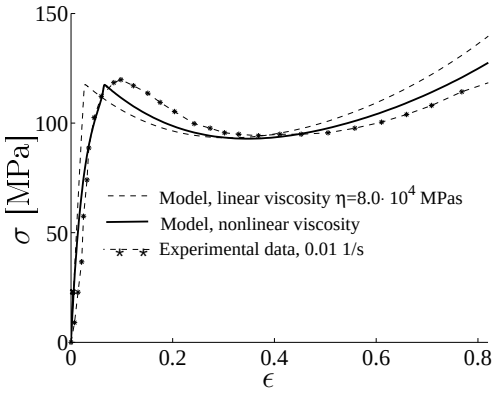

Figure 6.8: Comparison of the experimental and the model responses for PMMA under uniaxial compression at $\dot{\epsilon} = 0.01$ 1/s. Experimental data for PMMA is taken from Arruda *et al.* (1995). The parameters needed in (6.11) are $r = 4.0$, $a = 10,000$ s, $b = 2.6$ and $\eta_0 = 8.0 \cdot 10^4$ MPas.

Since only relatively small strain rate changes are considered in this work, more realistic models that take account of the coupling between temperature and strain rate are of no interest here. Despite this simple description, the model response for $\dot{\epsilon} = 0.01$ 1/s exhibits reduced hardening in large strains, which corresponds well with the experimental result for PMMA, cf. Fig. 6.7(b). In contrast to the convex $\gamma - N$ curve present in Fig. 6.6, the growth of N is described by a concave curvature. Despite the viscoplastic constitutive description, a linear dashpot with a constant η is generally inadequate to represent viscous effects in amorphous polymers under loading rate changes. Based on the work by Bardenhagen *et al.* (1997) and Khan and Zhang (2001), viscosity η is assumed to be a nonlinear function of both the strain and strain rate, i.e.

$$\eta = \epsilon_e^r \frac{\eta_0}{(1 + (a\dot{\epsilon}_e)^2)^b} \tag{6.11}$$

where r, a, b and η_0 are material parameters. In the relation (6.11), the first term ϵ_e^r represents increase in viscosity with increasing elastic strain, while the second term reduces viscosity with the increasing strain rate. This feature has been attributed to the disentanglement, cf. Khan and Zhang (2001). Fig. 6.8 represents the stress response at $\dot{\epsilon} = 0.01$ 1/s as $\epsilon_e := 1 + \ln(v_{11}^e)$ is used in (6.11). Compared to the EBPA model response at $\dot{\epsilon} = 0.01$ 1/s in Fig. 6.7(b), the response of the nonlinear viscosity model shows reduced hardening which is in better agreement with the experiment. Moreover, the model is able to capture the nonlinear initial response prior to the macroscopic yield point well.

6.2.4 Uniaxial compression - non-monotonic loading

In this section, influence of the dwell stress level and duration of the dwell period on the bisphenol A polycarbonate (BPA-PC) is investigated. In addition, the BPA and the EBPA models are evaluated by comparing their results with the experiments on BPA-PC and on PMMA under cyclic loading. Based on the experimental data taken from Dreistadt *et al.* (2009) for BPA-PC, and Anand and Ames (2006) for PMMA, the EBPA model is calibrated by using the least-square fitting. The elastic constitutive parameters for BPA-PC are $E = 3700$ MPa and $\eta = 5.0 \cdot 10^4$ MPas, apart from the PMMA parameters $E = 2700$ MPa and $\eta = 8.0 \cdot 10^4$ MPas. For both the materials, the Poisson's ratio is $\nu = 0.37$ and the stiffness of the intermediate spring is given by $E_1/E = 0.35$, cf. Fig. 6.1. The material parameters resulting from the calibration are given in Table 6.2. For completeness, the BPA model parameters are also given in Table 6.2.

In the first experiment, the specimen is loaded up to the true strain of 0.75 followed by unloading, during which the resulting force is linearly removed. The specimen is then kept unstressed for 400 days. Since the mechanical behavior after the dwell period is not of interest here and the duration of the test prior to dwell is short, the initial age of the specimen can be considered large compared to the test time and thus the aging effects can be neglected, cf. Govaert *et al.* (2000) and Klompen *et al.* (2005). In accordance with the experiments, the strain rate 0.001 s^{-1} is considered in the simulations. In Fig. 6.9(a), the simulated BPA and EBPA responses are compared to the experimental data. As in the

Table 6.2: Constitutive parameters of the BPA and EBPA model for BPA-PC and PMMA. The parameters are obtained from the calibration to the tests performed at room temperature for uniaxial compression, cf. Dreistadt *et al.* (2009) and Anand and Ames (2006).

	E	s_0	s_{ss}	h_1	h_2	$\dot{\gamma}_0$	A	C^R	N	α
BPA-PC	MPa	MPa	MPa	MPa	MPa	s^{-1}	MPa^{-1}K	MPa		
BPA	2300	99	73	370		$2 \cdot 10^{15}$	241	14.0	1.85	0.08
EBPA	3700	100	56.5	205	40	$5.6 \cdot 10^{15}$	241	14.0	2.2	0.08
PMMA	MPa	MPa	MPa	MPa	MPa	s^{-1}	MPa^{-1}K	MPa		
BPA	3700	121	91	300		$5.6 \cdot 10^{15}$	241	14.4	2.45	0.08
EBPA	2700	121	63.3	184	38	$5.6 \cdot 10^{15}$	241	14.0	2.3	0.08

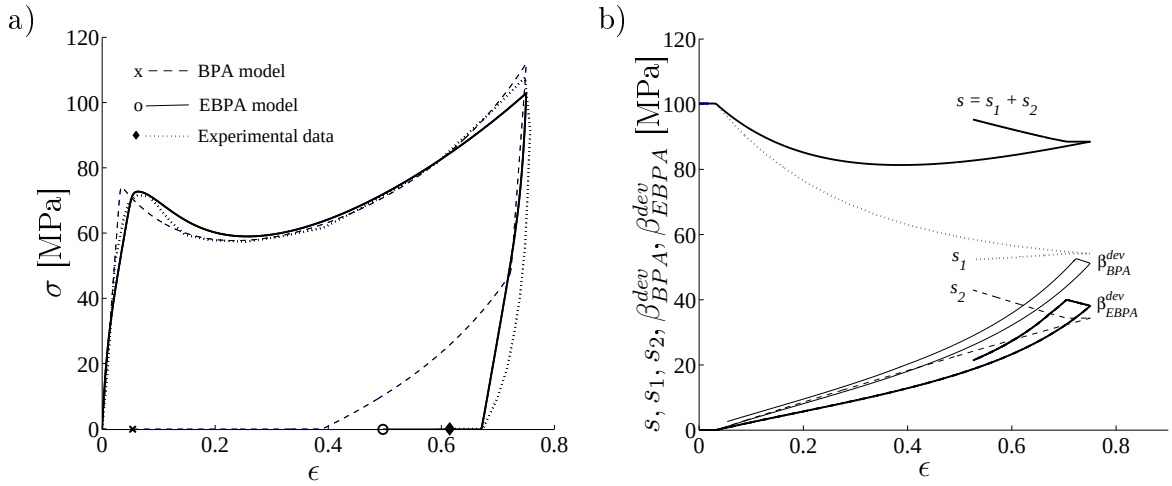

Figure 6.9: a) True stress vs true strain for uniaxial compression of bisphenol A polycarbonate. The experimental data is taken from Dreistadt *et al.* (2009). b) Athermal shear strength s and its components s_1 and s_2 vs true strain according to the EBPA model. β^{dev}_{BPA} and β^{dev}_{EBPA} denote the backstress components in the direction of the applied load.

previous examples, both the BPA and the EBPA model capture the experimental response accurately during monotonic loading. Once unloading is initialized, the experimental response shows more increasing strain than the model results. Later in the unloading phase, the BPA model shows a distinct threshold for reversed plasticity, whereas the EBPA model and the experimental response show a smooth transition, i.e. no distinct Bauchinger effect can be observed. The original BPA model predicts a premature Bauchinger effect which is initiated at 45 MPa, cf. Fig. 6.9(a). At the end of the unloading phase, the EBPA model response is close to the experimental strain 0.66, whereas the original BPA model predicts a strain of 0.39 which indicates the BPA model being incapable of predicting unloading. After a dwell period of 400 days, the permanent strain predicted by the EBPA model is approximately 0.50 whereas the experiment indicates a permanent strain of 0.62. The original BPA model is not able to predict recovery but results in a one-magnitude lower permanent strain of 0.062.

The athermal strength s, its components s_1 and s_2, and the backstress $\boldsymbol{\beta}^{dev}$ as the function of total strain are represented in Fig. 6.9(b). As shown, the new variable s_2, present in the EBPA model, increases along with the plastic deformation, and as a result the backstress is reduced. The maximum backstress prior to unloading is about 30% greater using the BPA model than the EBPA model. As a consequence, the EBPA model results show a lower Bauchinger effect than the BPA model predictions, cf. Fig. 6.9(a). Fig. 6.10(a) presents the model responses subjected to different pre-strains $\epsilon = 0.30$, $\epsilon = 0.45$ and $\epsilon = 0.60$ followed by unloadings to zero stress. The EBPA model predicts nonlinear unloading response, which meets the behavior observed in the experiments, cf. Hasan and Boyce (1995) and Weltevreden (2009). Again, the BPA model predicts a reversed plasticity which initiates at different stress levels depending on the pre-straining. If unloadings are continued past zero stress, it appears that the residual strain and stress are not dependent

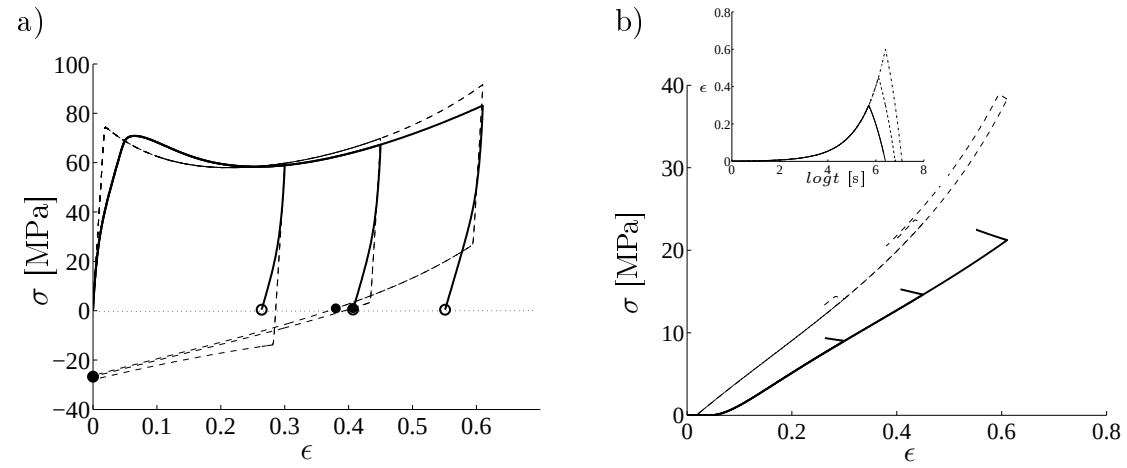

Figure 6.10: a) The BPA and EBPA model curves representing the pre-straining and unloading. b) Evolution of the backstress $\boldsymbol{\beta}^{dev}$. The pre-strains used are $\epsilon = 0.30$, $\epsilon = 0.45$ and $\epsilon = 0.60$. The BPA and EBPA model responses are highlighted by the dashed and solid line, respectively. The inset in b) presents the total strain vs logarithmic time predicted by the BPA model.

on the applied pre-strain, but converge approximately at the strain $\epsilon = 0$ and the tensile stress $\sigma \approx 27$ MPa. A premature Bauchinger effect present in the BPA model results is due to the exaggerated evolution of the backstress, cf. Fig. 6.10(b). In the inset, the total strain vs logarithmic time according to the BPA model is presented, showing relaxation of the strain to be an instantaneous process. However, the experiments as well as the EBPA model results indicate some retardation, cf. e.g. Fig. 6.9.

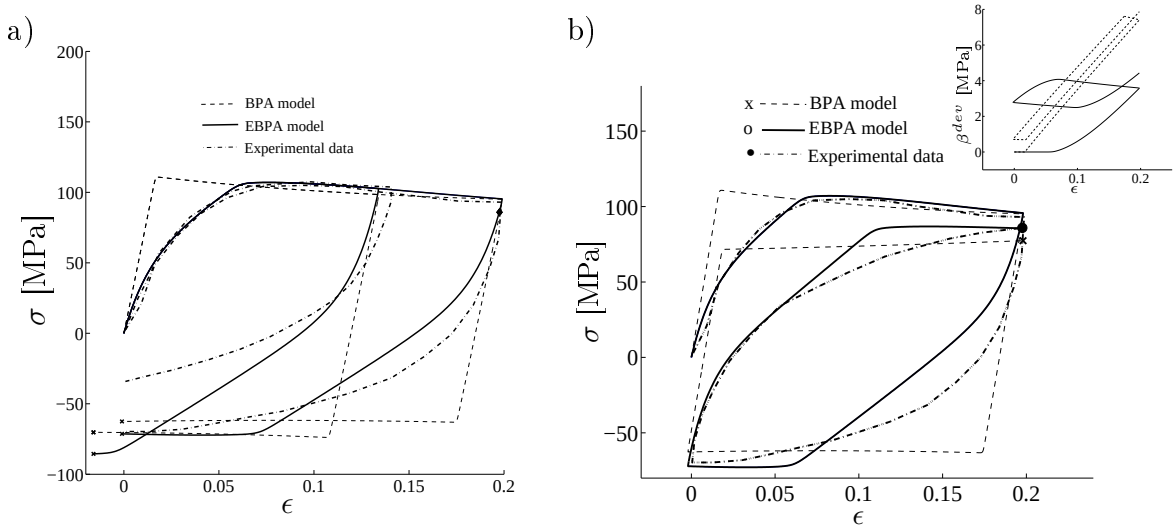

Figure 6.11: Comparison of the BPA and the EBPA model curves in small strains against the experimental data in which the specimen was compressed to strain level of $\epsilon = 0.20$ and then a) unloaded to $\epsilon = 0$ or b) strained via $\epsilon = 0$ to $\epsilon = 0.20$. The inset plot highlights the evolution of the backstress β^{dev}. Responses are calculated using the calibrated material parameters for PMMA. The experimental data is taken from Anand and Ames (2006).

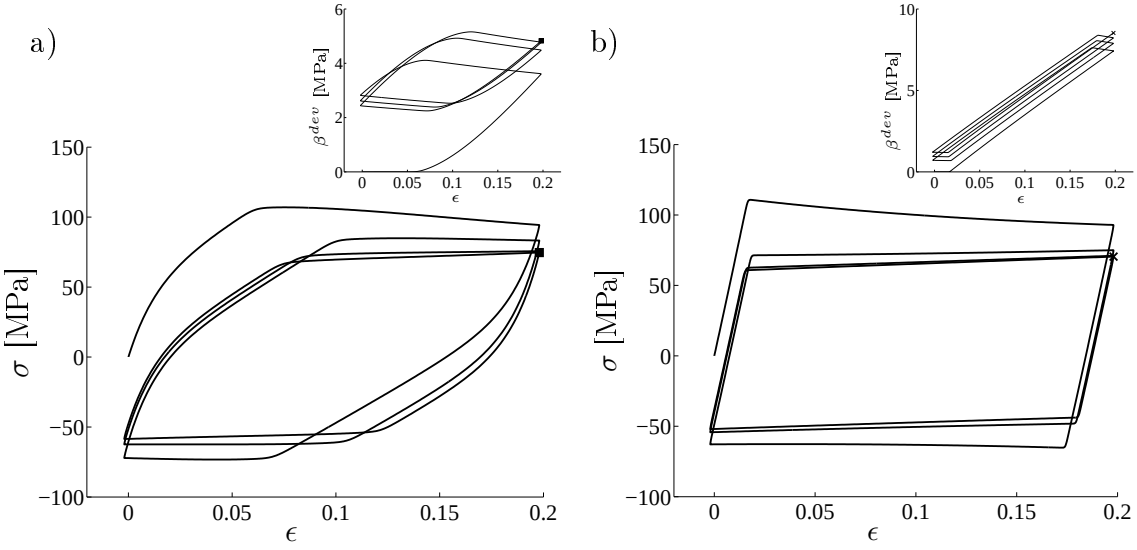

Figure 6.12: a) The EBPA and b) the BPA model responses under cyclic loading. The inset plots show the evolution of the backstress β^{dev}. Responses are calculated using the calibrated material parameters for PMMA, cf. Table 6.2.

Anand and Ames (2006) conducted uniaxial compression tests on PMMA involving both a single unloading and cyclic loadings, in which the specimen was pre-strained up to the two different limits 13.5% and 19.9%. Both the BPA and the EBPA model responses and the experimental data are shown in Fig. 6.11. Even if the EBPA model underestimates the stress at strains below 0.1 during the unloading phases, it does capture the loading phases as well as the initial unloading accurately. Due to the linear elastic constitutive description, the BPA model cannot satisfactorily reproduce experimental response during either loading or unloading.

Fig. 6.11(b) also shows the evolution of the backstress according to the models. Compared to the EBPA model result (solid line), the BPA model predicts significantly greater backstress during the loading phase, which then rapidly decreases during subsequent unloading. As a consequence, the BPA model predicts almost linear response both during initial unloading and initial reloading, followed by continued deformation at almost constant stress. In contrast to a purely elastic deformation, viscoplastic deformation results in a loss (dissipation) of mechanical energy which is equal to the area of the hysteresis loop through a loading cycle. It can be observed from Fig. 6.11(b) that the BPA model predicts much greater dissipation than the EBPA model. Moreover, the models show the Bauchinger effect which stabilizes during few cycles led to the saturated state of hardening, cf. Fig. 6.12. Since the influence of isotropic hardening in the EBPA model is small in this strain regime, cf. Fig. 6.9(b), both the model results and the amount of dissipation only deviate because of the different elastic constitutive descriptions.

Arruda *et al.* (1995) conducted experiments on PMMA in which a specimen was subjected to uniaxial compression up to the strain $\epsilon = 0.890$, then unloaded and finally kept unstressed until the two strain values $\epsilon = 0.659$ or $\epsilon = 0.832$ were reached. In order to reveal an anisotropic state of the material, the specimen was reloaded at the same strain rate

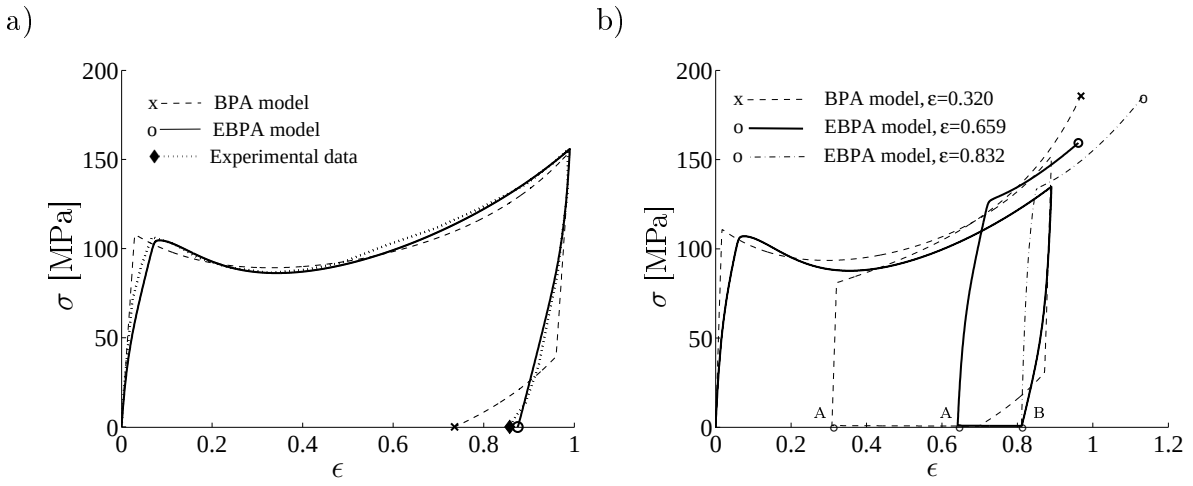

Figure 6.13: a) Comparison of the BPA and the EBPA model responses for PMMA under monotonic loading and subsequent unloading to zero stress. The experiment, performed at a constant strain rate $\dot{\epsilon} = 0.0003\,s^{-1}$, is taken from Anand and Ames (2006). b) Comparison of the model responses for PMMA: the anisotropic responses result from loading of an initially isotropic specimen followed by unloading and a dwell period at zero stress. The tests are performed at constant strain rate $\dot{\epsilon} = 0.001\,s^{-1}$ at room temperature, cf. Arruda *et al.* (1995). The positions A and B indicate the strains after the two different dwell periods.

and test temperature of its initial condition. In large strains, polymer chains must undergo a significant reorientation which is primarily retained upon unloading. As a consequence, reloading reveals anisotropy of the material which is manifested as increased hardening once the yield point is reached. Figs. 6.13 and 6.14(a) show the BPA and EBPA models' capability to predict the orientation-induced hardening behavior of PMMA. In contrast to the EBPA model, which captures monotonic loading, unloading and reloading followed by the prescribed dwell period well, the BPA model overestimates recovery during the dwell period and results in a premature Bauchinger effect which is initialized at $\sigma = 30$ MPa.

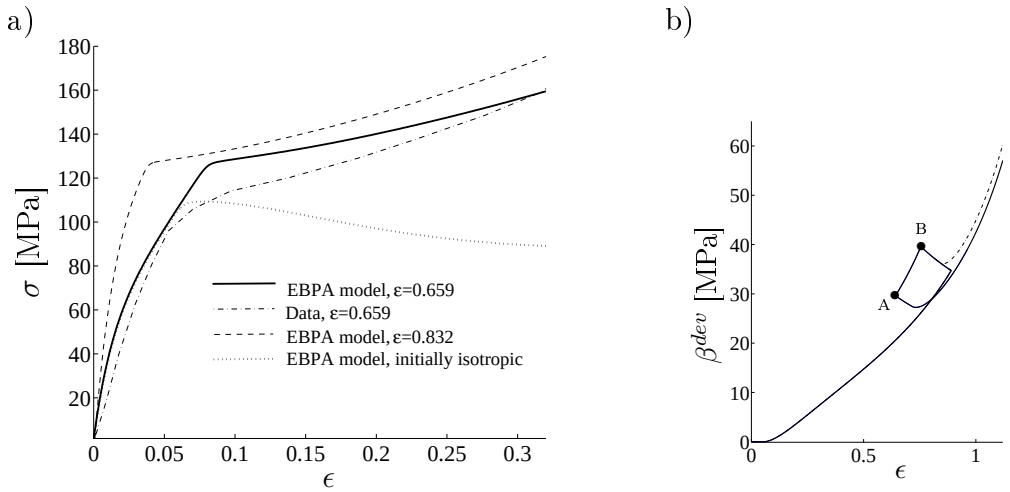

Figure 6.14: a) Uniaxial isotropic response and anisotropic responses resulting from the two different deformation histories depicted in Fig. 6.13(b) as the origin of reloading is set to $\epsilon = 0$. b) Evolution of the backstress during the deformation. The backstress responses at the end of the dwell periods are depicted by the letters A and B.

Fig. 6.14(a) represents the anisotropic response resulting from the deformation history as the origin of the reloading is set to $\epsilon = 0$. Upon reloading, the EBPA model results, which are followed by vastly different strain histories, exhibit very similar anisotropic responses being in good agreement with the experimental response.

Arruda *et al.* (1995) conducted birefringence measurements on PMMA that indicated that the same orientation state exists in each tests specimen and the resulting anisotropic response is virtually unaffected by the strain history. They showed that the different strain histories that resulted in equal backstresses, influence very similar subsequent anisotropic response. It also appears from Fig. 6.14(b) that the backstress responses evolving from the positions A and B are almost the same shape and therefore the EBPA model results in almost identical anisotropic stress-strain responses upon reloading from zero stress. Based on experimental observations, Hasan *et al.* (1993) and Melick *et al.* (2003) concluded that the mechanical history only influences the yield stress, whereas the subsequent state can be regarded as independent of any prior history. It can be concluded that the proposed EBPA model satisfactorily captures not only the mechanical behavior of an initially isotropic material but also the behavior of subsequent response in a pre-oriented material.

Dreistadt *et al.* (2009) also conducted uniaxial compression tests for repeated unloadings where the specimen was unloaded at five progressively increasing strain levels: $\epsilon = 0.05$, 0.13, 0.27, 0.45, and 0.59. After each unloading, the specimen was kept at a fixed nominal stress level during a prescribed dwell period. Here, two different stress levels are examined: $\pi = 59$ MPa and $\pi = 1.2$ MPa for the dwell time of 12,000 s. After the dwell period, the specimen is reloaded until the next unloading level is reached. The final unloading is performed to zero stress.

Let us first consider the stress-strain response for $\pi = 59$ MPa, cf. Fig. 6.15(a)-(b). During the first two dwell periods, exaggerated creep is predicted by the BPA model. Contrary to the experimental response, the predicted strain at the end of the second dwell period is close to the unloading strain value of the third cycle. Note, that the influence of the new variable s_2, present in the EBPA model, is small in this phase and therefore the models deviate only due to the different elastic constitutive description. It also appears from the simulations that neither the original nor the extended model can reproduce the stress peak during reloading but tend towards the monotonic loading path.

Next, let us consider the low dwell stress, $\pi = 1.2$ MPa. A comparison of Figs. 6.15(a)-(b) and 6.15(c)-(d) reveals that creep is progressively replaced by recovery when the dwell stress decreases. Even though the EBPA model overpredicts the recovery during the first cycle, it is superior to the BPA model during the next two cycles when the BPA model predicts almost elastic response. Moreover, the BPA model strongly overestimates the long-term recovery during the fourth cycle, whereas the EBPA model and the experimental response can be regarded as almost indistinguishable. As with the single unloading, the BPA model predicts a premature Bauchinger effect during the last unloading and as a result, the true strain is strongly underestimated at the end of the unloading phase, cf. Figs. 6.15(a) and 6.15(c).

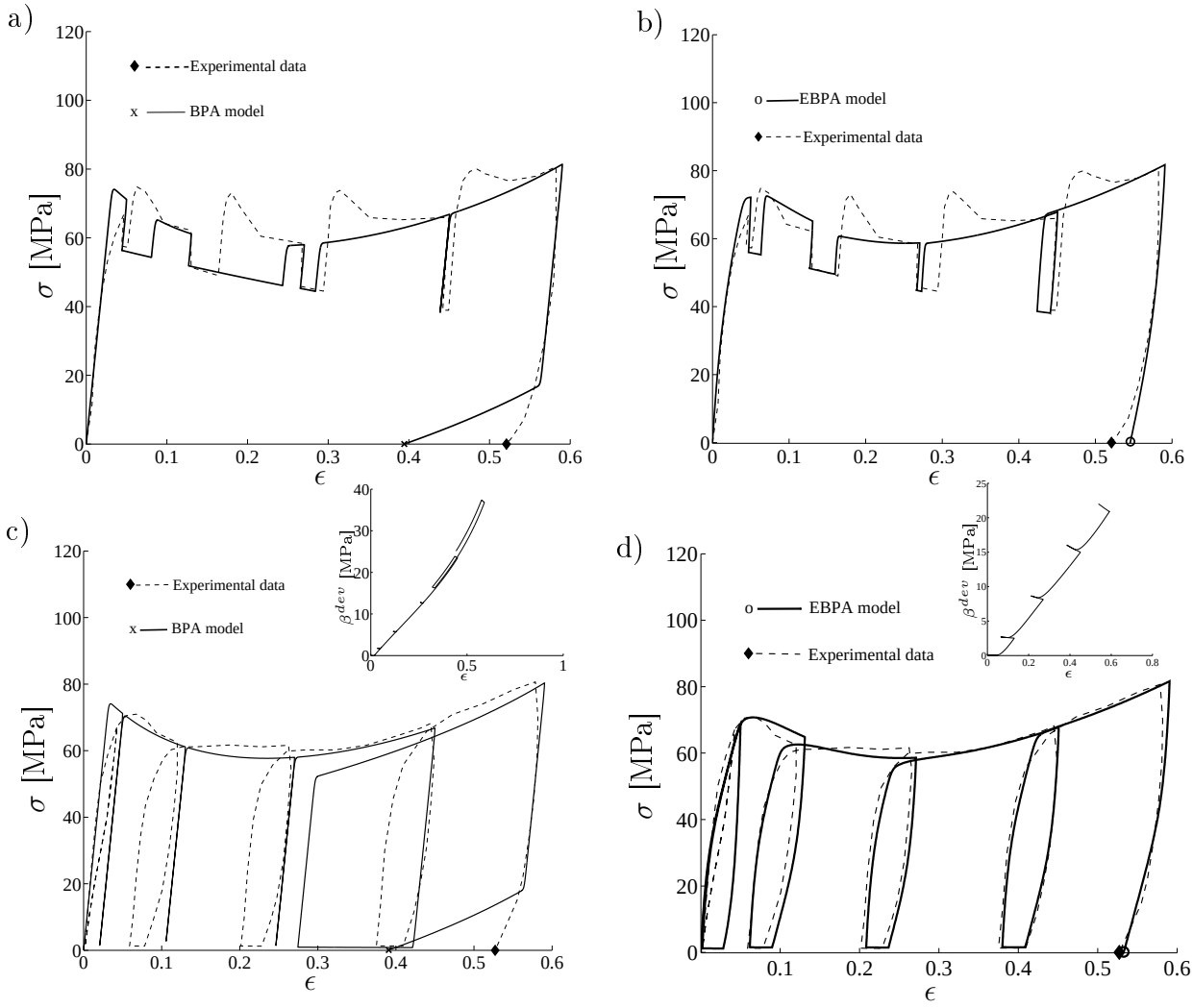

Figure 6.15: Uniaxial compression responses for BPA-PC according to the BPA and the EBPA model. The repeated unloadings are performed to $\pi = 59$ MPa a)-b) and $\pi = 1.2$ MPa c)-d). Experimental data is taken from Dreistadt *et al.* (2009).

The insets in Figs. 6.15(c) and (d) show the evolution of the backstress according to the BPA model and the EBPA model, respectively. The values of the backstress prior to the two last unloadings are much higher predicted by the BPA model than by the EBPA model. As a result, the BPA model predicts an excessive recovery or a premature Bauchinger effect during the subsequent dwell period or during the last unloading. Unlike the EBPA model, which predicts nearly similar repeated cycles, the BPA model response shows a marked drop in the backstress during the fourth dwell period as well as during the last unloading. Consequently, the BPA model result shows almost linear stress response upon subsequent reloading from zero stress.

7 Investigations on inhomogeneous deformation state

7.1 Algorithmic setting of the EBPA model

In order to use the original BPA model and the proposed EBPA model for the simulations of inhomogeneous deformation, they are implemented in the finite element method. Since long-term behavior will be investigated, the proposed algorithm is based on a fully implicit backward Euler method which allows large time steps to be used. Similar to the BPA model, the elastic rotation $\boldsymbol{R}^e$ in the EBPA model is chosen to be unity and consequently the plastic spin $\bar{\boldsymbol{W}}^p$ is nonzero. The plastic spin is numerically solved by introducing a skew-symmetric algorithmic plastic spin $\tilde{\boldsymbol{W}}^p$ which is determined so that the elastic part of the deformation gradient $\boldsymbol{F}^e$ is symmetric at the end of the integration interval, cf. Holopainen and Wallin (2012). To specify the orientation of the elastic intermediate configuration, the first component $\boldsymbol{F}_1^e$ in the decomposition (6.4) is chosen to be symmetric. For the sake of simplicity, the quantities at the known state t_n are indicated by the subscript n whereas the subscript $n+1$ for the updated state is omitted. In accordance with Weber and Anand (1990), the exponential update is applied to the plastic part of the deformation gradient $\boldsymbol{F}^p$, i.e.

$$\boldsymbol{F}^p = \exp(\Delta t \bar{\boldsymbol{L}}^p)\boldsymbol{F}_n^p. \tag{7.1}$$

A glance at (4.16) and (4.109) reveals that the exponential update (7.1) preserves the plastic incompressibility, i.e. $det(\boldsymbol{F}^p) = 1$. The tensor exponent is calculated by using the Pade approximation, cf. Steinmann and Stein (1996). Using (7.1) in (4.3), results in

$$\boldsymbol{F}^e = \boldsymbol{F}\boldsymbol{F}^{p-1} = \boldsymbol{F}\boldsymbol{F}_n^{p-1}\exp(-\Delta t \bar{\boldsymbol{L}}^p). \tag{7.2}$$

As with the homogeneous deformation, the viscous damping is described by a scalar targeted to the one part of the elastic stretch, $\boldsymbol{v}_2^e$. Based on the stress equilibrium (6.6), the strain rate evaluates according to

$$\frac{d}{dt}\big(\ln \boldsymbol{v}_2^e\big) = \frac{1}{\eta}(\boldsymbol{\mathcal{L}}^e(E) : \ln \boldsymbol{v}_1^e - \boldsymbol{\mathcal{L}}^e(E_1) : \ln \boldsymbol{v}_2^e). \tag{7.3}$$

In all, the non-linear system of the residuals is given by

$$\begin{aligned}
\boldsymbol{R}_1 &:= \boldsymbol{F}^e - \boldsymbol{F}\boldsymbol{F}_n^{p-1}\exp\Big(-\Delta t(\bar{\boldsymbol{D}}^p + \tilde{\boldsymbol{W}}^p)\Big),\\
\boldsymbol{R}_2 &:= \boldsymbol{F}^{e,T} - \boldsymbol{F}^e,\\
\boldsymbol{R}_3 &:= \tilde{\boldsymbol{W}}^{p,T} + \tilde{\boldsymbol{W}}^p,\\
\boldsymbol{R}_4 &:= \boldsymbol{F}_1^{e,T} - \boldsymbol{F}_1^e,\\
\boldsymbol{R}_5 &:= (\boldsymbol{\mathcal{I}} + \frac{\Delta t}{\eta}\boldsymbol{\mathcal{L}}^e(E_1)) : \ln \boldsymbol{v}_2^e - \frac{\Delta t}{\eta}\boldsymbol{\mathcal{L}}^e(E) : \ln \boldsymbol{v}_1^e - \ln \boldsymbol{v}_{2,n}^e,\\
R_6 &:= (s_1 - s_{1,n} - \dot{s}_1\Delta t)/s_{ss},\\
R_7 &:= (s_2 - s_{2,n} - \dot{s}_2\Delta t)/s_{ss}
\end{aligned} \tag{7.4}$$

where the parameter s_{ss} was defined in $(6.2)_1$. It should be mentioned that the nonlinear residuals $\boldsymbol{R}_4$, $\boldsymbol{R}_5$ and R_7 are omitted in the original BPA model. Note also, that the residuals $\boldsymbol{R}_2$ and $\boldsymbol{R}_4$ consist of three and the residuals $\boldsymbol{R}_3$ and $\boldsymbol{R}_5$ of six linearly independent equations. Compared to the other approaches referred in this thesis, stress rates which need a specific treatment involving e.g. objectivity, do not explicitly appear in the proposed numerical algorithm. The nonlinear system (7.4) is solved using the Newton-Raphson method, i.e. $\boldsymbol{Y}^{i+1} = \boldsymbol{Y}^i + \Delta\boldsymbol{Y}$ where $\boldsymbol{Y} := [\boldsymbol{F}^e \ \tilde{\boldsymbol{W}}^p \ \boldsymbol{F}^e_1 \ s_1 \ s_2]$ is the vectorized form of the state variables. The increment of the internal variables is given by

$$\Delta\boldsymbol{Y} = -\boldsymbol{J}^{-1}\boldsymbol{R}, \quad \text{where} \quad \boldsymbol{J} := \frac{\partial \boldsymbol{R}}{\partial \boldsymbol{Y}} \tag{7.5}$$

is the Jacobian and $\boldsymbol{R} := [\boldsymbol{R}_1 \ \boldsymbol{R}_2 \ \boldsymbol{R}_3 \ \boldsymbol{R}_4 \ \boldsymbol{R}_5 \ R_6 \ R_7]$ is the vectorized form of the residuals. For convenience, the steps of the numerical integration algorithm for updating the internal variables are summarized in Table 7.1. Linearization of the stress-strain relation needed in an implicit finite element solution procedure is discussed in Miehe (1998), Stein and Sagar (2008), Holopainen and Wallin (2012) and Holopainen (2012). The performance of the proposed integration scheme and the algorithmic tangent stiffness (ATS) tensor that enters the linearization of the equilibrium equations was evaluated during simulations. The equilibrium state was typically found within 3-5 iterations.

Table 7.1: Algorithmic update of internal variables based on the multiplicative decomposition of the deformation gradient.

1. Load data: $\boldsymbol{F}$, $\boldsymbol{Y}_n := [\boldsymbol{F}^e_n \ \tilde{\boldsymbol{W}}^p_n \ \boldsymbol{F}^e_{1,n} \ s_{1,n} \ s_{2,n}]$.
2. Set $k = 0$ and initialize $\boldsymbol{F}^p|_{k=0} = \boldsymbol{F}^{e-1}_n \boldsymbol{F}$, $\boldsymbol{F}^e_2|_{k=0} = \boldsymbol{F}^{e-1}_{1,n} \boldsymbol{F}^e_n$.
3. Implicit update of the internal variables:
   `WHILE` $\|\boldsymbol{R}\| >$ tol
   (i) Compute $\boldsymbol{\tau}$ by (6.6) and $\boldsymbol{\beta}$ by (4.110).
   (ii) Compute $\dot{\gamma}^p$ by (4.75) and $\bar{\boldsymbol{D}}^p$ by (4.109).
   (iii) Compute the residuals $\boldsymbol{R}$ according to (7.4).
   (iv) Compute the Jacobian $J := \partial\boldsymbol{R}/\partial\boldsymbol{Y}$.
   (v) Update internal variables, $\boldsymbol{Y} \leftarrow \boldsymbol{Y}_n + \Delta\boldsymbol{Y}$ by (7.5) and set $k \leftarrow k + 1$.
   `END WHILE LOOP`
4. Store updated variables $\boldsymbol{Y} := [\boldsymbol{F}^e \ \tilde{\boldsymbol{W}}^p \ \boldsymbol{F}^e_1 \ s_1 \ s_2]$ and proceed to the equilibrium iteration for $\boldsymbol{F}$.

7.2 Comparison of the BPA and EBPA model predictions for long-term behavior

In the subsequent examples, the ability of the proposed model to predict intrinsic material behavior as well as inhomogeneous, localized deformation on amorphous glassy polymers is investigated. In the first example, the BPA model and the EBPA model are compared. A tapered sheet is subjected to tension followed by bending, then unloaded and finally relaxed for two months, cf. Fig. 7.1. The boundary at $y = 0$ is clamped and the displacement at $y = L$ is prescribed during tension and subsequent bending. After these two loading phases, the displacements $u_x/L = 0.2$ and $u_y/L = 0.2$ are reached and then the resulting force f is linearly removed during 60 s. The constitutive parameters used in the simulations are given in Table 6.2.

The initial geometry and the deformed meshes are shown in Fig. 7.1. The three stages of deformation correspond to: the end of the second displacement controlled phase, the end of unloading and the end of the dwell period. At each stage, a contour plot of the plastic stretch $\bar{\lambda}^p_{ec}$, defined by (4.105), illustrates the localization phenomenon. After the loading phase, the plastic deformation is clearly localized and the localized region remains almost constant during continued deformation. To highlight the difference between the model predictions after long-term dwell, the deformed meshes predicted by both the BPA and the EBPA model are shown in Fig. 7.1(d). In contrast to the EBPA model result, the initial shape of the specimen is almost recovered during the dwell period with the BPA model.

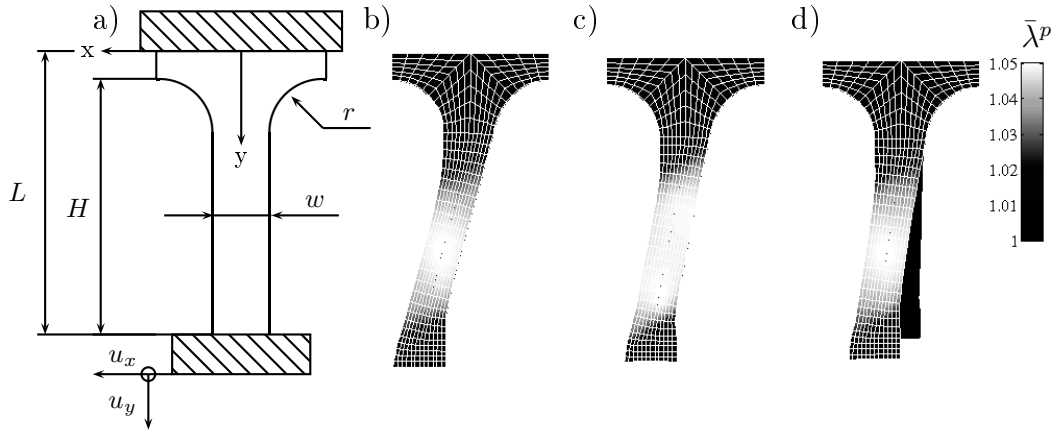

Figure 7.1: a) The geometry of the BPA-PC specimen subjected to combined tension and bending. The geometry is governed by $w/L = 1/5$, $r/L = 1/5$ and $H/L = 9/10$. Visualization of the plastic stretch $\bar{\lambda}^p_{ec}$ in the deformed meshes at the end of b) loading (by EBPA), c) unloading (by EBPA), and d) dwell period of two months (by both the BPA and EBPA model). The element mesh consists of 450 mixed 4-node plane elements.

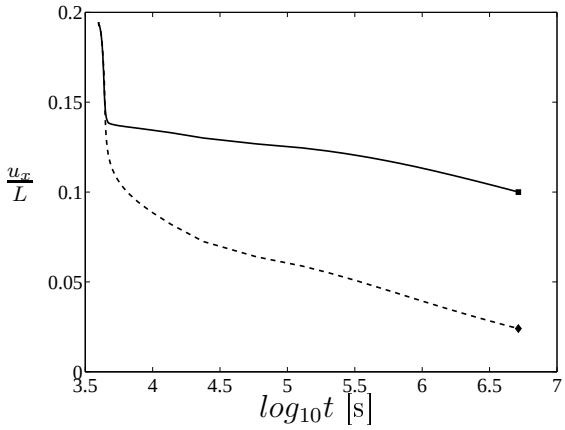

Figure 7.2: The displacement component u_x vs time during unloading and the dwell period of two months. The solid and dashed lines present the EBPA and BPA responses, respectively. The markers ■ and ♦ indicate the final positions.

In Fig. 7.2, the simulated displacement component u_x versus the time is presented. During unloading, the model predictions are very similar albeit a slight deviation can be observed at the end of the unloading phase. The predicted displacement at the end of unloading is approximately $u_x/L = 0.125$ with the BPA model and $u_x/L = 0.137$ with the EBPA model. After the dwell period, the simulated displacement is $u_x/L = 0.022$ according to the BPA model which is well below the EBPA model result, $u_x/L = 0.100$, cf. also Fig. 7.1(d). Based on the discussion in Sec. 6.1, we conclude that the amount of isotropic hardening in relation to the amount of kinematic hardening is of major importance when modeling recovery.

7.3 Evaluation of shear band propagation in a thin sheet

In this example, influence of the intrinsic material behavior, boundary conditions and initial imperfection on the initiation and the propagation of shear bands along a parallel-piped solid are investigated. It will be shown that the material parameters which are suitable for modeling homogeneous deformation behavior cannot be used to predict typical S-shaped response under inhomogeneous deformation. The specimen with the initial length $2L$ and initial width $2w$ subjected to the simple shear deformation is shown in Fig. 7.3. The initial geometry is given by the ratio $L/w = 7.5$. Variations in the thickness are only significant to second order terms in strain, and thus plane strain condition can be assumed to prevail. As the first attempt, a relatively coarse mesh consisting of 6×42 4-node plane elements is employed. The boundary at $y = 0$ is clamped and the displacement on the boundary $y = 2w$ is prescribed by the constant deformation rates $\dot{u}_x/2w = 7.5 \cdot 10^{-3}\ s^{-1}$ and $\dot{u}_y = 0$. During the loading phase, the resulting forces f_x and f_y at $y = 2w$ are monitored. In order to trigger the initiation of a macroscopic shear band propagation due to some inhomogeneity in the material, an initial imperfection of the shear strength s_0 of the form

$$\Delta s_1 = \xi s_0 \exp\left[-\frac{(x-L)^2 + (L/w)^2(y-w)^2}{0.01(L^2 - w^2)}\right] \tag{7.6}$$

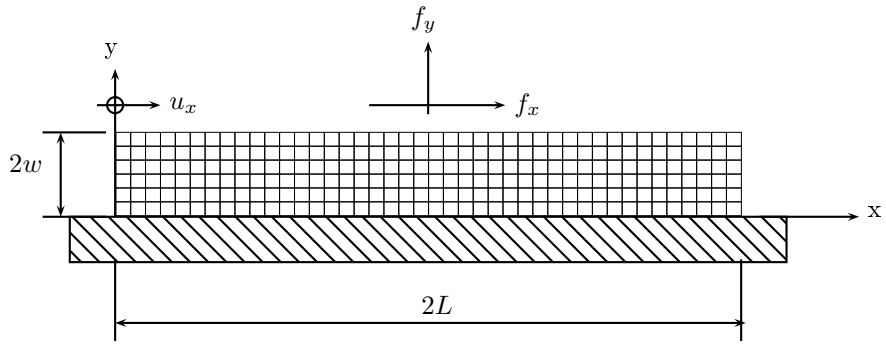

Figure 7.3: The geometry and finite element mesh of the rectangular specimen subjected to the plane strain simple shear. The geometry is given by $L/w = 7.5$.

is employed. In (7.6), ξ determines the intensity of the imperfection. Hence, the initial shear strength is $s_0 - \Delta s_1$.

The EBPA model response based on the material parameters given in Table 6.1 is shown in Fig. 7.4(a). The overall response of the specimen is presented in terms of the shear stress, the normal stress and the applied shear strain which are defined by $\tau := f_x/(2L)$, $\sigma := f_y/(2L)$ and $\gamma := u_x/(2w)$, respectively. Once the shear stress maximum is reached, a marked drop in the shear stress and a rise in the normal stress can be observed. It can be assumed that these responses do not represent real material behavior. The model which can capture mechanical behavior of amorphous glassy polymers under different homogeneous deformation states collapses as the same parameter values are applied to inhomogeneous deformation. So, next the ability of the localization phenomena and the boundary effects to explain this discrepancy is investigated.

Since experimental results for the plane strain simple shear are not available, the EBPA model is calibrated to the experimental data for homogeneous shear deformation. The parameters obtained from the calibration are listed in Table 7.2.

Based on the parameters given in Tables 6.1 and 7.2 the initial and the recalibrated EBPA model response are depicted in Fig. 7.4(a). Even if the model responses deviate from the experimental data in the initial, viscoelastic region, the calibrated model captures

Table 7.2: The values of the EBPA model parameters. Calibration of the EBPA model is based on the experiments for simple shear given in G'Sell and Gopez (1985).

E	η	s_0	s_{ss}	h_1	h_2	$\dot{\gamma}_0$	A	C^R	N	α
MPa	MPa	MPa	MPa	MPa	MPa	s^{-1}	$\text{MPa}^{-1}K$	MPa		
2600	$1.5 \cdot 10^5$	96	76	720	38	$5.6 \cdot 10^{15}$	240	13.8	2.22	0.08

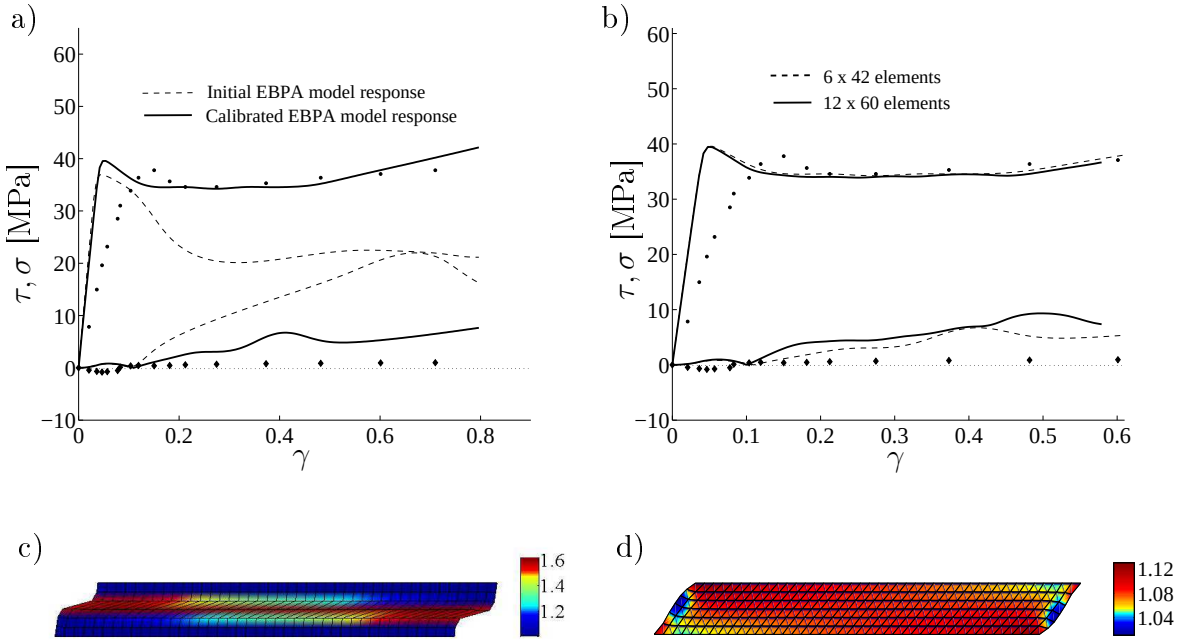

Figure 7.4: a) The initial and calibrated stress responses under the plane strain simple shear. b) The influence of the mesh on the predicted shear and the normal stress response. Experimental data points of the shear and normal stress under homogeneous deformation are depicted by the markers "•" and "⧫", respectively. Experimental data is taken from Wu and Van der Giessen (1994). Based on c) the initial and d) the calibrated parameters, the deformed meshes at $u_x/(2w) = 0.80$ are visualized by the plastic stretch $\bar{\lambda}^p_{ec}$, defined by (4.105).

experimental data in large strains fairly well. Since the material response according to the EBPA model is intrinsically rate-dependent, the mesh sensitivity can be assumed to be small, cf. Needleman (1988). Fig. 7.4(b) shows the simulated responses under plane strain simple shear for two different regular meshes consisting of 6×42 and 12×60 4-node plane elements. As shown, the shear stress responses are virtually indistinguishable and the difference between the normal stress responses can also be considered as relatively small. However, the coarse mesh depicted in Figs. 7.4(c-d) is not fine enough to satisfactorily present neither the shear band propagation nor the thickness of the shear band. In order to resolve these matters, the mesh consisting of 12×60 elements will be used in subsequent considerations.

Fig. 7.5(a) compares the EBPA model and the original BPA response, which is based on the parameters given in Table 6.1. Opposite to the compression responses, the difference of the initial shear responses between the models is shown to be small. The model results are almost identical in small strains up to 0.06 but they differ considerably from the experimental response. As was shown in Fig. 6.9(b), the influence of the shear strength s_2 in the EBPA model is negligible in this phase and thus the BPA and the EBPA models only deviate because of the different elastic constitutive descriptions, cf. (4.113) and (6.6), respectively. It can be assumed that the difference between the model predictions and the experimental data is due to the initiation of fine shear bands already in an early stage of localization.

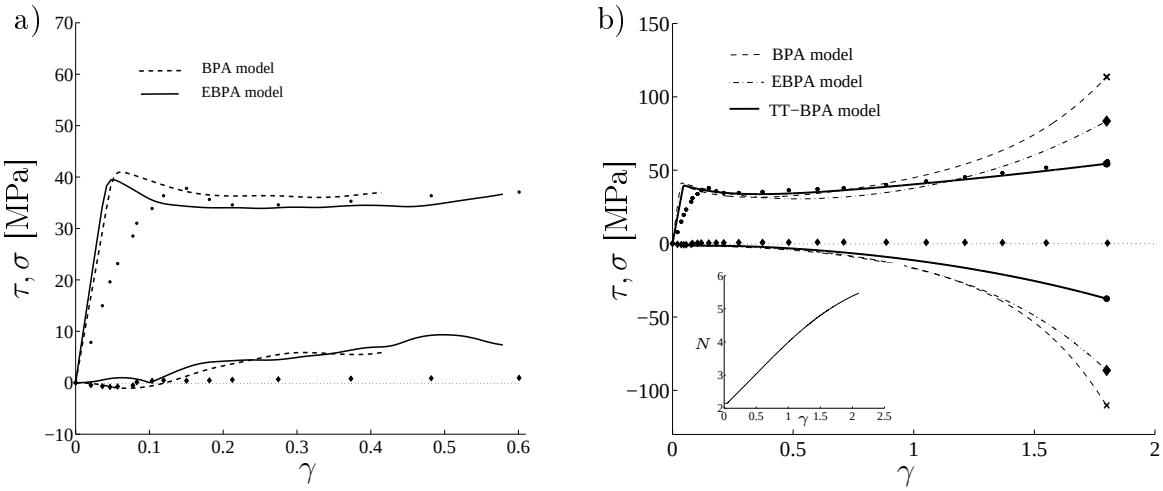

Figure 7.5: a) Comparison of the BPA and the EBPA model responses under the plane strain simple shear. b) Comparison of the BPA, EBPA and TT-BPA model responses for homogeneous simple shear deformation and evolution of N during deformation based on the evolution equation (6.7). Experimental data points of the shear and the normal stress are depicted by the markers "•" and "⧫", respectively. Experimental data is taken from Wu and Van der Giessen (1994).

Apart from the initial response, both the models capture the experimental large strain response relatively well; the BPA model gives the upper bound and the EBPA model the lower bound, cf. Fig. 7.5(a). The differences between the model predictions in the normal stress are larger than those in the shear stress. In strains greater than 0.1, the models predict increasing tension whereas the experimental normal stress response shows almost zero stress. Moreover, the normal stress responses under homogeneous shear deformation show increasing compression opposite to the plane strain simple shear, cf. Fig. 7.5(b).

The deformed meshes are depicted in Fig. 7.6. The three stages of deformation correspond to: $u_x/2w = 0.15$, $u_x/2w = 0.38$ and $u_x/2w = 0.60$. The first two stages are visualized by a contour plot of the plastic stretch, $\bar{\lambda}^p_{ec}$. The localization of the plastic deformation is initialized at the center of the specimen and it widens in the direction perpendicular to the shear direction. A glance at Fig. 7.4 reveals that the shear stress drops owing to the intrinsic softening once the shear band is initialized. During continued deformation, the localized zone rapidly expands towards the free edges. In addition to the continuous zone, small localized regions can be observed around the corners of the specimen. In order to clearly show the expected propagation of shear bands at large strains, the deformed mesh is visualized by the normalized plastic shear strain γ^p/Γ^p in which $\Gamma^p := \gamma - f_x/(2L\mu)$ and μ is the shear modulus. At $u_x/2w = 0.60$, the shear band pattern consists of criss-crossing paths which diagonally expand from the corners towards the center of the specimen.

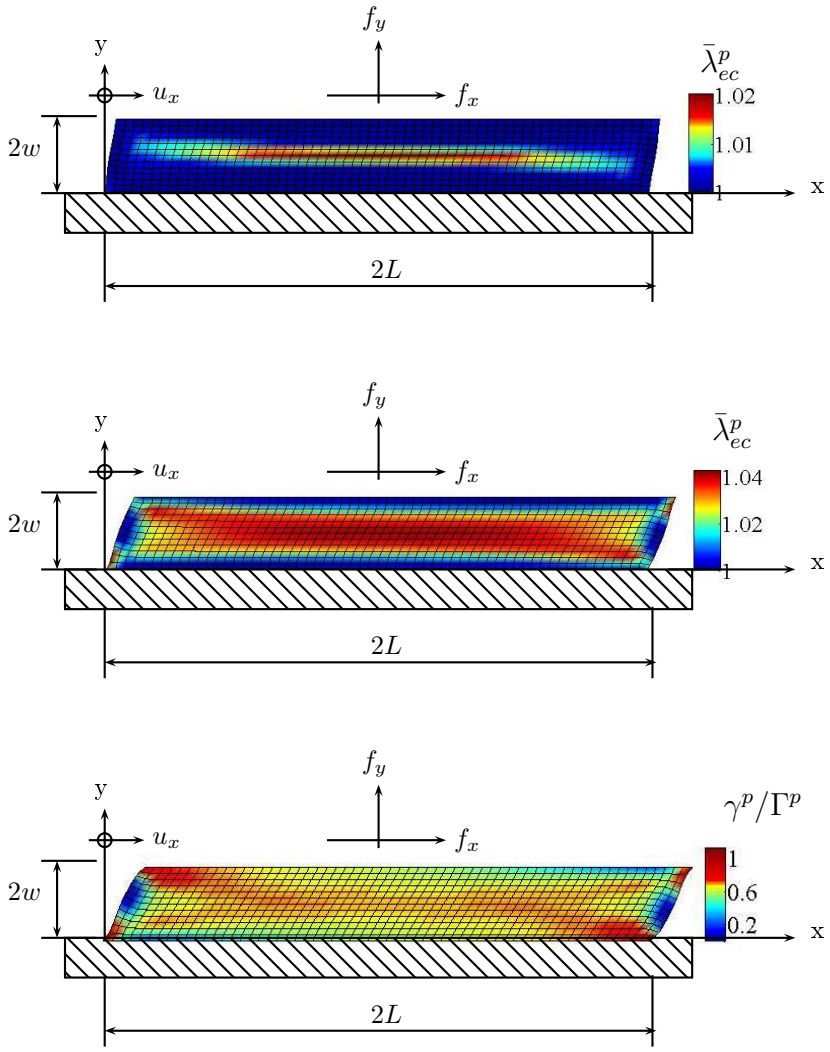

Figure 7.6: The geometry of the specimen subjected to the plane strain simple shear. The deformed meshes at $u_x/(2w) = 0.15$ and $u_x/(2w) = 0.38$ are visualized by the plastic stretch $\bar{\lambda}^p_{ec}$, whereas the normalized plastic shear strain γ^p/Γ^p is chosen to illustrate the shear band propagation at $u_x/(2w) = 0.60$. The intensity of the initial imperfection is $\xi = 0.01$.

7.3.1 Edge effects and influence of the entanglements

During deformation, the free edges become curved with an S-shaped or a convex curvature, cf. Fig. 7.4(c-d). Comparisons of the responses in Fig. 7.4(a) and the deformed shapes in Figs. 7.4(c-d) reveal that the softening in the material is to some extent due to the deformation of the boundaries. Wu and Van der Giessen (1994) investigated boundary effects in simple shear deformation by increasing the ratio L/w. According to their observations, in the specimen having infinite length, the absence of free edges led to a marked reduction of the deformation inhomogeneity and to the loss of shear band propagation in the shear direction. To evaluate the edge effects, the stress responses for homogeneous simple shear deformation are also presented in Fig. 7.5(b). In accordance with the experimental data

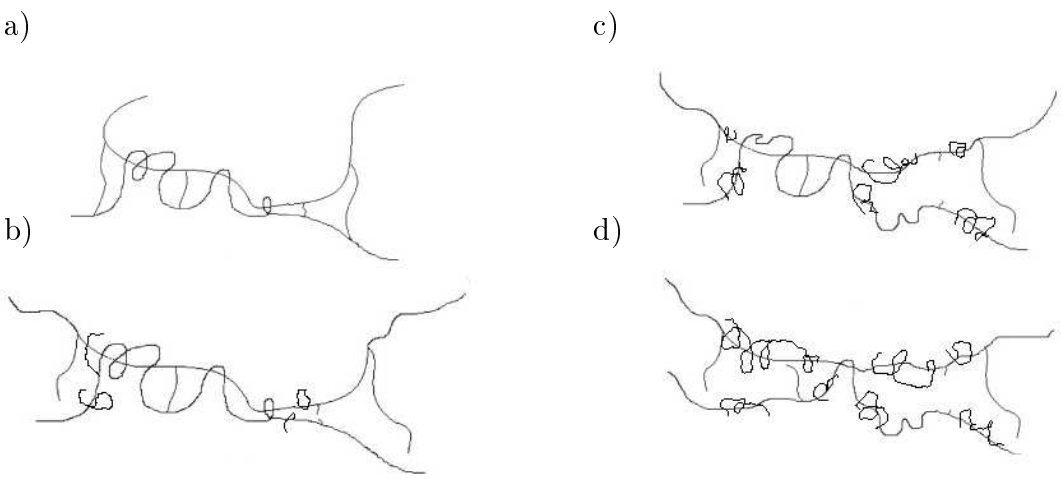

Figure 7.7: Illustration of the disentanglement process: a) initial network, b) deformed network near the limit of the chain extensibility, c) disentanglement of chains and d) local failure due to breakdown of the entanglements. While the number of entanglements between the two chains decrease, coiled substituent side chains result in an increase in the number of chain segments between the entanglements.

taken from G'Sell and Gopez (1985), the shear rate $\dot{\gamma} = 0.003$ is employed in the simulations, cf. Sec. 6.2.2. The material parameters are given in Table 6.1. Once the strain 1.0 is reached, the model responses show more hardening in the material than do the experimental data. As a result of shear band propagation and the deformation of boundaries, the shear force f_x needed for further inhomogeneous deformation remains almost constant, which agrees more closely with the experiments, cf. 7.5(a). Also, the normal stresses of opposite sign in Figs. 7.5(a-b) can be explained by the edge effects: the free boundaries under homogeneous deformation remain straight lines, whereas under inhomogeneous deformation they obtain a convex or S-shaped curvature. The values of the tensile normal stress are even higher as the boundaries are S-shaped.

Based on the evolution equation (6.7), the influence of the number of entanglements on the stress responses is also investigated. Using the EBPA model parameters in Table 7.2, one obtains the initial values $m_0 = 8.56 \cdot 10^{26}$ m^{-3} and $N_A = 7.53 \cdot 10^{27}$ m^{-3}. The other parameters needed in the model are chosen to be $c_1 = c_2 = 0.43 m_0$, $m_u = 1.1 m_0$ and $m_l = 0.64 m_0$. Based on the relation (6.9) and the model assumptions under consideration, it can be concluded that under shear deformation the number of entanglements and chain density decrease while the number of kinks N increases. As is depicted in Fig. 7.5(b), the locking stretch $\sqrt{N}$ during the homogeneous shear deformation reaches almost a twofold increase which denotes significant disentanglement in the material. Once some chains reach their limit of extensibility, the entanglements connected to these chains slip open while coiled neighboring chains result in an increase in the number of rigid links and chain segments between entanglements, cf. Fig. 7.7. In contrast to the homogeneous deformation, the number of entanglements grows slightly due to the localization phenomenon but its influence on the macroscopic stress responses is negligible, cf. Fig. 7.8. Moreover, the sim-

ulations indicate that the number of entanglements alters only slightly as the parameters in (6.7) are varied. Since this simple rule is not able to capture disentanglement during inhomogeneous deformation, also another rule for the chain density will be introduced later on. However, it can be concluded that in localized regions (shear bands) compression perpendicular to the chain direction increases and this together with the extension of chains increases the number of entanglements in relation to the homogeneous shear deformation.

As shown, the reduced number of entanglements is of a major importance when modeling homogeneous local deformation behavior in shear, whereas the inhomogeneous deformation is dominated by the propagation of shear bands and by the boundary conditions. One consequence of this is that under homogeneous deformation the EBPA model predicts less softening and more orientational hardening than under inhomogeneous deformation. It can be concluded that the intrinsic softening promotes the initiation of shear bands, whereas the kinematic hardening is seen to be a driving force for widening of shear bands. The numerical results in Wu and Van der Giessen (1994) also show that there is no evidence of shear band propagation without intrinsic softening in the material. Since softening in the EBPA model is primarily controlled by the softening slope parameter h_1 and the intensity s_{ss}/s_0, their values under inhomogeneous deformation need to be significantly increased. The goal of the subsequent sections is to find the mechanisms which, once implemented in the model, allow the same material parameters to be used for both homogeneous and inhomogeneous deformation modes.

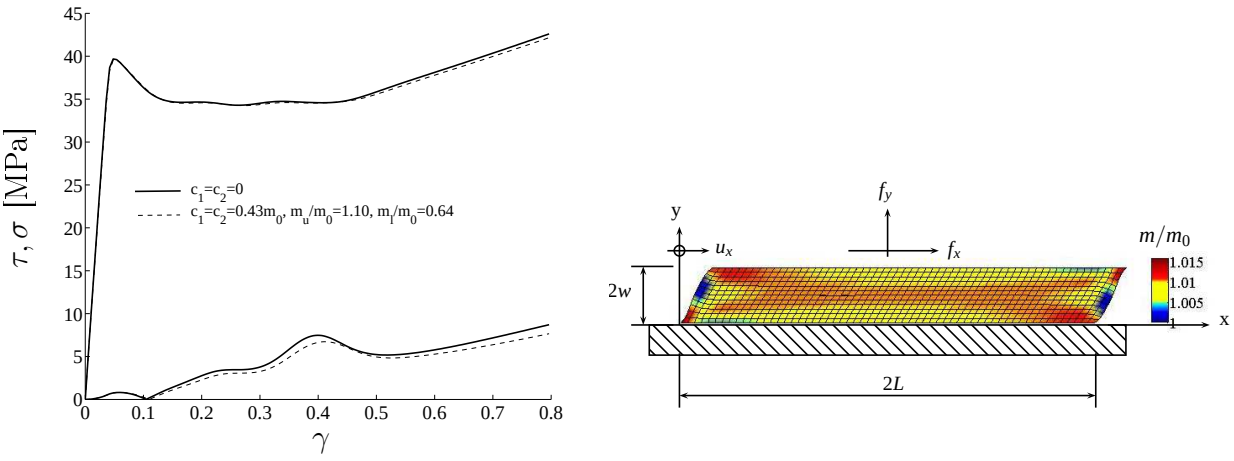

Figure 7.8: Influence of the number of entanglements on the overall stress vs strain response. Deformed mesh of the rectangular specimen is visualized by the number of entanglements m/m_0. The parameters used in the simulation are given in Table 7.2.

7.4 Experiment and simulation of cold drawing process of a PC specimen

7.4.1 Test arrangement and the computational model

In order to evaluate the propagation of inhomogeneous deformation and to study the influence of the microstructural mechanisms to this process, cold drawing experiments on PC were performed. Based on the experiments, the accuracy of the EBPA model and its numerical implementation are also evaluated. Cold drawing, also termed neck propagation, is a standard technique which is used to produce anisotropic characteristics and hardening in polymers. The test specimen under consideration is dumbbell-shaped, and a layout of the testing arrangement is depicted in Fig. 7.9. The details of the specimen's geometry are specified in ISO 527-2. The displacement at $y = 0$ is fixed by a grip and the displacement at $y = L$ during drawing is prescribed by a constant deformation rate. Since in essence propagation of plastic instability along the specimen is a mechanical phenomenon, isothermal conditions are assumed to prevail. To restrain an increase in temperature due to the dissipative heating, a slow cross head speed $\dot{u} = 2$ mm/min was used in the test. The elongation was restricted to $u = 40$ mm to prevent localized deformation at the interface of the gauge section and the grips. Unloadings to different dwell levels were performed at a constant rate 1 kN/min. During the tests, the displacement u and the applied load f were monitored. The tests were performed by using the Instron© 5967 tension/compression electromechanical testing machine equipped with a variety of load cells. The machine gives a force measurement with error less than 0.5% of the reading down to 1/500 of load cell capacity, 30 kN. The testing machine was controlled by Blue Hill 3 software. The software was used to make three types of tests for the specimens:

1. The test specimen is drawn until the elongation of $u = 15$ mm or $u = 40$ mm is reached. The drawing is followed by unloading to zero stress. Finally, the specimen is relaxed for one month.
2. As with the first test concerning the elongation up to $u = 40$ mm, but several loading cycles are performed involving unloadings to $f = 60$ N. Unloadings are initialized at progressively increasing levels $u = 2.0$ mm, $u = 8.4$ mm, $u = 15.8$ mm and $u = 39.3$ mm. The first three unloadings are followed by a dwell period of 120 s when the load level is kept at constant.
3. As with the second test, but the dwell level of $f = 1000$ N is applied.

In addition, the first test was recorded by a digital camera which acquired the images of the deformed shape at intervals of one millimeter.

Tomita (1999) and also Miehe *et al.* (2009) investigated the thickness-reduction of the dumbbell-shaped PC-specimen during a cold drawing experiment. The experimental results obtained using optical measurements showed that the thickness-reduction of the sample remains small until the deformation starts to localize. The thickness-reduction reached its maximum value of 20-25% (≈ 1 mm) being constant over the localized zone. According

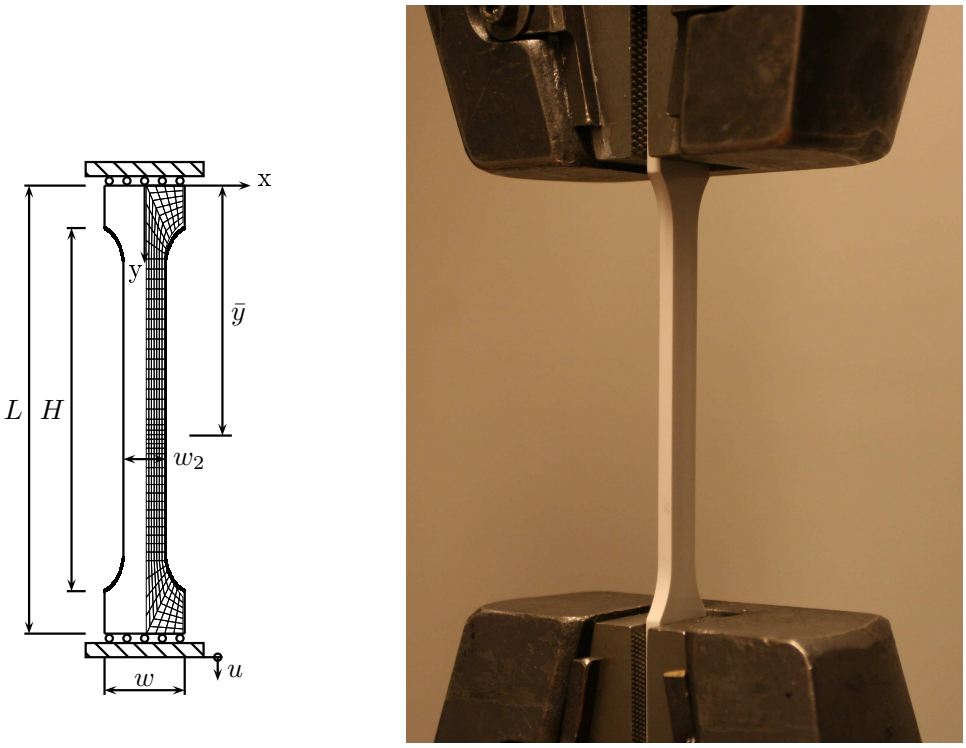

Figure 7.9: The layout of the test arrangement. The test specimen under study is dumbbell-shaped, the geometry is given by $H/L \approx 0.90$, $w/L \approx 0.17$, $w_2/L \approx 0.09$ and $t/L \approx 0.035$ where t denotes the specimen's thickness. Neck initiation is depicted by $\bar{y}$. The details of the specimen's geometry are specified in ISO 527-2. The tests were performed in the Laboratory of DMS at TUT.

to our tests, the reduction of the width in the gauge section was virtually the same, 22% ($\approx$ 2.2 mm). Wu and Van der Giessen (1995) investigated influence of a reduction of the cross sectional area (geometric softening) in relation to the intrinsic softening. Even though the thickness-reduction was moderate, the intrinsic softening dominated the localization phenomenon involving neck pattern and the rate of neck propagation. Moreover, the thickness of the specimen in relation to the other dimensions can be considered relatively large and thus plane strain condition is assumed to be suitable for the calibration.

Since the initial amorphous structure of the material in the model is considered as homogenous, the localization is triggered by introducing a small initial imperfection

$$\Delta w_2 = w_2 \xi_0 \tag{7.7}$$

so that the width of the gauge section at $y = \bar{y}$ is $w_2 - \Delta w_2$, cf. Fig. 7.9. In the first experiment, neck was initiated near the center of the specimen, i.e. $\bar{y} = L/2$, whereas in the second and the third experiment neck started to propagate at $\bar{y} = 0.55L$. In the numerical analysis, only a quarter and a half of the specimen are modeled because of the symmetry of the geometry and boundary conditions. The finite element discretization employed is of a mesh with 196 and 392 4-node plane elements, respectively. Moreover, there exist several studies that show the initial response of amorphous polymers to be heterogeneous. Tomita

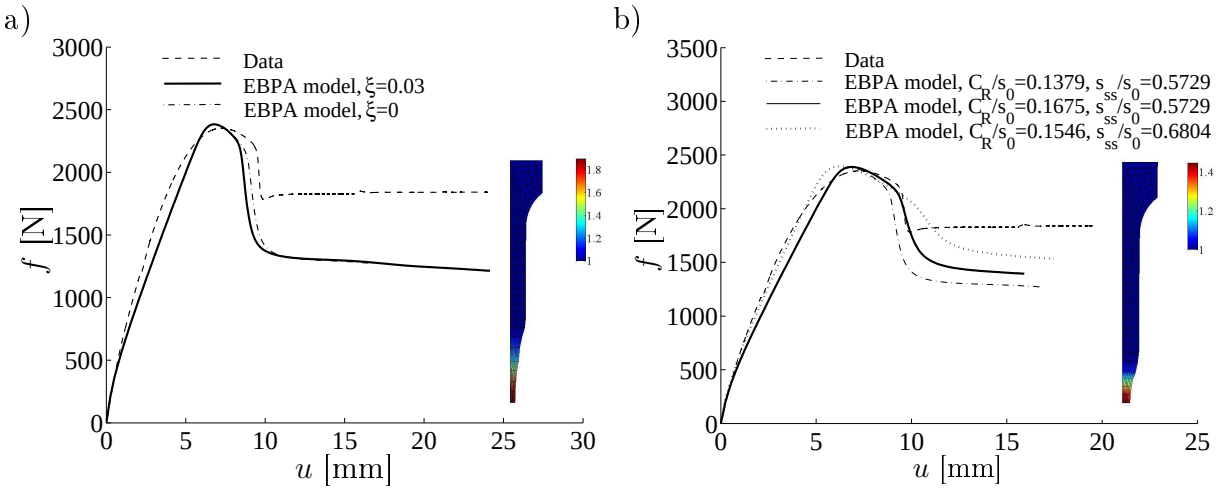

Figure 7.10: Effect of a) the intensity ξ and b) the orientation hardening parameter C_R and the saturation value s_{ss} on the predicted force vs elongation response. The rest of the parameters are listed in Table 6.2. The deformed meshes for $\xi = 0.03$ and for the ratio $C_R/s_0 = 0.1675$ are visualized by the plastic stretch $\bar{\lambda}^p_{ec}$ at the end of loading. The initial mesh is also disturbed according to (7.7) using the intensity $\xi_0 = 0.002$.

and Uchida (2003) proposed that the heterogeneity should be taken into account either by the inhomogeneous distribution of chain density or by the initial heterogeneous shear strength distribution. In the EBPA model, the chain density is included in the modeling of kinematic hardening via the backstress, whereas the shear strength s_1 evolves according to (6.2). In addition to the width reduction (7.7), the initial shear strength distribution in the EBPA model is disturbed by the following form

$$\Delta s_0 = \xi s_0 \cos\Big(\frac{\pi(\bar{y} - y)}{\bar{y}}\Big), \;\; s_0 = s_0 - \Delta s_0, \tag{7.8}$$

where ξ is the intensity, cf. Wu and Van der Giessen (1995).

7.4.2 Calibration for inhomogeneous deformation

As well as the material of the test specimen (Lexan® 223R) differing from the PC-polymers given in Tables 6.1 and 6.2, the localization phenomenon which was discussed in Sec. 7.3 necessitates that some of the material parameters needs to be calibrated to the data of the cold drawing experiment. The calibration is initialized using the BPA-PC parameters for homogeneous deformation given in Table 6.2.

The influence of the intensity ξ, the orientation hardening parameter C_R and the saturation value s_{ss} on the predicted $f - u$ response is shown in Fig. 7.10. As the intensities s_{ss}/s_0 and C_R/s_0 decrease, the response shows stronger intrinsic softening, whereas no significant effect due to the change of the intensity ξ can be observed, cf. also Wu and Van der Giessen (1995). It is also found that the localized zone does not extend but is concentrated during further elongation. However, experimental investigations show that the plastic instability (necking) does not continue to localize, but tends to propagate along

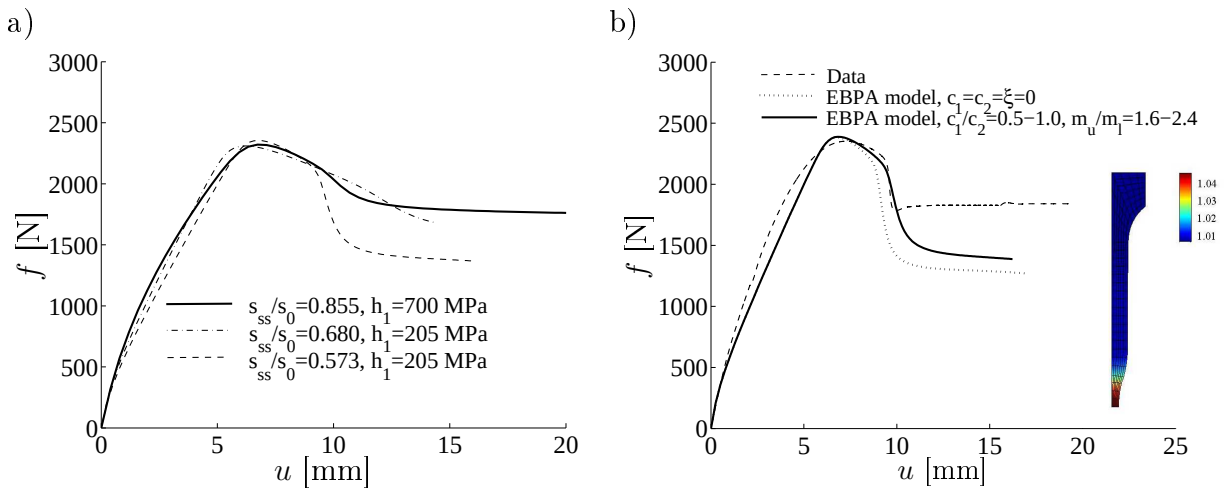

Figure 7.11: Influence of a) the saturation value s_{ss} and the hardening slope h_1 and b) the ratios m_u/m_l and c_1/c_2 on force vs elongation response. In b), the deformed mesh at the end of loading is visualized by the chain density m/m_0. The intensity of the initial imperfection in (7.7) is set to be $\xi_0 = 0.002$ while $\xi = 0$ in (7.8).

the sample, cf. G'Sell and Jonas (1979), G'Sell and Gopez (1985), Arruda and Boyce (1990a) and Wu and Van der Giessen (1995). If higher values for C_R/s_0 and s_{ss}/s_0 are applied while the rest of the parameters are kept the same, neck does not stabilize and the response shows only a gradual softening slope. As it is pointed out in Fig. 7.11(a), high values of h_1 result in a deep post-yield drop and compensate for the reduced softening slope as the values of C_R/s_0 and s_{ss}/s_0 are increased.

In addition to the strain softening behavior, we will now study the influence of the number of entanglements to the localization phenomena. The evolution equation for the number of entanglements is given by (6.7). As the condition $m_l/m_o < m_o/m_u$ is satisfied, and the ratio c_1/c_2 is chosen to be large enough, the influence of the shear deformation reduces with regard to tension. Fig. 7.11(b) presents the effect of the intensities m_u/m_l and c_1/c_2 on both the $f-u$ response and the evolution of the chain density. A raise in the values m_u/m_l and c_1/c_2 in (6.7) results in an increase in the chain density while the number of statistical links N decreases. According to the model assumptions, this denotes that the polymer chains extend and align with the loading direction while compression perpendicular to the chain direction increases. Despite the use of a relative-large range of the model parameters, the simulations indicated that the growth of the chain density within localization is minor ($\approx 5\%$) and only a small change in the $f-u$ response can be observed.

Once the calibrated values $c_1 = c_2 = 0$, $h_1 = 720$ MPa, $s_{ss} = 77$ MPa and $s_0 = 96$ MPa for monotonic loading have been found, the influence of the viscosity η on the model response for cyclic loading is studied, cf. Fig. 7.12. During the first cycle, the response is viscoelastic and unlike in the experimental data, some creep can be observed. Creep tends to increase as the viscosity decreases. In large strains, creep is progressively replaced by recovery. The higher values of the viscosity and the dwell stress are applied, the smaller

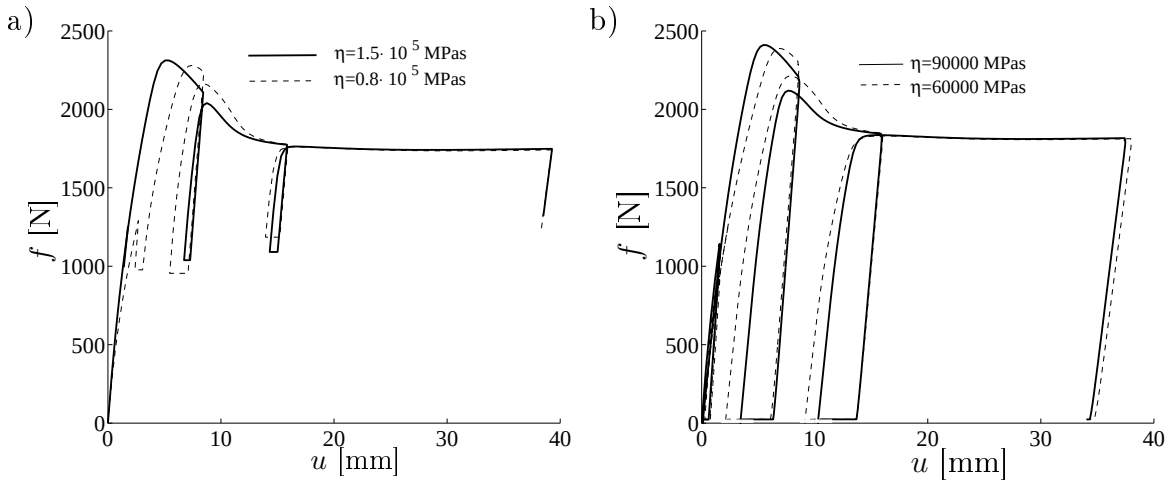

Figure 7.12: Influence of the viscosity η on the force vs elongation response at two different dwell levels a) $f = 1$ kN and b) $f = 60$ N. In the simulations, the fitting $c_1 = c_2 = 0$, $E = 2550$ MPa, $s_{ss}/s_0 = 0.80$ and $h_1 = 720$ MPa is employed. The rest of the parameters are listed in Table 6.2. The intensities of the initial imperfections in (7.7) and (7.8) are set to be $\xi_0 = 0.002$ and $\xi = 0$, respectively.

amount of recovery can be observed. The influence of the viscosity on the large-strain response is relatively small during monotonic loading but it dominates the response prior to the macro-yield point as well as recovery at both dwell levels $f = 60$ N and $f = 1$ kN. Recovery is most accurately predicted by a relatively high value $\eta = 1.5 \cdot 10^5$ MPas while the Young's modulus needs to be reduced to $E = 2550$ MPa to better capture the initial response. It should be noticed that the experimental response for cold drawing can be captured fairly well using the calibrated parameters for plane strain simple shear, cf. Table 7.2.

7.4.3 Evaluation of the model results

During the tests, the displacement u versus applied load f was monitored. The experimental response as well as both the EBPA and the BPA model responses are presented in Figs. 7.13 and 7.14. Apart from the recalibrated softening parameters $s_0 = 92$ MPa and $s_{ss} = 69$ MPa, the BPA model response is obtained using the material parameters given in Table 6.2. According to the EBPA model, the yield point is reached at $u \approx 5.5$ mm which slightly differs from the experimental data thanks to the relatively high viscosity applied to the model. Due to the elastic constitutive description, the BPA model predicts almost linear initial response and as a result, the displacement at the yield point is underestimated. Once the yield point is passed, the responses show a significant drop in force, which is due to softening in the material. During continued deformation, the localized zone extends more or less at constant force, which indicates that stable neck is present, cf. Stokes and Nied (1986).

A comparison of Figs. 7.13 and 7.14 reveals that the magnitude of recovery decreases as the dwell level increases. In contrast to the EBPA model, unloadings to $f = 60$ N are

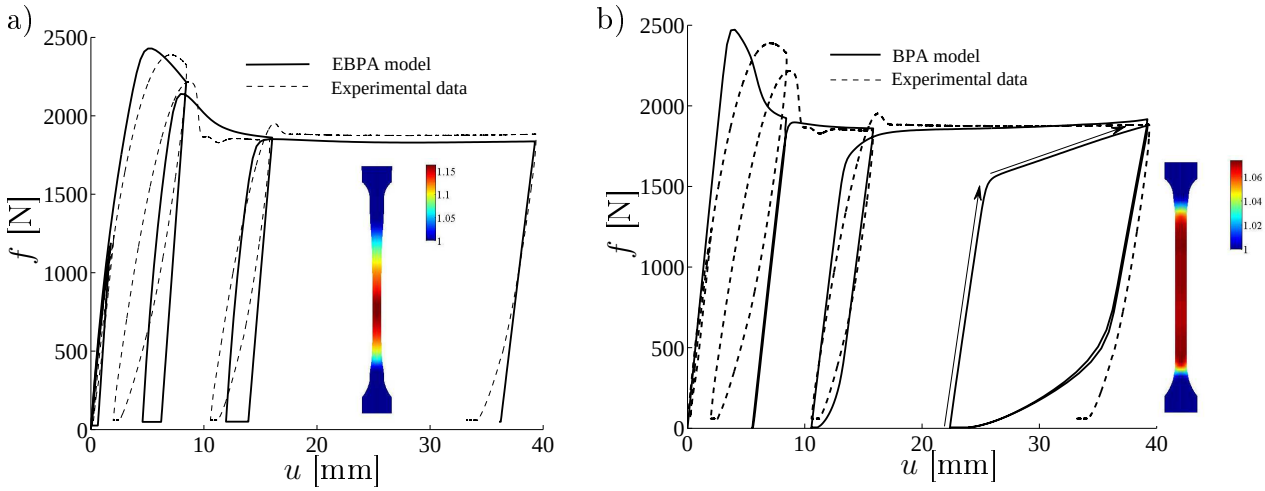

Figure 7.13: Comparison of a) the EBPA and b) the BPA model with the experimental PC-response. A dumbbell-shaped specimen is subjected to the extension at a cross-head speed $\dot{u} = 2$ mm/s. The unloadings are performed to $f = 60$ N followed by the dwell period of $t = 120$ s. In the BPA model response, the arrow indicates an additional loop. The deformed shapes at the end of loading are visualized by the plastic stretch $\bar{\lambda}^p_{ec}$.

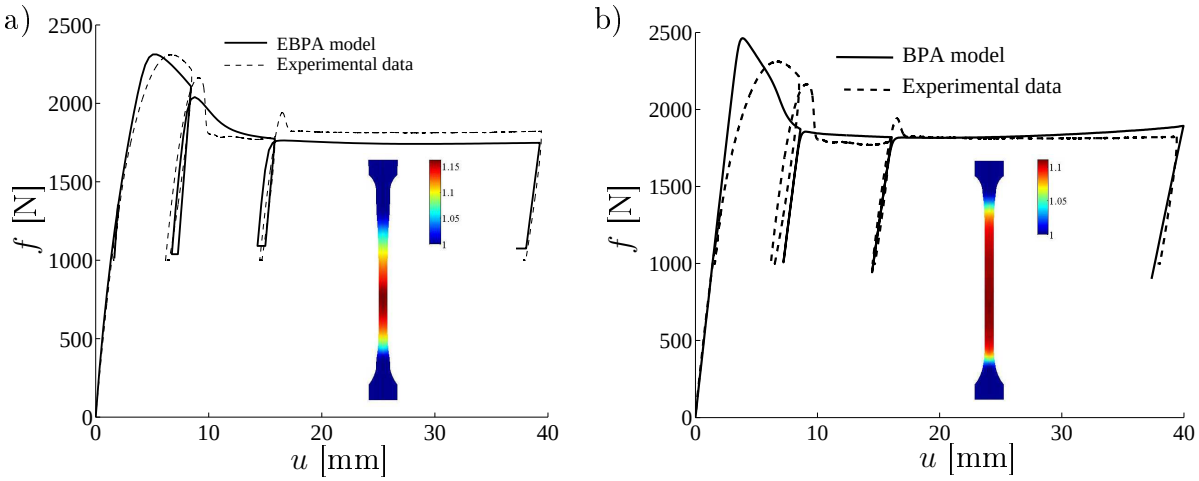

Figure 7.14: Comparison of a) the EBPA and b) the BPA model with the experimental PC-response. A dumbbell-shaped specimen is subjected to the extension at a cross-head speed $\dot{u} = 2$ mm/s. During the dwell period of 120 s, the force $f = 1000$ N is kept at constant. The deformed shapes at the end of loading are visualized by the plastic stretch $\bar{\lambda}^p_{ec}$.

not satisfactorily captured by the BPA model which predicts an almost elastic response during the second cycle and a premature Bauchinger effect during the last unloading to zero stress. If an additional loop is performed, only a small cyclic shift of the hysteresis loop during this last unloading can be observed, i.e. the BPA model shows the saturated state of hardening, cf. Fig. 7.13(b). Comparison also reveals that the BPA model in relation to the EBPA model results in less plastic stretching and more diffuse neck. The difference tends to increase as the dwell level is reduced. Unlike with the model responses, small

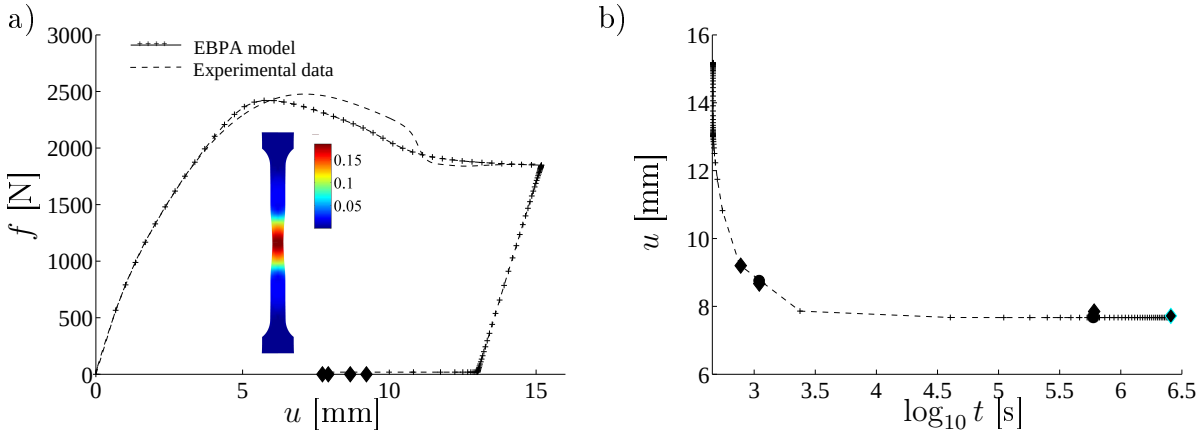

Figure 7.15: a) Comparison of the EBPA model and the experimental PC-response involving long-term dwell. b) The displacement u vs time during the dwell period of one month. The markers • and ♦ (almost superposed) indicate the elongations at 60 s, 300 s, after one week and after one month according to the EBPA model and the experiment, respectively. The deformed shape at the end of the loading phase is visualized by s_2/s_0.

peaks during reloadings can be observed in the experimental response. However, the peaks occur in a narrow strain regime and do not influence the subsequent deformation behavior. It can be concluded that the models are able to capture the characteristic features of load-elongation response during monotonic loading. In contrast to the BPA model, the EBPA model captures not only the elongation where the softening is initialized, but also amount of softening as well as recovery during the dwell periods at prescribed forces.

In order to investigate the amount of relaxation, the specimen is drawn until the elongation $u = 15$ mm is reached and then the load is linearly removed. Both the force-elongation response and the elongation versus time are depicted in Fig. 7.15. During relaxation, the length of the specimen is measured at four different phases: $t = 60$ s, $t = 300$ s, after one week and after one month. As shown, the EBPA model accurately captures the experimental data through the whole relaxation period. The new variable s_2, which in the EBPA model controls isotropic hardening in the material, increases along with the plastic deformation and reaches considerable values ranging $0.10-0.15s_0$. Similar to homogeneous deformation, we conclude that the amount of isotropic hardening in relation to kinematic hardening increases according to the EBPA model, and as a result, long-term recovery is significantly reduced.

The development of inhomogeneous deformation during the first test is presented in Fig. 7.16. The average plastic stretch $\bar{\lambda}^p_{ec}$, defined by (4.105), is chosen to visualize the phenomenon. For comparison, the images recorded during the first test are presented in Fig. 7.17. The selected stages of deformation depict the initiation, stabilization and propagation of neck. As the necked region approaches the grips, the $f-u$ response exhibits hardening again. In small strains below the macro yield point, the material behavior is viscoelastic and the stretch field is uniform. Further extension develops inelastic strain

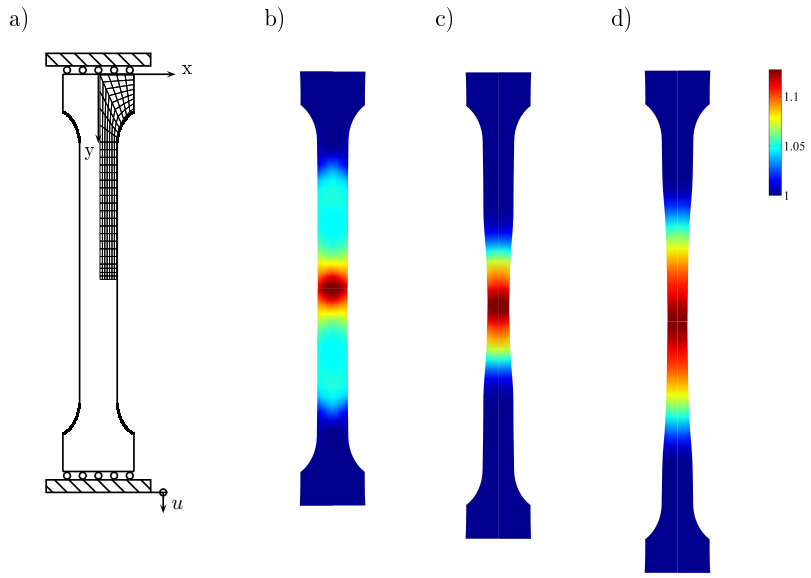

Figure 7.16: a) The geometry and finite element mesh of a dumbbell shaped specimen. The deformed shapes are visualized by the plastic stretch $\bar{\lambda}^p_{ec}$ at three different phases: b) $u = 10$ mm, c) $u = 20$ mm and d) at the end of the last unloading. The simulation using the EBPA model is performed at constant deformation rate $\dot{u} = 2$ mm/min at room temperature. In the simulations, the fitting, $\xi = 0$, $\xi_0 = 0.002$, $c_1 = c_2 = 0$, $E = 2550$ MPa, $s_{ss}/s_0 = 0.80$, $\eta = 1.5 \cdot 10^5$ MPas and $h_1 = 720$ MPa, was used. The rest of the parameters are listed in Table 6.2.

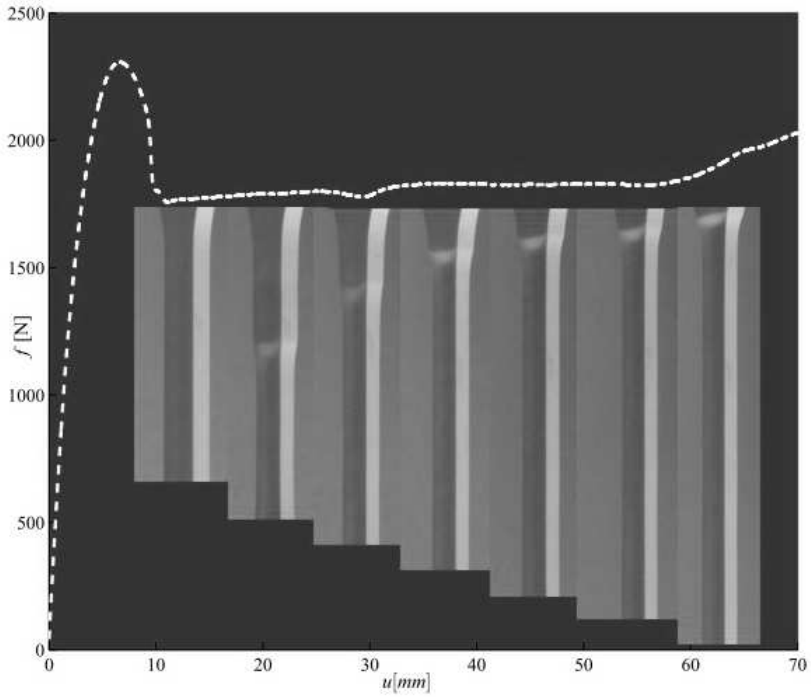

Figure 7.17: Snapshots of a dumbbell shaped test specimen during elongation: $u = 6$ mm, $u = 20$ mm, $u = 30$ mm, $u = 40$ mm, $u = 50$ mm, $u = 60$ mm and $u = 70$ mm. The test was performed at a constant cross-head speed $\dot{u} = 2$ mm/min at room temperature.

localization in the material, which extends from the center of the specimen towards the grips, cf. phases (b-d) in Fig. 7.16. The localized zone is not concentrated but expands

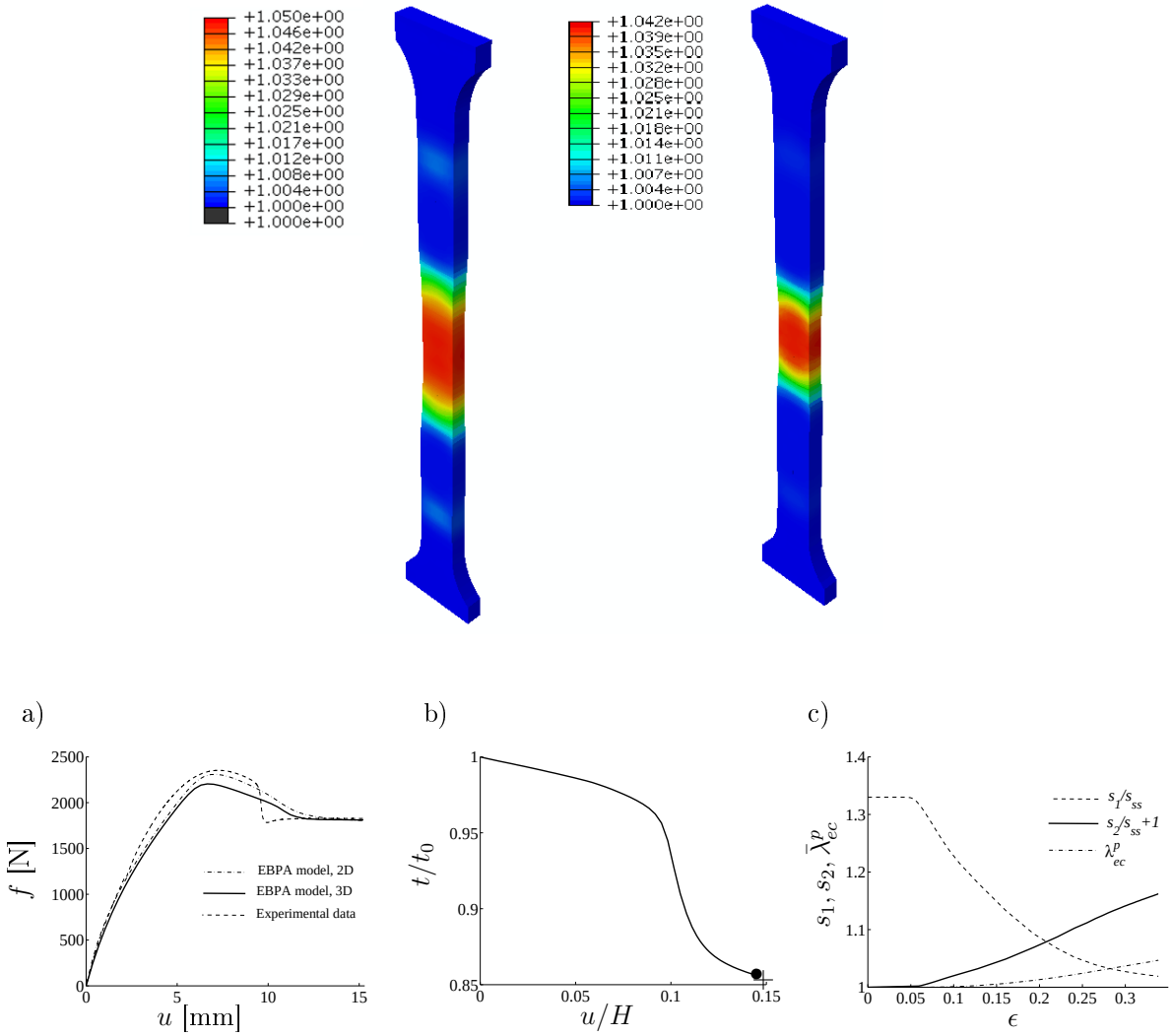

Figure 7.18: a) Comparison of the experimental and the EBPA model responses for two- and three-dimensional deformation. b) The thickness-reduction ratio t/t_0 at $x = 0$ and $y = (L+u)/2$. c) The development of s_1, s_2 and the plastic stretch $\bar{\lambda}^p_{ec}$ in the middle of the specimen. The markers • and + indicate the thickness ratio according to the model and the experiment, respectively. The deformed shapes during the stabilized neck, $u = 15$ mm and $u = 20$ mm, are visualized by $\bar{\lambda}^p_{ec}$.

through the gauge section, i.e. the neck is rather diffuse. Comparison of Figs. 7.13, 7.14, 7.16 and 7.17 reveals that, according to both the BPA model and the experiment, the localized zone extends and reaches the end of the gauge section more rapidly than in the EBPA model. The deformed shapes are characterized by a smooth width reduction which is initialized at the center and moves towards the grips during elongation. Compared to the EBPA model result, the test specimen exhibits a rather sharp neck profile, which is probably due to the neglected volume changes (geometric softening) associated with the three-dimensional deformation, cf. Wu and Van der Giessen (1995), Steenbrink *et al.* (1997) and Zaïri *et al.* (2008).

In order to investigate the thickness-reduction and its influence on the macroscopic load-elongation response, the simulation was performed using a three-dimensional finite-

element code where the EBPA model was employed. The finite element discretization is of a mesh with 8-node linear hybrid brick elements (constant pressure). In addition to the displacements, the logarithmic strain field ϵ in the loading direction is monitored. Fig. 7.18(a) shows the influence of the deformation mode on the $f-u$ response. Even though the model responses slightly differ during the softening phase, the results are virtually indistinguishable once neck has been stabilized. Fig. 7.18(b) shows a rapid decrease also in section thickness, which is due to softening in the material. Since the relative thickness reduction is almost equal with the relative width reduction ($\approx 22\%$), geometric softening which appears as the difference between the true and the nominal stress responses is significant. With further elongation, the thickness-reduction reaches a plateau at almost the same phase with the axial force indicating stabilization of necking. As shown, the thickness-reduction in relation to the elongation is small, $(t_0 - t)/u \approx t_0/H$ where t_0 and t are the initial and current thickness, respectively. Moreover, the softening/hardening behavior in the material is very similar to that observed under uniaxial compression, cf. Figs. 6.9(b) and 7.18(c).

The deformed shapes of the test specimen are also presented in Fig. 7.18. A comparison with Fig. 7.16 reveals that the deformation mode has not marked influence on the neck propagation and the intensity of plastic stretching under change of the modes remains almost unaltered. G'Sell *et al.* (2002) conducted tensile tests on amorphous PET that indicated the importance of strain-induced volume changes on plastic instability due to the damage processes. They concluded that the kinetics of plastic instability (the rate of neck growth) is a combination of the shear band propagation and damage evolution.

7.5 Investigation of void growth

It is widely acknowledged that the macroscopic mechanical behavior of amorphous glassy polymers stems from three major microstructural characteristics: the number of entanglements and statistical links between the entanglements, the growth of shear bands, and the extent of free volume around the chain molecules, cf. e.g. Argon (1973), Hasan and Boyce (1995), Steenbrink and Van der Giessen (1998b) and Anand and Gurtin (2003). However, most of the current models are based on the assumption that the plastic deformation only evolves because of the development and propagation of shear bands without volume changes. The objective of this section is to investigate the amount of void growth, the shear band formation in the ligaments between the voids and the possibility to void coalescence during deformation. Here, the concept of free volume is employed to describe the voids or the loosely packed regions in the PC under consideration. In contrast to rubber-toughened polymers, the void is considered as conceptual with no clear physical interpretation. However, since the voids are evenly distributed in the material, the growth of voids is approximated by using the models which are conventionally applied to the modeling of void growth due to cavitation of small rubber particles (second-phase particles) or impurities present in polymer-rubber blends. An example of these polymer blends is PC incorporating small polyacrylonitrile-butadiene-styrene (ABS) particles, cf. e.g. Pijnenburg

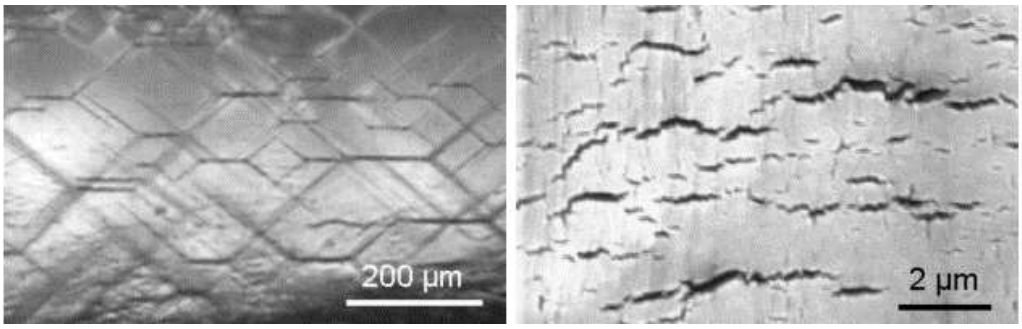

Figure 7.19: Transmission optical micrograph of shear bands which form a honeycomb network in a PET sample subjected to uniaxial tension. Scanning electron micrograph on the right side shows crazes of about 1 μm in length. The tensile axis is vertical. After G'Sell *et al.* (2002), Figs. 7-8.

et al. (2005).

Onset of the volume changes in amorphous glassy polymers are the growth and coalescence of existing voids in addition to the nucleation and growth of new voids. G'Sell *et al.* (2002) investigated the influence of damage (crazing, cavitation of rubber particles and micro-cracking within the matrix material) on the plastic deformation and stability in PET and high-impact polystyrene (HIPS). Based on the optical micrographs, cf. Fig. 7.19, they concluded that shear bands are nucleated from the tips of existing crazes, rather than the crazes being nucleated at the intersection of fine shear bands. To trigger a transition from crazing to shear yielding, some heterogeneity, which relieves the build-up of high hydrostatic stress, is needed in the amorphous structure, cf. Melick (2003). They also showed that the thickness of the ligaments within the structure is crucial. As a result of the damage processes, volume strains in relation to total strains, i.e. the plastic dilatation, was found to be significant. G'Sell *et al.* (2002) concluded that the onset of plastic deformation is crazing and the plastic stability is essentially controlled by damage processes. Mahajan *et al.* (2010) conducted MD simulations to investigate the role of deformation-induced disentanglement to void nucleation in amorphous glassy polymers. They concluded that disentanglement increases under highly triaxial stress states, which results in void nucleation being increased. They also pointed out that porous regions are created at the locations where almost all the polymer chains have slipped away except a few that are firmly anchored at their ends and pulled taut, cf. Fig. 7.7.

Due to the existence of voids around the chain molecules, the yield behavior of amorphous glassy polymers depends on hydrostatic pressure. In subsequent considerations, damage is ascribed to the distributed growth of void volume during plastic deformation. The damage mechanism is schematically illustrated in Fig. 7.20. During nucleation and initial growth of voids, the deformation is considered as homogeneous. Once the coalescence of voids is initialized, the transformation to the localized deformation phase takes place.

Micromechanical models are frequently invoked to investigate the bifurcation away from a nominally uniform state of deformation. The following features should be included in

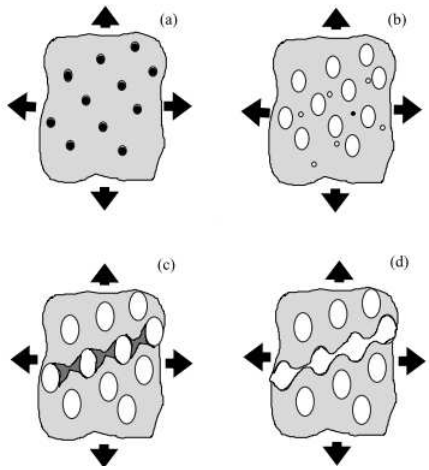

Figure 7.20: A schematic representation of the dilatational damage mechanism: a) nucleation of voids, b) void growth, c) initialization of void coalescence and d) the coalesced voids. The figure is modified from the original taken from Alibadi (2001).

models suitable for multi-phase polymers:

- A geometric description of a representative volume element (RVE) used to embody the essence of the microstructure under study.
- The constitutive description of the mechanical behavior of each phase.
- The constitutive description of the phase interfaces.
- A treatment of homogenization for predicting the macroscopic mechanical behavior of the RVE.

With regard to the concept of free volume, only the constitutive model for the matrix material (PC) is of an interest and needs to be defined. The interface between the void and the matrix material is modeled as a traction-free boundary for the matrix phase. It is also assumed that each RVE deforms periodically, being identical to the neighbors. In order to ensure the compatibility of such a deformation field, periodic boundary conditions are also imposed on each RVE. The growth of voids by the the plastic deformation in propagating shear bands is studied on the basis of finite element analyses of the planar RVE approach, also referred to as a Simple Square Array (SSA) or a planar cell model. The planar cell model has been shown to yield sufficiently accurate predictions for the macroscopic behavior of the two-phase aggregate as long as the triaxiality of the stress state is low, the void volume fraction is low ($< 8\%$) and the response is not dominated by the interaction between the voids, cf. Steenbrink and Van der Giessen (1998b) and Socrate and Boyce (2000). According to this model, unit cells represent a material with a doubly periodic packing of cylindrical voids, cf. Fig. 7.21. The initial circular cross section of the voids is chosen for computational convenience.

The directions of the principal macroscopic stress align with the coordinate axes x_1, x_2 and x_3 and the initial dimensions of the cell in x_1- and x_2-directions are given in terms of the half-spacings b_0 and h_0, respectively. The initial radius of the void is denoted by

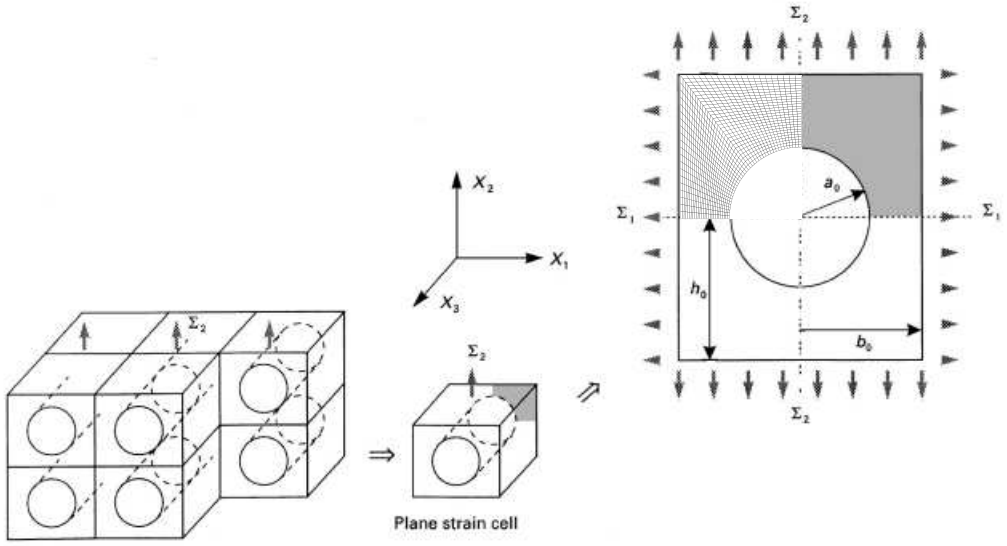

Figure 7.21: Illustration of the planar cell model for a periodic material involving cylindrical voids. Due to the symmetry, the meshed area is considered in the finite element analyses. The figure is modified from the original taken from Steenbrink and Van der Giessen (1998b).

a_0. Since the plane strain condition prevails, the strain rate $\dot{E}_3$ vanishes. Due to the symmetry, only the meshed region needs to be analyzed. Since the region is subjected to the far-field tension, the boundaries are assumed to remain straight during deformation without shear tractions. The deformation rate $\dot{u}_2$ on the boundary $x_2 = h$ is prescribed by a constant applied strain rate $\dot{E}_2 = \dot{u}_2/h$ where h is the deformed height of the cell, i.e. $h = h_0 + u_2$. Similarly, $b = b_0 + u_1$ is the current width of the cell. In terms of the applied loads f_1 and f_2, the macroscopic principal stresses in the direction of x_1 and x_2 are defined as $\Sigma_1 := f_1/h$ and $\Sigma_2 := f_2/b$, respectively. To investigate the influence of the stress state on void growth, the strain rate $\dot{E}_1$ at $x_1 = b$ is prescribed so that

1. The nominal stress ratio or equivalently the ratio of the applied loads $\nu_R := f_1/f_2$ remains constant during deformation.
2. The true stress ratio $\nu_R := \Sigma_1/\Sigma_2$ is kept constant.

Applying Hooke's law in plane strain state, the rate of the principal stress Σ_2 at each instant is prescribed by the applied strain rate $\dot{E}_2$ according to

$$\dot{\Sigma}_2 = E_m(\nu\frac{\dot{u}_1}{b} + (1-\nu)\frac{\dot{u}_2}{h}) = \frac{\dot{f}_2}{b} - \frac{f_2}{b^2}\dot{u}_1 \tag{7.9}$$

where E_m is an overall elastic modulus. As with the stress rate $\dot{\Sigma}_2$, the rate of the transverse principal stress $\dot{\Sigma}_1$ is prescribed via the applied strain rate $\dot{E}_2$ as

$$\dot{\Sigma}_1 = E_m(\nu\frac{\dot{u}_2}{h} + (1-\nu)\frac{\dot{u}_1}{b}) = \frac{\dot{f}_1}{h} - \frac{f_1}{h^2}\dot{u}_2. \tag{7.10}$$

Due to the elastic isotropy, the overall elastic moduli in each direction are taken to be equal with E_m. Let us first consider a constant nominal stress ratio. Based on (7.9) it is possible to extract $\dot{f}_2$, and its substitution into (7.10) together with $\dot{f}_1 = \nu_R \dot{f}_2$ yields

$$\dot{u}_1 = \frac{b}{h} \frac{\nu_R(1-\nu-\hat{f}_2) - \nu h/b}{(1-\nu)h/b - \nu_R(\nu+\hat{f}_2)} \dot{u}_2. \tag{7.11}$$

In (7.11), the dimensionless variable $\hat{f}_2 := f_2/E_m b$ was introduced. According to the Goodier (1933) solution for elastic media, the highest value of the effective stress τ occurs at the equator of the void, i.e. at $x_1 = a_0$. Therefore, the plastic deformation is initialized at the equator. Since $\hat{f}_2 \ll \nu$, the solution is not sensitive to the value of the overall elastic modulus E_m and it is chosen to be constant. According to the simulations, the values ranging from $E_m = 900$ MPa to 3000 MPa have no marked influence on the macroscopic stress-strain response under consideration. Moreover, the void volume fraction has only a small influence on the elastic material properties in porous media, cf. Steenbrink *et al.* (1997). According to Hooke's law for plane strain state, $E_m = E/(1+\nu)(1-2\nu)$.

Let us now consider a constant true stress ratio. Since $f_1 = \nu_R h f_2/b$, the loading rate in the x_1-direction becomes

$$\dot{f}_1 = \nu_R \frac{h}{b}(\dot{f}_2 + f_2 \frac{\dot{u}_2}{h} - f_2 \frac{\dot{u}_1}{b}).$$

Once the loading rate $\dot{f}_2$ is solved from (7.9), substitution of $\dot{f}_1$ and $\dot{f}_2$ into (7.10) results in

$$\dot{u}_1 = \frac{b}{h} \frac{\nu_R - \nu(1+\nu_R)}{1-\nu(1+\nu_R)} \dot{u}_2. \tag{7.12}$$

In contrast to the constant nominal stress state, the velocity $\dot{u}_1$ under a constant true stress state does not explicitly depend on the load f_2. The only dimensions involved in the model are the initial radius a_0, the width b_0 and the height h_0. Considering $b_0 = h_0$, the solution only depends on the ratio a_0/h_0 which can equivalently be given by the initial void volume/area fraction

$$f_{v0} = \frac{dV_{v0}}{dV_{c0}} = \frac{\pi a_0^2}{4 b_0 h_0} = \frac{\pi}{4}\Big(\frac{a_0}{h_0}\Big)^2 \tag{7.13}$$

where dV_{v0} and dV_{c0} are the initial void volume and the elementary apparent volume of the material, respectively, cf. Steenbrink and Van der Giessen (1998b) and Zaïri *et al.* (2008). In order to describe the macroscopic distortion, an overall effective strain E_e is defined as

$$E_e := \sqrt{\frac{2}{3}(E_i')^2} \tag{7.14}$$

where $E_i' := E_i - 1/3 \sum_i E_i$, $i = 1, 2, 3$. Moreover, the macroscopic effective stress is defined

in terms of the principal deviatoric stresses as

$$\Sigma_e := \sqrt{\frac{3}{2}(\Sigma_i^{dev})^2}. \tag{7.15}$$

Under plane strain state, the expressions of E_e and Σ_e become

$$E_e = \frac{2}{3}\sqrt{E_1^2 - E_1E_2 + E_2^2} \text{ and } \Sigma_e = \frac{\sqrt{3}}{2}|\Sigma_2 - \Sigma_1|.$$

For later purposes, let us define a macroscopic shear rate as $\dot{\Gamma} := 1/\sqrt{2}\dot{E}_2$, which represents the applied shear strain rate for the material without voids.

The EBPA model is employed in the finite element analyses, the constitutive parameters being given in Table 7.2. To accurately resolve the development of thin shear bands, a very fine mesh, especially near the equator $x_1 = a_0$, would be needed. The element mesh consisting of 566 4-node plane elements has been found to meet the case for finding the main characteristics of the shear band patterns and the magnitude of void growth during the deformation process. The size of the initial voids is assumed to be $a_0/h_0 = 0.2$, which according to (7.13) corresponds to the initial void volume fraction, $f_{v0} = 0.03$. The larger values are relevant for rubber-polymer blends in which cavitation of the rubber particles occurs. In order to capture the stress state in the specimen during the cold drawing process, the stress triaxiality ratio ν_R is assumed to be relatively low. The two values $\nu_R = 0$ and $\nu_R = 0.3$ are considered as representative in the gauge section.

7.5.1 Shear band patterns

The normalized plastic shear rate $\dot{\gamma}^p/\dot{\Gamma}$ is used to describe the shear band pattern during deformation. The distribution of $\dot{\gamma}^p/\dot{\Gamma}$ in the cell for the PC-material under study is shown in Fig. 7.22. According to the simulations, the difference between the $\dot{\gamma}^p/\dot{\Gamma}$-distributions under the constant nominal and true stress states can be considered as small, so the nominal stress state is chosen to illustrate the localization phenomena. Under both the triaxialities $\nu_R = 0$ and $\nu_R = 0.3$, the plastic deformation first localizes at the equator of the void and then rapidly expands around the void. Initially the shear band pattern is uniform involving a single band which appears at approximately 45° relative to x_2-direction. In view of the shape, these inclined shear bands are termed "wings" and they can frequently be observed under low triaxial loadings, cf. Sue and Yee (1988) and Steenbrink and Van der Giessen (1998b). During continued deformation, the material inside the band first softens and then hardens due to the stretching and alignment of the chain network. Once the stress inside the band becomes large enough, the surrounding material yields and results in the initiation and propagation of new bands.

Under low triaxiality, $\nu_R = 0$, two distinct and parallel shear bands have developed at $E_e = 0.10$, cf. Fig. 7.22(a). Even though delayed, a very similar propagation of wing-shaped bands can also be observed for higher triaxiality loading, $\nu_R = 0.3$, cf. Fig. 7.22(b). During further deformation, more shear bands appear until they accrete and form several

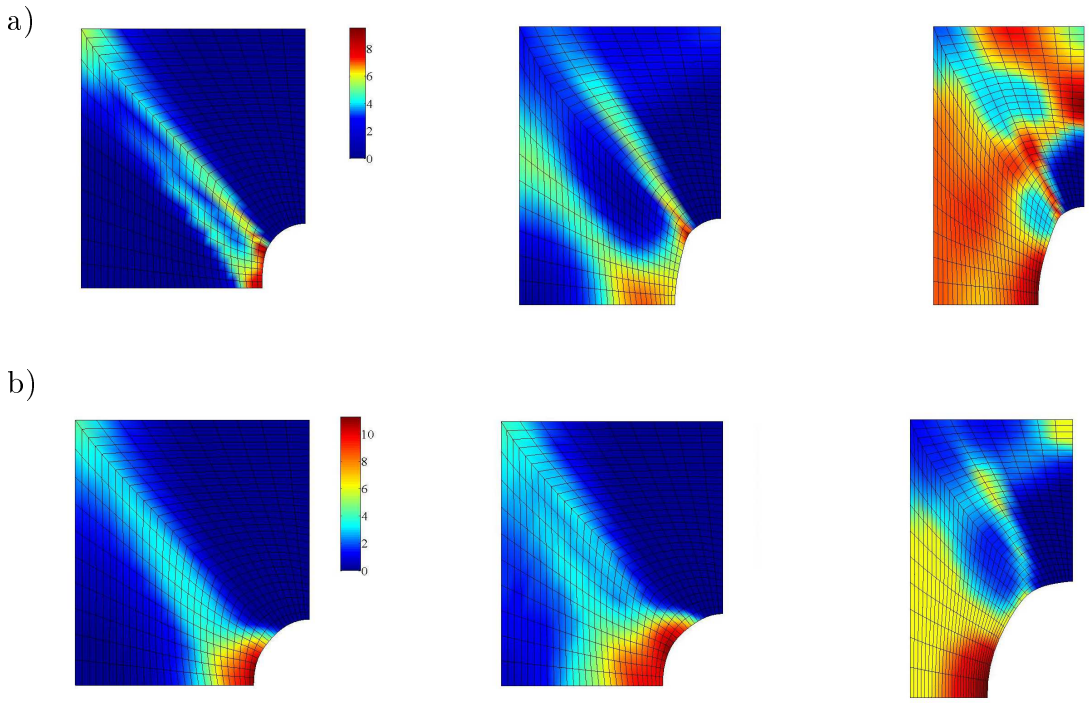

Figure 7.22: Deformed shape of the void with the initial size $a_0/b_0 = 0.20$ for low triaxial stress states a) $\nu_R = 0$ and b) $\nu_R = 0.3$ at three different phases, $E_e = 0.05$, $E_e = 0.10$ and $E_e = 0.20$. The deformed meshes of the cell are visualized by the normalized plastic shear rate $\dot{\gamma}^p/\dot{\Gamma}$. The material data for PC is given in Table 7.2. The applied strain rate is $\dot{E}_2/\dot{\gamma}_0 = 1.2 \cdot 10^{-19}$.

discrete zones. As is shown in Fig. 7.22, the region of the localization extends through the ligament leading to a strong interaction between the neighboring voids. As a result of inhomogeneous deformation, the void grows into a strongly prolate shape while the material is drawn into the ligament between the voids. As was mentioned above, the unit cell model cannot accurately predict the pattern of localized deformation in this phase. Better agreement may be obtained, e.g., with the RVEs based on a staggered square array which is the two-dimensional analog to a three dimensional BCC-lattice (Body Centered Cubic array of voids), cf. e.g. Steenbrink and Van der Giessen (1998a) and Socrate and Boyce (2000) for more detailed account.

Void growth and softening/hardening characteristics

During deformation, the applied force f_2 is also monitored and the corresponding macroscopic effective stress Σ_e versus the effective strain E_e responses for different stress states, as well as parameter values h_1 and s_{ss}, are shown in Fig. 7.23(a). As the stress triaxiality ratio increases from zero to 0.3, a marked drop in the the $\Sigma_e - E_e$ response can be observed, whereas the influence of the softening slope h_1 on the response can be regarded as small. In contrast to the influence of h_1, a reduction of the saturation value s_{ss} considerably decreases the effective stress Σ_e once the yield peak is reached. As it is shown in 7.23(b),

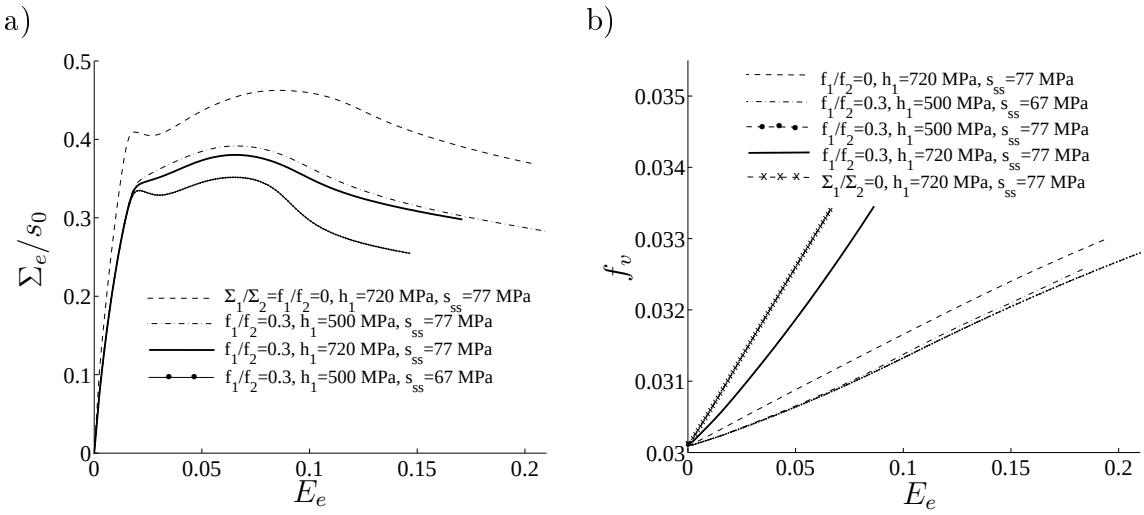

Figure 7.23: Effect of the stress state and the parameters h_1 and s_{ss} on a) the macroscopic effective stress-strain response and on b) void volume fraction-effective strain response for PC. The initial void size $a_0/b_0 = 0.20$ corresponds to the initial void volume fraction $f_{v0} = 0.03$. Rest of the parameters used in the simulations are listed in Table 7.2.

the triaxiality also strongly influences void growth: the higher the triaxiality is applied the faster the growth. Unlike with the overall effective stress response, void growth is substantially accelerated by the softening slope h_1 whereas the influence of the saturation value s_{ss} on the $f_v - E_e$ response remains relatively small. Moreover, the true stress ratios in conjunction with the high value $h_1 = 720$ MPa lead to an unrealistic void growth. A reduction of h_1 results in the difference between the $f_v - E_e$ responses at different stress states is considerably reduced. As the higher triaxiality $\nu_R = 0.3$ and the lower value of $h_1 = 500$ MPa are applied, void growth is approximately 10%, which can be considered realistic for the PC under study. It can be concluded that the stress state in the cell is similar to the constant nominal stress state rather than to the constant true stress state, the overall stress triaxiality remains low during deformation and the softening slope should be substantially reduced.

A comparison of Figs. 7.22 and 7.23(a) reveals that the first shear band is initialized once the macroscopic effective yield stress is reached. Under uniaxial macroscopic tension $\nu_R = 0$, softening inside the band appears as a drop in the $\Sigma_e - E_e$ response, whereas the response for $\nu_R = 0.3$ only exhibits a reduced hardening. Hardening of the material takes place since the portion of the localized zone compared to the viscoelastic region at this phase is small. During continued deformation, the region of localization expands while the macroscopic response shows a reduction, this being due to the stronger intrinsic softening inside the new bands compared to hardening within the highly concentrated regions.

Influence of the entanglements and hydrostatic pressure in ligament

Based on the evolution equation (6.7), the role of the entanglement density in the propagation of shear bands and void growth is investigated. Fig. 7.24 pertains to the PC-polymer

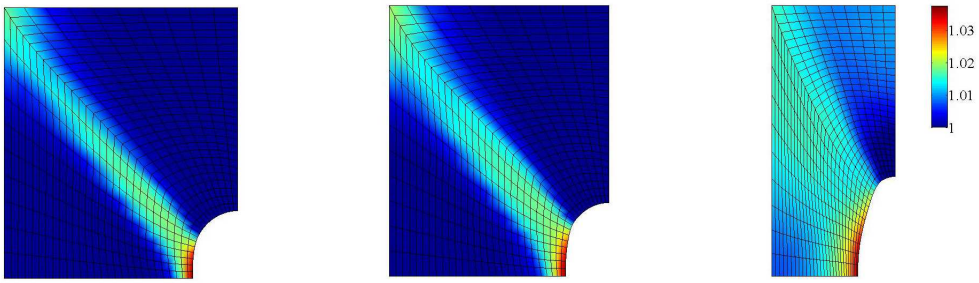

Figure 7.24: Deformed shape of the void with the initial size $a_0/b_0 = 0.20$ for low triaxial stress state $\nu_R = 0$ at three different phases, $E_e = 0.05$, $E_e = 0.10$ and $E_e = 0.20$. The deformed meshes of the cell are visualized by the relative chain density m/m_0.

under low triaxial stress state $\nu_R = 0$ and the initial void volume fraction $f_{v0} = 0.03$ as the number of entanglements is allowed to vary. According to the simulations, the number of entanglements has only a small influence on the deformation behavior in relatively small strains, i.e. the distribution of the normalized plastic shear rate $\dot{\gamma}^p/\dot{\Gamma}$ accurately conforms to the two first distributions in Fig. 7.22(a). Thus, the deformed mesh is only visualized at the last phase $E_e = 0.20$ by $\dot{\gamma}^p/\dot{\Gamma}$, cf. Fig. 7.25(b). Moreover, the deformed meshes of all three different phases $E_e = 0.05$, $E_e = 0.10$ and $E_e = 0.20$ are visualized by the relative chain density m/m_0, cf. Fig. 7.24. A glance at Fig. 7.22(a) reveals that the strongest growth of the entanglement density initially appears within the shear bands. In contrast to the formation of shear band patterns during further deformation, the region with the highest entanglement density does not divide into two parallel zones but remains continuous and widens in its lateral direction. Under the largest strain $E_e = 0.20$, the distribution of the entanglement density considerably differs from shear band propagation. However, similar to the shear band pattern, the growth of the entanglement density beyond the equator of the void is small, ranging between 0.5% - 2%.

Let us then consider the effective stress-strain responses in Fig. 7.25(a). As shown, an increase in the number of entanglements leads to a slightly reduced initial overall stiffness. Once the strain level $E_e \approx 0.12$ is passed, the effective stress-strain response for an increased entanglement density shows a small increase in effective stress meanwhile the response for the constant entanglement density shows reduction. The differences between the responses can be explained by the softening behavior. In comparison with the plastic shear rate in Fig. 7.22(a), the intensity of the localization phenomenon, and as a result the amount of intrinsic softening, are substantially reduced and only a one sharp shear band around the void can be observed, cf. Fig. 7.25(b). It can also be observed from Figs. 7.22(a) and 7.24 that the size and shape of the void are almost unaffected by the present changes in the entanglement density.

Fig. 7.26 presents the distribution of the hydrostatic pressure p for the low triaxial loading states $\nu_R = 0$ and $\nu_R = 0.3$ at $E_e = 0.20$. Similar to purely elastic mean stress fields, cf. Goodier (1933), the highest absolute values of p are found at the equator of the void. Moreover, the values around the void are approximately 20% larger for $\nu_R = 0.3$

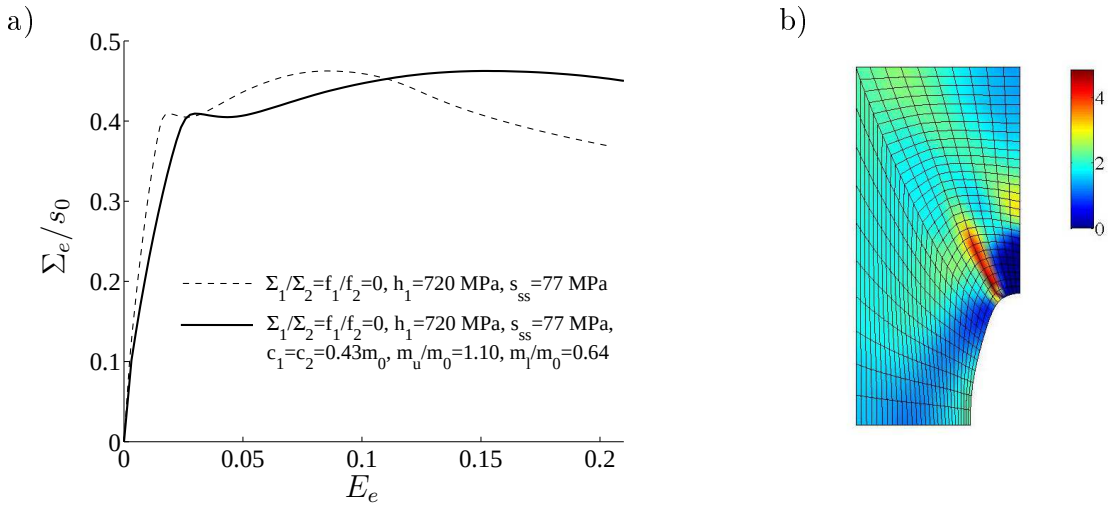

Figure 7.25: a) Influence of the number of entanglements on the macroscopic effective stress-strain response. b) Deformed mesh at $E_e = 0.20$ for low triaxial stress state $\nu_R = 0$ is visualized by the the normalized plastic shear rate $\dot{\gamma}^p/\dot{\Gamma}$. The initial void size $a_0/b_0 = 0.20$ corresponds to the initial void volume fraction $f_{v0} = 0.03$. The rest of the parameters used in the simulations are listed in Table 7.2.

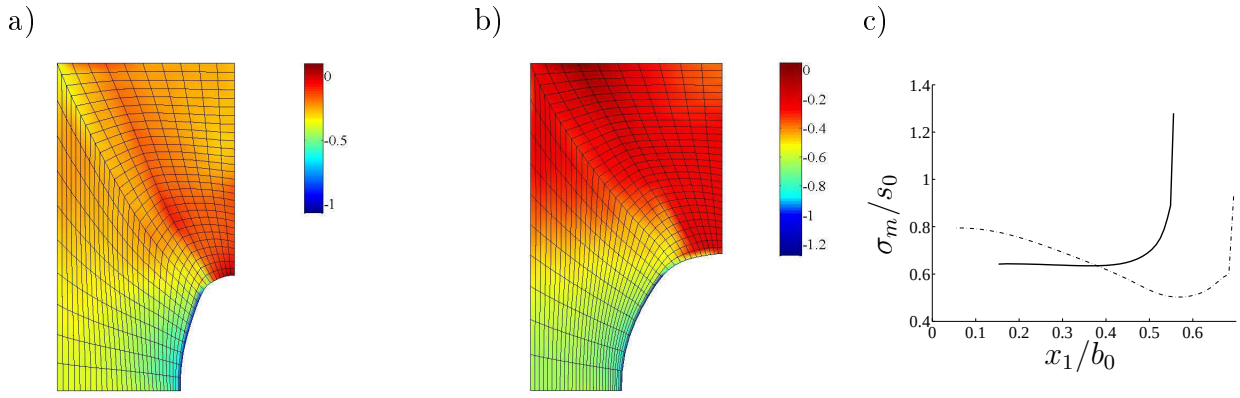

Figure 7.26: Distribution of the hydrostatic pressure $p/s_0 = -1/3trace(\Sigma)/s_0$ for low triaxial nominal stress states a) $\nu_R = 0$ and b) $\nu_R = 0.3$ at $E_e = 0.20$. c) Mean stress $\sigma_m := -p$ distributions for $\nu_R = 0.3$ beyond the equator at $x_2 = 0$. The solid line corresponds to the distribution in b) meanwhile the dot-and-dash line represents the distribution near the maximum of Σ_e at $E_e = 0.12$, obtained by using a very fine mesh. The initial size of the void is $a_0/b_0 = 0.20$.

than under uniaxial macroscopic tension, $\nu_R = 0$. Fig. 7.26(c) shows the influence of the mesh on the mean stress σ_m ($\sigma_m := -p$) distribution along the equatorial plane at $x_2 = 0$. Owing to the highly concentrated plasticity in the ligament, the elastic mean stress field is disturbed and high values of σ_m beyond the equator can be found by using a fine mesh. Since necking is closely related to high mean stress concentrations, cf. Steenbrink *et al.* (1997), neck propagation in the ligament between the voids may be possible during further deformation. At the present instant, however, the deformed shape of the void is prolate rather than oblate which implicates that the ligament elongates without necking.

The numerical results also show that the hydrostatic pressure around the void rapidly

increases and, once the yield point is passed, reaches relatively stable values, ranging between $1.0s_0 - 1.2s_0$. Assuming that the initiation of craze is controlled by the value of the hydrostatic pressure during initial yielding, void growth is attributed to crazing around the voids. Under such circumstances, some of the molecules break and the microstructure of the polymer around the voids alters substantially. As a result, the pronounced localization within the ligaments and crazing around the voids increase the interaction between the voids, which may lead to collapse of the ligament by necking and eventually to coalescence of neighboring voids. As a consequence, void coalescence in relation to void growth substantially increases in large strains, and this property should be taken into account in the models.

7.6 Investigation of the damage behavior

Amorphous glassy polymers exhibit several damage processes such as crazing, cavitation of rubber particles, or impurities and micro-cracking within the matrix material. In this context, damage is ascribed to the distributed growth of void volume (increased porosity) and crazing during localized deformation. Concerning void growth, many of the inelastic damage models available for amorphous glassy polymers are based on the explicit knowledge of the yield surface involving a large number of material parameters to be identified, cf. Gologanu *et al.* (1997), Seeling and Van der Giessen (2002), Pijnenburg *et al.* (2005), Zaïri *et al.* (2008) and Zaïri *et al.* (2011). However, the damage processes observed in amorphous glassy polymers are complex phenomena and their modeling seems to require such complexity. The models developed for metals have initially been considered for that purpose, cf. Rice and Tracey (1969) and Needleman and Tvergaard (1984). A widely used dilatational plasticity model is the one introduced by Gurson (1977) and later modified by Tvergaard (1981). The Gurson model is based on the assumption that the deformation mode of the material surrounding a void is homogenous. According to this model, softening behavior in the material results from the growth of voids, i.e. the model does not possess the intrinsic ability to predict localized deformation by void coalescence. However, as it was pointed out in the preceding section, the voids become coalesced in very large strains which cannot be achieved e.g. during the cold drawing experiment under consideration. Hence, the difference between the model calibrations for homogeneous and inhomogeneous deformation can be ascribed to the nucleation and growth of voids instead of void coalescence.

7.6.1 Modeling of void growth

In order to investigate the damage behavior caused by void growth, macroscopic constitutive relations in the EBPA model are modified by using an augmented Gurson model, which also takes the nucleation of new voids into account. The proposed model is formulated in terms of the multiplicative decomposition of the total deformation gradient into an elastic and a plastic part and it is implemented in a finite element setting.

The damage evolution is assumed to be isotropic and it is represented by a void volume fraction $f_v = dV_v/dV_c$, which is the average measure of a void-matrix aggregate with the initial value $0 \leq f_{v0} \leq f_v < 1$, cf. (7.13). Since the inelastic Gurson potential Φ^p acts as both a yield function and a potential for plastic flow, the theory is considered as associative. To better predict the instability in the material due to the interaction of voids, Tvergaard (1981) proposed a modified Gurson damage model in which the inelastic potential is given by

$$\Phi^p(\tau, \sigma_m, f_v, \sigma_e) = \tau^2 + 2 f_v q_1 \sigma_e^2 \cosh(\frac{3}{2} q_2 \frac{\sigma_m}{\sigma_e}) - \sigma_e^2 (1 + q_1^2 f_v^2) \tag{7.16}$$

where $\sigma_m := 1/3 trace(\boldsymbol{\sigma})$ is the macroscopic mean stress. In accordance with the previous approaches by Tvergaard (1981) and Becker and Needleman (1986), the microscopic effective stress of the solid ligaments σ_e is introduced separately from the macroscopic effective stress τ. The microscopic effective stress σ_e is determined from the condition $\Phi^p = 0$. Based on the potential (7.16), the rate of plastic deformation is governed by the modified normality rule

$$\boldsymbol{d}^p = \dot{\Lambda}^p \frac{\partial \Phi^p}{\partial \boldsymbol{\sigma}} \tag{7.17}$$

where $\dot{\Lambda}^p$ is a scalar valued parameter defined below. The kinematic hardening effect is included in the model via the macroscopic effective stress $\tau(\tilde{\boldsymbol{\sigma}})$, which was defined by (4.109). As with the BPA model, the intrinsic softening is modeled via the athermal shear strength s_1, which is taken to evolve according to (6.2).

In contrast to the original Gurson spherical model for incompressible, rigid-plastic material, Tvergaard (1981) suggested that the values $q_1 = q_2 = 1$ in (7.16) need to be replaced by $q_1 = 1.5$ and $q_2 = 1.0$ to better capture bifurcation away from the nominally homogeneous deformation. For amorphous glassy polymers, however, the constant values of q_1 and q_2 cannot satisfactorily predict either void growth or the change of the void shape during deformation. To capture the expected characteristics of void growth, Zaïri *et al.* (2008) suggested that q_1 and q_2 should be considered as internal variables given by the following empirical power laws:

$$q_1 = q_{10}(1 + c p_v)^{N_v}, \quad q_2 = q_{20}(1 + c p_v)^{N_v} \tag{7.18}$$

where q_{10}, q_{20}, c and N_v are constitutive parameters and p_v denotes an internal variable defined subsequently. The low values of q_{10} and q_{20} indicate weak interactions between the voids while softening in the material decreases, cf. Zaïri *et al.* (2008). In the flow rule (7.17), a scalar parameter $\dot{\Lambda}^p$ was introduced. This can be determined from equivalence between the plastic power which is dissipated into the porous media and into the corresponding solid ligaments between the voids, i.e.

$$\tilde{\boldsymbol{\sigma}} : \boldsymbol{d}^p = (1 - f_v)\sqrt{2}\sigma_e \dot{p_v}. \tag{7.19}$$

In (7.19), $\dot{p_v}$ denotes the effective plastic strain rate, which is chosen to be equal to the plastic shear strain rate $\dot{\gamma}^p$ given in (4.75). Since γ^p is monotonically increasing, cf. Figs.

6.9 and 7.18, the variables q_1 and q_2 given by (7.18) increase during deformation. Moreover, since $\dot{\gamma}^p > 0$, a glance at (4.58) reveals that $\sigma_e > 0$. This condition must be handled with care, since it is not generally satisfied by the solution of $\Phi^p = 0$. It then follows from (7.17) and (7.19) that

$$\dot{\Lambda}^p = \sqrt{2}(1 - f_v)\sigma_e\dot{\gamma}^p(\tilde{\boldsymbol{\sigma}} : \frac{\partial\Phi^p}{\partial\boldsymbol{\sigma}})^{-1}.$$

Based on the normality rule (7.17), the rate of plastic deformation takes the following form

$$\begin{aligned} \boldsymbol{d}^p &= \sqrt{2}(1 - f_v)\dot{\gamma}^p\sigma_e(2\tau^2 + \Xi trace(\tilde{\boldsymbol{\sigma}}\,))^{-1}(\tilde{\boldsymbol{\sigma}}^{dev} + \Xi\boldsymbol{i}), \\ \Xi &:= q_1 q_2 f_v \sigma_e \sinh\big(\frac{3}{2}q_2\frac{\sigma_m}{\sigma_e}\big). \end{aligned} \tag{7.20}$$

It should be noticed that the condition $\Phi = 0$ yields $\sigma_e = \tau$ if $q_{10} = q_{20} = 0$, i.e. no interaction between the voids exists. Under this condition, a realistic assumption is that damage does not evolve, i.e. $\dot{f}_v = 0$ and the normality rule (7.20) is equal with (4.109) for the plastic deformation through shear yielding. Compared to (4.109), (7.20) allows dilative plastic flow to be evolved in the material.

The damage process due to the presence of voids can be separated into the two phases, cf. Fig. 7.20(a-b) and (c-d). First, the homogenous deformation takes place with void nucleation and growth, which is followed by the localized deformation due to void coalescence. The corresponding evolution law for the first phase is additively decomposed into the two parts

$$\dot{f}_v = \dot{f}_g + \dot{f}_n, \quad f_v(0) = f_{v0} \tag{7.21}$$

where $\dot{f}_g$ describes the growth of existing voids under plastic stretching being defined as

$$\dot{f}_g = 3(1 - f_v)D_h^p. \tag{7.22}$$

In (7.22), $D_h^p := 1/3 trace(\boldsymbol{d}^p)$ is the plastic volumetric strain rate. The nucleation of new voids is assumed to be significant but the process is not well understood yet. It is a material intrinsic property being dependent on the strength of the polymeric material as well as on the size and shape of existing voids. Large voids usually nucleate new voids earlier than small voids, and inclusions with different length scales may also lead to different nucleation criteria, cf. Zhang *et al.* (2000). To capture the accelerated damage due to the nucleation of new voids, Chu and Needleman (1980) proposed the following strain-controlled law for the nucleation rate

$$\dot{f}_n = \frac{f_N}{s_v\sqrt{2\pi}}\exp\big(-\frac{1}{2}\big(\frac{\gamma^p - \varepsilon_N}{s_v}\big)^2\big)\dot{\gamma}^p \tag{7.23}$$

where f_N is a constant which denotes the volume fraction of voids caused by void nucleation. The mean value ε_N of the normal distribution describes the critical strain beyond which the first new voids appear. Since not all the inclusions/particles will nucleate new voids, the parameters f_N, ε_N and the standard deviation s_v are obtained from calibration to the material's macroscopic response.

One important aspect is the ability of the proposed model to account for the real defor-

mation behavior as well as quantitative damage prediction. For the numerical evaluation of the model, the constitutive equations (7.4) are completed by the integration of the void volume fraction rates given by (7.22) and (7.23). It should be noticed that the plastic shear γ^p, which is needed in (7.23), is available from the solution of the hardening variable s_2, cf. (6.2).

7.6.2 Calibration and evaluation of the augmented EBPA model for void growth

The augmented Gurson model in conjunction with the EBPA model is calibrated to data obtained from the cold drawing experiment. In the calibration, the same element mesh as before is employed. Since the model includes a relatively large number of parameters, the calibration is initialized using the parameters for rubber-toughened PMMA (RTPMMA) taken from Zaïri *et al.* (2008). Both the calibrated and the parameters for RTPMMA are listed in Table 7.3. By analogy to the initial shear strength distribution (7.8), the values of f_N, or alternatively the initial porosity f_{v0}, can be disturbed. However, the calibration indicated that their influence on the macroscopic $f-u$ response is small as the intensity of the initial imperfection varied between $\xi = 0 - 0.03$. In the subsequent simulations, the intensity ξ is kept at zero and the localization is triggered according to (7.7) using $\xi_0 = 0.002$. Calibration also indicated that

- the growth of void volume suppresses the isotropic softening effect,
- the change in the initial void volume fraction from $f_{v0} = 0$ to $f_{v0} = 0.05$ only has a small effect on the macroscopic $f-u$ response,
- the values $c > 0$ which influence damage evolution via (7.18), reduce void growth.

Since the PC polymer under study is not interspersed by small rubber particles, and the influence of a low initial void volume fraction on the macroscopic response is negligible, we set $f_{v0} = 0$. Moreover, numerical investigations under low triaxial stress states indicate that the influence of the initial void volume fraction on the macroscopic elastic properties, as well as on the Gurson's yield function, is small, cf. Steenbrink *et al.* (1997).

Having less intrinsic softening due to void growth allows the softening slope h_1 and the intensity s_{ss}/s_0 to be reduced to a level which agrees more closely with the values obtained from the calibration for homogeneous deformation. As a consequence, the intensity $s_{ss}/s_0 = 0.80$, which was previously employed in the EBPA model, is reduced to 0.65. It can be concluded that the difference between the calibrations for homogeneous and inhomogeneous deformation is strongly affected by void growth in the material.

The influence of the parameters q_{10}, q_{20} and c on the overall force-elongation response is shown in Fig. 7.27. As the parameters q_{10} and q_{20} are decreased, neck stabilizes in a reduced range, followed by a weak hardening which is initialized at $u = 22 - 24$ mm. The applied load f is seen to be increased by the nonzero values of c, i.e. the interaction between the voids compensates for the reduction of intrinsic softening and allows for the

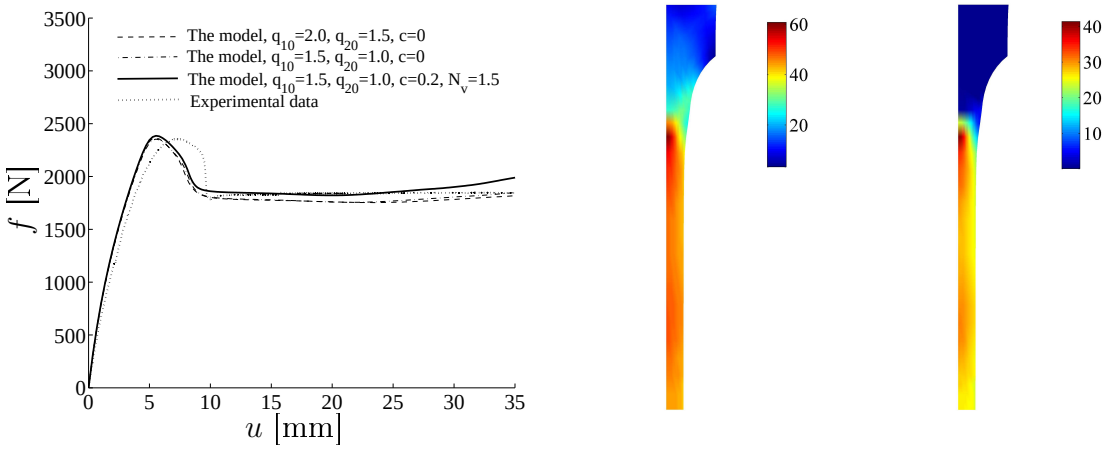

Figure 7.27: Influence of the parameters q_{10}, q_{20} and c on $f-u$ response. Based on the calibrated parameters in Table 7.3 the deformed shapes at $u = 35$ mm are visualized by the microscopic effective stress σ_e of ligaments and by the difference $\sigma_e - \tau$.

lower intensity s_{ss}/s_0 to be used. A comparison between the EBPA model responses in Figs. 7.13(a) - 7.15(a) and the damage model result in Fig. 7.27 also reveals that the stress drop after the yield point becomes deeper. The distribution of the effective stress σ_e of the ligaments and the difference $\sigma_e - \tau$ are also presented in Fig. 7.27. Apart from the highly concentrated region around the interface of the gauge section and the grip, the effective stress is propagated similarly to the localized deformation. At the end of loading, the values of σ_e in the gauge section are approximately three times greater than the values of the macroscopic effective stress τ, which indicates a strong interaction between the voids and the possibility to void coalescence during further deformation.

Based on the model simulations the plastic stretch distributions are highlighted in Fig. 7.28. It can be observed that damage reduces the intensity of the plastic stretching, while the localized deformation expands more rapidly along the specimen. A glance at Fig. 7.17 reveals that the necked region which is predicted by the combined EBPA and the damage model reaches the end of the gauge section simultaneously with the experiment.

Fig. 7.29 presents the total growth of void volume and the influence of the hardening slope h_1 on the void growth. The values ranging between $385 - 560$ MPa are seen to have only a minor effect on void growth. It can also be observed that the void nucleation is prohibited until the elongation $u \approx 5$ mm is reached. This threshold corresponds ap-

Table 7.3: Constitutive parameters of the damage model for RTPMMA and PC. Calibration of the proposed model is performed to data obtained from the cold drawing experiment. The RTPMMA parameters are taken from Zaïri *et al.* (2008).

	η	h_1	s_{ss}	ε_N	s_v	f_N	q_{10}	q_{20}	c	N_v
	MPas^{-1}	MPa	MPa							
RTPMMA				0.03	0.15	0.15	0.9	1.2	0.2	1.5
EBPA for PC	$1.5 \cdot 10^5$	385	61	0.03	0.15	0.05	1.5	1.0	0.2	1.5

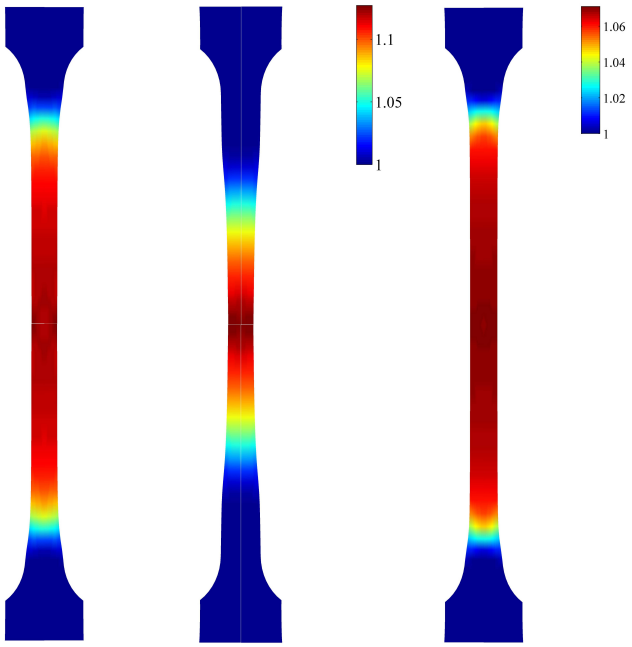

Figure 7.28: Distribution of the plastic stretch $\bar{\lambda}^p_{ec}$ at the end of loading ($u = 40$ mm) according to the BPA model, the EBPA model and the EBPA model in conjunction with the damage model (on the right). The simulation based on the damage model is performed using the calibrated material parameters given in Table 7.3.

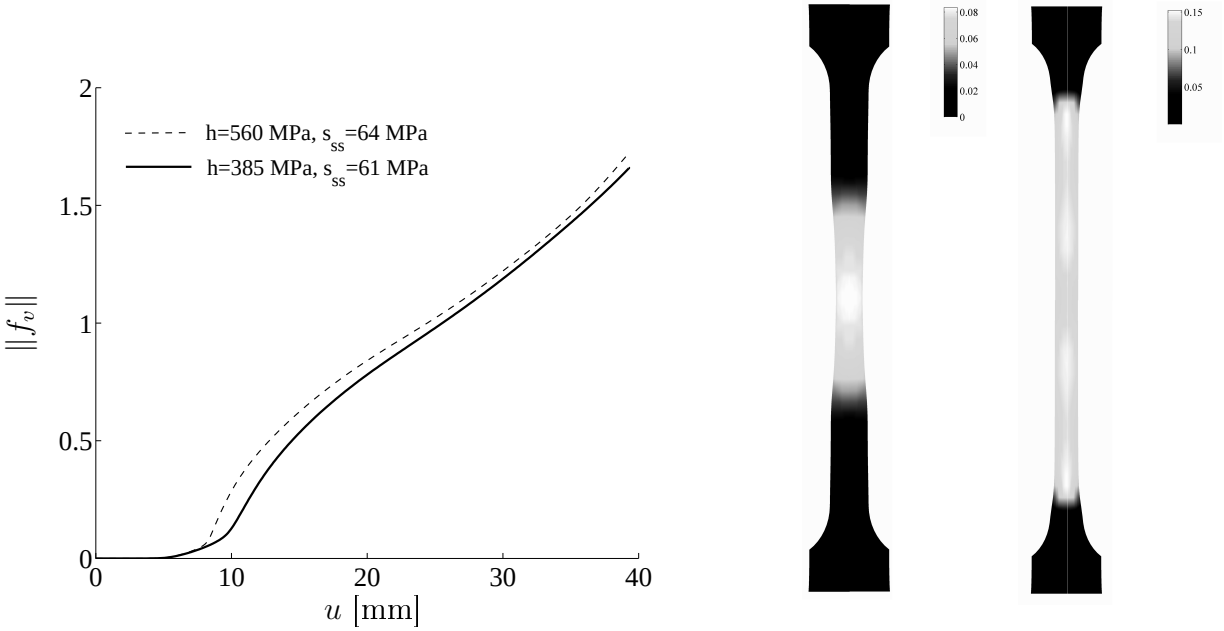

Figure 7.29: Influence of the parameter h_1 on void growth, which is represented by the norm of void volume fraction $\|f_v\| := \sqrt{\sum_i (f_{v,i} \cdot f_{v,i})}$ where $f_{v,i}$ are the extrapolated values of void volume fraction at the nodes of the mesh. The deformed shapes at $u = 20$ mm and at the end of loading are visualized by void volume fraction f_v. The highest porosity f_v is highlighted in white.

proximately to the elongation prior to the yield drop. Once the yield point in the stress response is passed, the voids grow rapidly and increase the porosity in the localized zone, cf. Fig. 7.29. Similar to the plastic stretching, the highest values appear in a region which gradually expands from the center of the specimen towards the grips during elongation. At the end of loading, the porous region covers the gauge section entirely, and the highest porosity occurs in the two separate regions beyond the mid-plane, $y = L/2$.

As has been shown, the EBPA model, along with the augmented Gurson model for void growth, is able to predict the transformation from the homogeneous deformation phase to the localized deformation phase well. Applying this model, the difference between the model parameters, which result from the calibration for homogeneous and inhomogeneous deformation, also decreased considerably. A shortcoming of the model is that the force-elongation response during neck shows a premature hardening while the void volume fraction grows and attains values too high for unvoided polymers.

7.6.3 Modeling of crazing

Under compression, amorphous polymers frequently show ductile localized deformation behavior, which is due to shear yielding with small volume changes. In contrast to the shear yielding mechanism, which involves shear band propagation and eventual fracture by a chain scission in large strains, the governing mechanism of inelastic deformation under tension is a dilatational localization in zones of fibrillation, termed crazing, cf. Anand and Gearing (2004) and Argon (2011). More precisely, crazing is assumed to result from disentanglement in highly concentrated regions of maximum principal stress. Disentanglement nucleates new micro-voids which grow and coalesce to form initial crazes and cause stretching and eventually failure of the thin fibrils between the two faces of the initial crazes, cf. Kramer (1983) and Basu *et al.* (2005). As a result of the breakdown of the fibrils, crazes widen leading to local brittle failure while material behavior at the macroscopic level still shows a little ductility. In all, the nominally brittle failure can be separated into the three different phases: craze-initiation, widening and craze-breakdown.

Despite all the active research carried out during the last decades, the governing micromechanism that controls crazing is still not fully understood. Experimental investigations have shown a major importance of the entanglement density in macroscopic failure through crazing or shear yielding. Initial plastic deformation through shear yielding in amorphous glassy polymers is usually followed by crazing or alternatively crazing propagates on stable manner, cf. Ishikawa and Ogawa (1981) and G'Sell *et al.* (2002). Examples of the polymers in the first group are e.g. PC and PMMA, and polymers involving stable crazing are e.g. HIPS and ABS that are frequently used in toughened polymer blends. According to Ishikawa and Ogawa (1981), decrease of temperature and increase of the strain rate result in more brittle failure in amorphous glassy polymers, i.e. the difference between the time instants for craze-initiation and breakdown decreases. They also pointed out that the void nucleation is a precursor to crazing and crazes initiate due to high mean stress

concentrations around the micro-voids, cf. also Fig. 7.26.

In recent years, cohesive-surface models have been widely applied to the numerical simulation of craze-initiation, growth and breakdown with the finite element method, cf. e.g. Estevez *et al.* (2000) and Pijnenburg *et al.* (2005). In a finite element setting, however, cohesive interface approaches allow for the nucleation and growth of the crack only along the element boundaries. In order to avoid mesh dependence and priori assumptions concerning the orientation of interface elements for crazing, an alternative, continuum-based model is proposed here. According to this model, craze-initiation which takes place during shear yielding is followed by widening of crazes and failure due to the breakdown of the fibrils. A simple craze-initiation criterion is introduced and the transition from shear-flow to craze-flow is carried out by a change of the flow rule, where the inelastic deformation is taken to occur in the direction of the local maximum principal stress. Once the local critical plastic strain is reached, crazes rapidly widen which eventually leads to local fracture or chain-breakdown under compression or tension, respectively.

The craze-initiation can be governed by strain- or stress-based criteria. Argon and Hannoosh (1977) conducted tension-torsion stress-controlled experiments on thin-walled tubular specimens, which indicated that there is a time delay between the application of stress and the first appearance of crazing. At the stress levels, where the equivalent stress τ and the mean normal stress σ_m exceed 0.4 - 0.5 of the yield stress, the delay time considerable decreases and as a result craze-initiation can be considered as instantaneous event. Since the crazing process in the present drawing experiments occurs in stress levels higher than 0.4 - 0.5 of the yield stress, the incubation time for craze-initiation can be assumed negligible and a time-independent criterion can be applied in the proposed model.

In general, the development of crazing may be expected to have directional properties. Based on the assumption that the crazes grow in the direction of the maximum principal tensile stress, Anand and Gearing (2004) proposed that crazing initiates when the mean stress is positive $\sigma_m > 0$, and the highest principal stress σ_1 reaches a σ_m-dependent critical value $\sigma_1 = \sigma^{cr}(\sigma_m) > 0$. They estimated the critical value σ^{cr} from the tension experiments on a smooth-bar, notched-bar and a compact tension specimen. They observed that the curve for craze-initiation just prior to the yield-peak load is reasonably-well captured by the function

$$\sigma^{cr} = c_1 + \frac{c_2}{\sigma_m} \tag{7.24}$$

where c_1 and c_2 are positive parameters. In general, stress-based criteria may be difficult to define with precision from experiments due to inaccuracies in controlling local stress states and the sites of craze-initiation, cf. Argon and Hannoosh (1977). For this reason, a corresponding strain-based criterion needs to be determined. It can be assumed that the crazes are initiated if the following two conditions are satisfied:

[1.] The highest principal tensile stress and the mean normal stress are positive, i.e. $\sigma_1 > 0$ and $\sigma_m > 0$,

[2.] the craze-strain ζ^p, which evolves in the direction of the highest principal tensile stress, reaches a critical value $\zeta^p := \int \dot{\zeta}^p \mathrm{d}t = \zeta^p_{cr} > 0$. Correspondingly, $\sigma_1 = \sigma^{cr} > 0$.

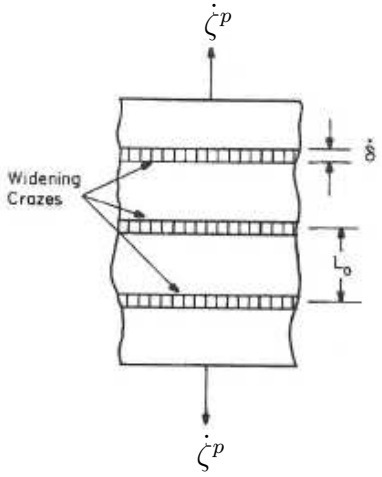

Figure 7.30: Widening of crazes at an average spacing L_0. The macroscopic tensile craze strain rate $\dot{\zeta}^p$ is determined by the thickening rate $\dot{\delta}$ of crazes. After Argon (1999), Fig. 7.

Once crazing has been initiated, the transition from shear-flow to craze-flow takes place while the plastic flow aligns with the direction of the maximum principal stress σ_1, and the inelastic deformation begins to evolve through widening of the crazes. Instead of attempting to represent a detailed scheme for craze-widening, cf. Kramer and Berger (1990) and Estevez *et al.* (2000), a continuum-based model, which defines the inelastic deformation as an average over a microstructural representative volume element, is proposed. It is assumed that the material element contains enough plate-like craze regions that allow for macroscopically smooth craze-widening process prior to failure. The magnitude of the craze-flow is given by the macroscopic tensile craze-strain rate $\dot{\zeta}^p$ and it evolves as long as σ_1 is positive. Following Argon (1999), $\dot{\zeta}^p$ is assumed to be accounted for by the thickening rate $\dot{\delta}$ of the active planar crazes which are separated by an average spacing L_0, cf. Fig. 7.30. Thus the average tensile craze-strain rate becomes $\dot{\zeta}^p = \dot{\delta}/L_0$. In terms of the eigenvectors $\boldsymbol{n}_1$ associated with the highest principal stress, the transition from shear-flow to craze-flow is given by

$$\boldsymbol{d}^p = \begin{cases} \dot{\zeta}^p \boldsymbol{n}_1 \otimes \boldsymbol{n}_1 & \text{if the conditions [1]-[2] are satisfied,} \\ \dot{\Lambda}^p (\tilde{\boldsymbol{\sigma}}^{dev} + \Xi \boldsymbol{i}) & \text{otherwise} \end{cases} \tag{7.25}$$

where $\dot{\Lambda}^p := \sqrt{2}(1-f_v)\dot{\gamma}^p \sigma_e (2\tau^2 + \Xi trace(\tilde{\boldsymbol{\sigma}}))^{-1}$ and $\Xi := q_1 q_2 f_v \sigma_e \sinh\big(3/2 q_2 \sigma_m/\sigma_e\big)$, cf. (7.20). The magnitude of the rate of plastic deformation $\dot{\zeta}^p = |\boldsymbol{d}^p|$ is determined such that some continuity during the transition from shear-flow to craze-flow is ensured. The equality between the plastic work rate in the porous material per unit volume and the dissipation in the matrix material is governed by

$$\tilde{\boldsymbol{\sigma}} : \boldsymbol{d}^p = (1-f_v)\sqrt{2}\sigma_e \dot{\gamma}^{p*} \left(\frac{\sigma_1}{\sigma_1^*}\right)^m \tag{7.26}$$

where the quantities with the superscript (*) are determined at the instant when the change in the flow rule is triggered. It then follows from (7.23) that nucleation of new voids is

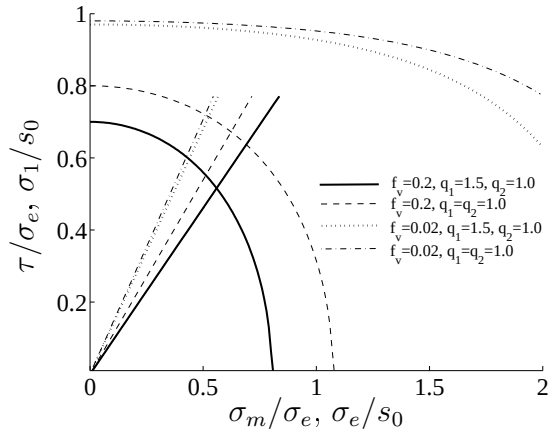

Figure 7.31: The potentials (7.16) and (7.28) in $\tau - \sigma_m$ and $\sigma_1 - \sigma_e$ space, respectively. The influence of the two different values $f_v = 0.02$, $f_v = 0.2$ and $q_1 = 1.0$, $q_1 = 1.5$ are investigated.

governed by the constant rate $\dot{\gamma}^{p*}$ during crazing. Since the experiments show an increased craze widening velocity with the applied stress intensity, cf. e.g. Estevez *et al.* (2000), the plastic work rate is reformulated in terms of the stress ratio σ_1/σ_1^*. The parameter m in (7.26) is found from the calibration to the experimental data. During shear flow, the stress ratio σ_1/σ_1^* remains unity and the plastic shear strain rate $\dot{\gamma}^p$ evolves according to (4.75), i.e. (7.26) equals with (7.19). It follows from (7.25) and (7.26) that the magnitude $\dot{\zeta}^p = |\boldsymbol{d}^p|$ is given by

$$\dot{\zeta}^p = \sqrt{2}(1 - f_v)\sigma_e \dot{\gamma}^{p*} (\frac{\sigma_1}{\sigma_1^*})^m (\tilde{\boldsymbol{\sigma}} : \boldsymbol{n}_1 \otimes \boldsymbol{n}_1)^{-1}. \tag{7.27}$$

The microscopic effective stress σ_e of ligaments is determined from the potential $\Phi^p = 0$, which for the craze-flow is modified such that the flow becomes oriented in the direction of the highest principal stress, i.e.

$$\Phi^p(\sigma_1, f_v, \sigma_e) = \frac{\sigma_1^2}{2} + 2 f_v q_1 \sigma_e^2 \cosh(\frac{q_2}{2}\frac{\sigma_1}{\sigma_e}) - \sigma_e^2(1 + q_1^2 f_v^2). \tag{7.28}$$

Alternatively, employing the function (7.28) in the flow rule (7.17) (replacing $\dot{\Lambda}^p$ by $\dot{\zeta}^p$) and taking advantage of $\partial\sigma_1/\partial\boldsymbol{\sigma} = \boldsymbol{n}_1 \otimes \boldsymbol{n}_1$ also results in the craze-flow rule (7.25), where $\dot{\zeta}^p$ is given by (7.27). Fig. 7.31 presents the potentials in (7.16) and (7.28) for different values of f_v and q_1. The stress trajectories in $\sigma_1 - \sigma_e$ space show proportionality between the macroscopic principal stressing and microscopic stress in ligaments between the voids.

Since the final craze-breakdown can be considered as a physically unclear process, cf. Kramer and Berger (1990) and Estevez *et al.* (2000), a simple criterion for craze-breakdown and fracture are proposed as a first attempt. Following Anand and Gearing (2004), the craze-breakdown under condition $\sigma_1 > 0$ occurs when the local craze-strain ζ^p reaches a threshold value $\zeta_t^p > \zeta_{cr}^p > 0$. In the situations where $\sigma_1 \leq 0$, ductile fracture by molecular chain-scission is initialized as the plastic stretch $\bar{\lambda}_{ec}^p$ reaches a threshold $\bar{\lambda}_t^p$. The two

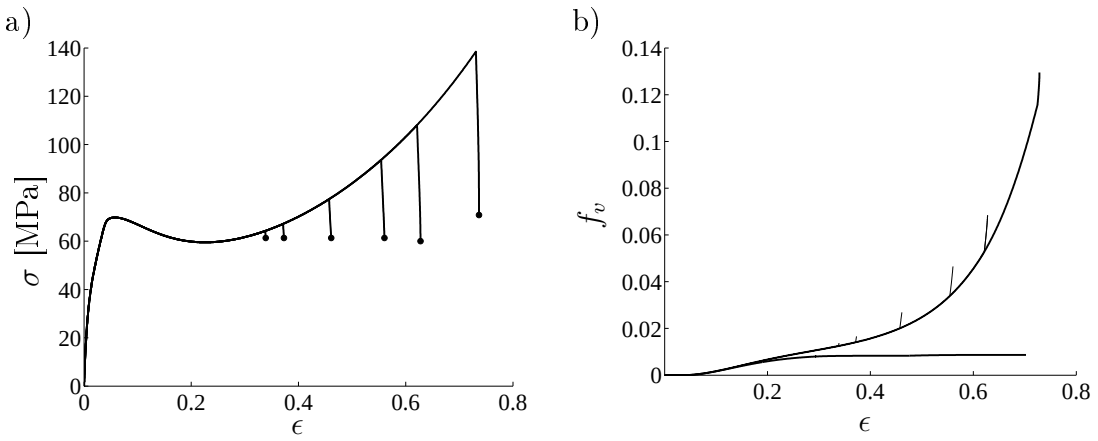

Figure 7.32: a) True stress vs true strain and b) void volume fraction for uniaxial tension of BPA-PC according to the model. Craze-initiation is prescribed by the plastic stretch at $\bar{\lambda}^p_{ec} = 1.04$, $\bar{\lambda}^p_{ec} = 1.05$, $\bar{\lambda}^p_{ec} = 1.08$, $\bar{\lambda}^p_{ec} = 1.12$, $\bar{\lambda}^p_{ec} = 1.15$ and $\bar{\lambda}^p_{ec} = 1.20$. In b), the curve involving a plateau represents void nucleation ($f_g = 0$) being virtually independent on craze-initiation. The simulation covers the time period of 750 s at $\dot{\epsilon} = 0.001$ 1/s.

thresholds ζ^p_t and $\bar{\lambda}^p_t$, in relation to the craze-initiation criteria $\zeta^p = \zeta^p_{cr}$, define the length of the crazing process.

The proposed constitutive model for crazing is implemented in a finite element program. The non-linear system of the residuals (7.4) is augmented by the integration of the strain rate $\dot{\zeta}^p$ for crazing.

7.6.4 Calibration and evaluation of the augmented EBPA model for void growth and crazing

Based on the simulations of the cold drawing experiment for monotonic loading the influence of crazing on the overall load-elongation response and neck propagation is evaluated. In the simulations, the same element mesh as before is employed. The critical value ζ^p_{cr} and the parameter m for the evaluation of craze-flow are obtained from the calibration to the overall load-elongation curve. Based on the discussion above, cf. also G'Sell *et al.* (2002), the plastic deformation in large strains evolves primarily due to crazing and typically shows an increased rate of evolution once crazing has been initialized in the material. Since the stress level decreases during the crazing process, the plastic work rate in the porous material and the dissipation in the matrix material decrease, and as a result, the void volume fraction tends to increase, cf. (7.26). This effect is shown in Fig. 7.32. To prevent an excessive void growth during crazing, the amount of existing voids as well as their growth need to be limited in the model. Consequences of this restriction are that crazing promotes void nucleation and the dissipation alters due to the stress σ_e in the ligaments between the voids.

The influence of crazing on void growth is shown in Fig. 7.33. A comparison with the responses of purely porous material reveals that crazing, which initiates once the yield point is passed, increases significantly void growth during the neck. Similar effect was

also observed in amorphous entanglement network through MD simulations, cf. Mahajan *et al.* (2010). Reducing void nucleation setting $f_N = 0.02$ in (7.23) compensates for the growth which in turn, as already touched upon, suppresses the initiation of new crazes. The difference can be further illustrated by the void volume fractions given in Figs. 7.29 and 7.33. Due to crazing, localized region (in terms of $\bar{\lambda}^p_{ec}$) in the gauge section shows more pronounced intensity of porosity, whereas the area and shape of the porous region remain virtually unaltered during crazing.

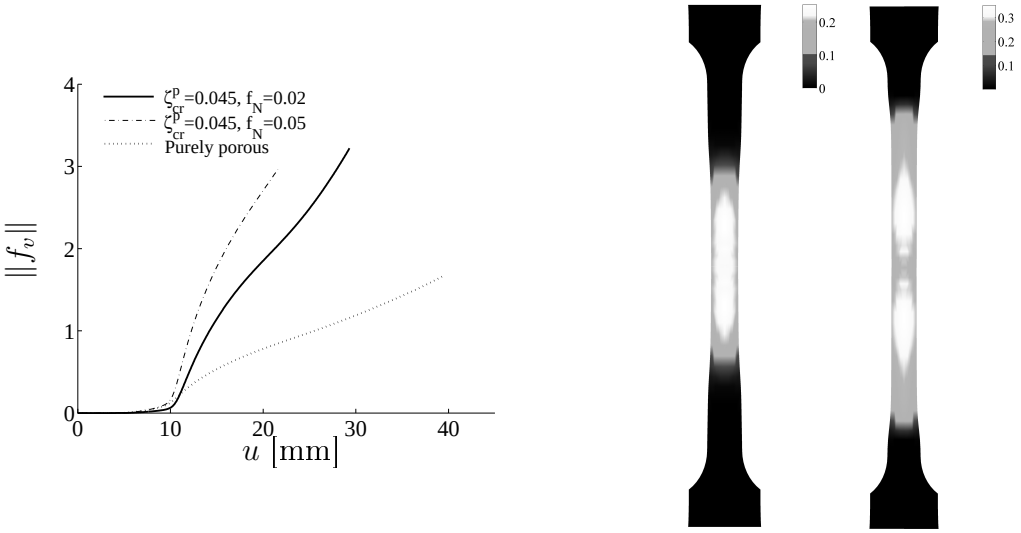

Figure 7.33: Influence of crazing on void growth, which is represented by the norm of void volume fraction $\|f_v\| := \sqrt{\sum_i (f_{v,i} \cdot f_{v,i})}$ where $f_{v,i}$ are the extrapolated values of void volume fraction at the nodes of the mesh. Using $f_N = 0.02$, the deformed shapes at $u = 20$ mm and at $u = 30$ mm are visualized by the void volume fraction f_v. The white color indicates the highest porosity.

An excessive void growth during necking is suppressed by choosing the critical strain for craze-initiation to be $\zeta^p_{cr} = 0.42$, which value approximately corresponds to the elongation $u = 21$ mm and to the plastic stretch $\bar{\lambda}^p_{ec} = 1.055$ in the early-stage of hardening. Moreover, crazing is assumed to result from disentanglement in highly concentrated regions of maximum principal stress, which nucleates new micro-voids and allows their coalesce to form initial crazes rather than larger voids. Thus, use is made of an assumption that the growth of existing voids is inhibited by crazing, i.e.

$$\dot{f}_g = \begin{cases} 0 & \text{during crazing,} \\ 3(1 - f_v) D^p_h & \text{otherwise.} \end{cases} \tag{7.29}$$

Since the stretching in relation to the limiting stretch $\sqrt{N}$ in a representative volume element can be regarded as small during the entire cold drawing process, craze-breakdown barely initiates and will be neglected in the subsequent numerical simulations. To exclude the integration of ζ^p_{cr}, the corresponding stress criterion $\sigma^{cr} = 62$ MPa for craze-initiation can be used in the simulations. This threshold as well as the values $\bar{\lambda}^p_{ec} = 1.05 - 1.12$ in Fig.

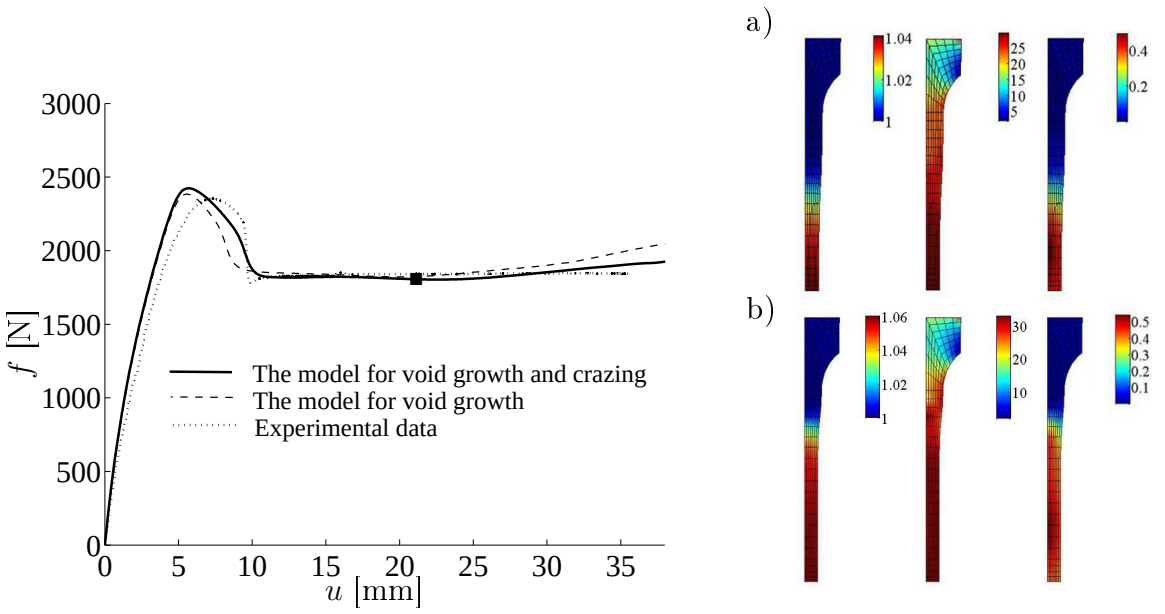

Figure 7.34: Influence of void growth and crazing on the overall $f-u$ response. The marker ■ indicates the position at first craze-initiation. The void fraction parameter in (7.23) is $f_N = 0.02$ and the rest of the parameters is given in Table 7.3. The deformed meshes at a) $u = 20$ mm and b) $u = 33$ mm are visualized by the plastic stretch $\bar{\lambda}^p_{ec}$, mean stress σ_m and by the craze-strain ζ^p.

7.32 for craze-initiation are reasonable-well captured by the parameters $c_1 = 36$ MPa and $c_2 = 650$ MPa, cf. (7.24). Due to necking, the stress ratio σ_1/σ_1^* remains almost unaltered (near unity) during elongation and thus the parameter m in (7.27) is chosen to vanish.

In the numerical analysis, the same element mesh as before is employed. Since crazing in a finite element setting evaluates through the integration points, the influence of the mesh does need attention. Simulations with considerably finer mesh, however, indicated only a small mesh-sensitivity on both the $f-u$ response and localization phenomenon.

In Fig. 7.34, both the porous and the crazed response is depicted. It is found that the void volume fraction, albeit it is almost one magnitude lower compared to the result in Fig. 7.33, has the effect of making the descending portion in the force-elongation curve more gradual. Crazing, however, is seen to compensate this effect. Owing to crazing, premature hardening which appears in the augmented EBPA model predictions for purely porous material is substantially reduced in the model predictions for crazed material. This is in better agreement with the experimental response that shows very stable neck.

To evaluate the stability of macroscopic deformation during drawing, a simple model proposed by Melick (2003) is applied. By this approach, the macroscopic tensile deformation is related to the intrinsic deformation parameters that govern yield, strain softening and strain hardening, determined from the experiments. The draw ratio of the neck $n_R := \sigma_{y,r}/C_R$, where $\sigma_{y,r}$ is the rejuvenated yield stress and C_R the strain hardening modulus, is employed as a representative estimator for stable neck. Details of this approach are found in Appendix B. The tensile limit and equilibrium curve of stable neck according to the experiment and the models are presented in Fig. 7.35.

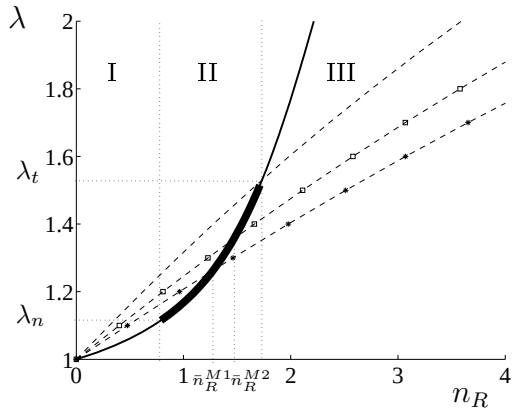

Figure 7.35: Stability of neck. The solid and dashed line represent the experimental equilibrium curve of stable neck growth and the stable neck limit, respectively. The trajectories with the markers $*$ and $\square$ are the stable limits according to the model for void growth and for void growth and crazing, respectively.

The stretch λ_n represents initiation of stable neck. The value λ_n is estimated from the ascending portion of experimentally observed uniaxial compression response by taking $\sigma = \sigma_y$, i.e. the stress state is large enough to induce yield in the material. Due to localization, the equilibrium curve is initially zero, i.e. strain softening is triggered by localization in region I. The thick line in region II, where the draw ratio ranges between $n_R = 0.7 - 1.7$, indicates stable neck upon drawing. The upper bound $n_R = 1.7$ is the value where the dashed line of tensile limit and the solid line of the equilibrium curve intersect. In region III, stable neck cannot be formed since maximum draw ratio for stable neck is already reached. Compared to the stable portion of the experimental equilibrium curve, the models result in considerably reduced range for stable neck, i.e. $\bar{n}_R^{M1} < \bar{n}_R^{M2} < 1.7$ in Fig. 7.35. Since the rejuvenated yield stress $\sigma_{y,r}$ is extracted from the experiment, the ratio n_R can increase only due to a decrease of the hardening modulus C_R. By the definition $C_R := nkT$ employed, the reducing strain hardening modulus is attributed to disentanglement. Based on the idea that entanglements represent topological constraints and on the observation that the topology does not evolve considerably in glassy state, the network density in state-of-the-art models is taken to be constant during deformation. However, the present numerical results explicitly suggest that a reduction of C_R should be considered in the models.

Assuming disentanglement is related to elevated viscosity with increasing elastic strain, numerical simulations based on the simple expression (6.11) were performed to see if hardening reduces. However, the results indicated only a small influence of viscosity on the maximum attainable draw ratio and localized deformation. Disentanglement was also modeled by assuming that the network density n evolves with time t as

$$\frac{\partial n}{\partial t} = -n\frac{p_0}{\tau} \tag{7.30}$$

where τ denotes a time interval, needed that a particular entangled point vanishes, and

$$p_0 = \exp\Big(-\frac{U_0 - \beta\Delta b_{eq}}{kT}\Big) \tag{7.31}$$

is the probability that a particular chain slips through an entangled point. In the above

equation, U_0 is the activation energy, β is the activation volume and

$$\Delta b_{eq} = \sqrt{trace(\frac{1}{2}(\boldsymbol{\beta}^{dev})^2)}$$

represents the difference in network stress between the two strands of a chain connected to a common entangled point, cf. Basu *et al.* (2005) for a more detailed account. When (7.30) is employed, disentanglement evolves already during softening and numerical simulations indicate a significant increase in void growth during neck. The free volume between the chains decreases pressure, and consequently the Brownian motion of chains eases and viscosity decreases. Assuming crazing evolves due to disentanglement and a critical amount of porosity for the nucleation of crazes is reached at the last part of softening, use is made of an assumption that the growth of existing voids is attenuated during necking, i.e. the equation (7.29) is employed.

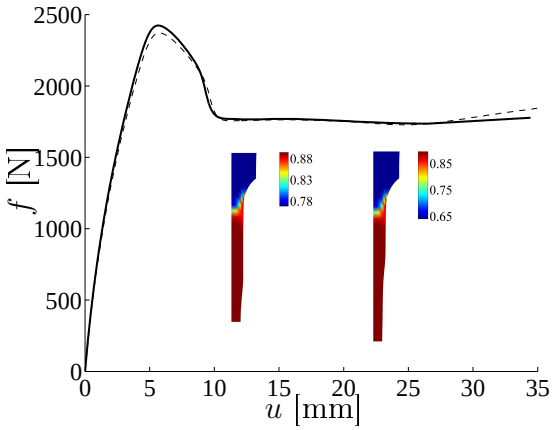

Figure 7.36: Influence of the reduction of network density n on $f-u$ response (solid line). The dashed line represents the response of the model for void growth and crazing. The parameters used in (7.30) are taken from Basu *et al.* (2005). The deformed shapes at $u = 12$ mm and $u = 22$ mm are highlighted by the network density ratio n/n_0. Using the EBPA model parameters, $n_0 = 3.4 \cdot 10^{27}$ m^{-3}.

The simulated $f-u$ response in Fig. 7.36 shows stabilizing effect due to disentanglement, i.e. the tensile limit of stable neck cannot be observed during elongation up to $u = 35$ mm. Loss of the network density 15% is reached at $u \approx 20$ mm, which value remains almost constant during further elongation. As it has been pointed out in preceding sections, similar effects cannot be observed if the network density alters without volume changes, i.e. the models for both void growth and crazing need to be applied. It can be concluded that the network density plays a pivotal role in determining the type of macroscopic failure through either shear yielding or crazing.

In order to evaluate possible craze-breakdown, the contour plot of the craze-strain ζ^p during the neck is shown in Fig. 7.34. The deformed meshes just prior to crazing and at $u = 33$ mm are also visualized by the plastic stretch $\bar{\lambda}^p_{ec}$ and the mean stress σ_m. A glance at the preceding results in Fig. 7.28 reveals that crazing has no notable influence on the localization of plastic deformation, i.e. the intensity and the rate of expansion remain virtually unaltered. It appears from Fig. 7.34 that the distribution of $\bar{\lambda}^p_{ec}$ is similar to the ζ^p-distribution which controls craze-initiation. The craze-strain ζ^p in its localized region ranges between $\zeta^p = 0.40 - 0.50$, which values with together the low intensity of the plastic stretching imply that the threshold ζ^p_t for craze-breakdown should be significantly greater than 0.50. In contrast to the expansion of localized deformation, the region of

pronounced mean stress rapidly propagates over the gauge section and reaches relatively stable values ranging between $27 - 32$ MPa. Since these values are higher than $0.4 - 0.5$ times the yield stress for PC, craze-initiation can be considered as an instantaneous process. As a conclusion of the present numerical results can be mentioned that crazing is seen to be a controlling mechanism for stable neck, whereas void growth governs the rate of neck propagation and the amount of intrinsic softening during localized deformation.

8 Summary and concluding remarks

This work is concerned with various aspects of the mechanical behavior and modeling of amorphous polymers. This work also provides an overview of micromechanically motivated constitutive models of amorphous glassy polymers developed over the past four decades. Special emphasis is devoted to the models of Arruda and Boyce (1991), Arruda and Boyce (1993a), Wu and Van der Giessen (1993), Anand and Ames (2006), Dupaix and Boyce (2007) and Miehe *et al.* (2009), these being representative of a whole range of current models. In these models, the chain network is represented by small cells and the constitutive description is based on Langevin chain statistics and the rate- and temperature-dependent Argon (1973) model. The models under consideration cover a broad range of strain rates as well as temperatures ranging from zero degrees to the glass transition temperature.

The microstructure of amorphous glassy polymers is formed by long linear molecular chains which form a network. The connections between the chains are formed by relatively weak secondary bonds called van der Waals forces. The secondary bonds are closely related to the physical entanglements: the increasing number of entanglements activates more bonds when the van der Waals forces grow and the resistance to slipping between chains increases. Due to the different microstructure, the ability to form entanglements during large deformation and a change of temperature differs between amorphous polymers. Entanglements also influence the mobility of chains during glass transition as well as mechanical properties, such as stress relaxation and creep.

During initial deformation, the chains slip against each other, and if the deformation rate is slow the chain molecules have enough time to relax and the amorphous structure remains unaltered. Once the yield limit is reached, the slipping between the chains increases and the response suddenly softens. In the large strain regime, the chains align with the loading direction which results in anisotropic response. As a majority of the chains have aligned with the loading direction and they have become fully stretched, a significant increase in stiffness of the polymer network can be observed. The described material behavior can be represented by an "S-shaped" response. In contrast to the glassy state, where only short-range motions can take place, the motion of individual chains near the glass transition temperature strongly increases and results in the material softening towards a melt.

The difference in the mechanical behavior under different conditions is explained by the amorphous network-structure. The primary variables for the description of the network structure are the initial and fully extended length of the chain segments between physical entanglements. Moreover, an average distribution of the chain segments, as well as the function of the entanglements, have to be defined. To allow for finite strains of polymer chains, non-Gaussian statistics have been employed and the motion of individual chains is allowed to fluctuate non-affinely around the macro-stretches. According to non-Gaussian statistics, an idealized chain consists of N statistically independent links of equal length l, and its fully extended length is given by $r_L = lN$. The initial length is defined by the

random walk-type mean-square value as $r_0 = l\sqrt{N}$. In recent models, the overall chain network is described by cells involving eight individual chain segments (8-chain model) or an infinite number of continuously distributed chains segments (full network model). Both the number of chains in a unit volume and the number of statistical links between the entanglements are typically considered to be constant. Due to the reduced set of chains, the models based on the 8-chain model are numerically more efficient than the full network models. However, the efficiency of the full network models can be improved using reduced integration schemes.

In a majority of the recent models, the initial material response is regarded as homogeneous. However, there exist a multiplicity of amorphous polymers having heterogeneous initial structure. Some heterogeneity is needed to relieve the build-up of high hydrostatic stress for a transition from crazing to shear yielding. In a part of the proposed models, the heterogeneity is accounted for by the inhomogeneous distribution of the chain density or by the initial heterogeneous shear strength distribution. In state-of-the-art models considered in this thesis, the plastic deformation stems from isotropic resistance due to chain segment rotations parallel with anisotropic resistance, which results from the stretching of the entire network and reorientation of the polymer chains. The notion for this hardening mechanism is usable under isothermal loading conditions well below the glass transition temperature T_g as well as it is motivated by the complete reversibility of plastic deformation at temperatures higher than T_g. In general, however, the strain hardening cannot be solely governed by the stretching of the network, but the hardening tends to decrease with temperature and, close to the glass transition temperature, the hardening is strongly influenced by the chain density of the polymer network. The strain hardening is also shown to alter with both the yield stress and viscosity of the material. Obviously, further research and validation is required concerning these topics.

In contrast to monotonic loading, most of the existing models are not able to accurately capture nonlinear unloading, creep and recovery, i.e. the transient effects after loading rate changes. These shortcomings are primarily a consequence of neglected viscoelastic effects. Even if models have been proposed for these purposes, they have been written under the assumption of small strains, or they include a large number of material parameters to be calibrated. The BPA model simulations performed in this work indicated that the backstress which was generated during the loading phase led to a premature Bauchinger effect and unrealistic recovery during long-term dwell. Motivated by these findings, an extension for the BPA model (termed the EBPA model) was proposed in this thesis. In contrast to the BPA model, the isotropic hardening is augmented by using an additional viscous dashpot, and the single linear spring is replaced by a simple Kelvin chain which is able to capture creep and nonlinear response during the loading cycles. The purpose of an additional viscous dashpot is to increase the amount of isotropic hardening in relation to the amount of kinematic hardening and thereby suppress the excessive Bauchinger effect and recovery during long-term dwell. Compared to the BPA model, only three new constitutive parameters need to be determined in the EBPA model.

The EBPA model is formulated in terms of the multiplicative decomposition of the total deformation gradient into an elastic and a plastic part. In order to use the proposed model in a finite element setting, an implicit integration algorithm was derived. Since the elastic rotation is constrained to be unity in the BPA model, the plastic spin generally is nonzero. To enforce this constraint, an algorithmic plastic spin is introduced in the integration algorithm. Due to the proposed viscoelastic description, the elastic deformation gradient must be further decomposed into the two parts and the rate form of the constitutive law must be derived. To specify the orientation of the elastic intermediate configuration, the first component of the elastic deformation gradient was chosen to be symmetric. As a result of the imposed symmetries of the elastic stretches, the rate form of the constitutive law was determined and introduced in the integration algorithm. Moreover, the tangent stiffness tensor consistent with the integration algorithm was derived and implemented in a finite element program. The numerical examples revealed that the numerical algorithms for updating the internal state variables as well as the equilibrium state are robust.

The EBPA model was calibrated for the different homogeneous deformation modes involving monotonic and non-monotonic loading conditions. Using the calibrated parameters, the predictive capability of the EBPA model was evaluated. Despite the relative simplicity of this model, comparison with the experiments showed that the model captures the nonlinear response of PC and PMMA during monotonic loading, unloading and creep well. Moreover, the calibrations indicated that a reduced evolution of the backstress in the EBPA model was crucial when modeling recovery. The proposed model was also found to be predictive for isothermal responses at various strain rates as well as for the large strain anisotropic responses of preoriented polymers.

The EBPA model was also calibrated to the force-displacement responses for inhomogeneous deformation acquired from cold drawing experiments on polycarbonate specimens. Various loading situations were experimented by using the Instron© tension/compression electromechanical testing machine provided by the Laboratory of Department of Material Sciences. It was shown that the parameters which were obtained from calibration to homogeneous deformation cannot be used to predict the experimental response of inhomogeneous deformation. In order to find the mechanisms that are able to explain this discrepancy, the models for the number of entanglements, void growth and crazing were implemented in a part of the EBPA model. Based on finite element analyses of the planar cell model, also the role of strain localization in the void growth, chain density as well as into the initiation and propagation of shear bands in the ligaments between the voids was addressed. The simulations showed that the initiation of shear bands promotes the intrinsic softening in the material, whereas the kinematic hardening is seen to be a driving force for widening of shear bands. The numerical results indicated also only a small influence of the number of entanglements and chain density on the macroscopic responses, whereas void grow significantly reduced intrinsic softening in the material. It was shown that the EBPA model, in conjunction with the modified Gurson model for void growth, predicts increased porosity and interaction between the voids and less intrinsic softening. As a re-

sult, the difference between the calibrated parameters for homogeneous and inhomogeneous deformation considerably decreased.

In order to suppress an excessive void growth during localized deformation and a premature hardening present in the simulations of the cold drawing experiment, a model for crazing was proposed in this thesis. In this model, crazing is assumed to result from disentanglement in highly concentrated regions of maximum principal stress, which nucleates new micro-voids. However, these voids do not grow, but coalesce to form initial crazes that widen and eventually cause local failure in the material. As a conclusion of the present numerical results can be mentioned that the plastic stability is essentially controlled by crazing, whereas void growth governs the rate of neck propagation and the amount of intrinsic softening during localized deformation.

Despite the active research carried out during the last two decades, the governing micromechanism that controls macroscopic mechanical behavior of amorphous glassy polymers is still not fully understood. A variety of models which are suitable only for a relatively narrow problem field and for a restricted set of amorphous polymers have been proposed. Moreover, the capability of the models to predict real material behavior is addressed only in a restricted set of loading situations. Thus the challenge is to develop accurate and reliable testing methods that contribute to the development of overall models suitable for predicting the material behavior at different length-scales, deformation states, temperatures as well as at different loading rates.

References

Adams, A. M., Buckley, C. P., and Jones, D. P. (2000). Biaxial hot drawing of poly(ethylene terephthalate): measurements and modelling of strain-stiffening. *Polymer*, **41**, 771–786.

Agah-Tehrani, A., Lee, E. H., Mallett, R. L., and Onat, E. T. (1987). The theory of elastic-plastic deformation at finite strain with induced anisotropy modeled as combined isotropic-kinematic hardening. *J. Mech. Phys. Solids*, **35**(5), 519–539.

Alibadi, M. H. (2001). *Nonlinear Fracture and Damage Mechanics.* WIT Press Southampton, UK.

Amin, A. F. M. S., Alam, M. S., and Okui, Y. (2002). An improved hyperelasticity relation in modeling viscoelasticity response of natural and high damping rubbers in compression: experiments, parameter identification and numerical verification. *Mechanics of Materials*, **34**(2), 75–95.

Anand, L. and Ames, N. M. (2006). On modeling the micro-indentation response of an amorphous polymer. *Int. J. Plasticity*, **22**, 1123–1170.

Anand, L. and Gearing, B. P. (2004). On modeling the deformation and fracture response of glassy polymers due shear-yielding and crazing. *Int. J. Solids Structures*, **41**, 3125–3150.

Anand, L. and Gurtin, M. E. (2003). A theory of amorphous solids undergoing large deformations, with application to polymeric classes. *Int. J. Solids Structures*, **40**, 1465–1487.

Argon, A. S. (1973). A theory for the low-temperature plastic deformation of glassy polymers. *Philosophical Magazine*, **28**(4), 839–865.

Argon, A. S. (1999). Craze plasticity in low molecular weight diluent-toughened polystyrene. *Journal of Applied Polymer Science*, **72**, 13–33.

Argon, A. S. (2011). Craze initiation in glassy polymers - revisited. *Polymer*, **52**, 2319–2327.

Argon, A. S. and Hannoosh, J. G. (1977). Initiation of crazes in polystyrene. *Philosophical Magazine*, **36**, 1195–1216.

Arruda, E. M. and Boyce, M. C. (1990a). An experimental and analytical investigation of the large strain compressive and tensile response of glassy polymers. *Polym. Engngn. Sci.*, **30**, 1288–1298.

Arruda, E. M. and Boyce, M. C. (1990b). Experimental and analytical investigation of the large strain compressive and tensile response of glassy polymers. *Polym. Engngn. Sci.*, **30**, 1288–1298.

Arruda, E. M. and Boyce, M. C. (1991). Anisotropy and localization of plastic deformation. In J. P. Boehler and A. S. Khan, editors, *Proc. Plasticity*, page 483. Elsevier Applied Science, London.

Arruda, E. M. and Boyce, M. C. (1993a). Evolution of plastic anisotropy in amorphous polymers during finite straining. *Int. J. Plasticity*, **9**, 697–720.

Arruda, E. M. and Boyce, M. C. (1993b). A three dimensional constitutive model for the large stretch behavior of rubber elastic materials. *J. Mech. Phys. Solids*, **41**, 389–412.

Arruda, E. M., Boyce, M. C., and Quintus-Bosz, H. (1993). Effects of initial anisotropy on the finite strain deformation behavior of glassy polymers. *Int. J. Plasticity*, **9**, 783–811.

Arruda, E. M., Boyce, M. C., and Jayachandran, R. (1995). Effects of strain rate temperature and thermomechanical coupling on the finite strain deformation of glassy polymers. *Mechanics of Materials*, **19**, 193–212.

Bardenhagen, S. G., Stout, M. G., and Gray, G. T. (1997). Three-dimensional, finite deformation, viscoplastic constitutive models for polymeric materials. *Mechanics of Materials*, **25**, 235–253.

Basu, S., Mahajan, D. K., and Van der Giessen, E. (2005). Micromechanics of the growth of a craze fibril in glassy polymers. *Polymer*, **46**, 7504–7518.

Beatty, M. F. (2003). An average-stretch full-network model for rubber elasticity. *Journal of Elasticity*, **70**, 65–86.

Becker, R. and Needleman, A. (1986). Effect of yield surface curvature on necking and failure in porous plastic solids. *J. Appl. Mech.*, **53**, 491–499.

Belytschko, T., Liu, W. K., and Moran, B. (2000). *Nonlinear Finite Elements for Continua and Structures.* John Wiley & Sons, Chichester.

Bergström, J. S. and Boyce, M. C. (1998). Constitutive modeling of the large strain time-dependent behavior of elastomers. *J. Mech. Phys. Solids*, **46**, 931–954.

Bonet, J. and Wood, R. D. (1997). *Nonlinear Continuum Mechanics for Finite Element Analysis.* Cambridge University Press, New York.

Bowden, P. B. and Jukes, J. A. (1972). The plastic flow of isotropic polymers. *Journal of Material Sciences*, **7**, 52–63.

Bowden, P. B. and Raha, S. (1970). The formation of micro shear bands in polystyrene and polymethylmethacrylate. *Philosophical magazine*, **22**, 463–482.

Boyce, M. C. and Arruda, E. M. (2000). Constitutive models of rubber elasticity: a review. *Rubber Chemistry and Technology*, **73**, 504–523.

Boyce, M. C. and Haward, R. N. (1997). *The post-yield deformation of glassy polymers. In: Haward R.N, Young R.J (Eds.), The Physics of Glassy Polymers. 2nd ed.* Chapman-Hall, London.

Boyce, M. C., Parks, D. M., and Argon, A. S. (1988). Large inelastic deformation of glassy polymers, Part I: Rate-dependent constitutive model. *Mechanics of Materials*, **7**, 15–33.

Boyce, M. C., Weber, G. G., and Parks, D. M. (1989). On the kinematics of finite strain plasticity. *J. Mech. Phys. Solids*, **37**, 647–665.

Brown, N. and Ward, I. M. (1968). Deformation bands in oriented PET. *Philosophical Magazine*, **17**, 961–981.

Caddell, R. M. and Woodliff, A. R. (1977). Macroscopic yielding of oriented polymers. *J. Mater.Sci.*, **12**, 2028–2036.

Cao, K., Wang, Y., and Wang, Y. (2012). Effects of strain rate and temperature on the tension behaviour of polycarbonate. *Materials and Design*, **38**, 53–58.

Capaldi, F. M., Boyce, M. C., and Rutledge, G. C. (2004). Molecular response of a glassy polymer to active deformation. *Polymer*, **45**, 1391–1399.

Chaboche, J. L. (2008). A review of some plasticity and viscoplasticity constitutive theories. *Int. J. Plasticity*, **24**, 1642–1693.

Christiansen, A. W., Bear, E., and Radcliffe, S. V. (1971). The mechanical behaviour of polymers under high pressure. *Phil. Mag.*, **24**, 451–467.

Chu, C. C. and Needleman, A. (1980). A void nucleation effects in biaxially stretched sheets. *ASME J. Engng. Materials Technol.*, **102**, 249–256.

Cohen, A. (1991). A pade approximant to the inverse langevin function. *Rheol Acta*, **30**(3), 270–273.

Colac, O. U. and Dusunceli, N. (2006). Modeling viscoelastic and viscoplastic behavior of high density polyethylene (HDPE). *ASME J. Engng. Materials Technol.*, **128**, 572–578.

Colac, O. U. and Dusunceli, N. (2008). The effects of manufacturing techniques on viscoelastic and viscoplastic behavior of high density polyethylene (HDPE). *Materials and Design*, **29**, 1117–1124.

Coleman, B. and Gurtin, M. E. (1967). Thermodynamics with internal state variables. *The Journal of Chemical Physics*, **47**, 597–613.

Courtney, T. H. (1999). *Mechanical Behavior of Materials.* McGraw-Hill, New York, 3nd edition.

Diu, B., Guthmann, C., Lederer, D., and Roulet, B. (1990). About the fundamental postulate of statistical mechanics. *Eur. J. Phys*, **11**, 160–162.

Dreistadt, C., Bonnet, A. S., Chevrier, P., and Lipinski, P. (2009). Experimental study of the polycarbonate behaviour during complex loadings and comparison with the Boyce, Parks and Argon model predictions. *Materials and Design*, **30**, 3126–3140.

Dupaix, R. B. and Boyce, M. C. (2005). Finite strain behavior of poly(ethylene terephthalate) (PET) and poly(ethylene terephthalate)-glycol (PETG). *Polymer*, **46**(13), 4827–4838.

Dupaix, R. B. and Boyce, M. C. (2007). Constitutive modeling of the finite strain behavior of amorphous polymers in and above the glass transition. *Mechanics of Materials*, **39**, 39–52.

Estevez, R., Tijssens, M. G. A., and Van der Giessen, E. (2000). Modeling of the competition between shear yielding and crazing in glassy polymers. *J. Mech. Phys. Solids*, **48**, 2585–2617.

Findley, W. N., Lai, J. S., and Onaran, K. (1989). *Creep and Relaxation of Nonlinear Viscoelastic Materials.* Dover, New York.

Flory, P. J. (1969). *Statistical Mechanics of Chain Molecules.* Interscience, New York.

Fried, J. R. (2009). *Polymer Science and Technology.* Prentice-Hall, United States, 2nd edition.

Ginzburg, B. M. (2005). On the "cold drawing" of semicrystalline polymers. *Journal of Macromolecular Science, Part B: Physics.*, **44**, 217–223.

Göktepe, S. (2007). *Micro-Macro Approaches to Rubbery and Glassy Polymers: Predictive Micromechanically-Based Models and Simulations. Doctoral thesis, Bericht Nr.: 1-20.* Stuttgart, Germany.

Gologanu, M., Leblond, J. B., Perrin, G., and Devaux, J. (1997). *Recent extensions of Gurson model for porous ductile metals. In: Suquet, P. (Ed.), Continuum Micromechanics.* Springer-Verlag, Berlin.

Goodier, J. (1933). *ASME Appl. Mech. Trans.*, **55**, 39.

Govaert, L. E., Timmermans, P. H. M., and Brekelmans, W. A. M. (2000). The influence of intrinsic strain softening and strain localization in polycarbonate: modeling and experimental validation. *ASME J. Engng. Materials Technol.*, **122**, 177–185.

G'Sell, C. and Gopez, A. J. (1985). Plastic banding in glassy polycarbonate under plane simple shear. *Journal of Materials Science*, **20**, 3462–3478.

G'Sell, C. and Jonas, J. J. (1979). Determination of the plastic behavior of solid polymers at constant strain rate. *Journal of Material Sciences*, **14**, 583–591.

G'Sell, C. and Jonas, J. J. (1981). Yield and transient effects during the plastic deformation of solid polymers. *Journal of Materials Science*, **16**, 1956–1974.

G'Sell, C., Hiver, J. M., and Dahoun, A. (2002). Experimental characterization of deformation damage in solid polymers under tension, and its interrelation with necking. *Int. J. Solids Structures*, **39**, 3857–3872.

Gurson, A. L. (1977). Continuum theory of ductile rupture by void nucleation and growth: Part I - yield criteria and flow rules for porous ductile media. *ASME J. Engng. Materials Technol.*, **99**, 2–15.

Harrysson, M., Ristinmaa, M., Wallin, M., and Menzel, A. (2010). Framework for deformation induced anisotropy in glassy polymers. *Acta Mechanica*, **211**, 195–213.

Hasan, A., Boyce, M. C., Li, X. S., and Berko, S. J. (1993). An investigation of the yield and postyield behavior and corresponding structure of poly(methyl methacrylate). *Polym Sci*, **31**, 185–197.

Hasan, O. A. and Boyce, M. C. (1995). A constitutive model for the nonlinear viscoelastic viscoplastic behavior of glassy polymers. *Polym. Engngn. Sci.*, **35**, 331–344.

Hasanpour, K. and Ziaei-Rad, S. (2008). Finite element simulation of polymer behavior using a three-dimensional, finite deformation constitutive model. *Comp. Struct.*, **86**, 1643–1655.

Haward, R. N. (1987). The application of a simplified model for the stress-strain curves of polymers. *Polymer*, **28**, 1485–1488.

Haward, R. N. and Thackray, G. (1968). The use of a mathematical model to describe isothermal stress-strain curves in glassy thermoplastics. *Proc. Roy. Soc. A.*, **302**, 453–472.

Haward, R. N. and Young, R. J. (1997). *The physics of glassy polymers 2nd. Ed.* Chapman-Hall, London.

Hochstetter, G., Jimenez, A., Cano, J. P., and Felder, E. (2002). An attempt to determine the true stress-strain curves of amorphous polymers by nanoindentation. *Tribology International*, **36**, 973–985.

Holopainen, S. (2011). *Modeling of Mechanical Behavior of Amorphous Glassy Polymers. Licentiate Dissertation. Report TFHF-1045*. Lund, Sweden.

Holopainen, S. (2012). Representations of m-linear functions on tensor spaces. Duals and transpositions with applications in continuum mechanics. *Accepted publication in Mathematics and Mechanics of Solids,* doi:10.1177/1081286512456199.

Holopainen, S. and Wallin, M. (2012). Modeling of long-term behavior of amorphous glassy polymers. *Accepted publication in ASME J. Engng. Materials Technol.,* doi:10.1115/1.4007499.

Hoy, R. S. and Robbins, M. O. (2007). Strain hardening of polymer glasses: entanglement, energetics, and plasticity. *Phys. Rev. Lett.*, **99**, 117801.

Huang, W. and Mura, T. (1972). Elastic energy of an elliptical-edge disclination. *Journal of Applied Physics*, **43**, 239–241.

Huber, N. and Tsakmakis, C. (2000). Finite deformation viscoelasticity laws. *Mechanics of Materials*, **32**(1), 1–18.

Ishikawa, M. and Ogawa, H. (1981). Brittle fracture in glassy polymers. *J. Macromolecules. Sci.-Phys. B 19*, **3**, 421–443.

James, H. M. and Guth, E. (1943). Theory of the elastic properties of rubber. *The Journal of Chemical Physics*, **11**, 455–481.

Kameda, J., Yokoyma, Y., and Allen, T. R. (2007). Strain-controlling mechanical behavior in noncrystalline materials I: Onset of plastic deformation. *Materials Science and Engineering*, **448**, 235–241.

Khan, A. and Zhang, H. (2001). Finite deformation of a polymer; experiments and modelling. *Int. J. Plasticity*, **17**, 1167–1188.

Khan, F. (2006). Loading history effects on the creep and relaxation behavior of thermoplastics. *ASME J. Engng. Materials Technol.*, **128**, 564–571.

Khan, F., Lopez-Pamies, O., and Kazmi, R. (2006). Thermo-mechanical large deformation response and constitutive modeling of viscoelastic polymers over a wide range of strain rates and temperatures. *Int. J. Plasticity*, **22**, 581–601.

Klompen, E. T. J., Engels, T. A. P., Govaert, L. E., and Meijer, H. E. H. (2005). Modeling of the post yield response of glassy polymers: influence of thermomechanical history. *Macromolecules*, **38**, 6997–7008.

Kramer, H. H. (1983). Microscopic and molecular fundamentals of crazing. *Advances in Polymer Science*, **52**, 1–56.

Kramer, H. H. and Berger, L. L. (1990). Craze growth and fracture. *Adv. Polym. Sc.*, **91**, 1–68.

Krempl, E. and Khan, F. (2003). Rate(time)-dependent deformation behavior; an overview of some properties of metals and solid polymers. *Int. J. Plasticity*, **19**, 1069–1095.

Li, J. C. M. and Gilman, J. J. (1970). Disclination loops in polymers. *Journal of Applied Physics*, **41**, 4248.

Love, A. E. H. (1944). *A Treatise on the Mathematical Theory of Elasticity.* Dover, New York.

Lu, J. and Ravi-Chandar, K. (1999). Inelastic deformation and localization phenomena in polycarbonate under tension. *Int. J. Solids Structures*, **36**, 391–425.

Lyulin, A. V., Li, J., Mulder, T., Vorselaars, B., and Michels, M. A. J. (2006). Atomistic simulation of bulk mechanics and local dynamics of amorphous polymers. *Macromol. Symp.*, **237**, 108–118.

Mahajan, D. K., Singh, B., and Basu, S. (2010). Void nucleation and disentanglement in glassy amorphous polymers. *Physical Review E.*, **82**, 1–8.

Melick, H. G. H. V. (2003). *Deformation and failure of polymer glasses. Doctoral thesis.* University Press Facilities, Eindhoven.

Melick, H. G. H. V., Govaert, L. E., and Meijer, H. E. H. (2003). On the origin of the strain hardening in glassy polymers. *Polymer*, **44**, 2493–2502.

Miehe, C. (1998). Comparison of two algorithms for the computation of fourth-order isotropic tensor functions. *Comp. Struct.*, **66**(1), 37–43.

Miehe, C. and Keck, J. (2000). Super-imposed finite elastic-viscoelastic-plastoelastic stress response with damage in filled rubbery polymers: experiment, modeling and algorithmic implementation. *J. Mech. Phys. Solids*, **48**(2), 323–365.

Miehe, C., Apel, N., and Lambrecht, M. (2002). Anisotropic additive plasticity in the logarithmic strain space: modular kinematic formulation and implementation based on incremental minimization principles for standard materials. *Comput. Methods Appl. Mech. Engng.*, **191**, 5383–5425.

Miehe, C., Göktepe, S., and Lulei, F. (2004). A micro-macro approach to rubber-like materials-Part I: the non-affine micro-sphere model of rubber elasticity. *J. Mech. Phys. Solids*, **52**, 2617–60.

Miehe, C., Göktepe, S., and Diez, J. M. (2009). Finite viscoplasticity of amorphous glassy polymers in the logarithmic strain space. *Int. J. Solids Structures*, **46**, 181–202.

Mulliken, A. and Boyce, M. (2006). Mechanics of the rate-dependent elastic-plastic deformation of glassy polymers from low to high strain rates. *Int. J. Solids Structures*, **43**, 1331–1356.

Needleman, A. (1988). Material rate dependence and mesh sensitivity in localization problems. *Comput. Methods Appl. Mech. Engng.*, **67**, 69–85.

Needleman, A. and Tvergaard, V. (1984). An analysis of ductile rupture in notched bars. *J. Mech. Phys. Solids*, **32**, 461–490.

Ortiz, C. and Hadziioannou, G. (1999). Entropic elasticity of single polymer chains of poly(methacrylic acid) measured by atomic force microscopy. *Macromolecules*, **32**, 780–787.

Perez, J. (1998). *Physics and Mechanics of Amorphous Polymers.* A.A. Balkema, Rotterdam.

Pijnenburg, K. G. W., Seeling, T., and Van der Giessen, E. (2005). Successively refined models for crack tip plasticity in polymer blends. *European Journal of Mechanics A/Solids*, **24**, 740–756.

Quintavalla, S. J. and Johnson, S. H. (2004). Extension of the Bergström-Boyce model to high strain rates. *Rubber Chemistry and Technology*, **77**(5), 972–981.

Raha, S. and Bowden, P. (1972). Birefringence of plastically deformed polymethylmetacrylate. *Polymer*, **13**, 174–83.

Rice, J. R. and Tracey, D. M. (1969). On the ductile enlargement of voids in triaxial stress fields. *J. Mech. Phys. Solids*, **17**, 201–217.

Robertson, R. E. (1966). Theory for the plasticity of glassy polymers. *The Journal of Chemical Physics*, **44**, 3950.

Seeling, T. and Van der Giessen, E. (2002). Localized plastic deformation in ternary polymer blends. *Int. J. Solids Structures*, **39**, 3505–3522.

Shampine, L. F., Reichelt, M. W., and Kierzenka, J. A. (1999). Solving index-1 DAEs in MATLAB and Simulink. *SIAM Review*, **41**(3), 538–552.

Socrate, S. and Boyce, M. C. (2000). Micromechanics of toughened polycarbonate. *J. Mech. Phys. Solids*, **48**, 233–273.

Srivastava, V., Chester, S. A., Ames, N. M., and Anand, L. (2010). A thermo-mechanically-coupled large-deformation theory for amorphous polymers in a temperature range which spans their glass transition. *Int. J. Plasticity*, **26**, 1138–1182.

Stachurski, Z. H. (2003). Strength and deformation of rigid polymers: the stress-strain curve in amorphous PMMA. *Polymer*, **44**, 6067–6076.

Steenbrink, A. C. and Van der Giessen, E. (1998a). *In: de Borst R, Van der Giessen E, editors. Material Instabilities in Solids*. Wiley.

Steenbrink, A. C. and Van der Giessen, E. (1998b). Studies on the growth of voids in amorphous glassy polymers. *Journal of Material Sciences*, **33**, 3163–3175.

Steenbrink, A. C., Van der Giessen, E., and Wu, P. D. (1997). Void growth in glassy polymers. *J. Mech. Phys. Solids*, **45**, 405–437.

Stein, E. and Sagar, G. (2008). Convergence behavior of 3D finite elements for Neo-Hookean material. *Engineering Computations: International Journal for Computer-Aided Engineering and Software*, **25**, 220–232.

Steinmann, P. and Stein, E. (1996). On the numerical treatment and analysis of finite deformation ductile single crystal plasticity. *Comput. Methods Appl. Mech. Engng.*, **129**, 235–254.

Stokes, V. K. and Nied, H. F. (1986). Solid phase sheet forming of thermoplastics, Parts I and II. *ASME J. Engng. Materials Technol.*, **108**, 107–118.

Sue, H.-J. and Yee, A. F. (1988). Deformation behaviour of a polycarbonate plate with a circular hole: finite elements model and experimental observations. *Polymer*, **29**(9), 1619–1624.

Sweeney, J. (1999). A comparison of three polymer network models in current use. *Computational and Theoretical Polymer Science*, **9**, 27–33.

Tomita, Y. (1999). Constitutive modeling of deformation behavior of glassy polymers and applications. *Int. J. Mech. Sci.*, **42**, 1455–1469.

Tomita, Y. and Tanaka, S. (1995). Prediction of deformation behavior of glassy polymers based on molecular chain network model. *Int. J. Solids Structures*, **32**(23), 3423–3434.

Tomita, Y. and Uchida, M. (2003). Characterization of micro- to macroscopic deformation behavior of amorphous polymer with heterogeneous distribution of microstructures. *Int. J. Mech. Sci.*, **45**, 1703–1716.

Treloar, L. R. G. (1946). The elasticity of a network of long-chain molecules: Part III. *Trans. Faraday Soc.*, **42**, 83–94.

Treloar, L. R. G. (1954). The photoelastic properties of short-chain molecular networks. *Trans. Faraday Soc.*, **50**, 881.

Treloar, L. R. G. and Riding, G. (1979). A non-Gaussian theory for rubber in biaxial strain. I. mechanical properties. *Proc. Roy. Soc. A.*, **369**, 261–280.

Tvergaard, V. (1981). Influence of voids on shear bands instabilities under plane strain conditions. *Int. J. Fracture*, **17**, 389–407.

Volterra, V. (1907). Sur l'equilibre des carps elastiques miltiplement connexes. *Annls Ec. Norm. Sup.*, **24**, 401–517.

Wang, M. C. and Guth, E. J. (1952). Statistical theory of networks of non-Gaussian flexible chains. *The Journal of Chemical Physics*, **20**(7), 1144–1157.

Ward, I. (1983). *Mechanical Properties of Solid Polymers.* John Wiley & Sons, Weinheim.

Ward, I. M. and Sweeney, J. (2004). *An Introduction to the Mechanical Properties of Solid Polymers.* John Wiley & Sons, Chichester.

Weber, G. and Anand, L. (1990). Finite deformation constitutuve equations and a time integration procedure for isotropic, hyperelastic-viscoplastic solids. *Comput. Methods Appl. Mech. Engng.*, **79**, 173–202.

Weltevreden, E. (2009). *Strain hardening in polymer glasses, phenomenology and modeling. Master Thesis.* Eindhoven, the Netherlands.

Wu, P. D. and Van der Giessen, E. (1993). On improved network models for rubber elasticity and their applications to orientation hardening in glassy polymers. *J. Mech. Phys. Solids*, **41**(3), 427–456.

Wu, P. D. and Van der Giessen, E. (1994). Analysis of shear band propagation in amorphous glassy polymers. *Int. J. Solids Structures*, **31**(11), 1493–1517.

Wu, P. D. and Van der Giessen, E. (1995). On neck propagation in amorphous glassy polymers under plane strain tension. *Int. J. Plasticity*, **11**(3), 221–235.

Zaïri, F., Woznica, K., and Naït-Abdelaziz, M. (2005). Phenomenological nonlinear modelling of glassy polymers. *Comptes Rendus Mecanique*, **333**, 359–364.

Zaïri, F., Naït-Abdelaziz, M., Gloaguen, J. M., and Lefebvre, J. M. (2011). A physically-based constitutive model for anisotropic damage in rubber-toughened glassy polymers during finite deformation. *Int. J. Plasticity*, **27**, 25–51.

Zaïri, F., Naït-Abdelaziz, M., Gloaguen, J. M., and Lefebvre, J. M. (2008). Modeling of the elasto-viscoplastic damage behavior of glassy polymers. *Int. J. Plasticity*, **24**, 945–965.

Zener, C. (1948). *Elasticity and Anelasticity of Metals.* University of Chicago Press, Chicago.

Zhang, Y. and Huang, Z.-P. (2004). A model for the non-linear viscoelastic behavior of amorphous polymers. *Mechanics Research Communications*, **31**, 195–202.

Zhang, Z. L., Thaulow, C., and Ødegård, J. (2000). A complete Gurson model approach for ductile fracture. *Engng. Fract. Mech.*, **67**, 155–168.

Appendix A. Numerical treatment of the EBPA model

The evolution equations used in the simulations for homogeneous deformation are derived below. Once the uniaxial and plane strain compression case have been presented, the simple shear case is obtained by analogue and it is not presented here. In contrast to plane strain compression, which is simulated using monotonic loading, uniaxial compression is simulated using monotonic loading, unloading, and dwell. The total deformation gradient during uniaxial and plane strain compression can be expressed by

$$\boldsymbol{F} = v_{11}\boldsymbol{e}_1 \otimes \boldsymbol{e}_1 + v_{22}\boldsymbol{e}_2 \otimes \boldsymbol{e}_2 + v_{33}\boldsymbol{e}_3 \otimes \boldsymbol{e}_3, \tag{A.1}$$

where $\{\boldsymbol{e}_i,\ i = 1,2,3\}$ are the unit base vectors and v_{ii} are the principal stretches. Based on the polar decomposition the elastic part of the deformation gradient $\boldsymbol{F}^e$ in (6.4) can be written as

$$\boldsymbol{F}^e = \boldsymbol{v}^e\boldsymbol{R}^e = \boldsymbol{F}_1^e\boldsymbol{F}_2^e = \boldsymbol{v}_1^e\boldsymbol{R}_1^e\boldsymbol{v}_2^e\boldsymbol{R}_2^e. \tag{A.2}$$

Assuming $\boldsymbol{R}_1^e$ to be unity, it follows that the components of $\boldsymbol{R}_2^e$ and $\boldsymbol{R}^e$ are equal and (A.2) can be formally written as

$$\boldsymbol{v}^e = \boldsymbol{v}_1^e\boldsymbol{v}_2^e. \tag{A.3}$$

Since the total elastic deformation is also irrotational, the components of $\boldsymbol{F}^e$ and $\boldsymbol{v}^e$ are equal and (A.3) becomes $\boldsymbol{F}^e = \boldsymbol{v}^e = \boldsymbol{v}_1^e\boldsymbol{v}_2^e = \boldsymbol{v}_2^e\boldsymbol{v}_1^e$. Thus, the logarithm of $\ln \boldsymbol{v}^e$ is given by

$$\ln \boldsymbol{v}^e = \ln \boldsymbol{v}_1^e + \ln \boldsymbol{v}_2^e. \tag{A.4}$$

Substituting the material time derivative of (A.4) into (6.6) yields the following expression for the stress rate

$$\begin{aligned}\dot{\boldsymbol{\tau}} &= \boldsymbol{\mathcal{L}}^e(E) : \big[\frac{d}{dt}(\ln \boldsymbol{v}^e) + \boldsymbol{\eta}^{-1} : \boldsymbol{\mathcal{L}}^e(E_1) : \ln \boldsymbol{v}^e - \boldsymbol{\eta}^{-1} : (\boldsymbol{\mathcal{L}}^e(E_1) : \boldsymbol{\mathcal{L}}^{e-1}(E) + \boldsymbol{\mathcal{I}}) : \boldsymbol{\tau}\big] \\ &=: \boldsymbol{g}(\boldsymbol{\tau}, \ln \boldsymbol{v}^e; \frac{d}{dt}(\ln \boldsymbol{v}^e)).\end{aligned} \tag{A.5}$$

Employing the convected stress rate of the Kirchhoff stress

$$\boldsymbol{\tau}^{\triangledown} = \dot{\boldsymbol{\tau}} - \boldsymbol{l}\boldsymbol{\tau} - \boldsymbol{\tau}\boldsymbol{l}^T, \tag{A.6}$$

the rate form retains objectivity, cf. Belytschko *et al.* (2000). Another frequently used objective stress rate is the Jaumann rate of the Kirchhoff stress, which under these stress states becomes $\dot{\boldsymbol{\tau}}^J = \dot{\boldsymbol{\tau}} - \boldsymbol{\omega}\boldsymbol{\tau} + \boldsymbol{\tau}\boldsymbol{\omega} = \dot{\boldsymbol{\tau}}$.

In general, as with the isotropic elasticity tensor $\boldsymbol{\mathcal{L}}^e$, $\boldsymbol{\eta}$ is regarded as a fourth order tensor, given by

$$\boldsymbol{\eta} = \eta_1\boldsymbol{\mathcal{I}} + \eta_2\boldsymbol{i} \otimes \boldsymbol{i}$$

where η_1 and η_2 are viscosities that govern elastic shear and volumetric deformation, respectively. They may also depend on temperature and the elastic strain rate, cf. Hasanpour and Ziaei-Rad (2008). For a convenience, however, viscosity is regarded as a scalar in subsequent considerations.

In the experiments, unloading and dwell are controlled by a constant nominal or Piola-

Kirchhoff stress rate, $\boldsymbol{\pi}^{\triangledown}$, defined by

$$\boldsymbol{\pi}^{\triangledown} := \boldsymbol{\tau}^{\triangledown}\boldsymbol{F}^{-T} + \boldsymbol{\tau}\frac{d}{dt}(\boldsymbol{F}^{-T}). \tag{A.7}$$

During uniaxial and plane strain compression $(4.12)_2$, (6.2), (A.5) and (A.7) can be combined to yield a system of differential equations that governs the response in one material point. We will represent the governing equations as

$$\boldsymbol{M}(\boldsymbol{y})\dot{\boldsymbol{y}} = \boldsymbol{f}(\boldsymbol{y}), \tag{A.8}$$

where $\boldsymbol{M}, \boldsymbol{y}$ and $\boldsymbol{f}$ are defined below for both load cases. The system (A.8) is solved using a backward-differentiation based Runge-Kutta integration scheme, cf. Shampine *et al.* (1999).

Plane strain compression

In plane strain case, the principal directions remain unaltered and thus $d/dt \ln v^e_{ii} = \dot{v}^e_{ii} v^{e-1}_{ii}$, $i = 1, 2, 3$. A glance at $(4.12)_1$ and (4.9), and noting that the elastic deformation is irrotational, reveals that $\dot{v}^e_{ii} = d^e_{ii} v^e_{ii}$, i.e. $d/dt \ln v^e_{ii} = d^e_{ii} = d_{ii} - v^e_{ii}\bar{D}^p_{ii} v^{e-1}_{ii} = d_{ii} - \bar{D}^p_{ii}$. Assuming $\dot{\tau}_{22} = 0$ and $\tau_{22} = 0$ and using (A.5), the elastic deformation is constrained to satisfy

$$d_{22} = \frac{1}{\eta}\big(((\boldsymbol{\mathcal{L}}^e_1 : \boldsymbol{\mathcal{L}}^{e-1})_{22ii} + \delta_{2i})\tau_{ii} - \mathcal{L}^e{}_{1,22ii} \ln v^e_{ii}\big) + \bar{D}^p_{22}, i = 1, 2, 3, \tag{A.9}$$

where the notation $\boldsymbol{\mathcal{L}}^e_1 := \boldsymbol{\mathcal{L}}^e(E_1)$ was introduced for the sake of simplicity. In the numerical scheme, the component d_{11} is given. Based on (A.5) the nonzero components of the convected stress rate evolve according to

$$\begin{aligned}\tau^{\triangledown}_{jj} = &\left(\mathcal{L}^e{}_{jjii} d^e_{ii} - \frac{1}{\eta}\big(((\boldsymbol{\mathcal{L}}^e : \boldsymbol{\mathcal{L}}^e_1 : \boldsymbol{\mathcal{L}}^{e-1})_{jjii} + \mathcal{L}_{jjii})\tau_{ii} - (\boldsymbol{\mathcal{L}}^e : \boldsymbol{\mathcal{L}}^e_1)_{jjii} \ln v^e_{ii}\big)\right) - \\ &2\tau_{11} d_{11} =: g_{jj},\end{aligned} \tag{A.10}$$

$i = 1, 2, 3$ and $j = 1, 3$. Due to the plane strain compression state, a glance at (4.8) reveals that $v_{33} = 1$. Based on the multiplicative split (4.3) we conclude that $v^e_{33} = (\bar{V}^p_{33})^{-1}$. The system of differential equations (A.8) is now governed by the unit matrix as

$$\begin{bmatrix} 1 & 0 & 0 & 0 & 0 & 0 & 0 & 0 \\ 0 & 1 & 0 & 0 & 0 & 0 & 0 & 0 \\ 0 & 0 & 1 & 0 & 0 & 0 & 0 & 0 \\ 0 & 0 & 0 & 1 & 0 & 0 & 0 & 0 \\ 0 & 0 & 0 & 0 & 1 & 0 & 0 & 0 \\ 0 & 0 & 0 & 0 & 0 & 1 & 0 & 0 \\ 0 & 0 & 0 & 0 & 0 & 0 & 1 & 0 \\ 0 & 0 & 0 & 0 & 0 & 0 & 0 & 1 \end{bmatrix} \begin{bmatrix} \dot{\bar{V}}^p_{11} \\ \dot{\bar{V}}^p_{22} \\ \dot{\bar{V}}^p_{33} \\ \dot{v}^e_{22} \\ \tau^{\triangledown}_{11} \\ \tau^{\triangledown}_{33} \\ \dot{s}_1 \\ \dot{s}_2 \end{bmatrix} = \begin{bmatrix} \bar{D}^p_{11}\bar{V}^p_{11} \\ \bar{D}^p_{22}\bar{V}^p_{22} \\ \bar{D}^p_{33}\bar{V}^p_{33} \\ d^e_{22} v^e_{22} \\ g_{11} \\ g_{33} \\ h_1(1 - \frac{s_1}{s_{ss}})\dot{\gamma}^p \\ h_2\dot{\gamma}^p \end{bmatrix} \tag{A.11}$$

The rows 4-6 and 8 in (A.11) are needed only in the EBPA model. According to the BPA model,

the elastic deformation is constrained to satisfy

$$\ln v^e_{33} = -(\ln v^e_{11} + \frac{1-\nu}{\nu}\ln v^e_{22}). \tag{A.12}$$

Based on Eq. (A.12) the stress component in the direction of the applied load is given by

$$\tau_{11} = \frac{E}{(1+\nu)}(\ln v^e_{11} - \ln v^e_{22}). \tag{A.13}$$

Uniaxial compression

Due to the uniaxial stress state, the constraint (A.9) for the elastic deformation is reduced to

$$d_{33} = d_{22} = \frac{1}{\eta}\big(((\boldsymbol{\mathcal{L}}^e_1 : \boldsymbol{\mathcal{L}}^{e-1})_{2211})\tau_{11} - \mathcal{L}^e{}_{1,22ii}\ln v^e_{ii}\big) + \bar{D}^p_{22} \tag{A.14}$$

and d_{11} is given during the loading phase. Due to the symmetry, $v_{33} = v_{22}$ in (A.1) and thus it follows from (4.3) and (4.8) that $v^e_{33} = v^e_{22}$ and $\bar{V}^p_{33} = \bar{V}^p_{22}$. The only nonzero stress component is denoted by τ_{11}. During unloading and dwell, the component d_{11} is not prescribed but it is solved from (A.8). Based on (A.5)

$$\begin{aligned}\tau^{\triangledown}_{11} = \Big(&2\mathcal{L}^e{}_{1122}d^e_{22} + \mathcal{L}^e_{1111}(d_{11} - \bar{D}^p_{11}) - \frac{1}{\eta}\big(((\boldsymbol{\mathcal{L}}^e : \boldsymbol{\mathcal{L}}^e_1 : \boldsymbol{\mathcal{L}}^{e-1})_{1111} + \mathcal{L}^e{}_{1111})\tau_{11} - \\ &(\boldsymbol{\mathcal{L}}^e : \boldsymbol{\mathcal{L}}^e_1)_{11ii}\ln v^e_{ii}\big)|_{i=1,2,3}\Big) - 2\tau_{11}d_{11}.\end{aligned} \tag{A.15}$$

According to the simulations, the experimental response can be captured more accurately using the viscous damping only in the first direction, i.e. $\eta d^e_{22} = \eta d^e_{33} = 0$. This constrains the elastic deformation to be

$$\ln v^e_{33} = \ln v^e_{22} = -\nu \ln v^e_{11} \tag{A.16}$$

where ν is the Poisson's ratio. The stress rate equation becomes

$$\begin{aligned}\tau^{\triangledown}_{11} = \Big(&\mathcal{L}^e_{1111}(d_{11} - \bar{D}^p_{11}) - \frac{1}{\eta}\mathcal{L}^e_{1111}\big(((\boldsymbol{\mathcal{L}}^e_1 : \boldsymbol{\mathcal{L}}^{e-1})_{1111} + 1)\tau_{11} - \mathcal{L}^e_{1,11ii}\ln v^e_{ii}\big)|_{i=1,2,3}\Big) - \\ &2\tau_{11}d_{11} =: g_{11} + \varrho\dot{v}_{11}\end{aligned} \tag{A.17}$$

where

$$\begin{aligned}g_{11} &:= -\mathcal{L}^e_{1111}\bar{D}^p_{11} - \frac{1}{\eta}\mathcal{L}^e_{1111}\big(((\boldsymbol{\mathcal{L}}^e_1 : \boldsymbol{\mathcal{L}}^{e-1})_{1111} + 1)\tau_{11} - \mathcal{L}^e_{1,11ii}\ln v^e_{ii}\big)|_{i=1,2,3}, \\ \varrho &:= (\mathcal{L}^e{}_{1111} - 2\tau_{11})v^{-1}_{11}.\end{aligned}$$

Use of (A.1) in (A.7) results in $\pi^{\triangledown}_{11} = \tau^{\triangledown}_{11}v^{-1}_{11} - \tau_{11}v^{-2}_{11}\dot{v}_{11}$. During dwell and unloading $\pi^{\triangledown}_{11} = 0$ and $\pi^{\triangledown}_{11} = 2.3$ MPa/s, respectively. The governing differential equations (A.8) can now be summarized

as

$$\begin{bmatrix} 1 & 0 & 0 & 0 & 0 & 0 \\ 0 & 1 & 0 & 0 & 0 & 0 \\ 0 & 0 & 1 & 0 & 0 & -\varrho \\ 0 & 0 & 0 & 1 & 0 & 0 \\ 0 & 0 & 0 & 0 & 1 & 0 \\ 0 & 0 & v_{11}^{-1} & 0 & 0 & -\tau_{11} v_{11}^{-2} \end{bmatrix} \begin{bmatrix} \dot{\bar{V}}_{11}^p \\ \dot{\bar{V}}_{22}^p \\ \tau_{11}^{\triangledown} \\ \dot{s}_1 \\ \dot{s}_2 \\ \dot{v}_{11} \end{bmatrix} = \begin{bmatrix} \bar{D}_{11}^p \bar{V}_{11}^p \\ \bar{D}_{22}^p \bar{V}_{22}^p \\ g_{11} \\ h_1 (1 - \frac{s_1}{s_{ss}}) \dot{\gamma}^p \\ h_2 \dot{\gamma}^p \\ \pi_{11}^{\triangledown} \end{bmatrix} \tag{A.18}$$

The rows 3, 5 and 6 in (A.18) are needed only in the EBPA model. In the BPA model, the stress is given by (4.113) and the last row in (A.18) for unloading and dwell is replaced by

$$-v_{11}^e \dot{\bar{V}}_{11}^p + (1 - \ln v_{11}^e) \dot{v}_{11} = \frac{\pi_{11}^{\triangledown}}{E} (v_{11})^2.$$

Appendix B. Stability of neck drawing

A model to evaluate the stability of macroscopic deformation during drawing is presented below. In contrast to the original approach by Haward (1987), this model takes also strain softening, specific to amorphous polymers, into consideration, cf. Melick (2003). The macroscopic tensile deformation is related to the intrinsic deformation parameters that govern yield, strain softening and strain hardening, determined from the experiments. The true stress vs stretch curve in Fig. B.1(a) after the point λ_i is relatively well captured by the expression

$$\sigma = \kappa_t \sigma_{y,r} = \sigma_{y,r} + C_R(\lambda^2 - \frac{1}{\lambda}) \quad \Rightarrow \quad n_R := \frac{\sigma_{y,r}}{C_R} = \frac{\lambda^2 - \frac{1}{\lambda}}{\kappa_t - 1} \tag{B.1}$$

where $\sigma_{y,r}$ is the rejuvenated yield stress, C_R is the hardening modulus and n_R is the draw ratio of neck. Taking the stress of the stretched polymer to be $\sigma = \sigma_t$ in (B.1), defines the tensile limit $\lambda = \lambda_t$ for stable neck. For (semi-)crystalline polymers, however, the true stress

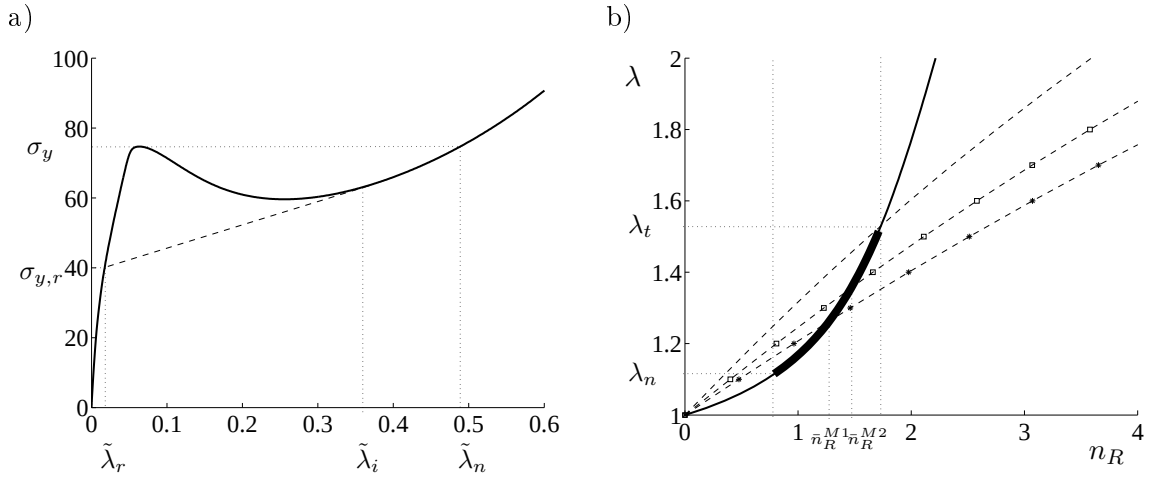

Figure B.1: a) Illustration of intrinsic strain softening in terms of the yield stress σ_y and the rejuvenated yield stress $\sigma_{y,r}$. The stress response during strain hardening is proportional to $\tilde{\lambda} = \lambda^2 - 1/\lambda$. b) Stability of neck. The solid and dashed line represent the equilibrium curve of stable neck growth and the stable neck limit, respectively. The trajectories with the markers $*$ and $\square$ are the stable limits according to the model for void growth and for void growth and crazing, respectively.

is not able to represent a reversed transition after the macroscopic yield point, which effect the nominal (engineering) stress does capture. This feature is known as geometric softening. Also in testing of amorphous polymers, shear banding and necking make generally the nominal stress more measurable quantity. By analogy to (B.1), but using the nominal stress $\pi := 1/\lambda\sigma$, the stress vs stretch relation is given by

$$\pi = \tilde{\kappa}_y \frac{\sigma_{y,r}}{\lambda_r} := \kappa_y \sigma_{y,r} = \frac{1}{\lambda}\big(\sigma_{y,r} + C_R(\lambda^2 - \frac{1}{\lambda})\big) \quad \Rightarrow \quad n_R := \frac{\sigma_{y,r}}{C_R} = \frac{\lambda^2 - \frac{1}{\lambda}}{\kappa_y \lambda - 1} \tag{B.2}$$

where $\tilde{\kappa}_y := \kappa_y \lambda_r$, λ_r is the stretch corresponding to the rejuvenated stress $\sigma_{y,r}$ and κ_y is a multiplier representing strain softening. The estimated stretch λ_n for a stable neck is reached when $\sigma = \sigma_y$ in (B.2), i.e. the stress state is large enough to induce yield in the material, cf.

Fig. B.1(a). This limit as well as $\sigma_{y,r}$ can be extracted from a uniaxial compression experiment, cf. Melick *et al.* (2003). Softening of the experimental response is typically characterized by the values $\kappa_y = 1.2 - 1.3$, cf. Figs. 6.4 and 7.17.

A non-dimensional quantity $\lambda = (u + L)/L$ is introduced for the evaluation of the true overall stress from cold drawing experiments, whereas the nominal stress $\pi := f/A_0$ is defined as the applied load f divided by the initial cross-section A_0. The hardening modulus $C_R = 14.0$ MPa and the position $u \approx 63$ mm in which stabilized neck ends define an approximation for the factor $\kappa_t = 1.9$, cf. Fig. 7.17.

Both the tensile limit of stable neck (B.1) and the equilibrium curve (B.2) are presented in Fig. B.1(b). The thick line indicates stable neck upon drawing. The upper bound $n_R = 1.7$ is the value where the dashed line of tensile limit and the solid line of the equilibrium curve intersect. For comparison, also the tensile limits resulting from the model responses are presented, determined by analogy to the experimental one. For both the models, $\kappa_y = 1.3$ is used. The values $n_R^{M1} \approx 1.25$ and $n_R^{M2} \approx 1.50$ are the upper limits for stable neck according to the models.

Tampereen teknillinen yliopisto
PL 527
33101 Tampere

Tampere University of Technology
P.O.B. 527
FI-33101 Tampere, Finland

ISBN 978-952-15-3005-0
ISSN 1459-2045